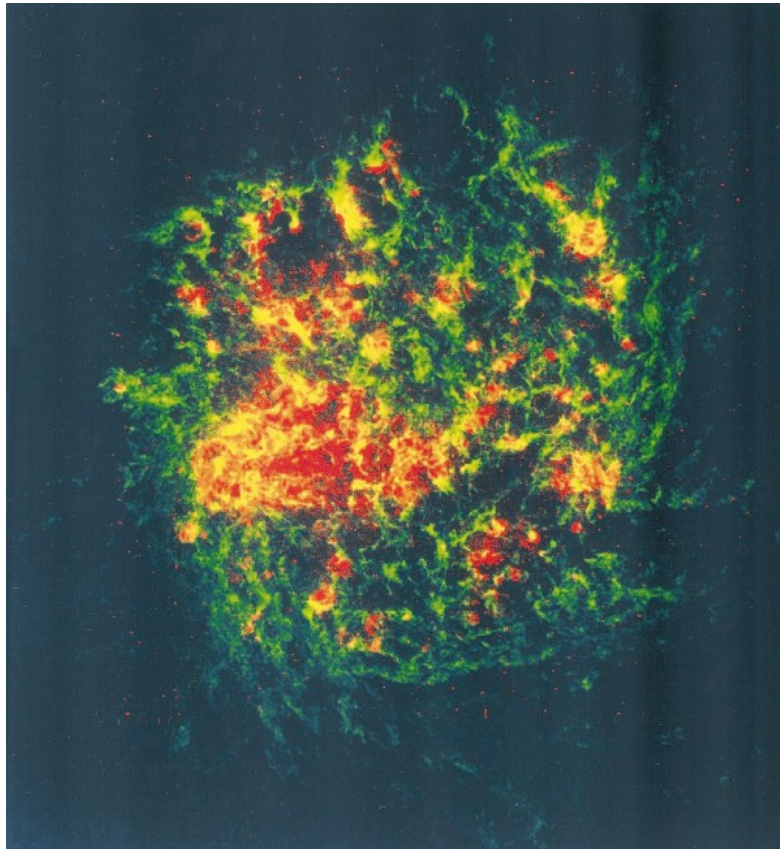


CHALMERS



The Effect of Turbulence on the Gravitational Instability of Galactic Discs

Master of Science Thesis

VOLKER HOFFMANN

Supervisor: Alessandro Romeo

Department of Earth and Space Sciences
Chalmers University of Technology
Gothenburg, Sweden, 2011
Master's Thesis 2011:05

MASTER'S THESIS

The Effect of Turbulence on the Gravitational Instability of Galactic Discs

Author

Volker Hoffmann

Supervisor

Alessandro Romeo

Department of Earth and Space Sciences
Chalmers University of Technology
Gothenburg, Sweden

May 2011

The Effect of Turbulence on the Gravitational Instability of Galactic Discs
Volker Hoffmann (volker@cheleb.net)

© Volker Hoffmann, 2011

Department of Earth- and Space Sciences
Chalmers University of Technology
SE-412 96 Gothenburg, Sweden
+46 31-772 1000

Onsala Space Observatory
SE-439 92 Onsala, Sweden
+46 31-772 5500

Cover: Distribution of atomic hydrogen in the Large Magellanic Cloud. Emission from the 21 cm line tracing neutral atomic hydrogen is coloured green and $H\alpha$ emission from ionized hydrogen is coloured red. The emissions reveal multi-scale patterns indicative of turbulent motions. The image is adopted from Kim et al. (1999).

ABSTRACT

In recent years, extragalactic astronomy has taken huge strides forward. In the local universe, state-of-the-art surveys provide high resolution maps of neighbouring galaxies. These allow us to investigate how stars form out of the turbulent interstellar gas in unprecedented detail (e.g. McKee & Ostriker, 2007; Leroy et al., 2008). Farther out, at redshifts $z \sim 1 - 3$, deep field observations have revealed a population of turbulent, clumpy, star-forming galaxies (e.g. Förster Schreiber et al., 2009). These suspected progenitors of present-day spiral galaxies have attracted great interest resulting in a large number of exploratory studies (e.g. Elmegreen et al., 2009; Burkert et al., 2010).

Based on the work of Toomre (1964), models of gravitational instability are frequently used to describe the conditions in the interstellar gas leading up to star-formation. As the cycle of formation and destruction of stars is inherently linked to the evolution of galaxies as a whole, so are models of gravitational instability. In light of evidence for turbulent motions in various epochs of galactic evolution, it is only natural to extend such models with descriptions of turbulence.

Using a phenomenological model of turbulence where densities and velocity dispersions follow power-laws, we extend existing models of gravitational instability. We use the result to investigate the gravitational instability of two different types of discs. Firstly, we consider the stability of a disc of neutral atomic hydrogen (HI) and molecular hydrogen (H_2) on scales below ~ 100 pc. Secondly, we analyse the stability of a disc of turbulent HI and stars on galactic scales above ~ 1 kpc. Finally, we apply the latter analysis to extend a previous investigation of nearby star-forming spiral galaxies by Leroy et al. (2008).

In the case of HI and H_2 , we find that the stability of H_2 alone (i) determines the type of stability of the disc containing both HI and H_2 , and (ii) dominates the stability properties of the disc. For a disc of HI and stars, we find that turbulence in HI rescales the stability characteristics as compared to a disc containing non-turbulent HI and stars. Applying the model of a disc of HI and stars to the aforementioned sample of galaxies, we discover that turbulence tends to (i) stabilize the disc, (ii) decrease the wavelength associated with the onset of instabilities, and (iii) decouple the dynamical response of stars and HI. We observe similar trends when lowering the gaseous velocity dispersion to investigate the stability in regions where the H_2 density exceeds that of HI.

The analysis carried out in this thesis will provide a useful framework for interpreting data from upcoming next-generation observations and simulations of high-redshift galaxies.

ACKNOWLEDGEMENTS

First and foremost, I would like to thank my supervisor Alessandro Romeo for his enormous dedication in advising me during this work. I will never forget his infectious enthusiasm in discussing topics ranging from the more arcane aspects of galactic dynamics and numerical methods to clever typesetting and writing tricks. Molto Grazie!

Secondly, I want to thank Joachim Wiegert who has been working on a very similar thesis topic. It has been a great experience having a fellow student around to discuss new ideas, but also more mundane things with.

I would further like to thank all staff and students at the Onsala Space Observatory for letting me use the facilities at this wonderful location and never turning away when I had questions ranging from organizational things to aspects of observational astrophysics and cosmology.

Finally, I also owe a debt of gratitude to both Christin and my family for supporting me through this work and putting up with me not visiting or getting in touch as much as I would have liked to.

Volker Hoffmann
Gothenburg, Sweden
May 2011

CONTENTS

1. Introduction	1
2. Galaxies, Turbulence, The Interstellar Medium	3
2.1. Galaxies and The Interstellar Medium	3
2.2. Turbulence in Incompressible Fluids	7
2.3. Turbulence in The Interstellar Medium	8
2.4. Chapter Summary	10
3. Theory of Galactic Disc Stability	11
3.1. Kinetic and Fluid Approach	11
3.2. Procedure and Assumptions	12
3.3. One-Fluid Case	13
3.3.1. Dispersion Relation, Marginal Stability Curve	13
3.3.2. The Velocity Dispersion, Accuracy of the Fluid Approach	15
3.4. Two-Fluid Case	17
3.4.1. Dispersion Relation, Marginal Stability Curve	17
3.4.2. The Two-Phase Region	18
3.4.3. Accuracy of the Fluid Approach	19
3.5. The Turbulent One-Fluid Case	19
3.5.1. Scaling Relations in the Cold ISM	19
3.5.2. Dispersion Relation, Stability Map of Turbulence	20
3.5.3. Stability Threshold, Saturation Scale	22
3.6. Chapter Summary	22
4. Stability of Turbulent Two-Component Discs	25
4.1. Comparison of One- and Two-Component Dispersion Relations	25
4.2. General Equations for Two Turbulent Components	28
4.2.1. Dispersion Relation	29
4.2.2. Marginal Stability Curve	30
4.2.3. The Parameter Space	31
4.3. Stability of Coupled Turbulent H _I and Turbulent H ₂	33
4.3.1. Stability Regime of the Coupled System	33
4.3.2. Extension: Turbulent Virialized and Toomre-like Components	36
4.3.3. The Effects of Varying s_0 , q_0 , and Λ_0	37
4.4. Stability of Coupled Gaseous and Stellar Disks	39
4.4.1. Marginal Stability Curves	41

4.4.2. Stability Threshold	47
4.4.3. Most Unstable Scale	50
4.4.4. Extension: Different Turbulent Scaling Exponents	53
4.5. Chapter Summary	55
5. Application to Nearby Star Forming Galaxies	57
5.1. The Star Formation Problem	57
5.2. The L08 Study of Star Formation in Nearby Galaxies	58
5.2.1. Star Formation Efficiency, Thresholds, and Phase Transitions	58
5.2.2. Surveys, Observations to Physical Quantities, Assumptions	59
5.2.3. Main Findings of the L08 Study	60
5.2.4. Effects of Uncertainties	63
5.3. Two-Component Gravitational Stability in 12 Spirals	64
5.3.1. The Improved Model	64
5.3.2. The Parameter Plane	65
5.3.3. Stability Threshold	72
5.3.4. Most Unstable Scale	76
5.3.5. Tight-Winding Condition	80
5.4. Chapter Summary	81
6. Conclusions	85
6.1. Conclusions	85
6.2. Topics for Further Investigation	86
A. Computation of Model Parameters and Stability Diagnostics	87
A.1. Physical Quantities	87
A.2. Model Parameters	87
A.3. Stability Diagnostics	88
A.3.1. Effective Stability Parameter, Most Unstable Wavelength	88
A.3.2. Stability Threshold, Most Unstable Scale	89
B. Radial Profiles of Model Parameters and Stability Diagnostics	91
Bibliography	117

INTRODUCTION

Throughout the last two decades, deep field observations have revealed a population of high-redshift galaxies very different from those in the local universe. Found at redshifts $z \sim 1 - 3$, some show elliptical or disc structures, but the majority exhibits irregular morphologies (Cowie et al., 1995; Elmegreen et al., 2004, 2005; Wadadekar et al., 2006). Regardless of morphological details, most feature numerous highly turbulent star-forming clumps with masses $M_{cl} \sim 10^7 - 10^9 M_{\odot}$ and sizes of $\ell_{cl} \sim 2$ kpc (Elmegreen & Elmegreen, 2005). The abundance of such clumps, existence of underlying stellar discs, and the decreasing age of the associated stellar population with redshift suggests that they represent early stages in the formation of present-day galaxies (Genzel et al., 2008; Elmegreen et al., 2009).

Being gas-rich with large amounts of molecular hydrogen (Tacconi et al., 2010), high-redshift galaxies form stars at rates of roughly $10 - 300 M_{\odot} \text{ yr}^{-1}$ (Daddi et al., 2004; Cresci et al., 2009) and have total stellar masses of $M_{\star} \sim 10^9 - 10^{11} M_{\odot}$ (Förster Schreiber et al., 2009). It is presently unclear how these clumps form and how star formation is triggered, but numerical simulations (e.g. Dekel et al., 2009b; Ceverino & Klypin, 2009; Agertz et al., 2009b) and observations (e.g. Bournaud et al., 2008; Shapiro et al., 2008) suggest that they result from either major merging events (Robertson & Bullock, 2008; Puech, 2010) or a combination of gravitational instabilities and external accretion (Genzel et al., 2006; Bournaud & Elmegreen, 2009).

In our neighbourhood, combinations of high-resolution surveys of neutral atomic hydrogen (THINGS; Walter et al., 2008), CO lines tracing molecular hydrogen (BIMA SONG, HERACLES; Helfer et al., 2003; Leroy et al., 2009), IR observations of old stellar populations and warm dust surrounding sites of star formation (SINGS; Kennicutt et al., 2003), as well as Far-UV maps tracing massive O and B stars (GALEX; Gil de Paz et al., 2007) have recently enabled us to characterize nearby galaxies in unprecedented detail. Using such data, we now have an ideal testbed to validate numerical simulations or evaluate different models of the conditions and processes governing star formation in high detail (e.g. Leroy et al., 2008).

By combining observations of distant and nearby galaxies, we gain insight into different epochs of galactic evolution. To successfully describe the processes in and between these epochs, we need to understand (i) the processes governing the distribution of gas and stars, (ii) how the gas contracts to form stars, (iii) how the stars feed back energy into the gas throughout their lives, and (iv) how their eventual death replenishes the reservoir of interstellar gas.

In this thesis, we are concerned with gravitational instabilities in the interstellar gas. These trigger gravitational collapse and are thought to culminate in the formation of protostellar cores (e.g. Elmegreen, 1999; McKee & Ostriker, 2007). Dating back to early work on spiral density waves, Safronov (1960) and Toomre (1964) independently presented an instability criterion for infinitely thin differentially rotating stellar discs, which can be extended to gaseous discs (Binney & Tremaine, 2008, §6.2). Soon after, Lin & Shu (1966) soon realized the importance of considering the contributions of both stars and gas in galactic discs, which led to the development of two-component models of gravitational instability (Jog & Solomon, 1984; Bertin & Romeo, 1988; Rafikov, 2001). Over time, further extensions were made to account for finite thickness discs (Shu, 1968; Romeo, 1990, 1992, 1994; Wiegert, 2010) and provide simple approximate two-component stability criteria (Wang & Silk, 1994; Wiegert, 2010; Romeo & Wiegert, 2011).

However, this framework of gravitational instability assumes that the gaseous interstellar medium is in approximate equilibrium with well defined surface densities and velocity dispersions (Romeo et al., 2010). Unfortunately, this only holds true for classical descriptions of the interstellar gas as a two- or three-phase medium in thermal pressure equilibrium (e.g. Field et al., 1969). More recent findings have established the interstellar medium of both nearby and high-redshift galaxies as being interspersed by clumpy filamentary structures with turbulent velocity and density fields (Elmegreen & Scalo, 2004; Burkert, 2006; McKee & Ostriker, 2007; Elmegreen et al., 2009; Burkert et al., 2010). In nearby galaxies, turbulence is manifested through scale dependent velocity dispersions of clouds of molecular hydrogen (Larson, 1981; Solomon et al., 1987; Bolatto et al., 2008; Hughes et al., 2010), which significantly affect the onset and scales of gravitational instabilities (Bonazzola et al., 1987; Vazquez-Semadeni & Gazol, 1995). Based on advances in numerical techniques, numerous simulations are presently exploring the effects of turbulence on gravitational instabilities in various parts of the interstellar gas (e.g. Wada et al., 2002; Kim & Ostriker, 2007; Agertz et al., 2009a).

Prevalent turbulent motions in various epochs of galactic evolution and the importance of two-component models of gravitational instability therefore motivate us to extend these models with descriptions of turbulence. After presenting a brief review of the turbulent interstellar medium in nearby galaxies in §2, we introduce the theoretical framework of gravitational instability and present the phenomenological model of turbulence first introduced by Romeo et al. (2010) in §3. We then extend these two-component models to allow for turbulence and study two different turbulent systems. In §4, one of the models is then applied to observations of nearby star forming galaxies previously analysed by Leroy et al. (2008). We further summarize computations of quantities with upper and lower bounds in appendix A and tabulate the radial profiles of these for the analysed spiral galaxies in appendix B.

This framework can be used to interpret coming high-resolution observations and simulations of high-redshift galaxies. In particular, (i) the search for scaling laws in high-redshift galaxies equivalent to those first noted by Larson (1981) in the local universes, and (ii) models describing the dynamical evolution from an instability point of view (e.g. Dekel et al., 2009a; Krumholz & Burkert, 2010) stand to profit.

GALAXIES, TURBULENCE, THE INTERSTELLAR MEDIUM

In the present chapter, the role of turbulence in the interstellar medium (ISM) of disc galaxies is introduced.

Current knowledge of galaxies and their components is briefly reviewed in §2.1. The role of galactic discs is established, and, after a review of the classic equilibrium ISM model, the turbulent ISM is described. In §2.2, the basic theory regarding incompressible turbulence is outlined. It is then extended upon in §2.3 for the compressible and fractal ISM.

2.1. Galaxies and The Interstellar Medium

This section is based on Karttunen et al. (2007) and Binney & Merrifield (1998). The descriptions of the classic and turbulent ISM are based on Burkert (2006). Other references are indicated where appropriate.

Galaxies consist of three distinct components: (i) various stellar populations, (ii) gaseous components forming the interstellar medium (ISM), and (iii) dark matter. Stellar populations are usually categorized into Population I, and Population II stars. Population I objects are young, hot stars with low metallicity,¹ whereas Population II stars are older, cooler, and have higher metallicity. The gaseous components are normally classified according to chemical species, pressure, temperature, and density. The dark matter component thus far eludes direct detection because it interacts solely through gravity.

The morphological classification of galaxies in use today is shown in figure 2.1. In this scheme, first introduced in Hubble (1936), galaxies are divided into two classes: (i) elliptical galaxies, and (ii) spiral galaxies, with spirals further subdivided into normal and barred spirals. Within these classes, morphological details mark further subtypes.

Elliptical galaxies lack discernible substructure apart from a spherical, elliptical, or triaxial brightness distribution, which generally falls off exponentially from the centre. These galaxies tend to have very little interstellar gas and are mostly populated by Population II stars. Since this work is concerned with the dynamics of spiral galaxies, ellipticals shall not be considered hereafter.

¹All elements heavier than helium are considered metals.

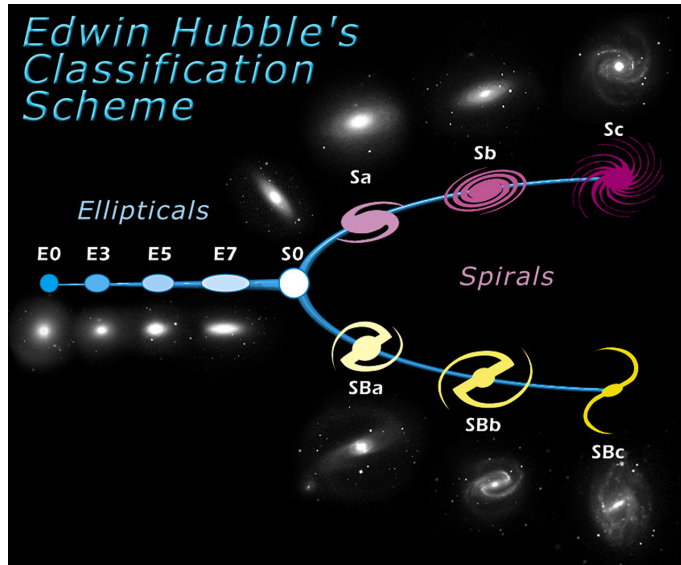


Figure 2.1.: The morphological classification of galaxies, commonly known as the “Hubble Tuning Fork“. Ignoring lenticulars (S0), the morphologic change from spheroids to ellipticals through spirals (top) and barred spiral (bottom) is shown from left to right. The image is in the public domain released by NASA, ESA, and ESO and can be obtained from <http://www.spacetelescope.org/images/heic9902o/>.

In spiral galaxies, most of the interstellar gas and stars are concentrated in a thin, rotating disc showing distinct spiral structure. The latter can vary in shape across different spiral galaxies, both with and without a central bar. The disc stars are typically Population I objects moving on approximately circular orbits with velocity dispersion of the order $\sigma \sim 20 - 40$ km/s (Dehnen & Binney, 1998). The disc is surrounded by a spherical bulge containing both Population I and II stars on highly eccentric orbits with velocity dispersions of the order $\sigma \sim 50 - 300$ km/s (Barroso, 2003). The bulge, in turn, is surrounded by a halo of lower stellar number density. For the most part, halo stars are Population II objects coalesced in global clusters with highly eccentric orbits.

The brightness profile (and thus the stellar number density) of the disc falls off exponentially from the centre of the disc. Since the bulge extends to about half the optical radius R_{25} , the distinction between disc and bulge is not particularly clear in the central regions. Moreover, as the bulge can have stellar number densities comparable to the disc, this means that the stellar disc is gravitationally coupled to the bulge in the inner regions.

Hereafter, only the stars and interstellar gas in the disc shall be considered. Additionally, the different stellar populations are treated as one, although the disc only contains very small amounts of stars which are not Population I.

The interstellar medium (ISM) in the disc consists mostly of atomic and molecular hydrogen, i.e. H I and H₂. The former is very diffuse and distributed through the entire disc while the latter is concentrated in giant molecular clouds (GMCS) drifting through the H I. The surface density (which is the observational counterpart of the number density) of H I is approximately constant throughout the disc (except for a dip at small radii), whereas the H₂ is concentrated in the inner regions, cf. figure 2.2. Note that the H I component tends to extend well beyond the optical radius R_{25} , which is not reflected in figure 2.2 (Binney & Merrifield, 1998, §8.2.2).

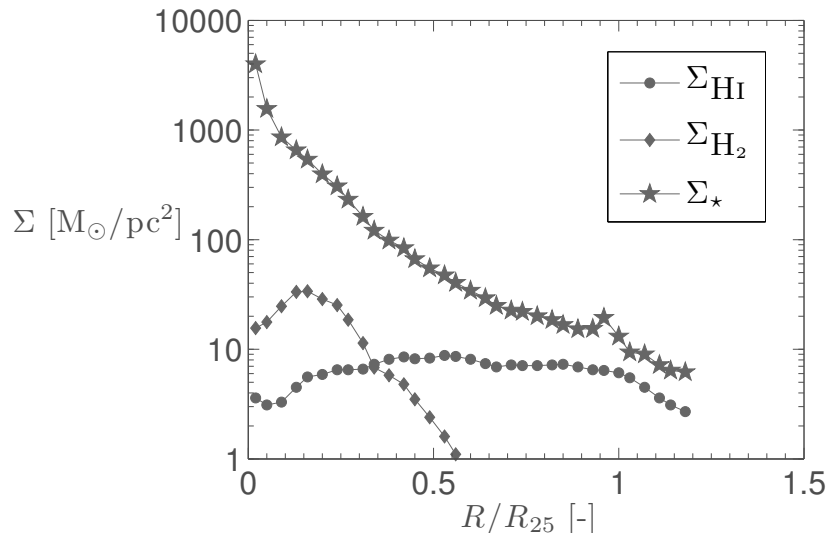


Figure 2.2.: Ring averaged HI, H₂, and stellar surface density Σ vs. fraction of the optical radius R/R_{25} in the disc of the representative galaxy NGC 7331. The data is adapted from Leroy et al. (2008). In the inner regions, H₂ dominates the gas surface density, whereas the HI density is approximately constant with radius, except for a dip towards the centre. The stellar surface density decreases exponentially with radius. Note that (i) towards the centre, the stellar surface density could also sample stars from the bulge population, and (ii) the HI distribution typically extends far beyond R_{25} , but this is not reflected in the data due to observational limitations.

Classically, this was modelled as a medium of two phases in thermal pressure equilibrium (Field et al., 1969). A dense cold phase of giant molecular clouds (GMCs) is embedded in a warm phase of diffuse atomic hydrogen (HI). At a temperature of $T \sim 10000$ K and number density $n \sim 100 \text{ cm}^{-3}$, the warm phase covers a large fraction of the total ISM volume. The cold phase at $T < 300$ K and $n \sim 0.1 \text{ cm}^{-3}$ dominates the total mass.

As the GMCs travel through the diffuse HI component, they gradually heat up as new stars form within them. This eventually causes them to disperse and become part of the diffuse component. On the other hand, as the HI cools, gravitational instabilities cause local fragmentation and collapse to GMCs. Smaller scale gravitational instabilities then lead to star formation. Through collisions, individual small GMCs grow over time.

A growing body of evidence, however, suggests significant deviations from this model on a wide range of scales (Elmegreen & Scalo, 2004; Burkert, 2006; McKee & Ostriker, 2007). Considering GMCs in the Milky Way on scales of $\ell \sim 10\text{--}100$ pc, Larson (1981) points out three important findings: (i) a power law relationship $S \propto \sigma^\alpha$ between size S and velocity dispersion σ , (ii) a power law relation $S \propto M_L^\beta$ between the size and the luminosity inferred mass M_L , and (iii) a correlation $M_V \sim M_L$ between the virial mass M_V and the luminosity inferred mass to order of magnitude. Extension of this work by Solomon et al. (1987) quantified the relation $S \propto \sigma^\alpha$ to $\alpha \simeq 0.5$ and further noted that GMCs have constant mean surface density, i.e. $\Sigma \simeq \text{const}$. Studies of extragalactic GMCs draw similar conclusions (Bolatto et al., 2008; Hughes et al., 2010).

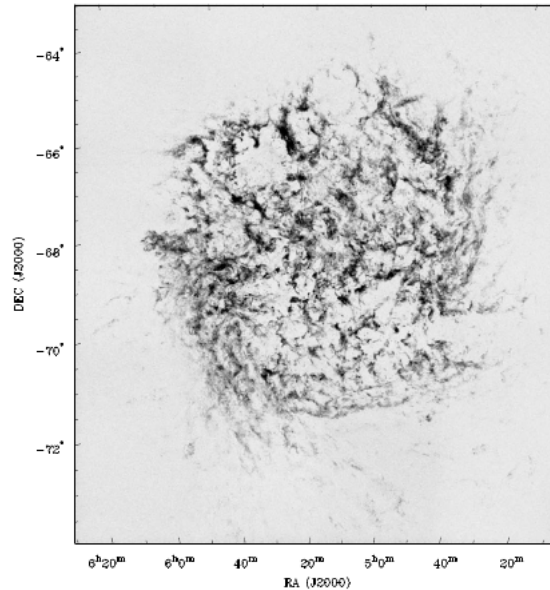


Figure 2.3.: Radio intensity for the 21 cm line tracing HI in the Large Magellanic Cloud. The filamentary structure on multiple scales is clearly visible. Taken from Burkert (2006), which had adapted it from Kim et al. (1999).

Combined with the fact that the observed velocity dispersions well exceed the values expected from thermal motions,² the first two relations are suggestive of the turbulent nature of GMCs, while the third suggests that GMCs are approximately in virial equilibrium. Moreover, since the velocity dispersion increases with size of the cloud, GMCs tend to be stable against gravitational collapse on large scales, but unstable on small scales where the velocity dispersion is too small to counteract self-gravity. As such, star formation, which is further aided by significant local overdensities resulting from a turbulent density field, is possible on small scales (Bonazzola et al., 1987; Vazquez-Semadeni & Gazol, 1995; McKee & Ostriker, 2007).

HI exhibits similar structure and scaling relations over a wide range of scales. Figure 2.3 shows a radio intensity map of the 21 cm line tracing atomic hydrogen in the Large Magellanic Cloud. The filamentary structure with HI shells on large scales along with substructure that can be identified as HI clouds is clearly visible. Using spectral methods, it is found that on scales of cloud structures at $\ell \sim 10 - 500$ pc, both HI density and velocity dispersion follow power law scaling similar to those observed in H₂ GMCs (Kim et al., 2007). On galactic scales $\ell \gtrsim 0.5$ kpc, the spectral signature of the radio intensity also indicates turbulent scaling (Begum et al., 2006; Dutta et al., 2008, 2009a,b), but disentangling the individual contributions of the velocity dispersion and density fluctuations is problematic (Lazarian & Pogosyan, 2000).

On large scales, both observations and simulations note a radial decline of the velocity dispersion ranging from $\sigma_{\text{HI}} \simeq 15 - 20$ km/s at small radii, to $\sigma_{\text{HI}} \simeq 10$ km/s at R_{25} , and further to values of $\sigma_{\text{HI}} \simeq 5$ km/s in the outer regions (Petric & Rupen, 2007; Agertz et al., 2009a; Tamburro et al., 2009).

²For cloud temperatures of $T \sim 15 - 25$ K, one expects $\sigma_{\text{H}_2, \text{thermal}} < 0.1$ km/s, (Bolatto et al., 2008), whereas $\sigma_{\text{H}_2} \simeq 0.5 - 6$ km/s is observed (Larson, 1981).

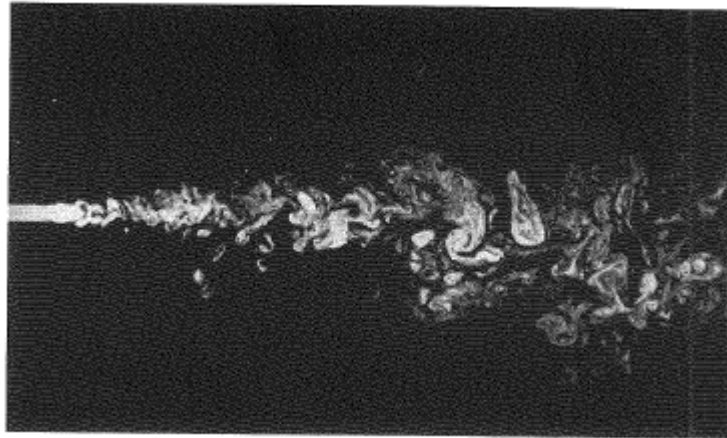


Figure 2.4.: Flow visualisation of a turbulent water jet. The image nicely demonstrates the concept of “eddies within eddies” in a turbulent flow. The picture is originally taken from van Dyke (1982), and was adapted from Frisch (1995) for this work.

2.2. Turbulence in Incompressible Fluids

The following is based on Elmegreen & Scalo (2004, §2, §4.6) and Frisch (1995, §3, §6.2).

Microscopically, turbulence refers to a state of deterministic chaos in a fluid. While the governing equations are deterministic, minimal changes in initial or boundary conditions of fluid elements result in a wildly different time evolution of the state parameters.

This suggests application of statistical methods to study the macroscopic implications. Fundamentally, such methods are based on the (averaged) relation of a quantity $A(r)$ measured at points a distance δr apart. For example, the structure function of order p is given by

$$S_p(\delta r) = \langle |A(r) - A(r + \delta r)|^p \rangle, \quad (2.1)$$

where $\langle \cdot \rangle$ indicates the average. Generally, the velocity field is studied, i.e. $A(r) = v(r)$.

Kolmogorov (1941) first presented a framework³ for the study of turbulence using such statistical methods. It is valid for incompressible flow and assumes, for the most part, homogeneity and stationarity, which means that the statistical properties of the turbulent flow are invariant under space and time translations.

Turbulent flows are characterized by prevalent vortex structures, called eddies. These are found on different scales with self-similar structure, cf. figure 2.4. The core idea of K41 theory is that energy is (through some unspecified process) injected into the flow at the scales of the largest eddies. The energy then cascades down to smaller and smaller scales (across “eddies within eddies”) until viscous forces become important and the energy is dissipated into heat at the dissipation scale. The range of scales where the energy cascades down is the inertial range.

In terms of the structure function this means that the measured velocity difference between two points depends on the separation of these points. The separation is interpreted as a characteristic scale.

³Hereafter referred to as K41 theory.

The most general result of the K41 theory is the 4/5-law. Following the assumption of statistical homogeneity and stationarity of the flow properties, it is found that second order structure function obeys

$$S_2(\ell) = -\frac{4}{5}\varepsilon\ell, \quad (2.2)$$

where ε is the flux of kinetic energy across the scale ℓ , which is equal to the rate of energy dissipation occurring at the dissipation scale. The most striking result of the 4/5-law is the fact that the energy flux is independent of scale.

With this knowledge and some intuitive arguments, the spectral signature of turbulent flows can be obtained. In particular, let ε be the energy flux across the scale ℓ , u_ℓ^2 be proportional to the kinetic energy at scale ℓ , and ℓ/u_ℓ be a characteristic timescale. The energy flux then is

$$\varepsilon \propto \frac{u_\ell^2}{\ell/u_\ell}. \quad (2.3)$$

For $\varepsilon = \text{const}$, this yields

$$u_\ell \propto \ell^{1/3}, \quad \frac{u_\ell}{\ell} \propto \ell^{-2/3}, \quad (2.4)$$

implying that (i) the largest eddies carry most of the flow velocity, and (ii) the smallest eddies carry most of the vorticity u_ℓ/ℓ . Since the kinetic energy is proportional to u_ℓ^2 , the above implies $u_\ell^2 \propto \ell^{2/3}$. Written in terms of the wavenumber $k = 1/\ell$, this means $u_k^2 \propto k^{-2/3}$. The kinetic energy per unit wavenumber then gives the energy spectrum

$$E(k) \propto \frac{u_k^2}{k} \propto k^{-5/3}. \quad (2.5)$$

This is called the 5/3-law and is another important result of the K41 theory. It shows that the spectral signature of a turbulent flow field across the inertial range is given by a power law with spectral index $\zeta = -5/3$. In literature related to the study of ISM turbulence, the energy spectrum is usually taken to be the average over the spatial dimensions of the power spectrum, i.e. $P(k) = E(k)$ for 1D, $P(k) \propto k^{-8/3}$ for 2D, and $P(k) \propto k^{-11/3}$ for 3D turbulence.

If, for example, in-situ visualisation of a flow field (with optical tracing or similar methods) is not possible, but the velocity field can somehow be obtained, computation of the energy spectrum could then indicate the turbulent nature of the flow. Within the context of this work, the obvious application is detection of turbulence in the ISM.

2.3. Turbulence in The Interstellar Medium

This section is based on Elmegreen & Scalo (2004, §3, §4.6) and Frisch (1995, §7.3, §8.5).

The ISM can be highly compressible depending on the local Mach number. Sub- and transonic regimes are incompressible whereas supersonic motion indicates compressibility. Additionally, the ISM shows filamental and cloud structures on a wide range of scales along with velocity dispersion and density scaling laws, cf. §2.1.

These considerations lead to two major properties of ISM turbulence that are at odds with the original K41 theory: (i) the energy flux across scales is not necessarily constant and energy does not necessarily cascade to smaller scales only, and (ii) a fractal nature is imposed on the ISM. These are now described in some detail.

Energy cascade. In a compressible medium, energy can be dissipated in the form of shocks at all scales. Moreover, energy is injected into the ISM through a number of different mechanisms, e.g. stellar winds, galactic rotation, fluid instabilities, or supernova explosions. It is appreciable that these processes inject energy into the medium at different scales. The ISM itself can further extend to scales even larger than the largest scales of energy injection.

Together, these facts indicate that energy is injected at a wide range of scales through different processes, and then cascades to both larger and smaller scales, where it can dissipate through shocks, viscous processes or other means.

As such, one would expect that turbulence in the ISM is unlikely to have the spatial or spectral signature indicated by the K41 relations (2.2) and (2.5). However, the observed signature of ISM turbulence is surprisingly close to the K41 case with an energy spectral index of $\zeta \simeq -5/3$ (Elmegreen et al., 2001).

Within the framework of K41 theory, the energy spectrum is linked to the velocity field. In ISM observations, however, the energy spectrum is linked to the radio intensity of the observations, which contains contribution of the turbulent velocity field as well as density fluctuations. While it is generally possible to disentangle the contributions, the procedure can be error-prone, especially for HI observations (Lazarian & Pogosyan, 2000).

Fractality. For incompressible fluids, the turbulent flow field is said to be space-filling, i.e. the total volume of space filled by N eddies with characteristic size L is constant. That is to say, if $N_0 = 2$ eddies of size $L_0 = 4$ fill a total space of $N_0 L_0 = 8$ at scale 0, the next smaller scale 1 must be occupied by, e.g. $N_1 = 4$ eddies of size $L_1 = 2$ such that $L_0 N_0 = L_1 N_1 = 8$.

For a compressible medium, energy injection and dissipation at different scales render this restriction invalid such that space-filling and self-similarity across different scales is not guaranteed. The medium is said to exhibit intermittency.

This can be dealt with by introducing a scale factor $0 < \beta < 1$ indicating which fraction of the space originally occupied by an eddy at a larger scale is also occupied by eddies on the next smaller scale. Assuming the fraction of occupied space p_ℓ at scale ℓ is a power law with index n , this means

$$p_\ell = \beta^n = \left(\frac{\ell}{\ell_0} \right)^{d-D}, \quad (2.6)$$

where $d - D$ is the codimension, and D the fractal dimension. For a three-dimensional space (as is the ISM), $d = 3$. The limiting case $D = 3$ corresponds to full space-filling.

This scaling has two distinct implications. Firstly, the fact that not the entire available space is filled imprints a fractal structure in the medium. This can be interpreted as tendency for filamentary structures to form,⁴ especially when the network of filaments is

⁴Compressibility is not a prerequisite for filamentary structures to form. It can, however, be an indication.

interpreted as a series of interconnected shocks. Secondly, the power law scaling of the space-filling fraction causes a dependence of the velocity distribution with scale. Both effects are indeed observed in the ISM, see §2.1.

2.4. Chapter Summary

In this chapter, observational knowledge of galaxies, the ISM, and the K41 turbulence theory were introduced. The most important points are:

- Galaxies are classified according to their morphology into elliptical, barred spirals and normal spirals. Ellipticals tend to be gas depleted and populated by old, metal rich Population II stars. Spiral galaxies have most of the gas and young Population I stars concentrated in a thin, differentially rotating disc. The disc is surrounded by a bulge and a halo of older Population II stars. Stellar velocity dispersions are higher for the bulge and halo populations and gravitational coupling between the disc, the bulge, and the halo populations can occur in the inner regions. The disc stellar surface density decreases exponentially with radius.
- The ISM exhibits filamentary structure on a wide range of scales. On kpc scales, diffuse HI with radially decreasing velocity dispersions $\sigma_{\text{HI}} \simeq 10$ km/s embeds pc-scale GMCs with velocity dispersions $\sigma_{\text{H}_2} \simeq 0.5 - 6$ km/s. HI further shows scale dependent velocity dispersion and density distribution. The velocity scaling saturates at scales of about 500 pc, whereas the density is scale dependent up to kpc scales. H₂ GMCs have scale dependent velocity distribution, but approximately constant surface density.

At galactic scales, the HI surface density is roughly constant with radius, while H₂ is concentrated in the inner regions. With turbulent velocity fields, GMCs tend to be stable against large scale collapse, but small scales are vulnerable to gravitational collapse leading to star formation. As H₂ is concentrated at small radii, so is star formation, and consequently the stellar surface density.

- Using statistical tools, the K41 theory of turbulence for incompressible fluids predicts energy injection at large scales, a subsequent energy cascade down to smaller scales, and eventually dissipation through viscous processes. In the ISM, energy is both injected (e.g. stellar outflows, differential rotation, fluid instabilities) and dissipated (e.g. shocks, viscous friction) at a wide range of scales. As such, energy likely cascades both to larger and smaller scales from the injection scale.

THEORY OF GALACTIC DISC STABILITY

As previously discussed, galaxies consist of different stellar populations and gaseous phases (fluids). While fundamentally different, the same tools can be used to investigate their gravitational stability in differentially rotating, thin galactic discs.

After outlining these differences in §3.1, basic assumptions are introduced in §3.2. The simplest case of a one-component medium is discussed in §3.3, which is then extended to two-components in §3.4. Finally, the one-component model is extended to account for turbulence in §3.5.

Note that, while this text is primarily based on Binney & Tremaine (2008), the foundations of spiral density wave theory and gravitational stability of stellar and gaseous discs date back to the works of Toomre (1964), Lin & Shu (1966), and Lin et al. (1969).

3.1. Kinetic and Fluid Approach

This section is based on Binney & Tremaine (2008, §1.2, §4.2, §5.2, App. F). Additionally, some of the more fundamental concepts are discussed at length in Shu (1992).

As discussed in §2, galaxies contain different stellar populations and gaseous components (fluids in different phases). Considered individually, the behaviour of the fluids is driven by short-range particle-particle interactions (collisions), while the stars interact exclusively through the gravity field generated by the entire population. The coupling between components occurs through the common gravitational field, which is a superposition of the individual fields.

The fluid components are described by the equations of fluid dynamics. In particular, in the presence of a gravitational potential, the fluid density, pressure, temperature, and velocity are coupled through (i) the continuity equation, (ii) Euler's equation, (iii) the energy equation, (iv) an equation of state, and (v) the Poisson equation. If the density of a such a system is perturbed, the gravitational potential is changed. This, in turn, affects the state parameters through the coupled fluid dynamic equations. Hereafter, this is referred to as the fluid approach.

Being non-collisional, stellar systems are instead described by a distribution function $f(\mathbf{x}, \mathbf{v}, t)$, which gives the probability of a star being located at coordinates \mathbf{x} with velocity \mathbf{v} at time t . The time evolution of the distribution function is described by the collisionless Boltzmann equation,¹ which is coupled to the gravitational potential (and thus to the stellar density through the Poisson equation). In analogy with the fluid case, a perturbation of the stellar density leads to a potential perturbation through the Poisson equation. This, in turn, affects the distribution function and thus (in a statistical sense) the kinematic variables \mathbf{x} and \mathbf{v} of the stars. This is the kinetic approach.

The kinetic approach is mathematically more tedious because non-collisional systems exhibit more complicated behaviour. Fortunately, if one is not interested in the complete physics of the non-collisional system, it can be treated as a fluid. The results from a kinetic and a fluid analysis agree to within a correction factor of a few percent in the parameters relevant in this work.

While the issue is briefly quantified in §3.3.2 and §3.4.3, for the remainder of this work, non-collisional system are treated as fluids. This saves mathematical complexity and allows focus on the stability analysis with acceptable accuracy.

3.2. Procedure and Assumptions

This section is based on Binney & Tremaine (2008, §6.2). Other references are indicated where needed.

As previously hinted, the key idea to analysing the stability properties of gravitating fluid systems is to perturb the density distribution of the system and study the resulting effect on the state variables. By comparing the original (unperturbed) density distribution to the resulting density distribution, a density wave is described. Thus, the principal task of stability analysis is the calculation of different possible density waves (modes). These modes should obey the wave equation, and the resulting density perturbation should be of the form

$$\rho_{\text{perturbed}} \propto \exp(-i\omega t), \quad (3.1)$$

where ω is the angular frequency of the density wave.

While this procedure is relatively straightforward for an isotropic, homogeneous, infinite fluid, real systems (galaxies) cause complications:

Galaxies are rotating. As such, they are not spherical, but flattened out to disc shape. This, in turn, means that the fluid is not isotropic or homogeneous in three dimensions. In this work, razor-thin discs are considered, so only two coordinates of interest remain. As such, the volume density ρ is replaced by the integrated surface density $\Sigma = \int \rho(z) dz$.

To consider thickness effects, hydrostatic equilibrium can be imposed for the fluid in the z direction perpendicular to the disc, which leads to the definition of a disc scale height h . For the thin-disc approximation to be valid for a particular (thick) disc, the condition $kh \ll 1$ must be fulfilled (Romeo et al., 2010, §2.1), where k is the wavenumber of the density wave.

¹Also known as the Vlasov equation.

For more details, see, e.g. Fridman et al. (1984, §V), Romeo (1990), Romeo (1992), and Wiegert (2010).

Differential rotation. The angular velocity depends on the radius, i.e. $\Omega = \Omega(R)$. This is accounted for by considering that the fluid elements are on near-circular orbits around the galactic centre.

Deviations from these circular orbits are described in terms of the epicyclic frequency κ , which is the frequency of a small orbit around the point orbiting the galactic centre (Binney & Tremaine, 2008, §3.2.3). By considering the epicyclic motion of fluid elements instead of their orbital motions around the galactic centre, differential rotation can be considered.

Spiral structure. The presence of spiral structure implies non-homogeneity even in the plane of the disc. Fortunately, if one imposes that resulting density waves are tightly wound (in the sense that the radial wavelength is much smaller than the radius), one obtains a locally valid analysis. Since a disc is locally homogeneous to within a few wavelengths of where the perturbation occurs, the analysis is valid.

This approximation is usually referred to as the tight-winding² approximation. More quantitatively, it requires that $kR \gg 1$, where k is the wavenumber of the density wave, and R the radius. It is very important to realize that the analysis is valid only locally, and that the condition $kR \gg 1$ needs to be checked carefully.

3.3. One-Fluid Case

This section is based on Binney & Tremaine (2008, §6.2.).

3.3.1. Dispersion Relation, Marginal Stability Curve

Keeping in mind the basic idea and difficulties of the stability analysis discussed in the previous section, the result for a single fluid component gives the dispersion relation (DR) for possible density wave modes

$$(\omega - m\Omega)^2 = \kappa^2 - 2\pi G\Sigma k + v_s^2 k^2, \quad (3.2)$$

where ω is the angular frequency, k the wavenumber, m the number of arms, and Ω the circular frequency of the density wave. The fluid is further described by the equilibrium surface density Σ , the epicyclic frequency κ , and the sound speed v_s . These typically vary throughout the disc. The gravitational constant is G .

For axisymmetric waves, $m = 0$, and thus

$$\omega^2 = \underbrace{\kappa^2}_{\text{rotation}} - \underbrace{2\pi G\Sigma k}_{\text{self-gravity}} + \underbrace{v_s^2 k^2}_{\text{pressure}}, \quad (3.3)$$

where the terms on the right hand side correspond to the contribution of rotation, self-gravity, and thermal motions (i.e. pressure) of the fluid.

²Also: WKB (in reference to the quantum mechanical analogy), or short-wavelength approximation.

For convenience, (3.3) can also be cast in the non-dimensional form

$$\frac{\omega^2}{\kappa^2} = 1 - \frac{k}{k_T} + \frac{Q^2}{4} \left(\frac{k}{k_T} \right)^2, \quad (3.4)$$

where the wavenumber k is now rescaled in terms of the Toomre wavenumber k_T and the Toomre parameter Q . Their meaning will be made clear momentarily.

Consider now the resulting density perturbation (3.1) and the DR (3.3). If $\omega^2 > 0$, the perturbation is oscillating with frequency ω — the system is stable. For $\omega^2 < 0$, the resulting perturbation increases in amplitude over time — the system is unstable. With this in mind, note that rotation and pressure have a stabilising effect on the system, whereas self-gravity destabilizes the system.

For a given location in the disc, Σ , v_s , and κ are fixed, and ω^2 depends only on k . Since (3.3) is quadratic in k , there is potentially a range of unstable wavenumbers where $\omega^2 < 0$. Stability on all scales can be demanded by imposing $\min\{\omega^2\} \geq 0$. This is fulfilled if the wavenumber k of the perturbation fulfils

$$k > k_T \equiv \frac{\kappa^2}{2\pi G \Sigma}, \quad (3.5)$$

where k_T is the Toomre wavenumber. Alternatively, the criterion can be written as

$$Q \equiv \frac{\kappa v_s}{\pi G \Sigma} > 1, \quad (3.6)$$

where Q is the Toomre stability parameter for differentially rotating thin fluid discs. If $Q \geq 1$, the disc is stable on all scales. Instability on some scales occurs for $Q < 1$.

Consider figure 3.1, showing the non-dimensional DR for $Q = 0.65 < 1$. Since the minimum of the DR lies below $\omega^2/\kappa^2 = 0$ (thin horizontal line), the system is unstable on a range of scales (shaded grey). If Q increases, the curve moves upwards until, at $Q = 1$, the minimum coincides with line $\omega^2/\kappa^2 = 0$. Increase of Q shifts the curve up further, increasing the stability.

In fact, the location (along the k/k_T axis) of the minimum of the DR yields the wavenumber at which instabilities first occur. This is the most unstable wavenumber \bar{k} .

Instead of studying the DR, one can follow the line of marginal stability $\omega = 0$. This leads to an expression for the minimum Q required for stability at wavenumber k . This describes the (non-dimensional) marginal stability curve (MSC)

$$Q^2 = 4 \left(\frac{k}{k_T} \right)^{-1} \left[1 - \left(\frac{k}{k_T} \right)^{-1} \right]. \quad (3.7)$$

When working with the MSC, it is more convenient to work with the scale $\ell = 1/k$ instead of the wavenumber k . Defining the Toomre scale $\ell_T = 1/k_T$ and the dimensionless scale $\Lambda = \ell/\ell_T$, the MSC is

$$Q^2 = 4\Lambda(1 - \Lambda). \quad (3.8)$$

This relation is shown in figure 3.2. Computing Q at some location in the disc, a value above the curve implies stability at this scale, whereas a value below the curve implies instability at this scale. The maximum $\max\{Q\} = \bar{Q}$ is the stability threshold. If $Q \geq \bar{Q}$, stability on all scales is guaranteed. The location of \bar{Q} along the Λ axis is the most unstable scale $\bar{\Lambda}$. It is at this scale that instabilities first set in if the system becomes unstable. Note that $\bar{\Lambda}$ must fulfil the tight-winding condition $kR \gg 1$ for the analysis to be valid.

In fact, for a one-fluid system, $\bar{Q} = 1$ (as shown before) and $\bar{\Lambda} = 0.5$. These will differ for two-component and turbulent one-fluid systems.

3.3.2. The Velocity Dispersion, Accuracy of the Fluid Approach

The sound speed v_s of gases is difficult to infer from observations. Fortunately, the observational equivalent of the sound speed is the line of sight (LOS) velocity dispersion σ_{LOS} of the gas, which can be determined (Romeo et al., 2010, §2.1). Moreover, recall that non-collisional systems can be treated as fluids up to a correction factor. In doing so, the LOS velocity dispersion of the non-collisional component $\sigma_{\text{LOS},k}$ takes the place of the sound speed v_s .

Starting with the next section, only σ shall be used in the relevant formulae. One should keep in mind that it refers to the LOS velocity dispersion of the component, and is equivalent to the sound-speed for a fluid component.

To characterize the error arising from treating a non-collisional component as a fluid, the relevant expressions for the MSCs are now compared. Following Toomre (1964, §V), Binney & Tremaine (2008) present the MSCs of a fluid Q_f and kinetic analysis Q_k as

$$Q_f = \frac{\kappa v_s}{\pi G \Sigma}, \quad Q_k = \frac{\kappa \sigma}{3.36 G \Sigma}, \quad (3.9)$$

where the different coefficients $\pi \simeq 3.14$ and 3.36 give a difference of 7%. This leads to a $\bar{\Lambda}_f = 0.5$ from a fluid analysis and $\bar{\Lambda}_k = 0.55$ from a kinetic analysis; a difference of 10%.

These differences are acceptable in light of the reduced mathematical complexity.

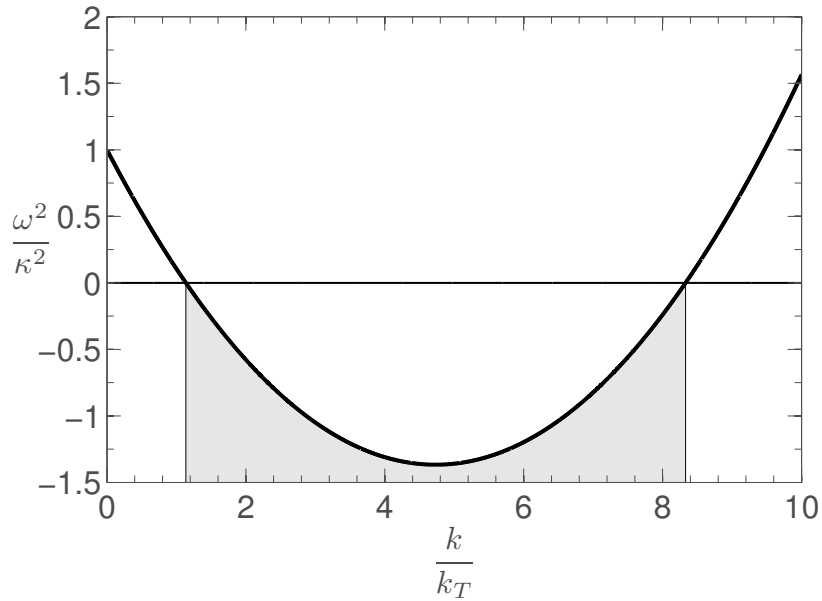


Figure 3.1.: Non-dimensional DR for $Q = 0.65 < 1$. The dimensionless value of the DR is plotted against the non-dimensional wavenumber k/k_T . The DR is quadratic with a minimum defined by Q . If $Q < 1$, the minimum is $\omega^2/\kappa^2 < 0$ and the system is unstable on a range of scales. If $Q \geq 1$, the system is stable on all scales (shaded grey). As Q changes, the curve shifts up or down, intersecting $\omega^2/\kappa^2 = 0$ (horizontal line) first at the most unstable wavenumber \bar{k} .

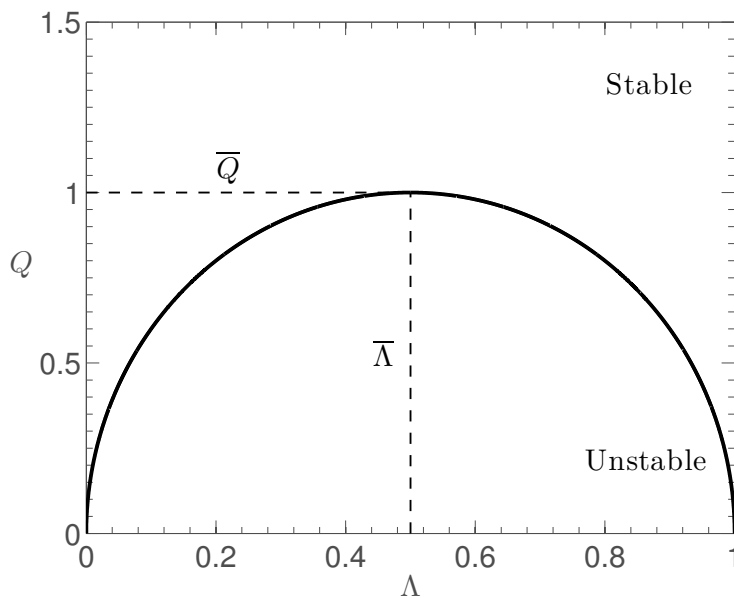


Figure 3.2.: Marginal stability curve Q vs. $\Lambda = \ell/\ell_T$. At a scale Λ , a value of Q above the curve means that the system is stable at this scale. whereas a value below the curve means instability at this (and other) scales. The maximum is the stability threshold \bar{Q} and a value of $Q \geq \bar{Q}$ means stability on all scales. The location of \bar{Q} along Λ is the most unstable scale $\bar{\Lambda}$. Instabilities first occur at this scale.

3.4. Two-Fluid Case

This section is based on Jog & Solomon (1984) and Bertin & Romeo (1988).

3.4.1. Dispersion Relation, Marginal Stability Curve

In analogy to the one-component case, a dispersion relation for the case of two fluids coupled through the Poisson equation can be derived. First presented by Jog & Solomon (1984), it reads

$$(\omega^2 - \omega_1^2)(\omega^2 - \omega_2^2) = (2\pi Gk\Sigma_1)(2\pi Gk\Sigma_2), \quad (3.10)$$

where ω_i^2 ($i = 1, 2$) are the one-component dispersion relations for the constituents, i.e.

$$\omega_i^2 = \kappa^2 - 2\pi Gk\Sigma_i + \sigma_i^2 k^2. \quad (3.11)$$

Clearly, (3.10) is quadratic in ω^2 with two solutions (branches)

$$\omega_{\pm}^2 = \frac{1}{2} \left[\omega_1^2 + \omega_2^2 \pm \sqrt{(\omega_1^2 - \omega_2^2)^2 + 4(2\pi Gk\Sigma_1)(2\pi Gk\Sigma_2)} \right], \quad (3.12)$$

where $\omega_+^2 \geq \omega_-^2$ by construction. Since the square root term is always positive, the positive branch ω_+^2 is always positive and real. This corresponds to stable oscillations, which are of no interest in the study of instabilities. As such, it is disregarded and only ω_-^2 considered.

As with the one-component case, the system can also be considered through the line of marginal stability. For a two-component system, Bertin & Romeo (1988) derived the non-dimensional form of the MSC corresponding to the branch ω_-^2 as

$$Q_1^2 = \left(\frac{2\Lambda}{\beta} \right) \left[(\alpha + \beta) - \Lambda(1 + \beta) + \sqrt{\Lambda^2(1 - \beta)^2 - 2\Lambda(1 - \beta)(\alpha - \beta) + (\alpha + \beta)^2} \right], \quad (3.13)$$

where

$$\alpha = \frac{\Sigma_2}{\Sigma_1}, \quad \beta = \frac{\sigma_2^2}{\sigma_1^2} \quad (3.14)$$

are the ratios of surface densities α , and sound speed (respectively, velocity dispersion) β of the two components. Further, $\Lambda = \ell/\ell_{T1}$ is the dimensionless scale, with $\ell_{T1} = 1/k_{T1}$ being the Toomre scale of the first component. As before, $\bar{Q} = \max\{Q_1\}$ is the stability threshold and $\bar{\Lambda}$ the associated most unstable scale.

Note that the MSC is formulated in terms of first component. To study the stability of the coupled system at a given location in the disc, the value of $Q_1 = \kappa\sigma_1/\pi G\Sigma_1$ must be computed and compared to the stability threshold \bar{Q} .

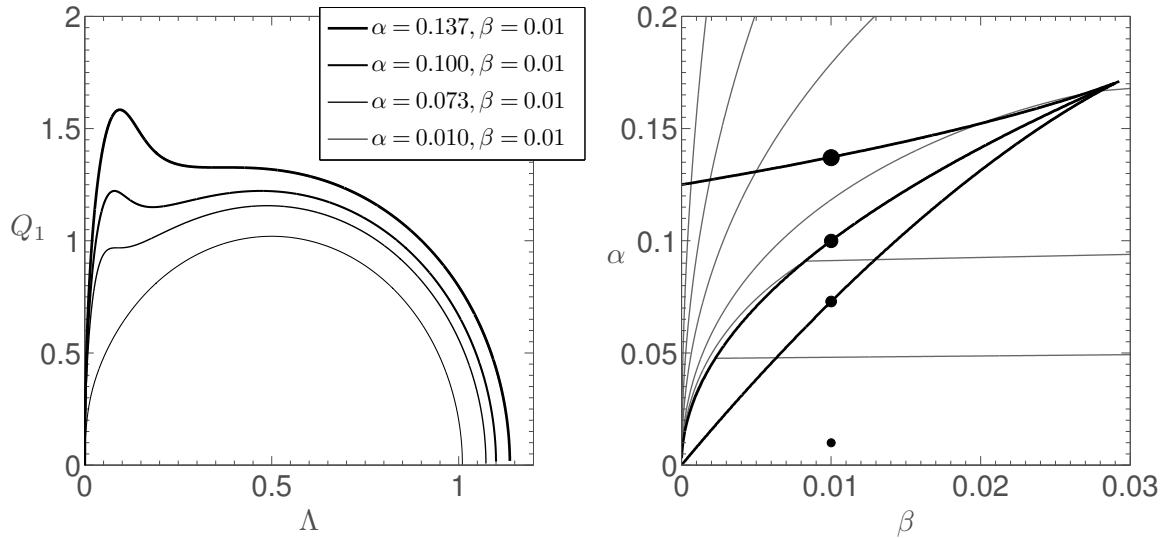


Figure 3.3.: *Left*: Marginal stability curves for different combinations of α and β . The two peaks at different Λ are associated with the two components. For the smallest α , the MSC has only one peak around $\Lambda \sim 0.5$. As α increases, a second peak appears at smaller Λ . Further increase first causes the peaks to be of the same height, then the peak at small Λ dominates until eventually the $\Lambda \sim 0.5$ peak disappears. *Right*: The $\beta - \alpha$ plane with the location of the MSCs in the left frame indicated (dot size correlates with curve thickness). The two-phase region is bounded by the outer thick black curves, marking the region where the MSC exhibits two peaks. The central black curve marks the transition where the two peaks have the same height. The thin grey curves are contours of the stability threshold $\bar{Q} = \{1.1, 1.2, 1.4, 2, 3, 5\}$ (starting from the bottom right corner going counterclockwise). Note the discontinuity of the contours across the transition line.

3.4.2. The Two-Phase Region

To study how (3.13) depends on α and β , the MSC is shown for different combinations thereof in figure 3.3. The left panel shows the MSC while the right panel indicates the location of the point in the $\beta - \alpha$ plane. Noting a fixed $\beta = 0.01$, the smallest value of $\alpha = 0.01$ yields a MSC that is remarkably similar to the one-component case. In fact, it is straightforward to show mathematically that the two-component marginal stability curve (3.13) approaches (and eventually collapses to) the one-component curve (3.8) as $\alpha \rightarrow 0$. In particular, as $\alpha \rightarrow 0$, $\bar{Q} \rightarrow 1$. This behaviour is consistent with the definition of α as the density ratio.

As α increases, the MSC diverges from the one-component behaviour, i.e. $\bar{Q} \neq 1$ and the MSC changes shape. At $\alpha = 0.073$, a second peak appears in the MSC at smaller Λ . However, the peak at $\Lambda \sim 0.5$ dominates. With increasing α , the height of the peak grows further until, at $\alpha = 0.1$, the peaks are of equal height. Further increasing α causes the small Λ peak to dominate until, at $\alpha = 0.137$, the $\Lambda \sim 0.5$ peak disappears.

This allows the definition of the two-phase region in the $\beta - \alpha$ plane. It is bounded by the outer thick black lines in the right panel of figure 3.3. Outside the two-phase region, the MSC only has one maximum; the response of the components are coupled and there is one well defined most unstable scale Λ at which instabilities first occur.

Inside the region, the response of the two-components is decoupled. The MSC exhibits two distinct peaks. The component associated with the higher peak is dominating the stability properties of the system. Physically, the presence of two peaks corresponds to two scales at which instabilities can manifest themselves, each with a different stability threshold. The thick black line in the middle corresponds to $\sqrt{\beta} = \alpha$. Along this transition line, the two peaks in the MSC are of equal height.

As α increases, \overline{Q} increases as well. This can be studied in the $\beta - \alpha$ plane by drawing contour levels for \overline{Q} . The contours $\overline{Q} = \{1.1, 1.2, 1.4, 2, 3, 5\}$ (starting from bottom right and going counterclockwise) are shown as thin grey lines in the right panel of figure 3.3.

3.4.3. Accuracy of the Fluid Approach

The original context for which Bertin & Romeo (1988) derived the two-component MSC was the study of a coupled system consisting of (i) a hot stellar component, and (ii) a cold gaseous component. In this work, both components are treated as a fluid, which — as described in §3.1 is only an approximation.

Using Bertin & Romeo (1988, Fig. 2), the error between a fluid-fluid and a fluid-kinetic (as would be appropriate for a cold gas disc coupled to a stellar component) treatment can be estimated. For fixed β , the error in \overline{Q} increases as α increases up to a maximum error of around 7% for $\alpha = 0.3$. The error on $\overline{\Lambda}$, on the other hand, is approximately constant at 5%.

Note that the values of α investigated put the corresponding MSCs in regime that is dominated by the peak at $\Lambda \sim 0.5$. Since this is the peak associated with the stellar component (which would have benefited from a kinetic treatment) in Bertin & Romeo (1988), it is not necessary to investigate the effects on the other peak.

As in the one-component case, the errors between a fluid and a kinetic treatment are below 10% and thus deemed acceptable. However, one should be aware, that — for a non-collisional component treated as a fluid — (i) \overline{Q} is larger, and (ii) $\overline{\Lambda}$ is smaller than the result obtained from a kinetic analysis.

3.5. The Turbulent One-Fluid Case

This section is based on Romeo et al. (2010) unless otherwise noted.

3.5.1. Scaling Relations in the Cold ISM

As discussed in §2, turbulence in the interstellar medium (ISM) results in power law behaviour of the energy spectra associated velocity dispersion and surface density. Consequently, both surface density Σ and velocity dispersion σ follow power laws of the form

$$\Sigma(k) = \Sigma_0 \left(\frac{k}{k_0} \right)^{-a}, \quad \sigma(k) = \sigma_0 \left(\frac{k}{k_0} \right)^{-b}, \quad (3.15)$$

where the Σ_0 and σ_0 are the surface density and velocity dispersion measured at a scale $\ell_0 = 1/k_0$. Hereafter, (3.15) shall be referred to as scaling relations and a and b as turbulent exponents.

Before proceeding, note that in the turbulent ISM, the total surface density is the sum of the mean surface density and density perturbations. The latter are driven by local compression and expansion, which are the signature of turbulent motions. In like fashion, the velocity dispersion is the sum of thermal velocity dispersion (a gauge of the temperature of the ISM) and the turbulent velocity dispersion. Thus:

$$\Sigma = \Sigma_{\text{mean}} + \delta\Sigma, \quad \sigma^2 = \sigma_{\text{thermal}}^2 + \sigma_{\text{turbulent}}^2. \quad (3.16)$$

In a warm ISM, the sound speed (and thus the thermal component of the velocity dispersion) is high. As such, motions in the gas are sub- or transonic and the medium is only minimally compressible. This means that the total surface density is dominated by the static mean density $\Sigma \sim \Sigma_{\text{mean}}$ and the velocity dispersion is dominated by the thermal component $\sigma^2 \sim \sigma_{\text{thermal}}^2$.

Conversely, in the cold ISM, the sound speed is low. The motions in the gas are supersonic and the gas is compressible. Therefore, the total surface density is dominated by the density fluctuations $\Sigma \sim \delta\Sigma$ and the velocity dispersion by the turbulent velocity dispersion $\sigma^2 \sim \sigma_{\text{turbulent}}^2$.

Since only the density perturbations and turbulent velocity dispersion scale as described by the relations (3.15), hereafter only the cold component of the ISM shall be treated. This limits the analysis to cold HI and H₂; c.f. §2.

3.5.2. Dispersion Relation, Stability Map of Turbulence

Substituting the scaling relations (3.15) into the one-component dispersion relation (3.3), one obtains the turbulent dispersion relation

$$\omega^2 = \underbrace{\kappa^2}_{\text{rotation}} - \underbrace{2\pi G \Sigma_0 k_0^a k^{1-a}}_{\text{self-gravity}} + \underbrace{\sigma_0^2 k_0^{2b} k^{2(1-b)}}_{\text{pressure}}, \quad (3.17)$$

where the contributions of rotation, self-gravity and pressure are again indicated for convenience. Expressed in non-dimensional form, the DR reads

$$\frac{\omega^2}{\kappa^2} = 1 - \frac{\mathcal{D}_\ell}{(\ell/\ell_T)} + \frac{Q_0^2}{4} \frac{\mathcal{V}_\ell^2}{(\ell/\ell_T)^2}, \quad (3.18)$$

where $Q_0 = \kappa\sigma_0/\pi G\Sigma_0$, $k_{T0} = \kappa^2/2\pi G\Sigma_0$, $\mathcal{D}_\ell = (\ell/\ell_0)^a$, and $\mathcal{V}_\ell = (\ell/\ell_0)^b$. The subscript 0 indicates that all variables describe conditions (and stability) at the scale $\ell_0 = 1/k_0$.

Depending on the choice of a and b , either the self-gravity or pressure term will dominate the dispersion relation and determine the stability properties of the system. Romeo et al. (2010) investigated the different cases and summarized them in the stability map of turbulence, which is reproduced in figure 3.4.

Various different regimes are identified in figure 3.4. The shaded lines indicate choices for a and b where stability on all scales is possible; provided certain conditions are met. In fact, these conditions appear remarkably similar to the original Toomre criterion (3.5) and the 2D

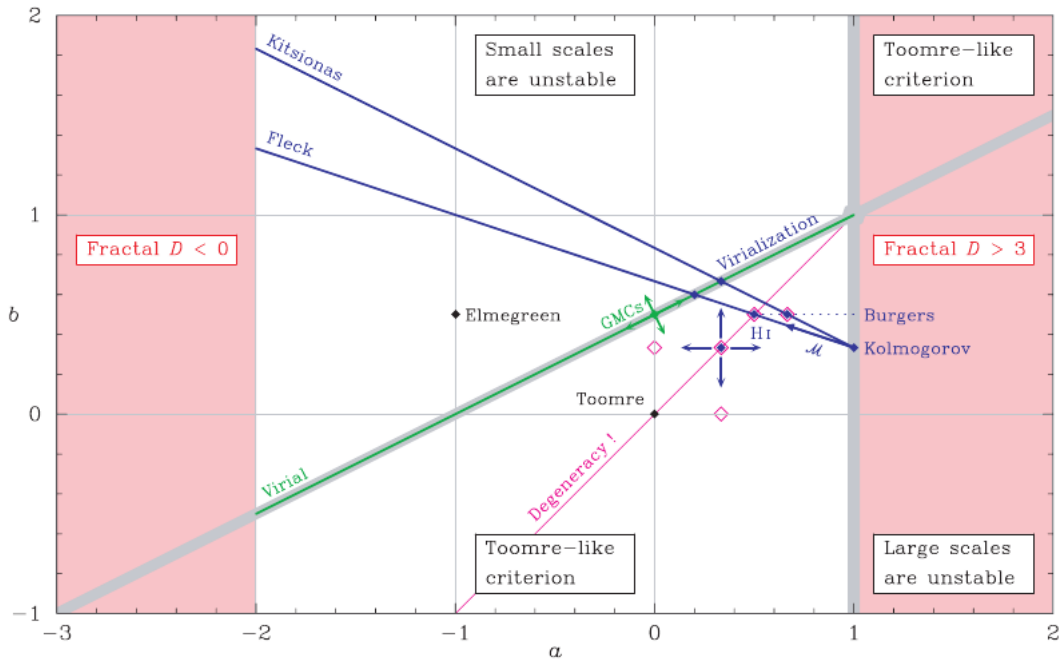


Figure 3.4.: Stability map of turbulence from Romeo et al. (2010). The scaling exponents (a, b) span the parameter plane. Note that a is limited to $-2 \leq a \leq 1$ due to the mass-size scaling relation $M \propto \ell^{a+2}$. The map is segmented by gray lines, and each segment corresponds to different dominant terms of the DR (3.17), and thus different stability regimes. The green diagonal line marks the location of virialized structures. The scaling relations obtained from observations and simulations of HI, and H₂ (see §2) mark the points $(a, b) = (0, 1/2)$ as locations for GMCs and $(a, b) = (1/3, 1/3)$ for diffuse HI. However, especially for HI, significant uncertainties are present. For a thorough discussion of this map, refer to Romeo et al. (2010).

Jeans criterion, except that they restrict k_0 instead of k . The latter shall be discussed in more detail in §5.

In all other regions, instabilities can occur on either (i) small scales, (ii) large scales, or (iii) a range of scales given by a Toomre-like stability criterion. In the latter case, the DR has a well-defined minimum, and the condition $\min\{\omega^2\} > 0$ can be imposed to require stability on all scales.

In addition to providing a theoretical map, scaling exponents derived from observations and simulation for diffuse HI and cold H₂ bound in giant molecular clouds (GMCs) are marked in figure 3.4. For example, the point $(a, b) = (0, 1/2)$ corresponds to observations of virialized GMCs where the density and velocity dispersion scale as $\Sigma = \text{const}$ and $\sigma \propto \ell^{1/2}$. In fact, the line $b = \frac{1}{2}(a + 1)$ corresponds to scaling implied for virialized structures.

HI is indicated to be populating the vicinity of $(a, b) = (1/3, 1/3)$. However, simulations and observations indicate a significant scatter around this point.

3.5.3. Stability Threshold, Saturation Scale

For combinations of a and b in the Toomre-like regime of the stability map of turbulence, i.e. $a < 1$ and $b < \frac{1}{2}(1 + a)$, stability on all scales again requires $Q \geq \bar{Q}$. In this regime, Romeo et al. (2010) obtain analytical expressions for both the stability threshold \bar{Q} and the most unstable scale $\bar{\Lambda}$.

It is found that turbulence affects \bar{Q} only if $a \neq b$. In particular, (i) for $a < b$, $\bar{Q} \propto \ell_0$, (ii) for $a > b$, $\bar{Q} \propto \ell_0^{-1}$, and (iii) for $a = b$, $\bar{Q} = 1$ (equal to the non-turbulent case). The line $a = b$ thus represents a degeneracy condition for \bar{Q} . On the other hand, $\bar{\Lambda}$ is affected by turbulence even if $a = b$ and scales as $\bar{\Lambda} \propto \ell_0^p$ with $p \leq 0$.

Recalling the discussion in §2, observations indicate that turbulence saturates at some scale, i.e. neither Σ nor σ can scale indefinitely. But how does this affect \bar{Q} and $\bar{\Lambda}$?

If ℓ_0 is associated with the saturation scale, a cut-off can be imposed on \mathcal{D}_ℓ and \mathcal{V}_ℓ appearing in (3.18), i.e.

$$\mathcal{D}_\ell = \begin{cases} (\ell/\ell_0)^a & \ell \leq \ell_0, \\ 1 & \text{otherwise.} \end{cases} \quad \mathcal{V}_\ell = \begin{cases} (\ell/\ell_0)^b & \ell \leq \ell_0, \\ 1 & \text{otherwise.} \end{cases} \quad (3.19)$$

Owing to the random nature of turbulence, the spectral signature of the saturation scale is unlikely to be in the form of a sharp cut-off at a well defined scale ℓ_0 , but appear as a smooth transition across a range of scales. However, (3.19) provides the most convenient description from a mathematical point of view. Moreover, at this stage, a more realistic description would serve no added purpose.

Based on using (3.19) in (3.18), it is found that neither \bar{Q} nor $\bar{\Lambda}$ scale indefinitely with ℓ_0 . There is always some value of ℓ_0 above (or below) which the turbulent system collapses to the behaviour of a non-turbulent system. The details are dependent on the choice of a and b .

3.6. Chapter Summary

In preceding sections, various concepts have been introduced, the most important being:

- The dispersion relation and the marginal stability curve describe the stability properties of the system. Both are always available in some form, regardless of the number of components and whether the fluid is turbulent or not.

The minimum of the dispersion relation determines whether the system can be stable on all scales or is unstable on some scales. The Toomre wavenumber k_T and Toomre parameter Q are linked to this condition. The maximum of the marginal stability curve is the stability threshold \bar{Q} . If the computed Q value at a given point in the disc exceeds \bar{Q} , the disc is stable on all wavelengths at this location. If a system becomes unstable, density perturbations first occur at the most unstable wavelength $\bar{\Lambda}$.

- The WKB and thin-disc approximations are used to simplify the analysis. The thin disc approximation imposes the restriction $kh \ll 1$, where h is the equivalent scale height if the disc were thick. The WKB approximation restricts the analysis to be a local one, and imposes the tight-winding condition $kR \gg 1$.

When applying the analysis to a set of data, the fulfilment of the conditions should be checked a posteriori. If they are not fulfilled, the analysis should be reassessed in terms of validity.

- The response of a two-component system can become decoupled depending on the relative surface densities and velocity dispersions of the components. If the system is decoupled, there are two scales at which instabilities can manifest themselves, each with a different stability threshold. The range of parameters that allow for the system to be decoupled gives rise to the two-phase region.
- Turbulence is introduced through scaling relations in the surface density Σ and velocity dispersion σ . This is limited to a cold ISM. In the warm ISM, the fluid is not sufficiently compressible and the mean density and thermal velocity dispersion dominate. Therefore, the turbulent scaling cannot be applied.

For a one-component system, if the surface density and velocity dispersion scale equally, the stability threshold of a one-component turbulent system is the same as for the equivalent non-turbulent system. The most unstable wavelength always differs.

STABILITY OF TURBULENT TWO-COMPONENT DISCS

In this chapter, the effects of turbulence on different two-component systems are investigated using the dispersion relation (DR) and marginal stability curve (MSC).

In §4.1, the general case of a two-component system is revisited and it is demonstrated that a two-component system is always less stable than the constituent components. Afterwards, §4.2 introduces the modifications required for turbulent scaling in the DR and MSC, as well as the parameter space.

Based on these, the stability of a coupled system of turbulent H_I and H₂ is discussed in §4.3. It is further demonstrated that the behaviour of this system can be extended to any system consisting of a Toomre-like and a virialized component. Finally, the stability of a stellar disc coupled to a potentially turbulent gaseous disc is discussed in §4.4.

4.1. Comparison of One- and Two-Component Dispersion Relations

In §3, the dispersion relation for a coupled two-component system was given. Repeated here for convenience, it is

$$(\omega^2 - \omega_1^2)(\omega^2 - \omega_2^2) = (2\pi Gk\Sigma_1)(2\pi Gk\Sigma_2) \quad (4.1)$$

with real valued solutions

$$\omega_{\pm}^2 = \frac{1}{2} \left[\omega_1^2 + \omega_2^2 \pm \sqrt{(\omega_1^2 - \omega_2^2)^2 + 4(2\pi Gk\Sigma_1)(2\pi Gk\Sigma_2)} \right], \quad (4.2)$$

where ω_i^2 ($i = 1, 2$) are the individual dispersion relations for the two components. Inspection of (4.1) and (4.2) shows that the response of the coupled system is related to (i) the response of the individual components, and (ii) some additional cross-terms. The latter arise from the coupling of the two components through the shared gravitational potential.

To study more quantitatively how the response of the coupled system relates to the response of the individual systems, (4.1) is rewritten as

$$(\omega^2 - \mathcal{M}_1^2) (\omega^2 - \mathcal{M}_2^2) = (\mathcal{P}_1^2 - \mathcal{M}_1^2) (\mathcal{P}_2^2 - \mathcal{M}_2^2), \quad (4.3)$$

where

$$\mathcal{P}_i^2(k) = \kappa^2 + \sigma_i^2 k^2, \quad (4.4)$$

$$\mathcal{M}_i^2(k) \equiv \omega_i^2(k)s = \kappa^2 + \sigma_i^2 k^2 - 2\pi Gk\Sigma_i, \quad (4.5)$$

i.e. $\mathcal{M}_i^2(k) = \omega_i^2(k)$ are the DRs of the individual components, and $\mathcal{P}_i^2(k)$ are dispersion relations of acoustic (sound) waves¹ associated with the components (Binney & Tremaine, 2008, App. F.3). The latter are strictly positive (\mathcal{P} - plus), whereas the former can have negative values (\mathcal{M} - minus).

Expanding and rearranging (4.3), one obtains

$$\omega^4 - \omega^2 \underbrace{(\mathcal{M}_1^2 + \mathcal{M}_2^2)}_{-p} + \underbrace{[\mathcal{M}_1^2 \mathcal{M}_2^2 - (\mathcal{P}_1^2 - \mathcal{M}_1^2) (\mathcal{P}_2^2 - \mathcal{M}_2^2)]}_q = 0. \quad (4.6)$$

Since, for any quadratic equation $x^2 + px + q = 0$, $x_1 + x_2 = -p$, this yields

$$\omega_-^2 + \omega_+^2 = \mathcal{M}_1^2 + \mathcal{M}_2^2, \quad (4.7)$$

because ω_-^2 and ω_+^2 are both real valued. Since $\omega_+^2 \geq \omega_-^2$ by construction, the inequalities

$$2 \min\{\mathcal{M}_1^2, \mathcal{M}_2^2\} \leq \mathcal{M}_1^2 + \mathcal{M}_2^2 = \omega_+^2 + \omega_-^2 \leq 2 \omega_+^2, \quad (4.8)$$

$$2 \max\{\mathcal{M}_1^2, \mathcal{M}_2^2\} \geq \mathcal{M}_1^2 + \mathcal{M}_2^2 = \omega_+^2 + \omega_-^2 \geq 2 \omega_-^2 \quad (4.9)$$

hold, such that

$$\omega_+^2 \geq \min\{\mathcal{M}_1^2, \mathcal{M}_2^2\}, \quad (4.10)$$

$$\omega_-^2 \leq \max\{\mathcal{M}_1^2, \mathcal{M}_2^2\}, \quad (4.11)$$

where $\max\{x, y\}$ selects the larger of the arguments x and y . Equivalently, $\min\{x, y\}$ selects the smaller. Thus, ω_+^2 is always larger than (or equal to) the smaller of \mathcal{M}_1^2 and \mathcal{M}_2^2 . On the other hand, ω_-^2 is always smaller than (or equal to) the larger of \mathcal{M}_1^2 and \mathcal{M}_2^2 . While these conditions are not particularly useful by themselves, their role shall become apparent momentarily.

From (4.4), note that $\mathcal{P}_i^2(k) \geq \mathcal{M}_i^2(k)$. This imposes restrictions on (4.3), i.e.

$$(\omega^2 - \mathcal{M}_1^2) (\omega^2 - \mathcal{M}_2^2) = \underbrace{(\mathcal{P}_1^2 - \mathcal{M}_1^2)}_{\geq 0} \underbrace{(\mathcal{P}_2^2 - \mathcal{M}_2^2)}_{\geq 0}, \quad (4.12)$$

$\underbrace{\hspace{10em}}_{\geq 0}$

¹The DR of acoustic waves presented in Binney & Tremaine (2008, App. F.3) does not contain the additional term κ^2 . This term arises from the differential rotation of the medium through which the waves propagate.

which implies

$$(\omega^2 - \mathcal{M}_1^2)(\omega^2 - \mathcal{M}_2^2) \geq 0. \quad (4.13)$$

To fulfil this condition, both terms on the left hand side (LHS) need to have the same sign, which leads to

$$\left. \begin{array}{l} (\omega^2 - \mathcal{M}_1^2) \leq 0 \\ (\omega^2 - \mathcal{M}_2^2) \leq 0 \end{array} \right\} \left. \begin{array}{l} \omega^2 \leq \mathcal{M}_1^2 \\ \omega^2 \leq \mathcal{M}_2^2 \end{array} \right\} \text{Case I,} \quad \left. \begin{array}{l} (\omega^2 - \mathcal{M}_1^2) \geq 0 \\ (\omega^2 - \mathcal{M}_2^2) \geq 0 \end{array} \right\} \left. \begin{array}{l} \omega^2 \geq \mathcal{M}_1^2 \\ \omega^2 \geq \mathcal{M}_2^2 \end{array} \right\} \text{Case II.} \quad (4.14)$$

Case I. From the inequality (4.10), the positive solution ω_+^2 is always larger than at least one of either \mathcal{M}_1^2 or \mathcal{M}_2^2 . This means that either $\omega_+^2 \leq \mathcal{M}_1^2$ or $\omega_+^2 \leq \mathcal{M}_2^2$ is not fulfilled.² Therefore, only the negative solution ω_-^2 guarantees that the condition is fulfilled. Since it must be smaller than both \mathcal{M}_1^2 and \mathcal{M}_2^2 , one obtains the further condition

$$\omega_-^2 \leq \min\{\mathcal{M}_1^2, \mathcal{M}_2^2\}. \quad (4.15)$$

This is an extremely important result. Since only the negative branch ω_-^2 for a two-component system is potentially unstable, this means that the DR of the two-component system is always below the individual DRs of the constituent systems. Physically, the two-component system is always less stable than the individual systems it is comprised of.

Case II. Equivalently, from (4.11), one finds that the negative solution ω_-^2 is always smaller than at least one of either \mathcal{M}_1^2 or \mathcal{M}_2^2 . As such, either $\omega_-^2 \geq \mathcal{M}_1^2$ or $\omega_-^2 \geq \mathcal{M}_2^2$ is not fulfilled.³ Thus, only the positive solution ω_+^2 guarantees fulfilment of the case, provided that

$$\omega_+^2 \geq \max\{\mathcal{M}_1^2, \mathcal{M}_2^2\}. \quad (4.16)$$

Since both ω_+^2 and \mathcal{P}_i^2 are larger than \mathcal{M}_i^2 , it is possible that \mathcal{P}_i^2 and ω_+^2 are related. To quantify this relation, consider again (4.3). If ω_+^2 is larger than \mathcal{P}_1^2 and \mathcal{P}_2^2 ($\omega_+^2 > \max\{\mathcal{P}_1^2, \mathcal{P}_2^2\}$), one of the terms on the LHS would be larger than the equivalent right hand side (RHS) term and equality would be lost. Correspondingly, if ω_+^2 is smaller than both \mathcal{P}_1^2 and \mathcal{P}_2^2 ($\omega_+^2 < \min\{\mathcal{P}_1^2, \mathcal{P}_2^2\}$), one of the LHS terms would be smaller than the corresponding RHS term and equality would be lost again. Recalling that $\mathcal{P}_i^2 \geq \kappa^2 > 0$, these considerations imply

$$0 < \kappa^2 \leq \min\{\mathcal{P}_1^2, \mathcal{P}_2^2\} \leq \omega_+^2 \leq \max\{\mathcal{P}_1^2, \mathcal{P}_2^2\}. \quad (4.17)$$

Figure 4.1 illustrates conditions (4.4), (4.5), (4.10), (4.11), (4.15), (4.16), and (4.17). In this order, it shows that

²Note that it is possible that both $\omega_+^2 \leq \mathcal{M}_1^2$ and $\omega_+^2 \leq \mathcal{M}_2^2$ are not fulfilled. This implies $\omega_+^2 \geq \mathcal{M}_1^2$ and $\omega_+^2 \geq \mathcal{M}_2^2$, which actually fulfils case II in (4.14). This situation is, however, not guaranteed.

³Again, it is possible that both $\omega_-^2 \geq \mathcal{M}_1^2$ and $\omega_-^2 \geq \mathcal{M}_2^2$ are not fulfilled. Then, $\omega_-^2 \leq \mathcal{M}_1^2$ or $\omega_-^2 \leq \mathcal{M}_2^2$ would fulfil case I in (4.14). Again, this cannot be guaranteed.

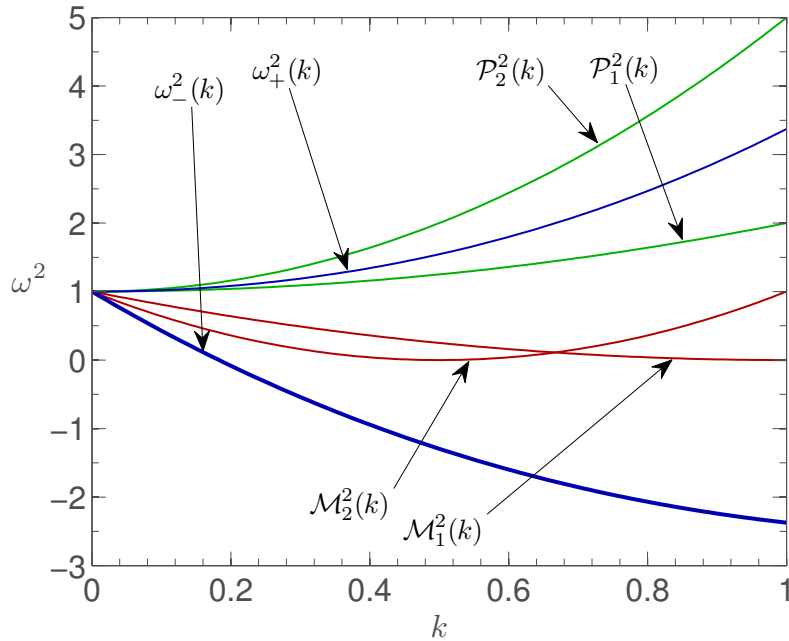


Figure 4.1.: Graphs of two-component $\omega_{\pm}^2(k)$ (blue), one-component $\mathcal{M}_{1,2}^2(k)$ (red), and acoustic wave $\mathcal{P}_{1,2}^2(k)$ (green) dispersion relations. For simplicity, the model parameters are $G = \pi = \kappa = 1$, $\Sigma_1 = \sigma_1 = 1$, $\Sigma_2 = \sigma_2 = 2$ and units are not indicated. The thick blue line is the potentially unstable branch ω_{-}^2 of the two-component dispersion relation. Note that for $k = 0$, all DRs have the value κ^2 . For a more detailed description, refer to the numerated list at the end of §4.1.

1. Acoustic waves are always more stable than density waves, i.e. $\mathcal{P}_i^2 \geq \mathcal{M}_i^2$, (4.4), (4.5).
2. The positive branch of the two-component DR is more stable than the more unstable one-component DR, i.e. $\omega_{+}^2 \geq \min\{\mathcal{M}_1^2, \mathcal{M}_2^2\}$, (4.10).
3. The negative branch of the two-component DR is more unstable than the most stable one-component DR, i.e. $\omega_{-}^2 \leq \max\{\mathcal{M}_1^2, \mathcal{M}_2^2\}$, (4.11).
4. The two-component system is always less stable than both constituent one-component systems, i.e. $\omega_{-}^2 \leq \min\{\mathcal{M}_1^2, \mathcal{M}_2^2\}$, (4.15).
5. The positive branch of the two-component DR is always more stable than both individual DRs, i.e. $\omega_{+}^2 \geq \max\{\mathcal{M}_1^2, \mathcal{M}_2^2\}$, (4.16).
6. The same positive branch is bounded by the DRs of the acoustic waves associated with the individual components, i.e. (4.17).

4.2. General Equations for Two Turbulent Components

In this section, the equations governing the stability of two-component systems are extended with turbulent scaling laws. Hereafter, a “classical system” refers to a system without any turbulent components. Reversely, a “turbulent system” refers to a system with at least one turbulent component.

4.2.1. Dispersion Relation

To describe a coupled system of two turbulent components (indexed by $i = 1, 2$), the turbulent scaling relations (3.15) for each component

$$\Sigma_i = \Sigma_{0i} \left(\frac{k}{k_0} \right)^{-a_i}, \quad \sigma_i = \sigma_{0i} \left(\frac{k}{k_0} \right)^{-b_i} \quad (4.18)$$

are substituted into the two-component DR (4.1) and its solution (4.2). The potentially unstable branch is thus given by

$$\omega_-^2 = \frac{1}{2} \left[\omega_1^2 + \omega_2^2 - \sqrt{(\omega_1^2 - \omega_2^2)^2 + 4(2\pi G k \Sigma_{01})(2\pi G k \Sigma_{02}) \left(\frac{k}{k_0} \right)^{-(a_1+a_2)}} \right], \quad (4.19)$$

where the constituent DRs are

$$\omega_i^2 = \kappa^2 - 2\pi G k \Sigma_{0i} \left(\frac{k}{k_0} \right)^{-a_i} + \sigma_{0i}^2 k^2 \left(\frac{k}{k_0} \right)^{-2b_i}. \quad (4.20)$$

Using the Toomre and Jeans⁴ wavenumbers,⁵

$$k_{Ti} \equiv k_{0,Ti} = \frac{\kappa^2}{2\pi G \Sigma_{0i}}, \quad k_{Ji} \equiv k_{0,Ji} = \frac{2\pi G \Sigma_{0i}}{\sigma_{0i}^2}, \quad (4.21)$$

(4.19) and (4.20) can be written in the non-dimensional forms

$$\frac{\omega_-^2}{\kappa^2} = \frac{1}{2} \left[\frac{\omega_1^2}{\kappa^2} + \frac{\omega_2^2}{\kappa^2} - \sqrt{\left(\frac{\omega_1^2}{\kappa^2} - \frac{\omega_2^2}{\kappa^2} \right)^2 + 4 \frac{k}{k_{T1}} \frac{k}{k_{T2}} \left(\frac{k}{k_0} \right)^{-(a_1+a_2)}} \right], \quad (4.22)$$

and

$$\frac{\omega_i^2}{\kappa^2} = 1 - \frac{k}{k_{Ti}} \left(\frac{k}{k_0} \right)^{-a_i} + \frac{k}{k_{Ti}} \frac{k}{k_{Ji}} \left(\frac{k}{k_0} \right)^{-2b_i}. \quad (4.23)$$

Using $k_{Ti}/k_{Ji} = Q_{0i}^2/4$, (4.23) can be rewritten to

$$\frac{\omega_i^2}{\kappa^2} = 1 - \frac{k}{k_{Ti}} \left(\frac{k}{k_0} \right)^{-a_i} + \left(\frac{k}{k_{Ti}} \right)^2 \frac{Q_{0i}^2}{4} \left(\frac{k}{k_0} \right)^{-2b_i}, \quad (4.24)$$

⁴The Jeans wavenumber determines the stability of a self-gravitating fluid with non-zero pressure. See Binney & Tremaine (2008, §5.2) for more information, but note that it describes the three-dimensional case.

⁵These wavenumbers are not the classical Toomre and Jeans wavenumbers discussed in §3.3 and Binney & Tremaine (2008, §5.2). They are the turbulent equivalents restricting k_0 instead of k . Since the classical Toomre and Jeans wavenumbers are not used hereafter, $k_{Ti} \equiv k_{0,Ti}$ and $k_{Ji} \equiv k_{0,Ji}$ are used for brevity.

and k/k_0 expressed as

$$\frac{k}{k_0} = \frac{k}{k_{T_i}} \frac{k_{T_i}}{k_{J_i}} \frac{k_{J_i}}{k_0} = \frac{k}{k_{T_i}} \frac{Q_{0i}^2}{4} \frac{k_{J_i}}{k_0}, \quad (4.25)$$

where $Q_{0i} = \kappa\sigma_{0i}/(\pi G\Sigma_{0i})$ is the familiar Toomre parameter of the i -th component valid at wavenumber k_0 . The advantage of expressions (4.24) and (4.25) is that they explicitly contain the stability parameters for virialized and Toomre-like components in the stability map of turbulence.⁶ In particular, Q_{0i} determines the stability of components in the Toomre-like⁷ region. The ratio k_{J_i}/k_0 determines the stability of components along the virial line given by $-2 < a_i < 1$, $b_i = \frac{1}{2}(a_i + 1)$.

It should be noted that the presence of two different stability criteria in (4.24) and (4.25) does not pose a problem. The impact of the factors Q_{0i} and k_{J_i}/k_0 changes depending on the choice of a_i and b_i . While both parameters influence the shape of the function, the stability (i.e., whether it is possible that $\omega_i^2/\kappa^2 < 0$) is only governed by one factor at a time.

4.2.2. Marginal Stability Curve

When attempting to understand the impact of different parameters on the stability of a system, it is generally more convenient to study the marginal stability curve (MSC) instead of the dispersion relation, cf. §3. However, the MSC is less universal in the sense that it is only valid if the system is Toomre-like, i.e. the DR has a distinct minimum.

Originally given by (3.13) for a classical system, the MSC can easily be adapted by scaling the surface density Σ_i and velocity dispersion σ_i of the relevant components in the same way as done in the DR. The MSC

$$Q_1^2 = \left(\frac{2\Lambda}{\beta}\right) \left[(\alpha + \beta) - \Lambda(1 + \beta) + \sqrt{\Lambda^2(1 - \beta)^2 - 2\Lambda(1 - \beta)(\alpha - \beta) + (\alpha + \beta)^2} \right] \quad (4.26)$$

then includes the scale dependent surface density and velocity dispersion by combining (3.14) with (3.15), such that

$$\alpha = \alpha_0 \left(\frac{\Lambda}{\Lambda_0}\right)^{a_2 - a_1}, \quad \beta = \beta_0 \left(\frac{\Lambda}{\Lambda_0}\right)^{2(b_2 - b_1)}, \quad (4.27)$$

where $\alpha_0 = \Sigma_{02}/\Sigma_{01}$, and $\beta_0 = \sigma_{02}^2/\sigma_{01}^2$ are surface density and velocity dispersion ratios measured at scale $\ell_0 = 1/k_0$. Further, $\Lambda = \ell/\ell_{T1} = k_{T1}/k$, and $\Lambda_0 = \ell_0/\ell_{T1} = k_{T1}/k_0$. Note that since

$$Q_1 = \frac{\kappa\sigma_{01}}{\pi G\Sigma_{01}} \left(\frac{\Lambda}{\Lambda_0}\right)^{b_1 - a_1} = Q_{01} \left(\frac{\Lambda}{\Lambda_0}\right)^{b_1 - a_1}, \quad (4.28)$$

⁶Cf. figure 3.4.

⁷Strictly speaking, the stability map of turbulence has two regions of Toomre-like stability. However, one of the regions is unphysical because the fractal dimension $D > 3$. As such, any reference to a ‘‘Toomre-like’’ region in the stability map of turbulence shall hereafter refer to the region $-2 < a_i < 1$, $b_i < \frac{1}{2}(a_i + 1)$.

$Q_1 = Q_{01}$ if $a_1 = b_1$. Since this is the case for both the coupled HI and H₂ system as well as the system of HI coupled to a stellar disc, the scaling of Q_1 does not need to be accounted for when these specific cases are studied.

The marginal stability curve of the form (4.26) is positive $Q_1^2 > 0$ for $0 \leq \Lambda \leq 1 + \alpha$, provided that α and β are not functions of Λ (Bertin & Romeo, 1988). If, on the other hand, α and β have a scale dependence as shown in (4.27), this range is modified. Retaining the lower limit $0 \leq \Lambda$, and writing $\Lambda \leq \Lambda_{\text{Zero}} = 1 + \alpha$ for the upper limit, one obtains

$$\Lambda_{\text{Zero}} = 1 + \alpha = 1 + \alpha_0 \left(\frac{\Lambda_{\text{Zero}}}{\Lambda_0} \right)^{a_2 - a_1}, \quad (4.29)$$

such that

$$0 = 1 + \alpha_0 \Lambda_{\text{Zero}}^{a_2 - a_1} \Lambda_0^{a_1 - a_2} - \Lambda_{\text{Zero}}, \quad (4.30)$$

with the upper zero given by a real valued solution Λ_{Zero} of (4.30). Due to the unpredictable order of the polynomial, a simple analytical solution for Λ_{Zero} cannot be stated. In this work, numerical solutions around the point $\Lambda = 1 + \alpha_0$ are searched instead.

4.2.3. The Parameter Space

In §3.4.2, the $\beta - \alpha$ plane was first introduced as a parameter space with a MSC $Q_1 = Q_1(\Lambda)$ associated with each point (β, α) in the plane. Considering figure 3.3, one can notice that the range of values spanned in both β and α is very small and that both the \bar{Q} contours as well as the transition line in the two-phase region approach the point $(\beta, \alpha) = (0, 0)$ very close to the vertical axis. In order to study the graph better at such small scales, a logarithmic scaling in both axes is more appropriate.

Moreover, the choice of β and α for the parameter plane is not particularly convenient if a link between observations and theoretical considerations is to be made. The former generally describe the physics of the system in terms of the velocity dispersion σ and the Toomre parameter Q , whereas the latter require σ^2 and Σ as parameters. To avoid unnecessary conversion, a more suitable set of parameters for the $\beta - \alpha$ plane can be chosen, i.e.

$$s = \frac{\sigma_2}{\sigma_1} = \sqrt{\beta}, \quad q = \frac{Q_2}{Q_1} = \frac{\sqrt{\beta}}{\alpha}. \quad (4.31)$$

Accounting for scale dependence in turbulent media, this can be written as

$$s = \frac{\sigma_2}{\sigma_1} = \underbrace{\frac{\sigma_{02}}{\sigma_{01}}}_{s_0} \left(\frac{\Lambda}{\Lambda_0} \right)^{b_2 - b_1}, \quad q = \frac{Q_2}{Q_1} = \underbrace{\frac{Q_{02}}{Q_{01}}}_{q_0} \left(\frac{\Lambda}{\Lambda_0} \right)^{(b_2 - a_2) - (b_1 - a_1)}, \quad (4.32)$$

such that

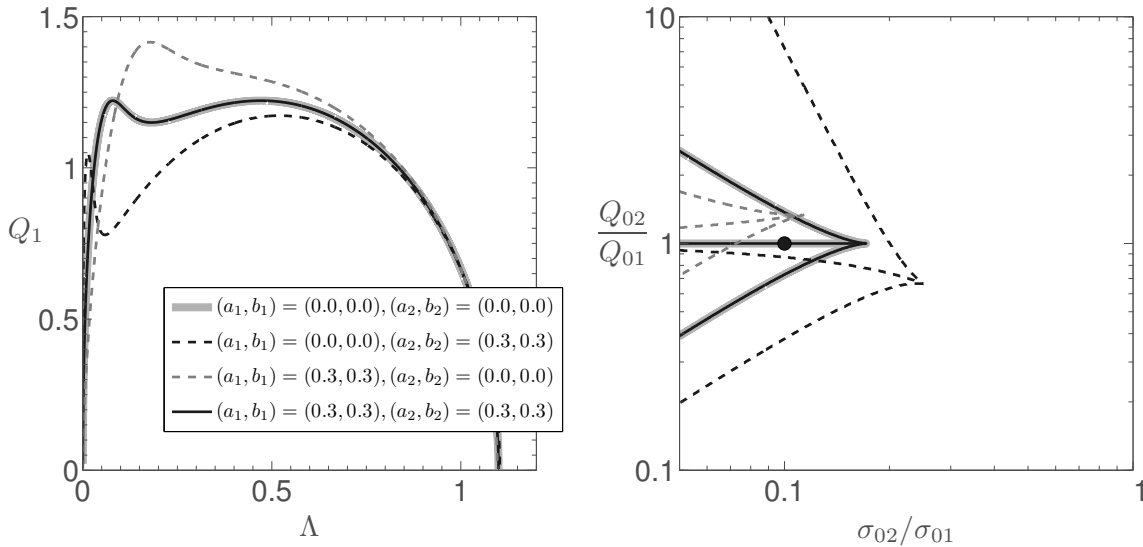


Figure 4.2.: Marginal stability curves (left) and two-phase regions (right) for four two-component systems with different scaling exponents, cf. figure legend. All turbulent components use $\Lambda_0 = 1$. While the classical system has the transition between dominating components at $q_0 = Q_{02}/Q_{01} = 1$, this transition line and the two-phase regions for the systems with only one turbulent component are displaced asymmetrically about $q_0 = 1$. Also note that the system of two turbulent components (with all scaling exponents equal) collapses to the classical case.

$$s_0 = \frac{\sigma_{02}}{\sigma_{01}} = \sqrt{\beta_0}, \quad q_0 = \frac{Q_{02}}{Q_{01}} = \frac{\sqrt{\beta_0}}{\alpha_0}, \quad (4.33)$$

where quantities with subscript 0 are values at scale $\Lambda_0 = \ell_0/\ell_{T1}$. Note that for a classical system, quantities are scale-independent, i.e. $s_0 = s$, and $q_0 = q$.

Figure 4.2 shows the MSC (left panel) and the two-phase regions for four cases of coupled systems in the logarithmic $s_0 - q_0$ parameter space (right panel): (i) the classical case of two non-turbulent components, (ii), (iii) the cases where either the first or the second component is turbulent and Toomre-like (with $a = b = 1/3$), and (iv) two Toomre-like turbulent components ($a_{1,2} = b_{1,2} = 1/3$).

In the classical case, the choice of $q_0 = q = Q_{02}/Q_{01} = 1$ corresponds to the case where both components have the same stability level, i.e. both MSC peaks are of equal height. On either side of the horizontal transition line, one of the peaks is higher than the other, meaning that one of the component dominates the stability behaviour of the coupled system. In particular, for $q_0 > 1$, $Q_{02} > Q_{01}$, and the peak associated with the first (less stable) component will dominate the stability of the coupled system. Conversely, for $q_0 < 1$, $Q_{02} < Q_{01}$, the peak associated with the second component will dominate and therefore determine the stability properties of the coupled system.

In the case of a system with one turbulent Toomre-like component, the symmetry about the $q_0 = 1$ line is broken and the transition line moves upwards, respectively downwards. This is caused by the different scalings laws of $(\sigma_{1,2}, \Sigma_{1,2})$, which appear in the MSC through (β, α) , and thus (s, q) . One might further expect a symmetry about the $q_0 = 1$ line when comparing

the cases of (i) $(a_1, b_1, a_2, b_2) = (0, 0, 1/3, 1/3)$, and (ii) $(a_1, b_1, a_2, b_2) = (1/3, 1/3, 0, 0)$, but such a consideration does not take into account that $s_0 = \sqrt{\beta_0}$ and $q_0 = \sqrt{\beta_0}/\alpha_0$ have not been inverted. In fact, when switching turbulent components and inverting q_0 and s_0 , a symmetric two-phase region is found around $(s_0, q_0) \sim (10, 1)$. However, for a disc of stars coupled to a turbulent gaseous component, the symmetric two-phase region is located in a part of the $s_0 - q_0$ plane that is nonphysical, cf. §4.4.1.

Finally, the case of two-turbulent Toomre-like components with the same scaling exponents collapses to the classical case of two non-turbulent components. This is in analogy to the behaviour described in §3.5.3, where a one-component turbulent system behaves equivalent to a non-turbulent system if the scaling exponents on both σ , and Σ are equal.

4.3. Stability of Coupled Turbulent HI and Turbulent H₂

As discussed in §2, atomic and molecular hydrogen are the most abundant elements in galactic discs. Additionally, both components exhibit scaling of the velocity dispersion and density distribution. The study of the stability properties of the combined system is therefore of interest.

4.3.1. Stability Regime of the Coupled System

In line with §3.5.1, the scaling exponents adopted are $(a_1, b_1) = (1/3, 1/3)$ for the HI component and $(a_2, b_2) = (0, 1/2)$ for the H₂ component, i.e.

$$\Sigma_{\text{HI}} = \Sigma_1 = \Sigma_{01} \left(\frac{k}{k_0} \right)^{-1/3}, \quad \sigma_{\text{HI}} = \sigma_1 = \sigma_{01} \left(\frac{k}{k_0} \right)^{-1/3}, \quad (4.34)$$

and

$$\Sigma_{\text{H}_2} = \Sigma_2 = \Sigma_{02} \left(\frac{k}{k_0} \right)^{-0}, \quad \sigma_{\text{H}_2} = \sigma_2 = \sigma_{02} \left(\frac{k}{k_0} \right)^{-1/2}, \quad (4.35)$$

such that the two-component DR becomes

$$\omega_-^2 = \frac{1}{2} \left[\underbrace{\omega_1^2 + \omega_2^2}_{\text{Term I}} - \sqrt{\underbrace{(\omega_1^2 - \omega_2^2)^2}_{\text{Term II}} + \underbrace{4(2\pi Gk\Sigma_{01})(2\pi Gk\Sigma_{02}) \left(\frac{k}{k_0} \right)^{-1/3}}_{\text{Term III}}} \right], \quad (4.36)$$

where the use of the terms I, II, and III shall become clear soon and the constituent DRs are

$$\omega_1^2 = \kappa^2 - 2\pi Gk\Sigma_{01} \left(\frac{k}{k_0} \right)^{-1/3} + \sigma_{01}^2 k^2 \left(\frac{k}{k_0} \right)^{-2/3}, \quad (4.37)$$

and

$$\omega_2^2 = \kappa^2 - 2\pi Gk\Sigma_{02} \left(\frac{k}{k_0}\right)^0 + \sigma_{02}^2 k^2 \left(\frac{k}{k_0}\right)^{-1}. \quad (4.38)$$

To determine the stability of the coupled system, the behaviour of (4.36), (4.37), and (4.38) needs to be considered. Since the HI component is Toomre-like, ω_1^2 decreases from $\omega_1^2(k=0) = \kappa^2$ to some minimum, after which it can increase again. Due to the constraint $\omega_-^2 \leq \min\{\omega_1^2, \omega_2^2\}$ (cf. §4.1), this means that ω_-^2 must decrease from $\omega_-^2(k=0) = \kappa^2$.

At larger k , ω_-^2 can either decrease further or increase again. To determine which is the case, the asymptotic behaviour of $\omega_-^2(k \rightarrow \infty)$ is studied. In this limit, ω_-^2 is dominated by terms proportional to k^γ for the largest $\gamma \geq 1$.

Working out all terms in ω_-^2 and selecting the largest powers of k from the three terms of (4.36), one obtains

$$\omega_-^2(k \rightarrow \infty) \propto k^{4/3} \left(\sigma_{01}^2 k_0^{2/3}\right) - \sqrt{k^{8/3} \left(\sigma_{01}^2 k_0^{2/3}\right)^2 + k^{5/3} \left(16\pi^2 G^2 \Sigma_{01} \Sigma_{02} k_0^{4/3}\right)}. \quad (4.39)$$

Since the $\sqrt{\cdot}$ is dominated by the first term, this becomes

$$\omega_-^2(k \rightarrow \infty) \propto k^{4/3} \left(\sigma_{01}^2 k_0^{2/3}\right) - \sqrt{k^{8/3} \left(\sigma_{01}^2 k_0^{2/3}\right)^2}, \quad (4.40)$$

$$\propto k^{4/3} \left(\sigma_{01}^2 k_0^{2/3}\right) - k^{4/3} \left(\sigma_{01}^2 k_0^{2/3}\right), \quad (4.41)$$

which means that the two terms proportional to $k^{4/3}$ balance one other as $k \rightarrow \infty$ and cannot be used to obtain the asymptotic behaviour of $\omega_-^2(k \rightarrow \infty)$. To do this, the next largest power of k in the three terms of (4.36) must be considered. One then obtains

$$\begin{aligned} \omega_-^2(k \rightarrow \infty) &\propto k \left(\sigma_{02}^2 k_0 - 2\pi G \Sigma_{02}\right) \\ &\quad - \sqrt{k^2 \left(-\sigma_{02}^2 k_0 + 2\pi G \Sigma_{02}\right)^2 + k^{5/3} \left(16\pi^2 G^2 \Sigma_{01} \Sigma_{02} k_0^{4/3}\right)}. \end{aligned} \quad (4.42)$$

Again, the first term dominates the $\sqrt{\cdot}$, such that

$$\omega_-^2(k \rightarrow \infty) \propto k \left(\sigma_{02}^2 k_0 - 2\pi G \Sigma_{02}\right) - \sqrt{k^2 \left(-\sigma_{02}^2 k_0 + 2\pi G \Sigma_{02}\right)^2}, \quad (4.43)$$

$$\propto k \left(\sigma_{02}^2 k_0 - 2\pi G \Sigma_{02}\right) - k \left(-\sigma_{02}^2 k_0 + 2\pi G \Sigma_{02}\right), \quad (4.44)$$

$$\propto k \left(\sigma_{02}^2 k_0 - 2\pi G \Sigma_{02}\right) + k \left(\sigma_{02}^2 k_0 - 2\pi G \Sigma_{02}\right), \quad (4.45)$$

$$\propto 2k \left(\sigma_{02}^2 k_0 - 2\pi G \Sigma_{02}\right). \quad (4.46)$$

The behaviour of $\omega_-^2(k \rightarrow \infty)$ is thus determined by the sign of $\sigma_{02}^2 k_0 - 2\pi G \Sigma_{02}$. In particular, if $\sigma_{02}^2 k_0 - 2\pi G \Sigma_{02} \leq 0$, ω_-^2 remains negative as k increases, which implies instability

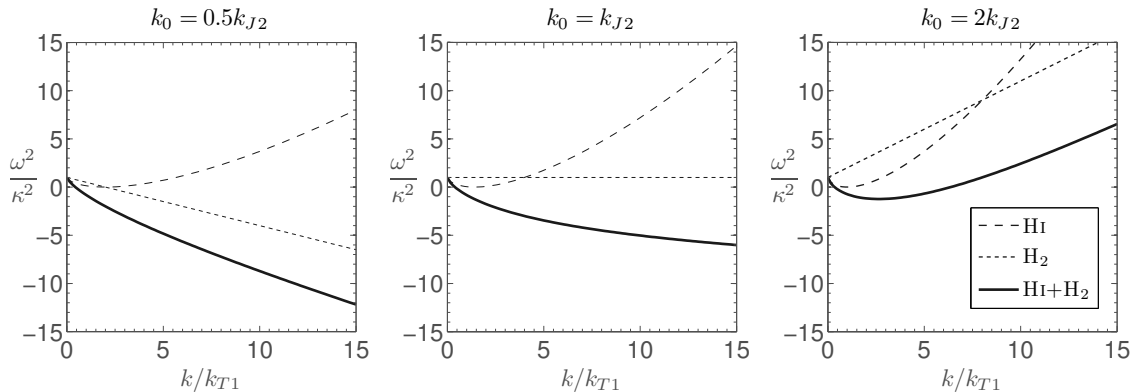


Figure 4.3.: Dimensionless turbulent dispersion relations for HI, H₂ (thin dashed lines), and the coupled HI + H₂ system (bold black line) for $s_0 = q_0 = 1$. In all panels, HI is Toomre-like and stable ($Q_{01} = 1$, $\omega^2/\kappa^2 \geq 0$). The leftmost panel shows H₂ unstable on small scales ($k_0 < k_{J2}$), such that the combined system behaves similarly. In the central panel, H₂ is marginally stable ($k_0 = k_{J2}$) and the combined system is still unstable at small scales. In the rightmost panel, H₂ is stable on all scales ($k_0 > k_{J2}$), but the combined system is now Toomre-like with a clearly defined minimum at \bar{k} . Moreover, at large k , the DR converges to a line parallel to the DR of the H₂ component.

at small scales. Conversely, if $\sigma_{02}^2 k_0 - 2\pi G \Sigma_{02} > 0$, ω_-^2 becomes positive at large k . In this case, ω_-^2 is Toomre-like.⁸

Rewriting the condition as

$$k_0 > \frac{2\pi G \Sigma_{02}}{\sigma_{02}^2} = k_{J2}, \quad (4.47)$$

one finds that this strongly resembles the stability criterion of virialized turbulent systems (such as H₂) described in Romeo et al. (2010, §2.3). This means that stability of the H₂ component is a necessary⁹ condition for a two-component system of turbulent HI and H₂ to be Toomre-like.

To illustrate condition (4.47), (4.24) and (4.25) are now written more explicitly for the HI and H₂ components in terms of Q_{01} (determines HI stability) and k_0/k_{J2} (determines H₂ stability). Using $Q_{01}/Q_{02} = 1/q_0$, $k_{T1}/k_{T2} = s_0/q_0$, and $k_{J1}/k_{J2} = s_0 q_0$, one obtains for HI

$$\frac{\omega_1^2}{\kappa^2} = 1 - \frac{k}{k_{T1}} \left(\frac{k}{k_0}\right)^{-1/3} + \left(\frac{k}{k_{T1}}\right)^2 \frac{Q_{01}^2}{4} \left(\frac{k}{k_0}\right)^{-2/3}, \quad (4.48)$$

and for H₂

⁸Recall that at small k , ω_-^2 decreases with k . If it increases at large k , it must have a well defined minimum. A DR exhibiting this shape means the system is Toomre-like.

⁹A necessary, but not sufficient condition because a virialized component is stable if $k_0 \geq k_J$ (Romeo et al., 2010, §2.3). The criterion derived here further requires $k_0 > k_J$, i.e. marginal stability (equality) is not sufficient.

$$\frac{\omega_2^2}{\kappa^2} = 1 - \frac{k}{k_{T1}} \frac{s_0}{q_0} \left(\frac{k}{k_0}\right)^0 + \left(\frac{k}{k_{T1}} \frac{s_0}{q_0}\right)^2 \frac{Q_{01}^2}{4} \frac{q_0^2}{1} \left(\frac{k}{k_0}\right)^{-1}, \quad (4.49)$$

where

$$\frac{k}{k_0} = \frac{k}{k_{T1}} \frac{k_{J1}}{k_0} = \frac{k}{k_{T1}} \frac{Q_{01}^2}{4} \frac{k_{J2}}{k_0} \frac{s_0}{1} q_0. \quad (4.50)$$

Using (4.48), (4.49), and (4.50), the non-dimensional two-component dispersion relation for turbulent HI and H₂ then is

$$\frac{\omega_-^2}{\kappa^2} = \frac{1}{2} \left[\frac{\omega_1^2}{\kappa^2} + \frac{\omega_2^2}{\kappa^2} - \sqrt{\left(\frac{\omega_1^2}{\kappa^2} - \frac{\omega_2^2}{\kappa^2}\right)^2 + 4 \frac{k}{k_{T1}} \frac{k}{k_{T1}} \frac{s_0}{q_0} \left(\frac{k}{k_0}\right)^{-1/3}} \right]. \quad (4.51)$$

Figure 4.3 shows the dispersion relations (4.48), (4.49), (4.51) for the three (from left to right) cases $k_0 < k_{J2}$, $k_0 = k_{J2}$, and $k_0 > k_{J2}$. In all panels, one can clearly see that the coupled system is less stable than the two individual systems on all scales. Furthermore, on small scales (large k), the DR of the coupled system converges to a line parallel to the DR of the H₂ component.

In the leftmost panel, $k_0 < k_{J2}$, and the H₂ component is unstable on small scales. Regardless of the stability of the HI component, the coupled system is also unstable on small scales. In the middle panel, the H₂ component is marginally stable with $k_0 = k_{J2}$. This is not enough for the coupled system to be stable, and it is still unstable on small scales. In the rightmost panel, the H₂ component is stable with $k_0 > k_{J2}$. This allows the coupled system to be stable on small scales. As such, the coupled DR has a distinct minimum at some value \bar{k} . It is thus Toomre-like.

4.3.2. Extension: Turbulent Virialized and Toomre-like Components

The considerations regarding a coupled system of turbulent HI and turbulent H₂ can be extended to the general case turbulent virialized and a Toomre-like components.

As per Romeo et al. (2010, §2.3), any virialized turbulent system is stable on all scales if $k_0 \geq k_J = 2\pi G \Sigma_0 / \sigma_0^2$ and unstable on small scales otherwise. If the virialized system is unstable on small scales, the dispersion relation is monotonically decreasing starting from κ^2 at $k = 0$. If the virialized component is stable, the DR is monotonically increasing starting from κ^2 at $k = 0$. The Toomre-like component also starts at κ^2 at $k = 0$, then decreases to some minimum, after which it increases again.

The system of both components is always less stable than the two constituents. As such, the DR is forced to decrease at small k to remain below the both the Toomre-like and virialized component. Since the Toomre-like component increases at k larger than the k associated with its minimum, the behaviour of the combined system only depends on the stability of the virialized system. In particular, if the virialized system is unstable on small scales, so is the combined system because it is always less stable. On the other hand, if the Toomre-like component is stable on all scales, the DR of the combined system can increase to larger values after passing the minimum imposed by the Toomre-like component.

However, whether the combined DR indeed increases is subject to further constraints. In particular, recall the two-component turbulent DR given by (4.19) with constituent DRs (4.20). Ignoring all coefficients to show only the k -dependence for all terms then gives

$$\omega_-^2 \propto \underbrace{k^{1-a_1} + k^{2-2b_1} - k^{1-a_2} + k^{2-2b_2}}_{\text{Term I: } \omega_1^2 + \omega_2^2} - \sqrt{\underbrace{\left(k^{1-a_1} + k^{2-2b_1} + k^{1-a_2} - k^{2-2b_2}\right)^2}_{\text{Term II: } (\omega_1^2 - \omega_2^2)^2} + \underbrace{k^{2-(a_1+a_2)}}_{\text{Term III: } 4(2\pi Gk\Sigma_1)(2\pi Gk\Sigma_2)}}. \quad (4.52)$$

Provided that Term II > Term III in the limit $k \rightarrow \infty$ and noting that the first terms $k^{1-a_1} + k^{2-2b_1}$ of Term I and Term II will cancel, the behaviour at large k is

$$\omega_-^2(k \rightarrow \infty) \propto 2 \left(k^{1-a_2} - k^{2-2b_2} \right), \quad (4.53)$$

which is indeed the generalization of (4.46) and (4.47) obtained in §4.3.1. It shows that the stability of the combined system is determined by the stability of the virialized component if the constraint

$$(\omega_1^2 - \omega_2^2)^2 > 2(2\pi Gk\Sigma_1)(2\pi Gk\Sigma_2) \quad (4.54)$$

for $k \rightarrow \infty$ is fulfilled. If (4.54) is not fulfilled, Term III will dominate $\omega_-^2(k \rightarrow \infty)$ with a negative contribution. In this case, the coupled system would not be Toomre-like, but unstable on small scales, even for a stable virialized component.

4.3.3. The Effects of Varying s_0 , q_0 , and Λ_0

To understand how the coupled system responds to changes, the effects of changes in the relative stability q_0 , velocity dispersion s_0 , and the scale Λ_0 are now considered. As long as the H_2 component is stable, the combined system is Toomre-like and can be described in terms of the MSC, which is advantageous because the stability threshold \bar{Q} and most unstable scale $\bar{\Lambda}$ can be obtained much easier than through the DR.

To ensure that the combined system is indeed Toomre-like, rewriting the condition (4.47) as

$$\frac{k_0}{k_{T2}} \frac{Q_{02}^2}{4} = \frac{k_0}{k_{T2}} \frac{k_{T2}}{k_{J2}} = \frac{k_0}{k_{J2}} > 1, \quad (4.55)$$

$$\frac{Q_{01}^2}{4} \frac{\beta_0}{\alpha_0} = \frac{Q_{02}^2}{4} > \frac{k_{T2}}{k_0} = \frac{k_{T1}}{k_0} \frac{1}{\alpha_0} = \frac{\ell_0}{\ell_{T1}} \frac{1}{\alpha_0} = \frac{\Lambda_0}{\alpha_0}, \quad (4.56)$$

gives the constraint¹⁰

¹⁰Recall that $Q_1 = Q_{01} \left(\frac{\Lambda}{\Lambda_0}\right)^{b_1-a_1} = Q_{01} \left(\frac{\Lambda}{\Lambda_0}\right)^{1/3-1/3} = Q_{01}$.

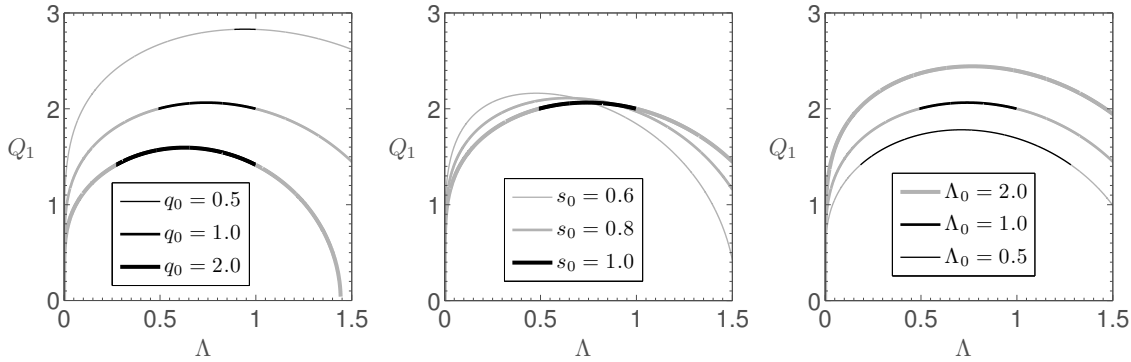


Figure 4.4.: Marginal stability curves for a disc of HI and H₂. In each panel, two of three parameters are held fixed while the third varies. *Left*: q_0 varies, $s_0 = \Lambda_0 = 1$, *Middle*: s_0 varies, $q_0 = \Lambda_0 = 1$, *Right*: Λ_0 varies, $s_0 = q_0 = 1$. At any given Λ , the combined system is only Toomre-like if (4.57) is fulfilled (black lines). If (4.57) is not fulfilled, the MSC is not a valid representation of the system (grey lines).

$$Q_{01}^2 = Q_1^2 > 4\Lambda_0 \frac{\alpha_0}{\beta_0} = 4\Lambda_0 \frac{1}{q_0} \frac{1}{s_0}, \quad (4.57)$$

which needs to be fulfilled for the MSC to describe a Toomre-like system. For any scale Λ along the MSC, (4.57) needs to be fulfilled. If not, the value of Q_1^2 is not a valid representation of the stability of the system at this scale.

Figure 4.4 shows the response of the system to changes in s_0 , q_0 , and Λ_0 . Additionally, the values for the stability threshold and most unstable scale are tabulated in table 4.1. Scales where the constraint (4.57) is fulfilled show the MSC as black line, other scales as a grey line. If the stability threshold is located at a scale at which (4.57) is not fulfilled, this is also indicated in table 4.1. The three panels and their implications are now discussed individually.

Relative Stability Recall that $q_0 = Q_{02}/Q_{01} = Q_{\text{H}_2}/Q_{\text{HI}}$ is a measure of the relative stability of two systems — even if one of the constituents is not Toomre-like. For $q_0 > 1$, H₂ is more stable than HI, and vice versa for $q_0 < 1$. Therefore, decreasing q_0 means that H₂ is destabilized relative to HI. Since H₂ dominates the response of the coupled system, it is reasonable to observe an increase of the stability threshold (i.e., the coupled system destabilizes) as the relative stability of H₂ is decreased by imposing lower values of q_0 .

Further note that, as q_0 decreases, the range in Λ for which the MSC is valid shrinks significantly. Again, this is in line with expectations because the stability on all scales for H₂ is a prerequisite for Toomre-like stability of the coupled system.

Velocity Dispersion Ratio. For the velocity dispersion ratio $s_0 = \sigma_{02}/\sigma_{01} = \sigma_{\text{H}_2}/\sigma_{\text{HI}}$, a similar argument can be made. Given the same relative stability q_0 , note that increasing s_0 further boosts the stability of H₂ with respect to HI. Since σ_{H_2} tends to increase the stability of the dominant H₂ component, the stability of the coupled system is increased as well — the stability threshold decreases.

It is further interesting to note, that for the case $q_0 = 1$, no value $s_0 < 1$ meets the criterion for the validity of the MSC. This suggests that the coupled system is always unstable on small scales for $s_0 < 1$ if $q_0 = 1$. On the other hand, for values $q_0 \neq 1$, it is expected that the coupled system is Toomre-like on wider range of s_0 .

q_0	s_0	Λ_0	\bar{Q}	$\bar{\Lambda}$	Note
0.5	1.0	1.0	2.83	0.94	
1.0			2.06	0.74	
2.0			1.59	0.63	
1.0	0.6	1.0	2.16	0.48	Not Toomre-like
	0.8		2.11	0.64	Not Toomre-like
	1.0		2.06	0.74	
1.0	1.0	0.5	1.78	0.71	
		1.0	2.06	0.74	
		2.0	2.44	0.77	Not Toomre-like

Table 4.1.: Dependence of stability threshold \bar{Q} , and most unstable scale $\bar{\Lambda}$ on $q_0 = Q_{02}/Q_{01}$, $s_0 = \sigma_{02}/\sigma_{01}$, and Λ_0 for a disc of HI and H₂. If condition (4.57) is not fulfilled, the system is not Toomre-like.

Scale Λ_0 . The effect of the coupled system destabilizing with increasing Λ_0 can be explained in a somewhat similar fashion. In particular, writing

$$\Lambda_0 = \frac{\ell_0}{\ell_{T1}} = \frac{k_{T1}}{k_0} = \frac{Q_1^2 k_{J1}}{4 k_0} = \frac{Q_1^2 k_{J2} \beta_0}{4 k_0 \alpha_0} = \frac{Q_1^2 k_{J2} s_0 q_0}{4 k_0 1 1}, \quad (4.58)$$

and noting that for fixed values of s_0 , q_0 , and Q_1 ,¹¹ the value k_0/k_{J2} is directly linked to the choice of Λ_0 . Since $k_{J2}/k_0 = (k_0/k_{J2})^{-1}$ determines the stability of the dominating H₂ component, increasing Λ_0 affects the stability of H₂ adversely. Since H₂ dominates the coupled system, this destabilizes the coupled system.

4.4. Stability of Coupled Gaseous and Stellar Disks

The analysis of turbulent HI and H₂ does not fully represent actual galactic systems because the coupling of the gaseous components to the stellar disc is not considered. Unfortunately, a complete analysis would require a three-component treatment, which is beyond the scope of this work. Instead, the cases of a stellar disc coupled to a turbulent, respectively non-turbulent gas component are considered. They are then compared by considering the effects on the (i) marginal stability curves, (ii) two-phase region, (iii) stability threshold $\bar{Q} = \max\{Q_\star\}$, and (iv) most unstable scale $\bar{Q}(\Lambda = \bar{\Lambda})$. For the turbulent gas, the effect of Λ_0 is also studied.

Since non-turbulent differentially rotating discs always have Toomre-like¹² stability, a stellar disc coupled to a gaseous disc is a system of two Toomre-like components. Therefore, the coupled system is also Toomre-like. This permits analysis of the coupled system in terms of the MSC. In like fashion, if the turbulent gaseous component is identified with a gas in the Toomre-like regime of the stability map of turbulence (e.g. HI), the turbulent gaseous component and the stellar component are again both Toomre-like, and so is the coupled system.

¹¹The choice of stability parameter of the HI component Q_1 is irrelevant because the stability regime of the coupled system is independent of the HI component.

¹²Recall that a Toomre-like system has a DR with a distinct minimum. While all non-turbulent system are Toomre-like, turbulent systems might not be.

Note that, hereafter, any mention of “classical system” refers to the case of a stellar disc coupled to a non-turbulent gaseous disc as first studied by Bertin & Romeo (1988), also cf. §3.4.2. Mentions of “turbulent system”, on the other hand, refer to the system of a stellar disc coupled to a turbulent gaseous disc.

In the following, the turbulent gaseous component is considered to be HI with scaling exponents $a_g = b_g = 1/3$. The choice is justified because only HI is turbulent on galactic scales $\ell \gtrsim 1$ kpc, whereas the scaling relations in H₂ are restricted to scales $\ell \lesssim 100$ pc. To reduce complexity, the effect of possible errors on the scaling exponents is not considered.

Using the logarithmic parameter space introduced in §4.2.3, and identifying the stellar disc as the first ($1 = \star$) and the gaseous disc as the second ($2 = g$) component, one can write

$$s_0 = \frac{\sigma_{0g}}{\sigma_{0\star}}, \quad q_0 = \frac{Q_{0g}}{Q_{0\star}}. \quad (4.59)$$

Since the stellar component is non-turbulent, $Q_{0\star} = Q_\star$, and $\sigma_{0\star} = \sigma_\star$, i.e. neither the stellar Toomre parameter nor the velocity dispersion scale. Furthermore, since $a_g = b_g = 1/3$ for HI, $Q_g = Q_{0g}(\Lambda/\Lambda_0)^{b_g - a_g} = Q_{0g}$, i.e. gaseous the Toomre-parameter is not scale-dependent¹³ either.

Thus, (4.59) becomes

$$s_0 = \frac{\sigma_{0g}}{\sigma_\star}, \quad q_0 = q = \frac{Q_g}{Q_\star}. \quad (4.60)$$

To investigate the physical implications of $\Lambda_0 = \ell_0/\ell_{T1}$, recall that until now the scale $\ell_0 = 1/k_0$ has been associated with the scale at which velocity dispersions and surface densities are measured. This is a very useful choice if observations are involved, but somewhat restricting from the point of view of a theoretical investigation.

Instead, it is convenient to interpret ℓ_0 as some scale of interest, not necessarily the measurement scale. If the measurement scale and this scale of interest are different, the equations become more involved, and this case shall not be considered in this work to avoid unnecessary complexity.

A particularly interesting choice for ℓ_0 is the scale at which the turbulent scaling of the velocity dispersion and surface density saturates such that they are independent of scale for $\ell > \ell_0$. Practically, this means imposing a cut-off in $\mathcal{L} \equiv (\Lambda/\Lambda_0)^p$ of the same form as discussed in §3.5.3, i.e.

$$\mathcal{L} = \begin{cases} (\Lambda/\Lambda_0)^p & \Lambda \leq \Lambda_0, \\ 1 & \text{otherwise.} \end{cases} \quad (4.61)$$

¹³The fact that Q is independent of scale if the turbulent exponents are equal ($a = b$) is a manifestation of the degeneracy condition discussed in §3.5.3, where it was shown that stability threshold of the system is independent of scale if $a = b$.

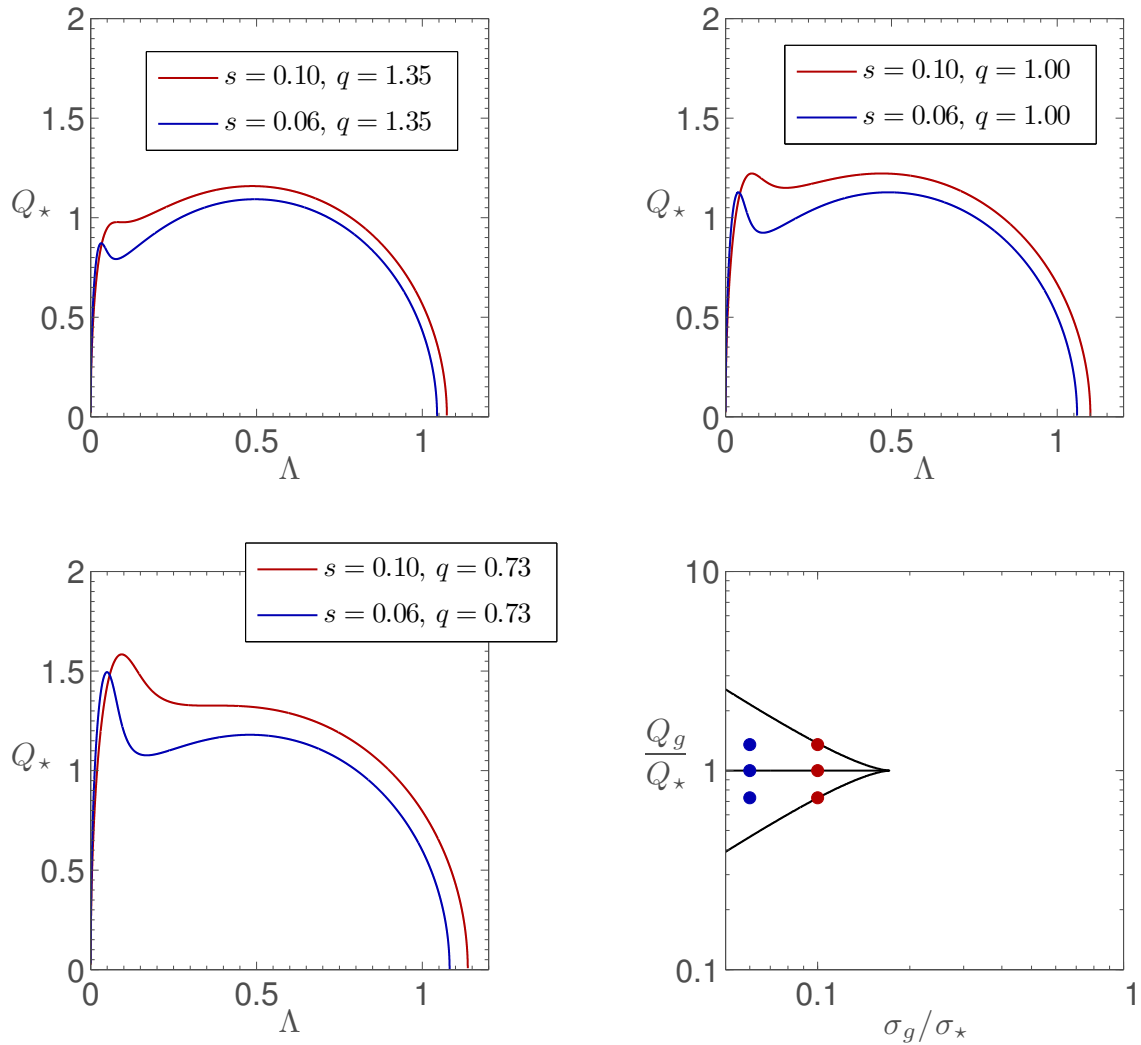


Figure 4.5.: Marginal stability curves for a classical system of a stellar disc coupled to a non-turbulent gaseous disc. Each panel shows the MSC along a different line of s . The bottom right panel shows the location of the MSCs in the $s - q$ plane along with the two-phase region.

4.4.1. Marginal Stability Curves

The Classical System

Figure 4.5 shows the MSCs and the two-phase region for a classical system. As discussed in §3.4.2 and §4.2.3, the two-phase region marks the range in the parameter space where the stability response of the system becomes decoupled in the sense that the MSC shows two distinct peaks at different scales. Depending on the exact location within the two-phase region, one of the peaks is higher and dominates the stability response.

Within the two-phase region, for $q = q_0 = Q_g/Q_* > 1$, the marginal stability curve is dominated by the peak at larger scales $\bar{\Lambda} \sim 0.5$. Since $q > 1$, $Q_g > Q_*$, and the gaseous component is more stable than the stellar component.

Since the degree of instability¹⁴ is driven by the less stable stellar component, the higher peak at $\bar{\Lambda} \sim 0.5$ is the stellar peak and the corresponding part of the two-phase region is referred to as stellar-dominated. For $q < 1$, on the other hand, $Q_g < Q_*$ such that the stellar component is more stable and the degree of instability is driven by the gas component. The dominant peak at $\bar{\Lambda} \sim 0.1$ is the gaseous peak¹⁵ and the part of the two-phase region is said to be gas-dominated.

Regardless of which peak is higher, the scales of the gaseous and the stellar peaks are hereafter indicated as $\bar{\Lambda}_g$ and $\bar{\Lambda}_*$. Recall that the largest peak gives the stability threshold \bar{Q} and is located at the most unstable scale $\bar{\Lambda}$. Depending on whether $q > 1$ or $q < 1$, $\bar{\Lambda} = \bar{\Lambda}_*$, or $\bar{\Lambda} = \bar{\Lambda}_g$.

From the shape of the marginal stability curve for different locations in the two-phase region, the primary effects of variations in s and q can be seen. For constant values of q , decreasing s causes the gaseous peak to move to smaller scales, while the location of the stellar peak remains unaffected, thereby increasing the separation of the peaks. Additionally, decreasing s also decreases the height of the marginal stability curves, and thus the stability threshold. This stabilizes the system.

For constant values of s , decreasing the value of q increases the height of the gaseous peak whereas the stellar peak seems to remain unaffected. Additionally, the location of the stellar peak seems to only be minimally affected by changes in q . For $q = 1$, the peaks are of equal height. This is the transition line. Increasing s for $q = 1$ will keep the two peaks at the same relative height and decrease their separation until the MSC exhibits only one single, very flat peak at the point in the $s - q$ plane where the boundaries of the two-phase region meet the transition line. This is called the triple point.

The Turbulent System

To study how turbulent scaling affects the system, it is useful to compare the turbulent MSCs to those of a classical system. Selecting an arbitrary point (s_0, q_0) in the parameter space for the system of a stellar disc coupled to a turbulent HI disc, the variables

$$s = s_0 \left(\frac{\Lambda}{\Lambda_0} \right)^{1/3}, \quad q = q_0, \quad (4.62)$$

enter the marginal stability curve $Q_* = Q_*(\Lambda, s, q)$. For the non-turbulent case, s and q are constant in the domain Λ of the MSC. However, for the turbulent system, $s = s(\Lambda)$ such that the value of s at each Λ varies.¹⁶ This means that, at $\Lambda = \Lambda_0$, the values of the MSCs for the classical and turbulent cases coincide, whereas for $\Lambda > \Lambda_0$, s is increased, and for $\Lambda < \Lambda_0$, s is decreased.

This is illustrated in figure 4.6. The left panel shows the scaling law for a choice of s_0 and the right panel the corresponding MSC for (i) the classical system, and (ii) the turbulent system. At $\Lambda = \Lambda_0$, the two curves coincide because the effective value of s for the turbulent system equals s_0 , which is constant with Λ for the classical system.

¹⁴I.e. the height of the largest peak in the marginal stability curve.

¹⁵In fact, the gaseous peak for classical systems is always located at $\bar{\Lambda} \sim \frac{1}{2}\alpha = \frac{1}{2}\frac{s}{q}$ (Bertin & Romeo, 1988).

¹⁶Note that, in the more general case of two Toomre-like turbulent components, it is possible that $q = q(\Lambda)$.

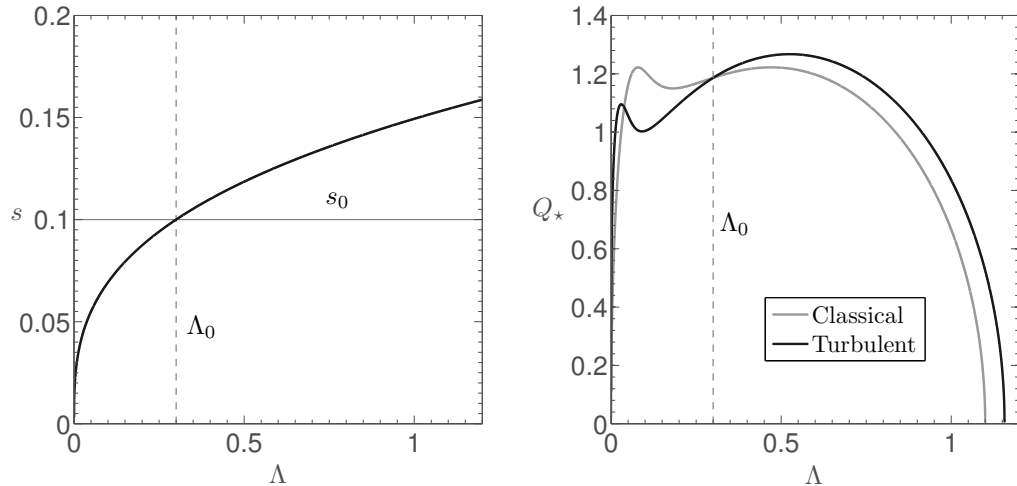


Figure 4.6.: *Left*: Scaled velocity dispersion ratio s as a function of scale Λ , and velocity dispersion ratio $s_0 = 0.1$ at scale $\Lambda_0 = 0.3$. *Right*: Marginal stability curve for a classical and a turbulent two-component system, cf. legend. At scale $\Lambda = \Lambda_0 = 0.3$, the two curves coincide.

Recalling the discussion in §4.4.1, lower values of s_0 shift the small scale peak to even smaller Λ and decrease the height of both peaks. As such, there are three possible choices for Λ_0 to significantly affect the shape of the marginal stability curve:

1. If $\bar{\Lambda}_g < \Lambda_0 < \bar{\Lambda}_*$, the gaseous peak is shifted to smaller Λ and the height decreased, whereas the stellar peak is increased in height but remains at approximately the same Λ .
2. If $\Lambda_0 < \{\bar{\Lambda}_g, \bar{\Lambda}_*\}$, both peaks increase in height, with the stellar peak affected more strongly. The gaseous peak is shifted to larger values of Λ , but the location of the stellar peak remains largely unaffected.
3. If $\{\bar{\Lambda}_g, \bar{\Lambda}_*\} < \Lambda_0$, both peaks are decreased in height with the gaseous peak affected more strongly. Additionally, the gaseous peak is shifted to smaller scales.

While these considerations give an indication of what happens to the MSC for various choices of Λ_0 , a thorough study of the effects in the $s_0 - q_0$ plane in terms of the shape of the MSC is complex and beyond the scope of this work. Instead of mapping the behaviour of the MSC throughout the $s_0 - q_0$ plane, the (i) change in the shape of the two-phase region, (ii) effect on the stability threshold \bar{Q} , and (iii) effect on the most unstable scale $\bar{\Lambda}$ are discussed in subsequent sections.

Now consider the case in which turbulence saturates at the scale Λ_0 . As per (4.61), a cut-off is applied in the scaling of $s(\Lambda)$ such that $s = s_0$ for $\Lambda \geq \Lambda_0$. The effect of this on the MSC is shown in figure 4.7, where the left panel shows $s = s(\Lambda)$ and the right panel shows the MSC for the classical system, the turbulent system with the cut-off, and the turbulent system without the cut-off. As before, two curves are seen for $\Lambda < \Lambda_0$, which coincide at $\Lambda = \Lambda_0$. However, instead of separating again for $\Lambda > \Lambda_0$, the cut-off causes the turbulent system to collapse to the classical case. This is emphasized by the dotted line indicating the shape of the MSC without a cut-off.

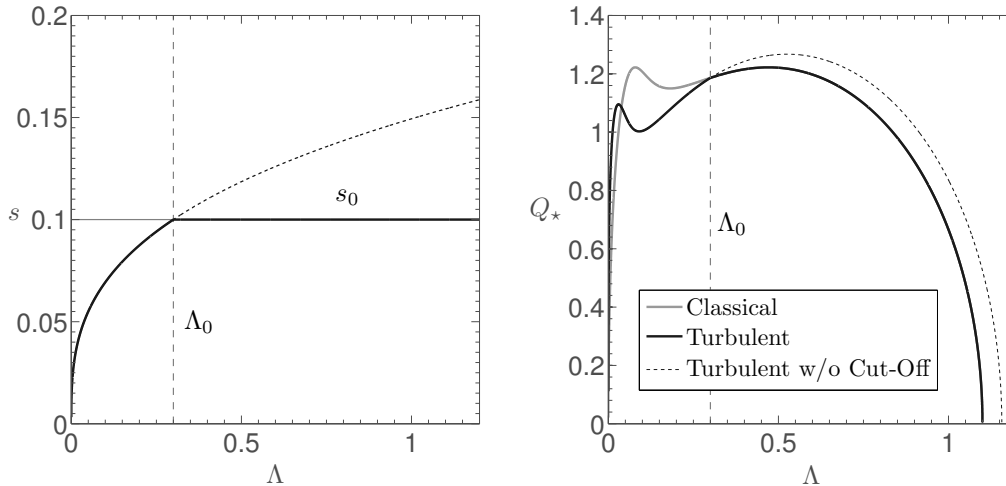


Figure 4.7.: *Left*: Scaled velocity dispersion ratio s as a function of scale Λ , and velocity dispersion ratio $s_0 = 0.1$ at scale $\Lambda_0 = 0.3$. Note how the scaling saturates at $\Lambda = \Lambda_0$. *Right*: Marginal stability curve for a classical and a turbulent two-component system. At scale $\Lambda = \Lambda_0 = 0.3$, the two curves are equal because $s = s_0$. Note the discontinuity at $\Lambda = \Lambda_0$, where the turbulent MSC collapses to the classical case. The non-saturated turbulent case is indicated for comparison.

The previous considerations for the effect of Λ_0 depending on its value relative to the scales associated with the two peaks needs some revision to account for the cut-off. In particular,

1. If $\bar{\Lambda}_g < \Lambda_0 < \bar{\Lambda}_*$, the gaseous peak is shifted to smaller Λ and the height decreased. The stellar peak remains unaffected.
2. If $\Lambda_0 < \{\bar{\Lambda}_g, \bar{\Lambda}_*\}$, both peaks remain unaffected.
3. If $\{\bar{\Lambda}_g, \bar{\Lambda}_*\} < \Lambda_0$, nothing changes compared to the case without saturation. Both peaks are decreased in height with the gaseous peak affected more strongly. Additionally, the gaseous peak is shifted to smaller scales.

Again, a full analysis of the behaviour of the MSC in the $s_0 - q_0$ plane will not be carried out hereafter. Instead, the stability threshold \bar{Q} and the most unstable scale $\bar{\Lambda}$ are studied in the $s_0 - q_0$ plane and compared to the case without saturation. Note that a study of the two-phase region is also not carried out because the cut-off causes discontinuities in the MSC that are misinterpreted as peaks by the algorithms employed. However, this does not affect the determination of \bar{Q} and $\bar{\Lambda}$ since the artificial peak can never be the global maximum of the MSC. Suitable modifications to distinguish real peaks from discontinuities are planned for the future.

Turbulent vs. Classical System

Figure 4.8 shows marginal stability curves (left panel) for four choices of s_0 and q_0 (right panel). Two points are located on the boundaries of the two-phase region of the classical system, one on the transition line of the same two-phase region, and the fourth point in the gas dominated regime of turbulent two-phase region, yet outside the two-phase region of the classical system.

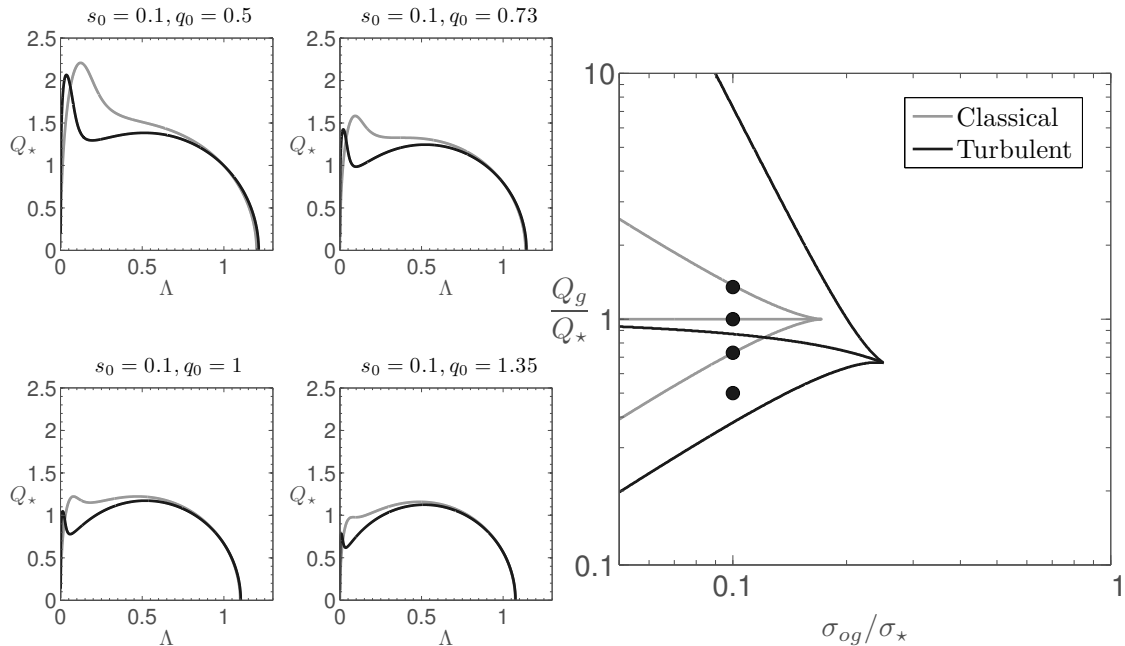


Figure 4.8.: *Left*: Marginal stability curves for the classical and turbulent ($\Lambda_0 = 1$) case of a stellar disc coupled to a gas disc. Observe that (i) the peak of the turbulent system is always below the peak of the classical systems (i.e. the turbulent system is more stable), (ii) the gaseous peak (at small scales) for the turbulent system is at smaller scales than for the classical system, and (iii) no large differences can be detected for the stellar (large scale) peak. *Right*: The two-phase region in $s_0 - q_0$ plane for the classical and the turbulent system. The markers indicate the location of the MSCs shown on the left. Note that the two-phase region for the turbulent system is larger than for the classical system.

The ranges of $s_0 = \sigma_{0g}/\sigma_*$ and $q_0 = Q_g/Q_*$ in figure 4.8 are limited to astrophysically relevant regimes. In particular, self-regulation¹⁷ implies that $1 \lesssim q = Q_g/Q_* \lesssim 10$, whereas the reason for $0.05 \lesssim s_0 = \sigma_{0g}/\sigma_* \leq 1$ is two-fold. Firstly, stars forming out of the gaseous component have no mechanism to decrease their thermal velocity dispersion through collisions because they are non-collisional. This provides the upper limit $s \leq 1$. Secondly, measurements of HI velocity dispersion $\sigma_g \sim 10$ km/s imply stellar velocity dispersions of $\sigma_* \sim 200$ km/s for $s_0 = 0.05$. Such velocity dispersions greatly exceed measurements of the disc population where $\sigma_* \sim 20$ km/s, and can only be achieved by bulge stars, cf. §2.1. As such, even the chosen limit on s_0 approaches nonphysical regimes.

Regarding the MSC and the two-phase region, three distinct properties can be noticed:

1. The two peaks of the turbulent system are always below the corresponding peaks of the classical system. Additionally, this seems to affect the gaseous peak much more strongly than the stellar peak, which is sensible because the gaseous component is the turbulent

¹⁷Self-regulation refers to the fact that Q is expected to not deviate significantly from unity. For $Q < 1$, the gas is gravitationally unstable, thereby forming protostellar cores and eventually stars. As stars are formed, the gas heats up, increasing the stability and thus Q . Over time, the gas cools and Q drops, again enabling star formation. This illustrates that extreme values of Q are not realistic and a gaseous component never departs too far from marginal stability at $Q = 1$.

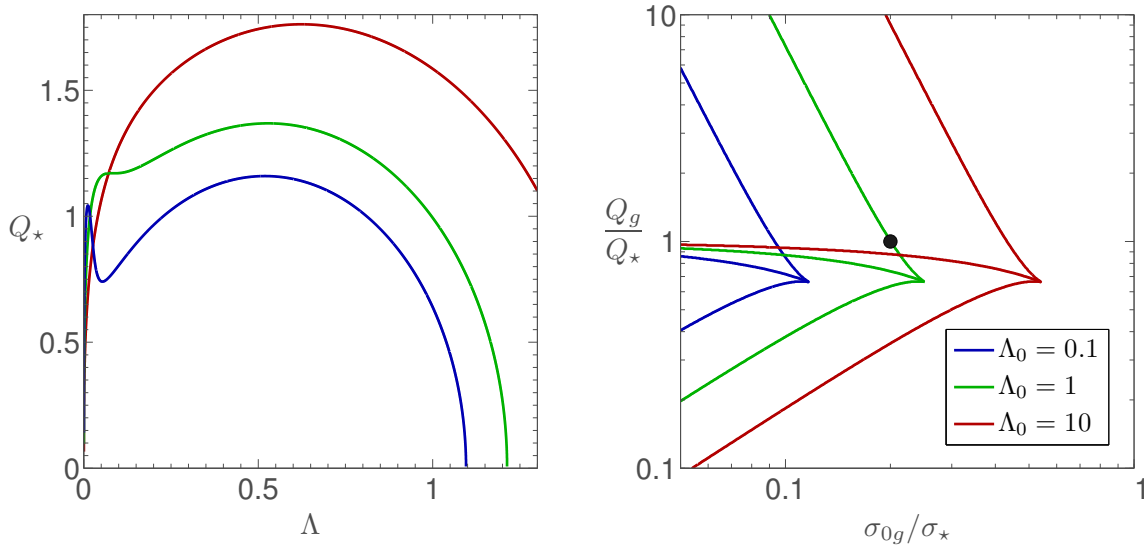


Figure 4.9.: Marginal stability curves (left) and two-phase regions (right) for a coupled system of stars and turbulent HI. The values $(s_0, q_0) = (0.2, 1)$ used for the MSC are marked in the right panel and values for Λ_0 are indicated in the legend.

one. Since both peaks are lowered, so is the stability threshold of system, indicating that the turbulent system is always more stable than corresponding classical system.

2. The gaseous peak for the turbulent system moves to shorter scales compared to the non-turbulent system, i.e. small scale instabilities move to even smaller scales. The stellar peak, on the other hand, does not seem to be affected.
3. The range of values in s_0 and q_0 for which the stability response is decoupled, is much larger for the turbulent system. As the axes are scaled logarithmically, the effect on the stellar dominated region is much larger than the effect on the gas-dominated region. Since the boundaries of the stellar-dominated part indicate the values for (s_0, q_0) for which the gaseous peak disappears, the increased size suggests that the gaseous peak — in addition to being shifted to smaller scales — also disappears later.

Note that these findings are restricted to $\Lambda_0 = 1$. In fact, subsequent sections demonstrate that the findings regarding the height of the peaks and the most unstable scale associated with the highest peak hold only for $\Lambda_0 \gtrsim 1$. On the other hand, the range in $s_0 - q_0$ for which the response is decoupled increases with respect to the classical case for $\Lambda_0 \gtrsim 0.1$.

Effect of Varying Λ_0

Figure 4.9 shows the MSCs (left) and two-phase regions (right) for turbulent systems with different values of $\Lambda_0 = \{0.1, 1, 10\}$. The choice of $(s_0, q_0) = (0.2, 1)$ is marked in the $s_0 - q_0$ plane. The obvious effect of increasing Λ_0 is the increased size of the two-phase region. In particular, the boundaries of the two-phase region are shifted along the s_0 axis. This is expected because only s changes depending on the scale when evaluating the MSC, cf. (4.62). Note that comparison with the classical two-phase region of figure 4.8 reveals that the turbulent two-phase region is always larger than the classical two-phase region for $\Lambda_0 \gtrsim 1$.

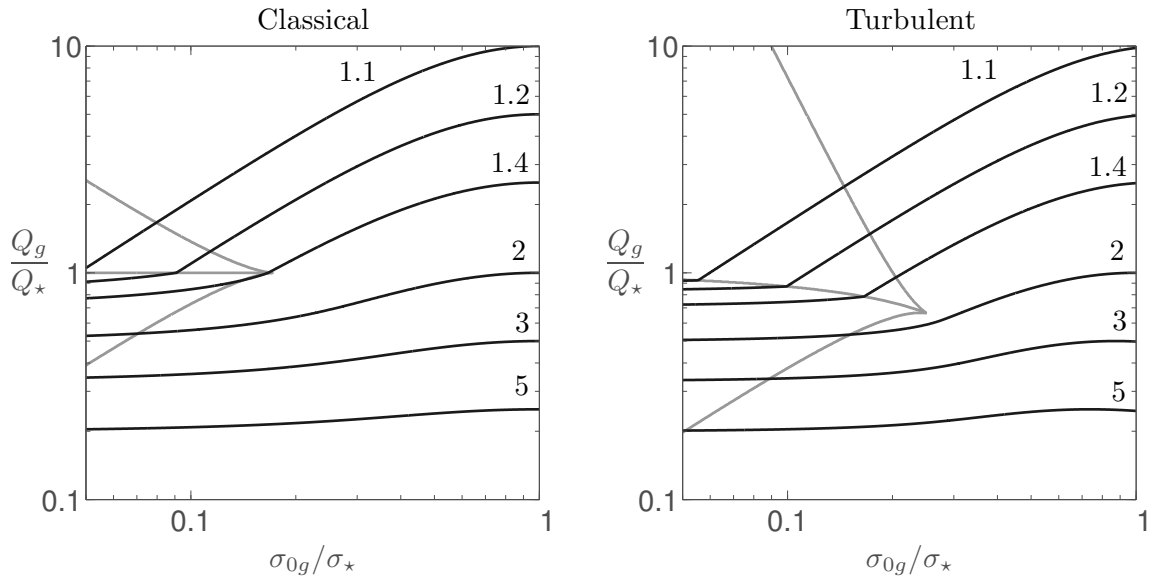


Figure 4.10.: Contours of \bar{Q} (black) superimposed on the two-phase region (grey) for the classical (left) and turbulent (right) two-component systems .

The behaviour of the two-phase region can be explained by recalling the discussion in §4.4.1 regarding the effect of Λ_0 on $s = s(\Lambda)$ and thus the MSC and two-phase region. In particular, for small values of Λ_0 , s is shifted to larger values on a wide range of scales $\Lambda > \Lambda_0$. Since figure 4.5 indicates that the two-phase region exists only at small values of $s \lesssim 0.2$, shifting all scales $\Lambda > \Lambda_0$ along the MSC to larger values of s effectively moves them outside the range of the two-phase region. As such, the two-phase region for the turbulent case with $\Lambda_0 = 0.1$ is smaller than the classical two-phase region. Conversely, large values of Λ_0 decrease the value of $s = s(\Lambda)$ for a wide range of scales $\Lambda < \Lambda_0$. Since the two-phase region exists at small values of $s \lesssim 0.2$, the size is increased.

Additionally, the changed size of the two-phase region checks with the behaviour of the MSC, which shows either a single peak, ($\Lambda_0 = 0.1$, point outside the two-phase region) two peaks of equal height ($\Lambda_0 = 1$, point on the boundary), or two peaks with one dominating ($\Lambda_0 = 10$, point in the stellar-dominated regime).

If Λ_0 is associated with the scale at which turbulence saturates, increasing Λ_0 means that a wider range of scales $\Lambda \leq \Lambda_0$ is subjected to turbulent motions. This means that the size of the two-phase region, and thus the range of values in s_0 and q_0 for which the stability response is decoupled, increases if turbulence affects a larger range of scales.

4.4.2. Stability Threshold

Stability Threshold and Two-Phase Region

Figure 4.10 shows the contours of the stability threshold superimposed on the two-phase region for classical (left) and turbulent (right) system. In both cases, the stability contours are discontinuous across the transition line, thereby highlighting the important distinction between the two regimes.

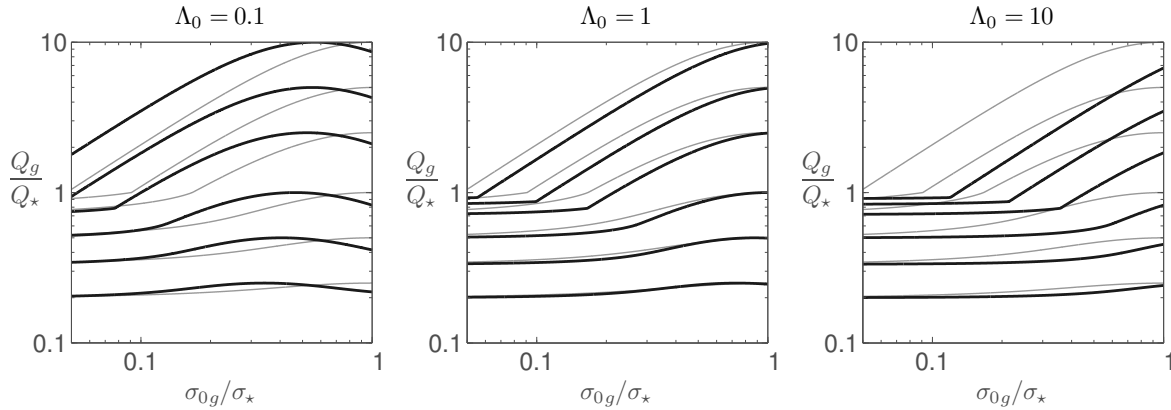


Figure 4.11.: Contours for (from top to bottom) $\bar{Q} = \{1.1, 1.2, 1.4, 2, 3, 5\}$ for the turbulent (black) and classical (grey) system. In general, the contours are shifted along positive s_0 as Λ_0 increases.

Below the transition line $q_0 \simeq 1$, the stability threshold is most sensitive to changes in the relative stability $q_0 = Q_g/Q_*$ of the two components. In particular, lowering the stability of the gaseous component with respect to the stellar component¹⁸ raises the stability threshold, thereby destabilizing the coupled system. As such, the stability properties of the coupled system are dominated by those of the gaseous component.

Since $q_0 = s_0/\alpha_0$, lowering the relative stability means that the ratio between $s_0 = \sigma_{0g}/\sigma_*$ and $\alpha_0 = \Sigma_{0g}/\Sigma_*$ changes, i.e. a change in one is not sufficiently balanced by a change in the other. Above the transition line and outside the two-phase region, \bar{Q} can change significantly even if the relative stability and thus the ratio $q_0 = s_0/\alpha_0$ is preserved, i.e. a change in s_0 causes α_0 to change such that q_0 remains constant. This means that the individual stability of both components remains the same, but rescaling s_0 and α_0 nonetheless changes the stability of the coupled system. However, changing the relative stability q_0 has a much larger impact on \bar{Q} than simply rescaling s_0/α_0 .

Note that the effect of s_0 and q_0 on the stability threshold is studied much more thoroughly in Wiegert (2010) and Romeo & Wiegert (2011), where a simple and convenient approximation for \bar{Q} is provided for the case of non-turbulent two-component discs.

Turbulent vs. Classical System

Figure 4.11 shows the superimposed \bar{Q} contours for the classical (grey) and turbulent (black) systems for different values of Λ_0 . The contour levels are the same as in figure 4.10. Considering the case for $\Lambda_0 = \{1, 10\}$, the contours are offset along the positive s_0 axis, which shows that the turbulent system is always more stable than the equivalent classical system for any choice of (s_0, q_0) .¹⁹ The effect is more pronounced for small values of \bar{Q} above the transition line $q_0 \simeq 1$ than below for larger values of \bar{Q} . This was previously discussed in §4.4.1 for a limited selection of points, but figure 4.11 shows that it holds for all points in the $s_0 - q_0$ plane, provided that $\Lambda_0 \gtrsim 1$.

¹⁸I.e. decreasing q_0 by decreasing Q_g while keeping Q_* constant.

¹⁹The contours for the turbulent system are shifted to higher values of s_0 and lower values of q_0 . As such, the value of \bar{Q} for a given (s_0, q_0) will be lower for the turbulent than for the classical system.

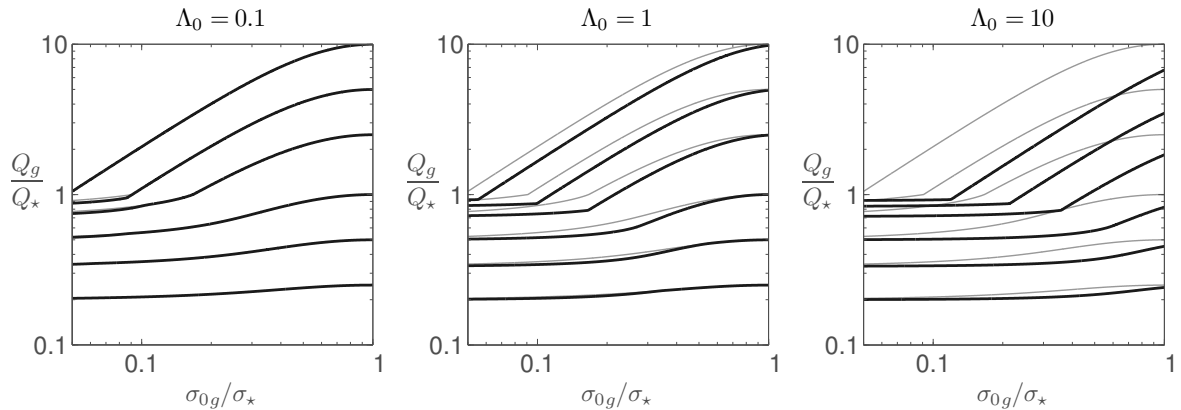


Figure 4.12.: Contours for (from top to bottom) $\bar{Q} = \{1.1, 1.2, 1.4, 2, 3, 5\}$ for the turbulent (black) and classical (grey) system. The turbulent scaling saturates at Λ_0 , which seems only affect the contours for $\Lambda_0 = 0.1$.

Additionally, the contours for $\Lambda_0 = 1$ appear to merge as $s_0 \rightarrow 1$ with a trend towards earlier merging for smaller values of q_0 . In fact, the \bar{Q} contours do not merge, but merely coincide at particular values of s_0 , depending on the choice of Λ_0 . This happens if the scale $\Lambda = \Lambda_0$ at which the MSCs coincide is approximately equal to the scale associated with the stability threshold, i.e. $\Lambda_0 = \Lambda \simeq \bar{\Lambda}$. For $\Lambda_0 = 1$, this occurs at $s_0 = 1$.

Effect of Varying Λ_0 and Saturation

As mentioned in the previous section, the turbulent contours are offset along the s_0 axis for increasing values of Λ_0 . For $\Lambda_0 \gtrsim 1$, the turbulent system is more stable (contours shift to the right) than the equivalent classical system. Otherwise, the turbulent system is less stable (contours shift to the left).

The shift along the s_0 axis can be explained by considering that $s = s(\Lambda)$, where $s < s_0$ for $\Lambda < \Lambda_0$ and $s > s_0$ for $\Lambda > \Lambda_0$. For small values of Λ_0 , a large part of the corresponding MSC is boosted to larger values of s , increasing the height of the MSC and thus the stability threshold. Conversely, for larger values of Λ_0 , a wider range of scales decrease s to smaller values, which in turn decreases the height of the MSC and the stability threshold. The net effect in the $s_0 - q_0$ plane is a shift of the contours along s_0 .

Consider now the case where the scaling laws saturate at scale Λ_0 , i.e. the scaling relations for $\{\sigma_g, \Sigma_g\} \propto (\Lambda/\Lambda_0)^p$ are modified according to (4.61). Figure 4.12 shows the corresponding \bar{Q} contours, where it can be seen that only the contours for $\Lambda_0 = 0.1$ are modified in the considered range of s_0 and q_0 .

Following the discussion in §4.4.1, recall that the turbulent and classical MSC merge at $\Lambda = \Lambda_0$, such that $s = s_0$ holds for scales $\Lambda \geq \Lambda_0$, and $s = s(\Lambda)$ for $\Lambda_0 < \Lambda$. For the turbulent system to collapse to the classical case in the range of scales at which the gaseous and stellar peaks occur, Λ_0 should be small. In particular, $\Lambda_0 < \bar{\Lambda}$ must hold. If Λ_0 is too large, the stability threshold is at a scale $\bar{\Lambda} < \Lambda_0$, where the non-saturated component of $s = s(\Lambda)$ determines its height and location. Note that figure 4.12 indicates that only $\Lambda_0 = 0.1$ is a small enough value for constraint $\Lambda_0 < \bar{\Lambda}$ to affect the considered parameter range.

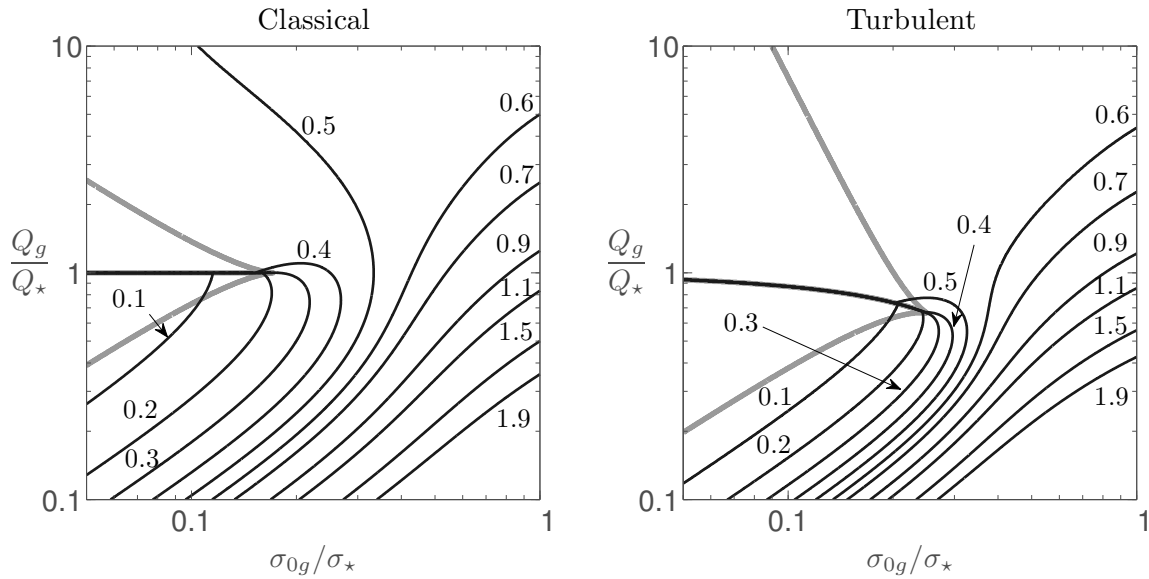


Figure 4.13.: Contours of $\bar{\Lambda}$ (black) superimposed on the two-phase region (grey) for the classical (left) and turbulent (right) two-component systems.

If one interprets Λ_0 as the cut-off scale, a system following turbulent scaling up to large scales ($\Lambda_0 = 10$) is dominated by turbulent effects on the stability threshold \bar{Q} in most of the $s_0 - q_0$ plane. In particular, the larger the saturation scale, the more stable the system. The stability threshold of system saturating at intermediate scales ($\Lambda_0 = 1$) behaves very similar to a classical system, except for a small increase in stability. In both cases, saturation does not influence the stability threshold in the considered ranges of s_0 and q_0 . On the other hand, a system where turbulent scaling saturates on small scales ($\Lambda_0 = 0.1$) behaves much like a classical system.

4.4.3. Most Unstable Scale

Most Unstable Scale and Two-Phase Region

Figure 4.13 shows contours for the most unstable scale $\bar{\Lambda}$ for the classical (left) and turbulent (right) systems superimposed on the corresponding two-phase regions. Note that contours $\bar{\Lambda} \leq 0.4$ (classical), respectively $\bar{\Lambda} \leq 0.5$ (turbulent), curve back to join the transition line and follow it. This is a numerical artifact caused by a discontinuous change of $\bar{\Lambda}$ across the transition line. In fact, if the contours of $\bar{\Lambda}_*$ and $\bar{\Lambda}_g$ were traced instead of $\bar{\Lambda}$, the discontinuity would not be present.

As expected, the most unstable scale is restricted to small values $\bar{\Lambda} \lesssim 0.1$ in the gas-dominated part of the two-phase region (below the transition line). In the stellar-dominated part (above the transition line), the most unstable scale is restricted to values of $0.4 \lesssim \bar{\Lambda} \lesssim 0.5$ for the classical system, and $0.5 \lesssim \bar{\Lambda} \lesssim 0.6$ for the turbulent system.²⁰ Outside the two-phase

²⁰These findings are in line with approximations derived in Bertin & Romeo (1988, §2.3), which show that $\bar{\Lambda} \sim 1/2 \alpha = 1/2 s/q$ in the gas-dominated regime, and $\bar{\Lambda} \sim 1/2 + \mathcal{O}(\alpha^2) = 1/2 + \mathcal{O}(s^2/q^2)$ in the stellar-dominated regime. For $s = s_0 (\Lambda/\Lambda_0)^p$, $\bar{\Lambda}$ rescales.

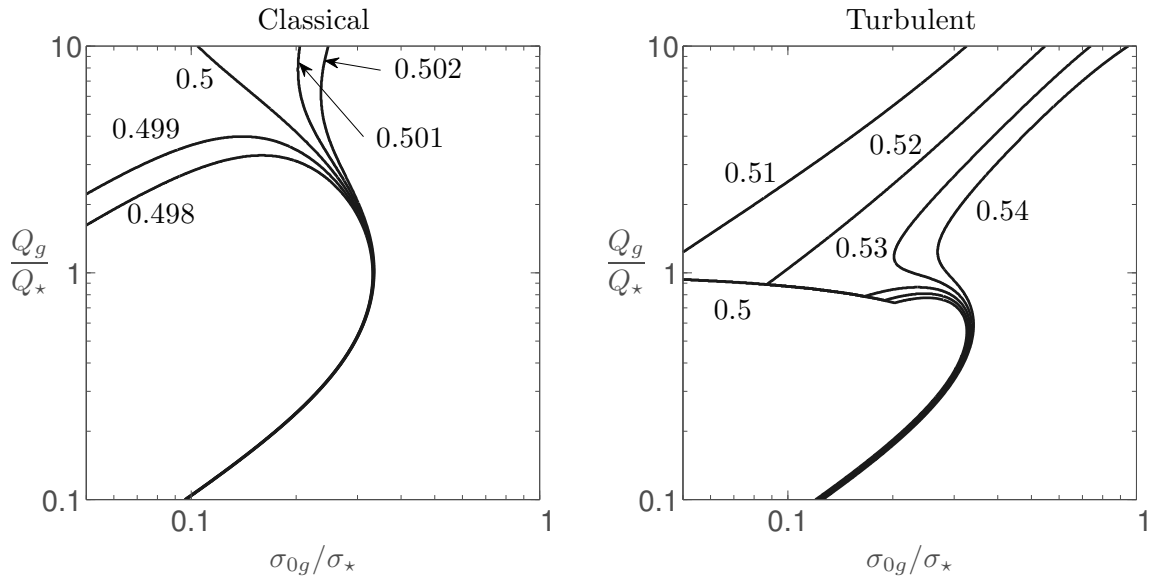


Figure 4.14.: Contours of $\bar{\Lambda}$ around the separatrix $\bar{\Lambda} = 0.5$. The left panel shows the classical case, where the separatrix is the limit between contours curving back to rejoin the transition line and contours tracing to large values of (s_0, q_0) . The right panel shows the turbulent case, where the $\bar{\Lambda} = 0.5$ contour is the smallest contour that curves back to the transition line but does not detach again.

region, the possible values for the most unstable scale are much less restricted with a general tendency towards larger values with increasing s_0 and decreasing q_0 .

In the classical case, note the presence of the separatrix $\bar{\Lambda} = 0.5$, which separates the $s_0 - q_0$ plane into two regions with regards to the permitted values of the most unstable scale. In the turbulent case, the contour $\bar{\Lambda} = 0.5$ does not seem to act as a separatrix. To investigate this further, figure 4.14 shows the $\bar{\Lambda}$ contours (i) in a very narrow range about the $\bar{\Lambda} = 0.5$ contour for the classical case, and (ii) for a few different values where the behaviour of the contour $\bar{\Lambda}$ changes significantly in the turbulent case.

In the classical case, the fact that contours with values just above and just below $\bar{\Lambda} = 0.5$ diverge from this line confirm $\bar{\Lambda} = 0.5$ to be a separatrix. In the turbulent case, the situation is more complicated because of the discontinuity of $\bar{\Lambda}$ across the transition line. Nevertheless, it seems that $\bar{\Lambda} = 0.5$ is the largest contour which curves back onto the transition line and does not disconnect from it. Contour levels $0.5 \lesssim \bar{\Lambda} \lesssim 0.53$ first curve back onto the transition line, but detach again at smaller values of s_0 . Contours $\bar{\Lambda} \gtrsim 0.53$ do not curve back onto the transition line at all. As such, the contour $\bar{\Lambda} = 0.5$ can also be considered a separatrix in the turbulent case as it marks the transition between contours curving back towards small s_0 as q_0 grows and those that do not.

Turbulent vs. Classical System

Figure 4.15 shows the $\bar{\Lambda}$ contours of the classical system (grey) and the turbulent system (black) for different values of Λ_0 . The contour levels are the same as those shown in figure 4.13. For $\Lambda_0 = \{1, 10\}$, the contours of the turbulent system are offset positively along the s_0 axis with respect to the classical system.

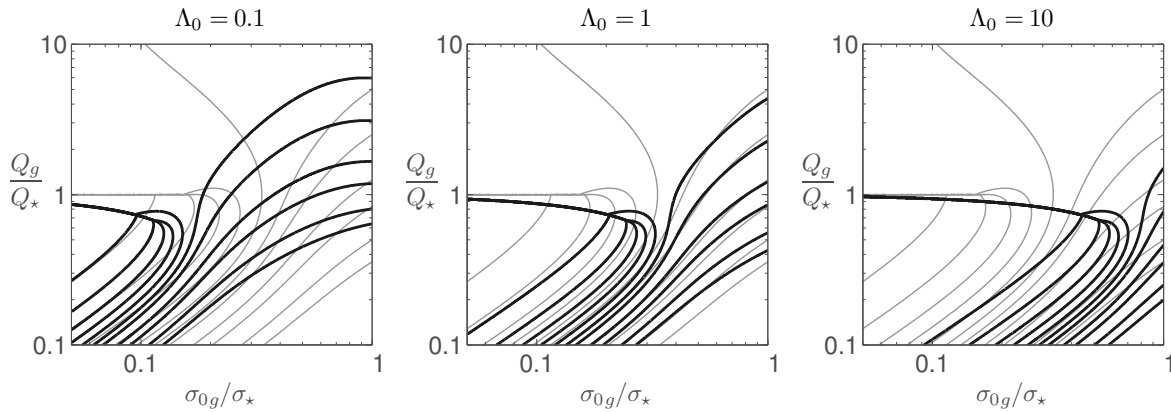


Figure 4.15.: Contours of the most unstable scale $\bar{\Lambda}$ for the turbulent system. The contours of the classical system are indicated in light grey for comparison. Contour levels are identical to figure 4.13.

For $\bar{\Lambda} < 0.5$, the contours curve back onto the transition line with the turbulent system having small values of $\bar{\Lambda}$ for any given (s_0, q_0) . For $\bar{\Lambda} > 0.5$, this is the same in the case of $\Lambda_0 = 10$. However, for $\Lambda_0 = 1$, some of the contours $\bar{\Lambda} > 0.5$ of the classical and turbulent case cross multiple times. As such, no universal statement about the relation of the values of $\bar{\Lambda}$ between the two cases can be made.

In the case of $\bar{\Lambda}_0 = 1$, the contours of the classical and turbulent system seem to be coinciding for $\bar{\Lambda} > 0.5$. In particular, for $(s_0, q_0) = (1, 1)$, the contours coincide exactly. For values $(s_0, q_0) \simeq (1, 1)$, the contours coincide close to the $s_0 = 1$ line. This illustrates the previous observation in §4.4.2 where the classical and turbulent contours of \bar{Q} coincided for $s_0 \simeq 1$ for $\bar{\Lambda} \simeq \Lambda_0 \simeq 1$.

Effect of Varying Λ_0 and Saturation

Comparing the three panels of figure 4.15 with the changes in \bar{Q} and the two-phase region shown in figures 4.11 and 4.9, it is not surprising to note that the $\bar{\Lambda}$ contours shift to the right with increasing Λ_0 . Note that only for $\Lambda_0 \gtrsim 1$, the most unstable scale within the gas-dominated part of the two-phase region shifts to smaller values.

As before, the behaviour can be explained in terms of the shape of the marginal stability curve as treated in §4.4.1 when the scaling $s = s(\Lambda)$ with $s < s_0$ for $\Lambda < \Lambda_0$, and $s > s_0$ for $\Lambda > \Lambda_0$ is considered. For small values of Λ_0 , a large number of scales $\Lambda > \Lambda_0$ has $s > s_0$, which means that the gaseous peak shifts to larger Λ . In the gas-dominated regime, the value of $\bar{\Lambda}$ at a point s_0 is then larger than that of an equivalent non-turbulent system. Since the $\bar{\Lambda}$ contours increase in value from left to right, this means a shift of the contours to the left.

Conversely, for large values of Λ_0 , a wide range of scales $\Lambda < \Lambda_0$ will have $s < s_0$. Since decreasing s shifts the gaseous peak to smaller scales, this means that a point s_0 in the $s_0 - q_0$ plane has a value of $\bar{\Lambda}$ smaller than the equivalent non-turbulent system. The $\bar{\Lambda}$ contours thus shift rightward.

Observe that not only the contours in the gas-dominated region, but all contours in the $s_0 - q_0$ plane are shifted along the s_0 axis. This indicates that the effect of Λ_0 on the stellar peak is also significant. This contrasts the discussion in §4.4.1, where it was suggested that

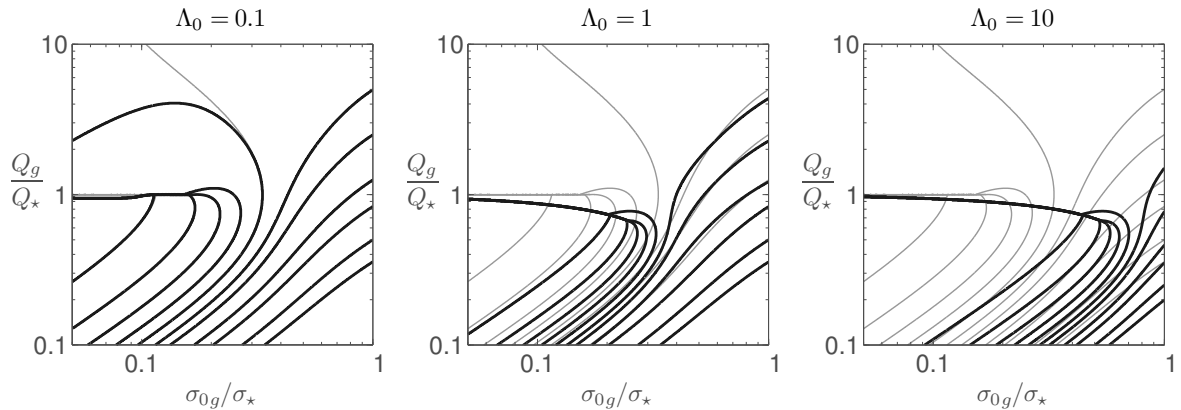


Figure 4.16.: Contours of the most unstable scale $\bar{\Lambda}$ for the turbulent system with saturation at scale Λ_0 . The contours of the classical system are indicated in light grey for comparison. Contour levels are identical to figure 4.13.

$\bar{\Lambda}_*$ is only weakly affected by changes in s . However, since the $\bar{\Lambda} \sim 0.5$ contour associated with the stellar component also shifts, this means that $\bar{\Lambda}_*$ is in fact more sensitive to changes in s than previously suggested.

Consider now figure 4.16, which shows $\bar{\Lambda}$ contours of the turbulent system where a cut-off of the form (4.61) is applied. As for the \bar{Q} case, no changes compared to the non-saturated system are visible for $\Lambda_0 = 1$ and $\Lambda_0 = 10$. The behaviour of $\Lambda_0 = 0.1$, however, differs significantly. Except for $\bar{\Lambda} = 0.5$, all $\bar{\Lambda}$ contours of the turbulent case coincide with the contours of the classical case in the entire parameter space. Recall that this was not the case for the \bar{Q} contours, where the merging only appeared at $s_0 \simeq 0.1$. This suggests that the cut-off affects the most unstable scales in a different fashion than the stability threshold.

In particular, one would expect the contour $\bar{\Lambda} = 0.5$ of the turbulent system to coincide with the corresponding contour of the classical system at least down to $s_0 \simeq 0.1$. However, the contours diverge around $s \simeq 0.3$. Barring further investigations, it is not clear whether this is an issue is a numerical error, a problem in the implementation of the cut-off, or a feature of the system.

As before, if Λ_0 is interpreted as the saturation scale of the system, this means that the range of scales over which the velocity dispersion and density fields are scale-dependent impacts that most unstable scale of the system significantly. In particular, the larger the saturation scale, the more are instabilities delegated to smaller scales, i.e. for a given (s_0, q_0) , the stability of the most unstable scale decreases as Λ_0 increases. Conversely, if the scaling saturates at very small scales $\Lambda_0 \lesssim 1$, instabilities are actually relegated to larger scales.

4.4.4. Extension: Different Turbulent Scaling Exponents

Figure 4.17 shows the two-phase regions and contours of the stability threshold for different scaling exponents of the gaseous components.

Comparing the original case of $a_g = b_g = 1/3$ to either of the two intermediate cases where $a_g \neq b_g$, one sees that the two-phase region and the shape of the \bar{Q} contours change differently depending on whether a_g or b_g is changed. If the exponent a_g of the gas surface density is

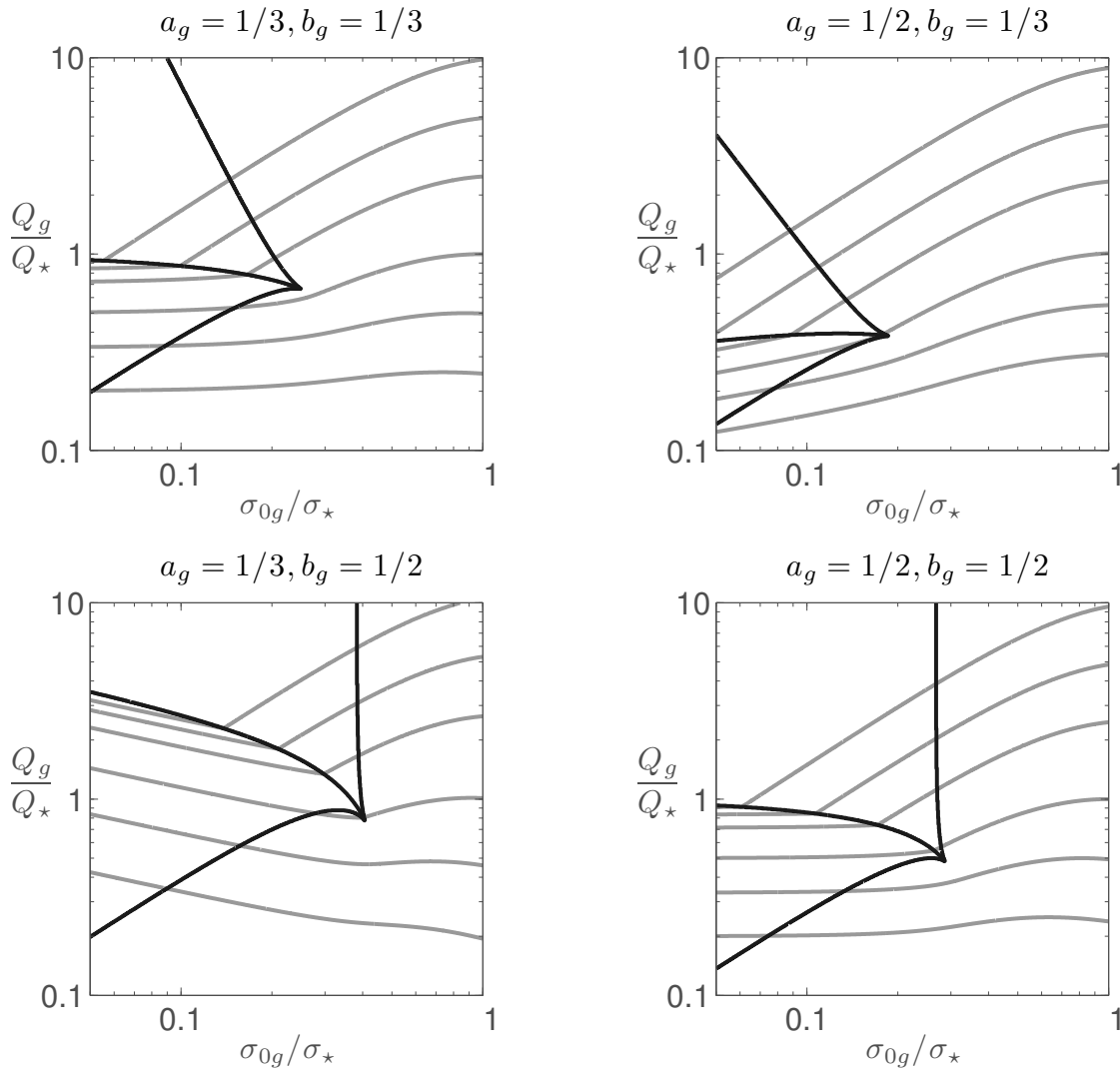


Figure 4.17.: Two-phase regions (black) and (from top to bottom) $\bar{Q} = \{1.1, 1.2, 1.4, 2, 3, 5\}$ contours (grey) for turbulent systems with different scaling exponents ($\Lambda_0 = 1$) of the gas component.

changed, the two-phase region is displaced downwards and becomes smaller. The basic shape of the \bar{Q} contours is retained along with the discontinuity across the transition line.

Changing the scaling exponent of the velocity dispersion b_g seems to shave a much stronger impact on two-phase region and stability threshold. Visually, one gets the impression that the two-phase region and the contours are tilted clockwise and then shifted towards the right top. The transition line is no longer approximately parallel to the $q_0 \simeq 1$ line, and the stellar-dominated part of the two-phase region is much larger. Additionally, the boundary of the stellar-dominated part of the two-phase region is almost vertical, i.e. $s_0 = \text{const}$.

If both scaling exponents are changed equally, the aforementioned effects seem to balance each other. While the two-phase region is much larger for $a_g = b_g = 1/2$, the gas-dominated region is now of a size more comparable to the $a_g = b_g = 1/3$ case and the apparent rotation of the two-phase region and the \bar{Q} contours have disappeared. The almost vertical boundary of the star-dominated region, however, remains.

While a thorough investigation of the effects of changing the scaling exponents is beyond the scope of this work, the most important trends are:

1. The size of the two-phase region is proportional to b_g , and inversely proportional to a_g with different proportionality factors. In particular, increasing the velocity dispersion scaling exponent significantly increases the region in which the stability response can become decoupled. The effect is stronger than the decrease in size of the two-phase region for an increased surface density scaling exponent, such that if both exponents are changed, the size of the two-phase region still increases. This disparity suggests that the turbulent velocity field drives the range of $s_0 - q_0$ where the stability response is decoupled.
2. The differences in the \overline{Q} contours are most noticeable when considering the cases with different scaling exponents. For $b_g = 1/2$, the apparent rotation and displacement of the contours implicates that a particular point (s_0, q_0) is associated with a higher stability threshold than in the $a_g = b_g = 1/3$ case, such that stability is decreased. This is unexpected because a more aggressive scaling of the velocity dispersion would suggest a stabilizing influence. The converse is true if the scaling exponent of the surface density term is larger and points (s_0, q_0) are promoted to a lower stability threshold such that the system becomes more stable. Again, this is unintuitive because a higher surface density generally destabilizes a system.

The overall effect on \overline{Q} of increasing the scaling exponents together and by the same amount seems to non-existent or at least very small. As such, it seems that the effect on stability for scaling exponents changed by the same amount is small.

3. Interestingly, the location of the transition line is shifted along the q_0 direction depending on which scaling exponent is larger. The cause for this is hard to determine without considering the marginal stability curves but is likely related to the fact that the relative stability of the gaseous and stellar components are affected (in addition to the stability of the coupled system). This suppresses (or amplifies) one of the two peaks stronger than if $a_g = b_g$, which causes different q_0 values needed for the peaks to be of equal height.

Beware that these trends are by no means certain to hold for all ranges of a_g and b_g within the Toomre-like regime. Further note that neither the behaviour of the most unstable scale $\overline{\Lambda}$ nor the shape of the marginal stability curves has been considered for the time being.

4.5. Chapter Summary

In this chapter, the dispersion relation and marginal stability curve for classical and turbulent systems were studied. These were then used to study the stability of (i) turbulent HI coupled to turbulent H₂, (ii) a stellar disc coupled to a non-turbulent gaseous disc, and (iii) a stellar disc coupled to a turbulent HI disc. Most importantly, it was found that:

- A two-component system is always less stable than the two individual constituent systems. For turbulent systems consisting of a virialized and a Toomre-like component, the stability of the virialized component determines the stability regime of the coupled system. In particular, if the turbulent virialized system is slightly more than marginally stable, the two-component system is Toomre-like, irrespective of the stability of the

Toomre-like component. If the virialized component is unstable or only marginally stable, the coupled system is unstable on small scales. The prototype of such a system is turbulent HI coupled to turbulent virialized H₂.

- For a disc of turbulent HI coupled to turbulent H₂, the H₂ component dominates the stability response of the coupled system. The more stable the H₂ component is relative to HI, the more stable the coupled system is. In like fashion, increasing the velocity dispersion of H₂ relative to HI also stabilizes the H₂ component and thus the coupled system. Larger values of Λ_0 tend to destabilize the coupled system.
- Coupled systems with Toomre-like stability are studied in the $s_0 - q_0$ plane. From evaluation of the MSC at each point (s_0, q_0) , the stability threshold \bar{Q} , the most unstable scale $\bar{\Lambda}$, and the number of peaks in the MSC is determined. These quantities are then plotted in the $s_0 - q_0$ plane to describe the stability of the system.
- For non-turbulent systems, the MSC is computed for constant values of (s, q) with the function domain Λ . For turbulent systems, $s = s(\Lambda)$ such that some parts of the MSC are boosted to larger and others to smaller effective values of s . This affects the stability threshold, the most unstable scale, and the size of the two-phase region depending on the choice of Λ_0 . Resulting from this, the size of the two-phase region changes, and the contours of \bar{Q} and $\bar{\Lambda}$ are shifted along the s_0 axis in the $s_0 - q_0$ plane.
- For $\Lambda_0 \gtrsim 1$, a turbulent system is always more stable with a smaller most unstable scale than the equivalent classical system. For $\Lambda_0 \lesssim 1$, the turbulent system is generally less stable and the most unstable scale shifts to larger values. On the other hand, the two-phase region of a turbulent system is always larger than the two-phase region of the equivalent classical system for $\Lambda_0 \gtrsim 0.1$. Moreover, the size of the stellar-dominated part increases much more than the size of the gas-dominated part.
- The scaling exponents of the turbulent component affect the stability threshold, most unstable scale and size of the two-phase region differently. For unequal exponents, increasing the exponent of the surface density seems to (i) stabilize the coupled system and (ii) increase the two-phase region, whereas increasing the velocity dispersion exponent seems to (i) destabilize the system, and (ii) decrease the two-phase region. The effect of the velocity dispersion scaling dominates such that increased, but equal, scaling exponents increase the size of the two-phase region. On the other hand, the stability threshold is not affected significantly.
- Different types of systems appear to respond differently to changes in Λ_0 . In particular, systems consisting of a turbulent and a virialized component (for example, turbulent HI and H₂) are destabilized more for larger values of Λ_0 . Conversely, systems consisting of two Toomre-like components (for example, HI and stars) tend to become more stable for larger values of Λ_0 .

APPLICATION TO NEARBY STAR FORMING GALAXIES

In this chapter, the theory developed in §4 is applied to study star formation in 12 nearby spiral galaxies. The treatment is an extension of a previous study conducted by Leroy et al. (2008)¹ in the sense that two-component stability, the effect of turbulence and modifications to some of the underlying assumptions are introduced.

After defining the star formation problem on galactic scales in §5.1, the sample, core assumptions, and conclusions of the original analysis of L08 are summarized in §5.2. Afterwards, the previous study is extended to include the aforementioned effects in §5.3.

5.1. The Star Formation Problem

As previously discussed, the primary constituents of galaxies are neutral atomic hydrogen HI, molecular hydrogen H₂, as well as different populations of stars. Over time, as HI dissipates energy through collisions, the medium becomes denser and GMCs form. Owing to turbulent density fields, local overdensities in these clouds undergo gravitational collapse and form protostellar cores (e.g. McKee & Ostriker, 2007).

The conditions required for such protostellar cores to form define the star formation problem on galactic scales. To study it in an appreciably complete manner requires extensive knowledge of the conditions in galaxies, the three most important of which are as follows.

1. The sites of star formation in galaxies. Tracing these is based on emissions characteristic to (i) short-lived stars or (ii) emissions from dust heated up by young stars. The multitude of available methods is reviewed in Kennicutt (1998). Results of such observations are then used to derive star formation rates.
2. The distribution of atomic and molecular hydrogen in the interstellar medium. Accounting for galactic rotation (where present), the HI and H₂ distributions are characterized through their respective surface densities and velocity dispersions. The HI distribution is generally mapped through the 21 cm line, and the H₂ distribution by means of using CO 1 → 0 or 2 → 1 transition lines as tracers (Wilson et al., 2009).

¹Hereafter, L08.

3. The distribution of the present stellar population in galaxies. Again, it is characterized by the surface density and velocity dispersion. It is now common to trace the stellar population through infrared (IR) observations (Pahre et al., 2004).

In recent years, surveys sharing a common subset of nearby galaxies have produced high resolution observations providing all of the aforementioned quantities at sufficiently high resolution. Taking advantage of this data, L08 aggregated the available information and analysed the star formation in 23 nearby galaxies. This analysis is now discussed.

5.2. The L08 Study of Star Formation in Nearby Galaxies

The primary aim of L08 is the investigation of possible correlations between the measured star formation efficiency² and (i) star formation laws describing star formation efficiency, (ii) models describing star formation thresholds, and (iii) models describing the formation of GMCs whose presence strongly correlates with sites of star formation. After discussing the basic ideas behind these models, the calculations of physical quantities and the surveys they are obtained from are outlined. This is followed by a summary of the core findings of L08.

5.2.1. Star Formation Efficiency, Thresholds, and Phase Transitions

Over the years, various star formation laws and efficiencies have been proposed. At their core, all are based on the notion that star formation is associated with a characteristic timescale τ over which stars form; $\text{SFE} \propto \tau^{-1}$. Different star formation laws then follow from a combination of physical assumptions and proposed timescales. Common choices for timescales are, for example, the orbital timescale τ_{orb} and the free-fall time of the gas τ_{ff} .³ Further assumptions include fixed or variable scale heights of the gaseous disc, or the significance of galactic shear arising from differential rotation.

However, observations suggest that star formation laws are not universal. This means that certain conditions must be fulfilled for star formation to take place such that it can be described by star formation laws. These conditions are referred to as star formation thresholds and frequently take the form of criteria regarding the gravitational or thermal stability of the interstellar gas.

Observations of both Milky Way and extragalactic GMCs have repeatedly identified GMCs as regions of concentrated star formation (Blitz, 1993; Fukui et al., 1999; Engargiola et al., 2003). The question of how both the phase transition from molecular hydrogen to neutral atomic hydrogen and star formation itself occurs within these clouds is thus part of the star formation problem. The efficiency of star formation within GMCs and whether it is linked to the environment outside the clouds is of particular interest.

As before, various approaches are used to describe how GMCs can form in the interstellar medium. Since the issue is generally considered a problem of phase transition, it is approached

²The star formation efficiency, SFE, is the star formation rate per unit of gas. As such, it is decoupled from the basic scaling between star formation rate and gas density and concentrates on describing how efficient gas is at forming stars.

³The orbital timescale τ_{orb} describes how long a parcel of gas takes to complete one orbit around the host galaxy, $\tau_{\text{orb}} \propto \Omega(R)/2\pi = 1/2\pi v(R)/R$, where $\Omega(R)$ is the angular velocity, and $v(R)$ the rotational velocity at galactocentric distance R . The free-fall timescale τ_{ff} describes the time a gas cloud of density ρ needs to undergo gravitational collapse; $\tau_{\text{ff}} \propto \rho^{-0.5}$ (Madore, 1977).

in terms of gas pressures and densities. Both continuous models describing the fraction of H₂ to HI as well as threshold models that give criteria for the formation of a cold HI phase (in which GMC formation is thought to be efficient) are available.

Note that in the context of both L08 and this work, a region is considered to be a GMC if it is H₂ dominated, i.e. if $\Sigma_{\text{H}_2} > \Sigma_{\text{HI}}$.

5.2.2. Surveys, Observations to Physical Quantities, Assumptions

To obtain the required measurements outlined in §5.1, L08 aggregates observations from a number of surveys. In particular, HI intensity maps, and by extension, rotation curves are available from The HI Nearby Galaxy Survey (THINGS, Walter et al., 2008) of the 21 cm line. CO 1 → 0 and 2 → 1 transition maps are available from the Berkeley-Illinois-Maryland Association Survey of Nearby Galaxies (BIMA SONG; Helfer et al., 2003) and the HERA CO-Line Extragalactic Survey (HERACLES; Leroy et al., 2009). Stellar surface densities are obtained from 3.6 μm IR observations of the Spitzer Infrared Nearby Galaxies Survey (SINGS; Kennicutt et al., 2003). Lastly, the star formation rate surface densities are derived by combining SINGS IR maps with FUV maps provided by the Galaxy Evolution Explorer Nearby Galaxies Survey (Gil de Paz et al., 2007).

The surveys share a common sample of 23 nearby galaxies, which is divided into 12 spiral, and 11 dwarf galaxies classified according to their total mass, rotational velocity, and *B*-band magnitude. Where required, spatial resolution is degraded to a common resolution of 800 pc for the spiral galaxies, and 400 pc for the dwarf galaxies. For the dwarf galaxies, H₂ surface densities are not available because of too large uncertainties in CO-to-H₂ conversion factor.

Referring to appendices A–D of L08 for a thorough discussion, the basic steps of how physical quantities are obtained from observations are now outlined. Major sources of uncertainties are, where present, also outlined. Note that, for all quantities, radial profiles are generated from the observed maps by means of suitable binning and averaging over rings.

Gas Surface Densities. HI surface densities are obtained from the integrated 21 cm line intensity. Averaging over rings, and accounting for inclination as well as helium fraction, Σ_{HI} is directly proportional to the line intensity.

H₂ surface densities are more complicated. Since H₂ lines cannot be observed directly, CO 1 → 0 and 2 → 1 transitions are used as tracers instead. As before, averaging over a suitable ring size and accounting for inclination, the radial CO distribution in the galaxy can be obtained. Assuming a constant conversion factor X_{CO} between CO and H₂, the CO distribution is then converted to an H₂ distribution.

The assumption of a constant value of X_{CO} is contested in literature. In fact, X_{CO} actually appears to vary depending on the location within the galaxy. To first order, it is expected to be lower than galactic average in H₂ dominated regions, and higher in dust-devoid regions with strong radiation fields. Since the former describes conditions in the central regions of spirals, it is likely that H₂ density in these regions is overestimated. The latter, on the other hand, describes conditions in low-mass dwarf galaxies, where different approaches to measure H₂ density yield estimates varying by orders of magnitude. As such, L08 treats the conversion factor in the dwarf galaxies as unknown, and therefore does not derive H₂ densities.

The lack of Σ_{H_2} introduces significant difficulties in the analysis of L08, which leads to the conclusion that the undetected H_2 content of the dwarf galaxies significantly affects the dynamics of these galaxies.

Rotation Curves. Rotation curves are obtained from the Doppler shift of the 21 cm line. In particular, the rotational velocity of each map-pixel is calculated by subtracting the systemic velocity from the measured radial velocity, with subsequent accounting for inclination. Once done, the data is fit to the function of the rotation curve

$$v_{\text{rot}}(R) = v_{\text{flat}} \left[1 - \exp\left(\frac{-R}{l_{\text{flat}}}\right) \right], \quad (5.1)$$

where $v_{\text{rot}}(R)$ is the rotational velocity at galactocentric radius R . The parameters v_{flat} and l_{flat} are the parameters obtained for each galaxy through the fit.

Stellar Surface Density. Stellar surface densities are computed based on $3.6 \mu\text{m}$ IR observations. In particular, the IR maps are inclination corrected and then converted to median profiles, which provides several distinct advantages over averaged profiles, cf. appendix C in L08. The profiles are then converted from $3.6 \mu\text{m}$ to K -band intensity, which is used to derive Σ_{\star} by adopting a mass-to-light ratio Υ_{\star}^K identical for the entire sample.

The major uncertainty in the derivation of the stellar surface density is the mass-to-light ratio Υ_{\star}^K . It depends on the metallicity, initial mass function, and previous star formation history of the galaxies. Changing some of these assumption, similar studies of the same dataset obtain values of Υ_{\star}^K about 30 – 40% higher (de Blok et al., 2008).

Gas Velocity Dispersion. Throughout the entire sample, a constant gaseous velocity dispersion of $\sigma_g = 11 \text{ km/s}$ is assumed. This value is typical of the outer regions of the 12 spiral galaxies, where the total surface density is dominated by the HI contribution, cf. §5.2.3.

Stellar Velocity Dispersion. Lacking direct measurements of the (radial) stellar velocity dispersion $\sigma_{\star,r} = \sigma_{\star}$, L08 obtains σ_{\star} from the stellar surface density under the assumptions of (i) hydrostatic equilibrium, (ii) constant scale height of the stellar disc, (iii) a constant relation between the stellar scale length and the scale height, and (iv) a constant relation between the radial and vertical velocity dispersions.

Star Formation Rate Surface Density. To obtain the star formation rate, L08 combines Far-UV and $24 \mu\text{m}$ observations. This combination is advantageous because both exposed and embedded star formation is traced. Exposed star formation is traced through Far-UV observations because emission at these wavelengths is dominated by light from O and B stars, which have relatively short lifetime. Obscured star formation is traced through $24 \mu\text{m}$ emissions, which are dominated by flux from dust grains that have been heated by UV photons from young stars. The star formation surface density Σ_{SFR} is thus proportional to a linear combination of the Far-UV and the $24 \mu\text{m}$ flux.

5.2.3. Main Findings of the L08 Study

In this section, variations of a number of quantities with respect to galactocentric radius are considered. Only the relations most relevant in the context of the present work are described here. For a more detailed account, please refer to L08.

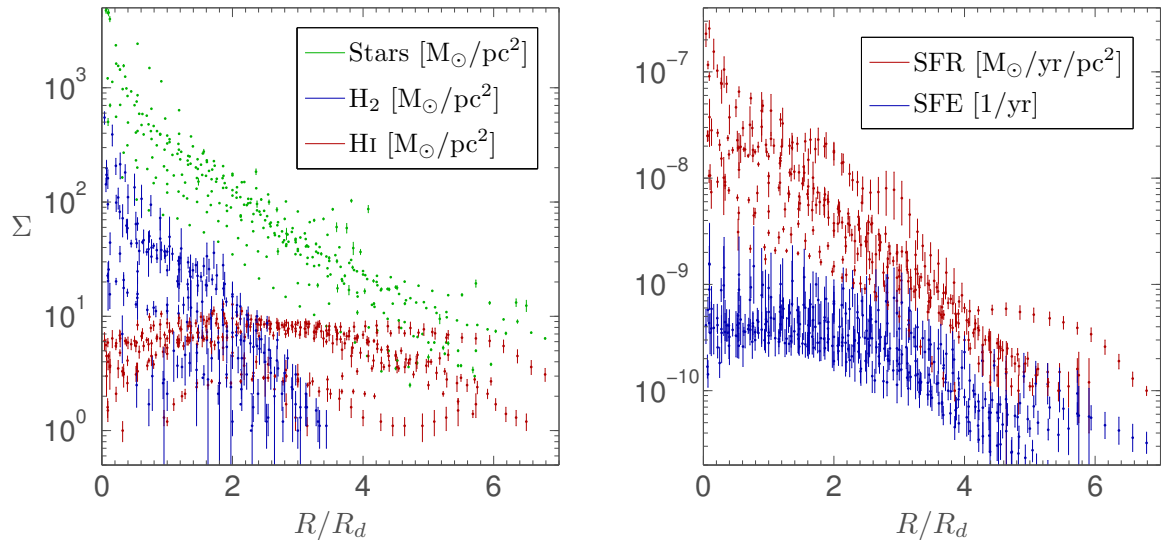


Figure 5.1.: *Left:* Surface densities of HI, H_2 , and the stellar disc vs. radius. Both H_2 and stellar surface density decrease exponentially outwards, while HI surface density is approximately constant. For $R \lesssim R_d$, $\Sigma_{H_2} > \Sigma_{HI}$, whereas for $R \gtrsim 2R_d$, $\Sigma_{H_2} < \Sigma_{HI}$. *Right:* Star formation rate (SFR) and star formation efficiency (SFE) vs. radius. The SFR decreases exponentially at all radii, whereas the SFE remains approximately constant up to $R \lesssim 2R_d$, but shows exponential decrease above. This coincides with the transition from a H_2 to an HI dominated gas.

Surface Densities, Star Formation Rate, Star Formation Efficiency

Figure 5.1 shows the profiles for the HI, H_2 , and stellar density (left panel) as well as the star formation rate (SFR) and star formation efficiency (SFE) (right panel). The horizontal axes are normalized to the stellar scale length R_d .

It is seen that both stellar and H_2 surface density decrease exponentially with radius and peak at values of $\Sigma_\star \sim 10^3$ M_\odot/pc^2 , respectively $\Sigma_{H_2} \sim 10^2$ M_\odot/pc^2 . The HI surface density, on the other hand, remains approximately constant with a peak of $\Sigma_{HI} \sim 10$ M_\odot/pc^2 at $R \simeq 2R_d$. At smaller and larger radii, HI surface density decreases, with smallest values found towards large radii. For $R \lesssim R_d$, H_2 dominates the total surface density of the gaseous component, and for $R \gtrsim 2R_d$, the situation is reversed. In the transition regime $R_d \lesssim R \lesssim 2R_d$, both components contribute equally. The stellar surface density is roughly an order of magnitude above the total gas density.

As with the H_2 and stellar surface densities, the star formation rate decreases exponentially with increasing radius. This suggests a power law relation $\Sigma_{\text{SFR}} \propto \Sigma_g^n$ between the star formation rate (surface density) Σ_{SFR} and the total gas surface density Σ_g , with possibly different exponents n depending on the dominant gas component.

In light of this, it is interesting to note that the star formation efficiency remains roughly constant in the range $0 \leq R \lesssim 2R_d$, but decreases exponentially beyond $R \gtrsim 2R_d$. This suggests that while H_2 dominated regions are more efficient in converting gas to stars, the H_2 surface density itself does not affect the star formation efficiency. HI, on the other hand, is less efficient at forming stars than H_2 , but its surface density has a larger effect on the efficiency.

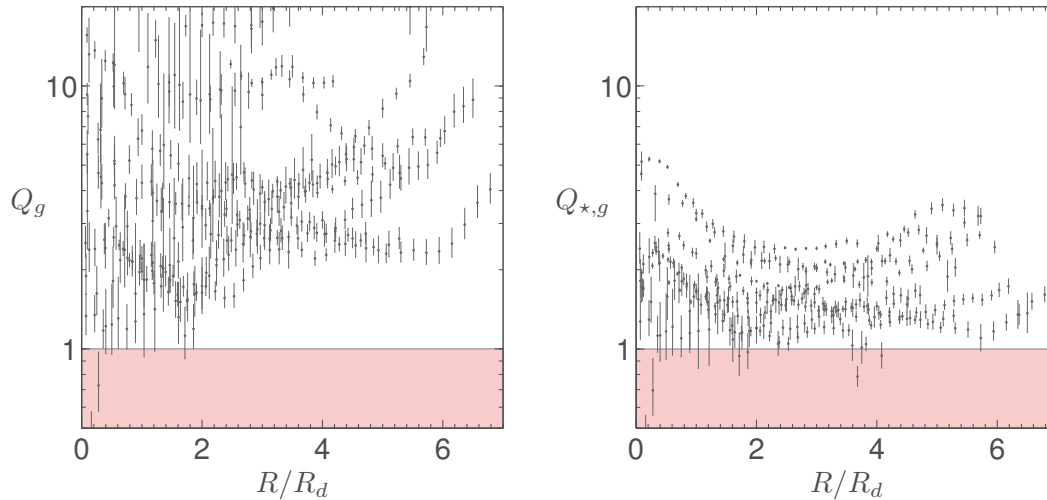


Figure 5.2.: The Toomre parameter Q vs. fractional radius R/R_d . As before, stability on all scales requires $Q \geq 1$, and the unstable range is shaded. *Left*: Toomre parameter Q_g for only the gaseous system. *Right*: Toomre parameter $Q_{*,g}$ for a system of a non-turbulent gaseous component coupled to a stellar component.

Beyond studying correlations between various measured or inferred quantities, L08 also considered how well various star formation laws reproduce the observed SFE. It is found that some of the considered star formation laws indeed reproduce observed SFEs in the inner regions of the spiral galaxies. However, the correlation is lost in both the outer regions of the spirals, and does not hold at all in the dwarf subsample.

On the other hand, a correlation between the hydrostatic pressure and the dominant phase of the ISM is found. This suggests that formation of GMCs out of neutral atomic hydrogen is, at least in part, a problem that can be approached from a thermal and pressure equilibrium point of view. Moreover, once GMCs have formed, these H_2 dominated regions are found to be associated with a constant SFE, irrespective of other environmental conditions.

Star Formation Thresholds

Figure 5.2 shows the Toomre parameter as a function of radius. The left panel shows the Toomre-parameter Q_g for the gaseous component alone, and the right panel the Toomre-parameter $Q_{*,g}$ for the system of stellar disc coupled to a gaseous disc.⁴ In both cases, stability on all scales is guaranteed if $\{Q_g, Q_{*,g}\} \geq 1$.

Comparing both panels of figure 5.2, one immediately notices that either case contains only few data points in the unstable regime. Furthermore, note that Q_g shows a much larger spread than $Q_{*,g}$. Since the coupled case is a more realistic description of the actual system, the narrow spread in the two-component case in fact supports the notion of self-regulation in the presence of a stellar component, cf. §4.4.1.

The fact that only few points can be found in the unstable range of Q suggests that either (i) one- and two-component gravitational stability does not provide a good indication for the

⁴To compute two-component stability, L08 uses a form of the stability criterion alternative (but equivalent) to that derived from the MSC in §3. For more details see Leroy et al. (2008, Eq. 16) and relevant references therein.

ability of the ISM to form stars, or that (ii) one or more of the assumptions discussed in §5.2.2 are not representative of the true conditions, which causes an overestimation of the stability level.

Before challenging the assumptions, however, note that the one- and two-component models used both in L08 and this work consider only the influences of gas pressure, self-gravity, and differential rotation. Effects from magnetic fields, finite disc thickness, supernova feedback, and turbulence are not considered. Since a complete model is not currently available, a later discussion in §5.3.3 focuses on the effects of (i) turbulence and (ii) different gas velocity dispersions.

L08 also investigated other thresholds not discussed here. In particular, considering the stabilizing effect of galactic shear, the inner regions of the dwarfs and spirals are found to be only marginally stable — a significant improvement over Q_g alone. Furthermore, L08 finds various threshold values for the gaseous surface densities, i.e. (i) a threshold of Σ_g above which the H_2 phase generally dominates, (ii) a maximum value of Σ_{HI} , where a higher total gas density is usually found to be attributed to H_2 , and (iii) a cut-off value of Σ_g marking the edge of the star forming parts of the disc.

5.2.4. Effects of Uncertainties

L08 identified the K -band mass-to-light ratio Υ_\star^K and the CO-to- H_2 conversion factor X_{CO} as the major sources of uncertainty. The potential impact of these uncertainties is now discussed qualitatively.

Mass-To-Light Ratio. Changes to Υ_\star^K cause the stellar surface density Σ_\star to be over- or underestimated. As such, any scaling relations involving Σ_\star are changed uniformly throughout the disc. This should not affect observed trends, and only affect details such as the exponents of power law fits.

While the stability parameter Q_g of the gas alone is not affected, the stability parameter $Q_{\star,g}$ of the coupled system is affected (cf. figure 5.2). In particular, increasing Υ_\star^K causes an increase in Σ_\star , which destabilizes the stellar component. Since the coupled system is less stable than the individual systems, it is also destabilized. Reversely, decreasing Υ_\star^K stabilizes the combined system.

Conversion Factor. Changes to the conversion factor affect the H_2 surface density Σ_{H_2} . Note that (i) X_{CO} is a function of galactic position, and that (ii) the adopted constant value for X_{CO} is likely larger than the true value in H_2 dominated regions. This means that the true value of Σ_{H_2} in the inner regions is smaller than what is actually used.

Depending on the severity of the underestimate, the finding of a constant SFE = $\Sigma_{\text{SFR}}/\Sigma_g$ in H_2 dominated regions (cf. figure 5.1) could be challenged because a decrease in total gas surface density corresponds to an increase in SFE. Note that, without a proper estimate of the expected error on X_{CO} , this possibility can neither be confirmed nor ruled out.

The stability of (i) the gaseous disc alone, (ii) the disc of gas and stars, can be expected to increase in the inner H_2 dominated regions because a decrease of the total gaseous surface density reduces the destabilising effect of self-gravity.

5.3. Two-Component Gravitational Stability in 12 Spirals

The analysis performed in L08 covered laws and thresholds concerning both star formation and HI-to-H₂ phase transitions. In the following, the work is extended by applying the two-component treatment of gravitational stability introduced in §3 and extended in §4. In particular, the effects of the (i) two-phase region, (ii) the stability threshold in the presence of turbulent scaling, and (iii) the most unstable scale in the presence of turbulent scaling are studied.

Further recall that L08 adopted a constant gaseous velocity dispersion of $\sigma_g = 11$ km/s throughout the entire disc. As discussed in §2.1, velocity dispersion in GMCs are, however, in the order of $\sigma_{\text{H}_2} \simeq 5$ km/s on the largest scales. As such, it can be expected that the choice of a gaseous velocity dispersion of $\sigma_g = 11$ km/s is not particularly suited for regions where the total gas surface density is dominated by the H₂ component. This likely leads to an overestimate of the stability level in the inner H₂ dominated regions — an effect that is now studied by introducing a lower velocity dispersion in regions where HI does not dominate.

To characterize the data points from the sample in a meaningful fashion, the median is frequently computed. Since the median of a distribution is the value where the probabilities of values being larger or smaller than the median are equal, it performs better in the presence of outliers than, for example, the average while also avoiding the search for a suitable weighting function.

5.3.1. The Improved Model

Before investigating the data points of the spiral galaxies in the $s_0 - q_0$ plane,⁵ they are first subdivided into three regions. Depending on the region, modifications to the model are then made to investigate the effects of different velocity dispersions and a turbulent HI component.

The Inner, Outer, and Transition Regions

Recall from §5.2.3 that HI and H₂ surface densities as well as the star formation efficiency behave distinctly different depending on the galactocentric radius. In particular, in the inner galactic regions $R \lesssim R_d$, H₂ dominates the total gas surface density, whereas in the outer regions $R \gtrsim 2R_d$, Σ_g is dominated by HI. In the transition regime $R_d \lesssim R \lesssim 2R_d$, the surface densities of HI and H₂ are comparable. The SFE, on the other hand, remains approximately constant throughout the inner and transition regions, but decreases exponentially beyond $R \gtrsim 2R_d$.

This suggests that an analysis of the sampled galaxies in the $s_0 - q_0$ plane could greatly benefit from considering the three regions separately. This is now done. Note that the convention of referring to the region $R \leq R_d$ as the inner region, $R_d < R \leq 2R_d$ as the transition region, and $R > 2R_d$ as the outer region is retained.

⁵Recall that $s_0 = \sigma_{0g}/\sigma_*$ is the velocity dispersion ratio, and $q_0 = Q_g/Q_*$ the relative stability of the two components at scale ℓ_0 .

Velocity Dispersion and Turbulence

Another advantage of separating the sample into regions is that it allows separate modifications to be applied to the model in each region. In particular, the effect of a velocity dispersion more representative of H₂ dominated regions as well as the introduction of turbulent scaling in HI dominated regions are easily implemented because (i) the choices are well justified, and (ii) the affected regions are clearly separated. The study of effects, such as radial variations of the CO-to-H₂ conversion factor, on the other hand, are more complicated to both implement and justify and are thus not considered.

As such, only the effects of a modified velocity dispersion and a turbulent HI component are investigated. The required changes to the model are now explained and motivated.

1. For $R \leq R_d$, where H₂ dominates, a model of a stellar disc coupled to a non-turbulent H₂ disc is selected to represent the observations. The gas component is considered to be predominantly H₂ and is associated with a velocity dispersion of $\sigma_g = 5$ km/s. This value is motivated by the GMC velocity dispersions observed at the largest scales, cf. §2.1. The gas component is considered non-turbulent because H₂ velocity and density fields only exhibit turbulent scaling below the resolution scale $\ell_0 = 800$ pc. See §2.1 for details.
2. In the transition regime $R_d < R \leq 2R_d$, the most suitable way to characterize the system is by means of a three-component model of a stellar disc coupled to a non-turbulent H₂ disc (at the resolution scale $\ell_0 = 800$ pc) and a turbulent HI disc. However, at present, a properly developed three-component model allowing for turbulence is not available.

As such, it is chosen to represent the system as a non-turbulent gas disc coupled to a stellar disc. For the gas component, a velocity dispersion of $\sigma_g = 8$ km/s is chosen as a middle ground between the velocity dispersions in the H₂ and HI dominated regions. It must be stressed that this is not an appropriate model for the regime where the H₂ and HI contributions are similar, but it is the best possible model given the constraints. It is hereafter avoided to draw any conclusions in this regime.

3. For $R > 2R_d$, where HI dominates, the system is considered to consist of a stellar disc coupled to a turbulent HI disc. The characteristic velocity dispersion $\sigma_{0g} = 11$ km/s at the resolution scale $\ell_0 = 800$ pc of L08 is retained, and turbulent scaling in the HI surface density and velocity dispersion with $a_g = b_g = 1/3$ is introduced.

5.3.2. The Parameter Plane

Before discussing the different regions separately in the $s_0 - q_0$ plane, all data points of both the spiral and the dwarf galaxies are considered; without binning into different regions. This serves to illustrate the problem caused by the lack of H₂ measurements in the dwarf galaxies and further motivates the omission of the dwarf subsample in this work.

Spirals and Dwarfs in the Astrophysically Relevant Part

The panels in figure 5.3 show the data points of the 12 spiral and 11 dwarf galaxies in the astrophysically relevant part of the $s_0 - q_0$ plane.⁶ In the left panel, the total surface density

⁶Since L08 provides Σ_* , σ_* , Σ_g , and σ_g measured at a scale ℓ_0 for each datapoint, computation of $s_0 = \sigma_{0g}/\sigma_*$ and $q_0 = Q_g/Q_* = (\sigma_g/\sigma_*)(\Sigma_*/\Sigma_g)$ is straightforward. Upper and lower bounds are calculated based on

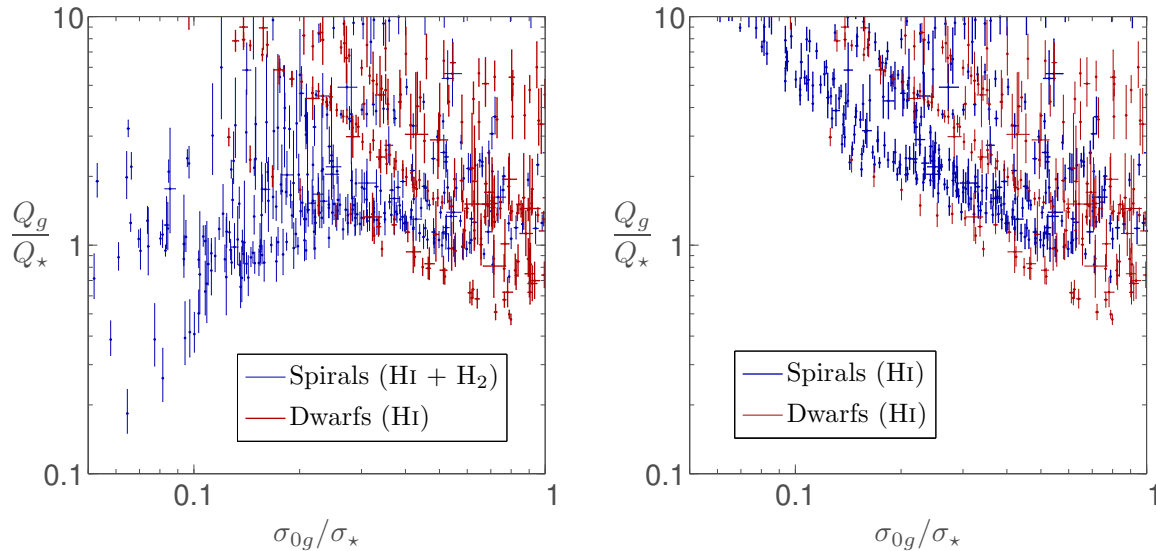


Figure 5.3.: Data points for the spirals and dwarf galaxies in the astrophysically relevant part of the $s_0 - q_0$ plane. Note that a significant part of the points in each subsample is located outside the physical region, cf. text. All points have constant velocity dispersion $\sigma_g = 11$ km/s. *Left:* Gas surface density for spiral galaxies is the sum of HI and H₂ surface densities. *Right:* Gas surface density for the spiral galaxies considering only the HI component.

of the spiral galaxies is the sum of the HI and H₂ surface densities, whereas in the right panel, only the contribution of the HI component is considered. For the dwarf galaxies, the total surface density is based only on HI since H₂ measurements are unavailable.

Note that 37% of data points associated with the dwarf galaxies are not located in the astrophysically relevant part of the $s_0 - q_0$ plane (and are thus not seen in the figure). For the spiral galaxies considering both the HI and H₂ contribution to the total surface density, this is only the case for 12% of the points — also cf. table 5.1.

Combining this with a visual inspection of figure 5.3, various distinct trends can be recognized. In particular, (i) not all data points fall in the region that is physical, (ii) the data points associated with the dwarf galaxies tend to be found at larger values of s_0 , and (iii) the dwarf galaxies contain fewer data points in the astrophysically relevant regime than the spiral galaxies. These trends are now discussed.

Data Points Outside the Physical Region. From the discussion of the astrophysically relevant region in §4.4.1, recall that, while small excursions outside the region along q_0 do not pose strong interpretational problems, data points outside the permitted range in s_0 do so because (i) $s_0 \leq 1$ is a limit imposed by the physics of the stellar component being non-collisional, and (ii) $s_0 \gtrsim 0.05$ is imposed from observational evidence regarding stellar velocity dispersion.

Considering only the spiral galaxies, the limits are, in fact, violated at either end of the valid range of s_0 . Since $s_0 = s = \sigma_g/\sigma_*$,⁷ this suggests that either (i) there are points where the stellar velocity dispersion is overestimated, and points where it is

the standard deviations given in L08. For more details, cf. appendix A.

⁷For now, the system is treated as non-turbulent, such that $s_0 = s$, and $q_0 = q$.

underestimated, (ii) there are points where the constant gaseous velocity dispersion is an overestimate, and points where it is an underestimate, or (iii) a combination thereof.

In fact, the third option is most likely because (i) the constant value of the gaseous velocity dispersion $\sigma_g = 11$ km/s is not representative of all galactic regions, and (ii) the assumptions of radially constant scale height, and exclusion of the gravitational coupling between the stellar and gaseous component when deriving the stellar velocity dispersion, likely cause local over- and underestimations of the true stellar velocity dispersion. On the other hand, it is possible that the effects of under- and overestimation balance one another.

While a thorough investigation of the different effects of gaseous and stellar velocity dispersions is deferred to future work, recall that the gaseous velocity dispersion is in fact modified to better represent the dominant gas component in this work.

Dwarf Galaxies, Larger s_0 Values, The Physical Region. The difference in locations of data points between the spirals and dwarfs suggests that some of the assumptions made during the derivation of the physical quantities are problematic. In particular, since only 6 out of the 11 dwarf galaxies are morphologically different from the spirals, it is hard to fathom such a striking difference between the two groups.

To investigate this, recall from §5.2.2 that due to large uncertainties in the CO-to-H₂ conversion factor, H₂ densities in the dwarf subsample are omitted. If the shift in location of the dwarf subsample in the $s_0 - q_0$ plane is related to this, removing the H₂ density component from the spiral subsample should reproduce a shift of the data to a similar region. The result of this is shown in the right panel of figure 5.3, where it can indeed be seen that the spiral sample is shifted to coincide much more with the dwarf subsample, such that 19% instead of 12% of the spiral galaxies are outside the physical region.

To explain the shift, recall that

$$q_0 = q = \frac{s}{\alpha} = \frac{\sigma_g}{\sigma_\star} \frac{\Sigma_\star}{\Sigma_{\text{HI}} + \Sigma_{\text{H}_2}} \quad (5.2)$$

increases if the H₂ component is suppressed, i.e. $\Sigma_{\text{H}_2} = 0$. This suggests that omitting the H₂ component in the dwarf subsample introduces problems also from the point of view of the two-phase region. In fact, L08 draws a similar conclusion based on the fact that the HI derived SFE in central parts of dwarf galaxies amounts to or even exceeds the SFE in the central and H₂ dominated parts of the spirals.

As mentioned before, to avoid issues arising from unavailable H₂ density measurements, the dwarf subsample is not considered in this work.

Comparison of Models for Each Region

Figure 5.4 shows the data points for the unmodified (L08) and modified (New) model with colour coding applied to indicate the region a point is associated with. The two-phase regions for the non-turbulent and turbulent models are also indicated.

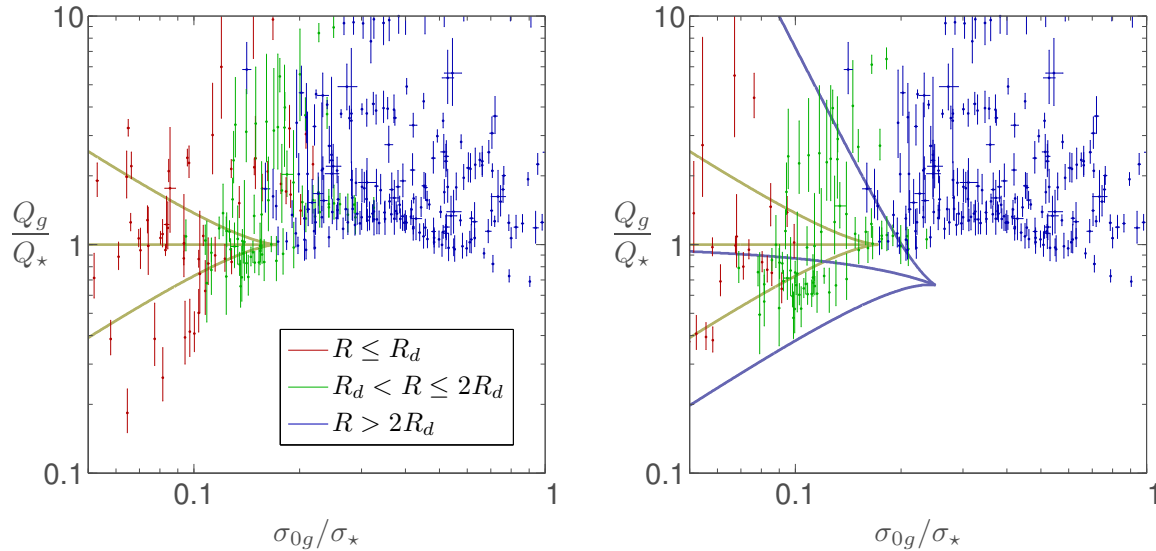


Figure 5.4.: Astrophysically relevant part of the $s_0 - q_0$ plane with data points colour-coded by region. *Left*: Original model with constant $\sigma_g = 11$ km/s across all regions and no turbulent scaling. The non-turbulent two-phase region is marked. *Right*: Modified model with variable σ_g and turbulent scaling in the outer regions. The non-turbulent and turbulent ($\Lambda_0 = 1$) two-phase regions are marked.

In both cases, it can be seen that points in the inner H_2 dominated regions have a tendency to populate the two-phase region, whereas points associated with the outer H_I dominated regions do not. Furthermore, points associated with the transition between H_2 and H_I dominance are frequently found just outside the two-phase region close to the triple point — also cf. table 5.1 and figure 5.5.

Along with figure 5.1, this indicates that a higher SFE and stellar surface density not only correlates with H_2 content, but also with the decoupling of the stability response. It is, however, unclear whether the decoupling tendency is related to (i) the formation of GMCs out of H_I , (ii) the formation of protostellar cores within the GMCs, or (iii) both. It is further possible that the correlation between a decoupled stability response and large H_2 surface densities is entirely coincidental. Unfortunately, it is presently unclear how this link can be investigated.

To better study the differences between the original and the modified models as applied to the data, figure 5.5 shows (i) the total number of points, (ii) the number of points in the astrophysically relevant region, and (iii) the number of points in the two-phase region for each of the three regions for the original and the modified model. Noting both this and the tabulated values in table 5.1, the two models are now compared separately for each region.

1. For $R \leq R_d$, fewer points are located in the physical part of the $s_0 - q_0$ plane for the modified model. Out of total number of points in the physical region, however, a larger fraction populates the two-phase region. Considering that $s_0 = \sigma_{0g}/\sigma_*$, decreasing σ_{0g} essentially shifts all points to smaller values of s_0 .⁸ In turn, this means that points with small values of s_0 tend to shift below the valid range of s_0 , and that points outside the two-phase region tend to shift towards it, and possibly inside.

⁸And to smaller values of q_0 , since $q_0 = Q_g/Q_* \propto \sigma_{0g}/\sigma_*$.

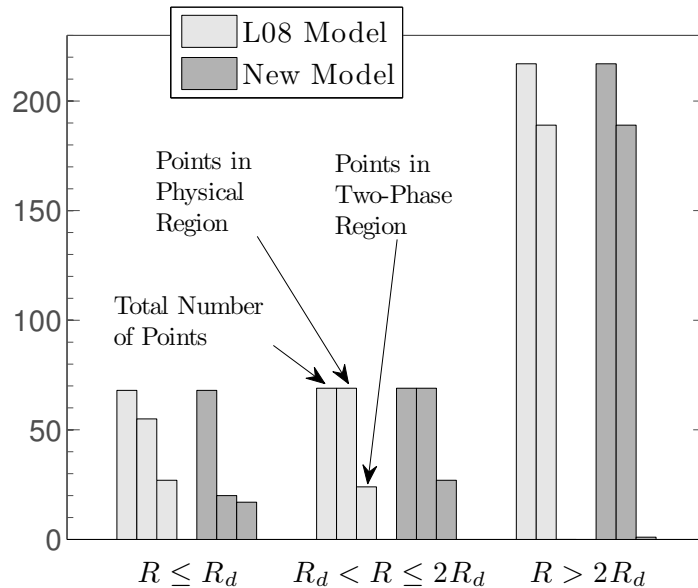


Figure 5.5.: Total number of data points, number of points in astrophysically relevant region, and number of points in two-phase region for the original L08 model and the new modified model. The counts are grouped by region, i.e. H_2 dominance, HI dominance, and the transition regime. Note that points are only counted to be in the two-phase region if they are in the astrophysically valid region.

The shift of points outside of the physical region presents a problem because the adopted value of $\sigma_g = 5$ km/s is more representative of the gaseous velocity dispersion in the region. This behaviour thus suggests that either (i) adopting $\sigma_g = 5$ km/s does in fact not represent the gaseous component well enough in the H_2 dominated region, or (ii) the original overestimate of the gaseous velocity dispersion through $\sigma_g = 11$ km/s is balanced by an overestimate of the stellar velocity dispersion.

- For $R_d < R \leq 2R_d$, the same general trend as for the H_2 dominated case is seen. In particular, the decreased gaseous velocity dispersion causes a shift towards smaller values of s_0 and q_0 . The net effect of this is not as dramatic as in the $R \leq R_d$ regime since the increase in the number of points for which the stability response is decoupled only increases minimally.
- For $R > 2R_d$, the introduction of turbulence does not affect the location of points in the $s_0 - q_0$ plane because turbulent scaling only affects s and q , whereas s_0 and q_0 are quantities valid at the scale ℓ_0 . The shape and size of the two-phase region, which differs significantly from the unmodified case, can however affect the number of points located within.

It is important to realize that each point in the turbulent outer region is associated with a unique two-phase region because $\Lambda_0 = \ell_0/\ell_{T\star}$ depends on the Toomre scale for each point. As such, the turbulent two-phase region in the right panel of figure 5.4 should not be used to determine whether a given point is located in the two-phase region. Being based on the median $\text{med}\{\Lambda_0\} \simeq 1$ across all points in this region, it should rather be used as visual aid. In practice, the location of a point inside the two-phase region is determined directly from the number of peaks in the MSC.

Sample	Gas	Region	a_{gas}	b_{gas}	σ_{gas}	In Two-Phase	In Astro	Total
S	H I + H ₂	All R	0	0	11 km/s	51 (16%)	313 (88%)	354
S	H I	All R	0	0	11 km/s	0	286 (81%)	352
D	H I	All R	0	0	11 km/s	0	190 (63%)	303
S	H I + H ₂	$R \leq R_d$	0	0	11 km/s	27 (49%)	55 (81%)	68
S	H I + H ₂	$R_d < R \leq 2R_d$	0	0	11 km/s	24 (35%)	69 (100%)	69
S	H I + H ₂	$R > 2R_d$	0	0	11 km/s	0	189 (87%)	217
S	H I + H ₂	$R \leq R_d$	0	0	5 km/s	17 (85%)	20 (29%)	68
S	H I + H ₂	$R_d < R \leq 2R_d$	0	0	8 km/s	27 (39%)	69 (100%)	69
S	H I + H ₂	$R > 2R_d$	1/3	1/3	11 km/s	1 (1%)	189 (87%)	217

Table 5.1.: Number of measurement points falling in the astrophysically relevant (In Astro) and the two-phase (In Two-Phase) regions for different models. The dwarf and spiral subsamples are marked D and S. Percentages of points in the two-phase region are relative to points in the physical region. Percentage of the latter, in turn, are relative to the total number of points.

While the increased size of the two-phase region suggests that turbulence tends to push points towards a decoupled stability response by increasing the size of the two-phase region, only one point actually reaches this regime. Recalling the large variations in the size of the two-phase region for other turbulent scaling exponents discussed in §4.4.4, no rigorous conclusions can be drawn without further study.

With this in mind, it can however be concluded that (i) turbulence increases the tendency of a decoupled stability response, that (ii) the values of the turbulent scaling exponents determine further details, and that (iii) overall, H I turbulence does not have a strong effect on the decoupling of the stability response.⁹

The Scale Λ_0

In the preceding section, it was pointed out that each point in the turbulent outer region is associated with a unique value of $\Lambda_0 = \ell_0/\ell_{T\star}$, where $\ell_0 = 800$ pc is the measurement scale and $\ell_{T\star} = 2\pi G\Sigma_\star/\kappa^2$ is the stellar Toomre scale unique to each point. Therefore, the value of Λ_0 is (inversely) proportional only to the $\ell_{T\star}$, which varies from point to point.

To determine how variations of $\ell_{T\star}$ affect Λ_0 across the sample, figure 5.6 shows the values of Λ_0 within the three regions (left panel) as well as the histogram of the distribution of Λ_0 (right panel). Additionally, the medians $\text{med}\{\Lambda_0\}$ along with the median absolute deviations $\text{mad}\{\Lambda_0\}$ are indicated figure 5.6 and tabulated in table 5.2 for each region. It can be seen that the data points span almost two orders of magnitude in Λ_0 with a wide peaked concentration of values around $\Lambda_0 \simeq 1$. Also note that, in the inner regions, there is a tendency towards slightly higher values of Λ_0 than in the outer regions.

The fact that the distribution only shows one central (and wide) peak indicates that the median is a suitable representation of the sample. In particular, if the distribution exhibited bimodality with possible skew towards a peak and/or long tails, use of the median is more

⁹This point is motivated by the fact that, while turbulence implies a tendency of points to reach the two-phase region, most points in fact do not.

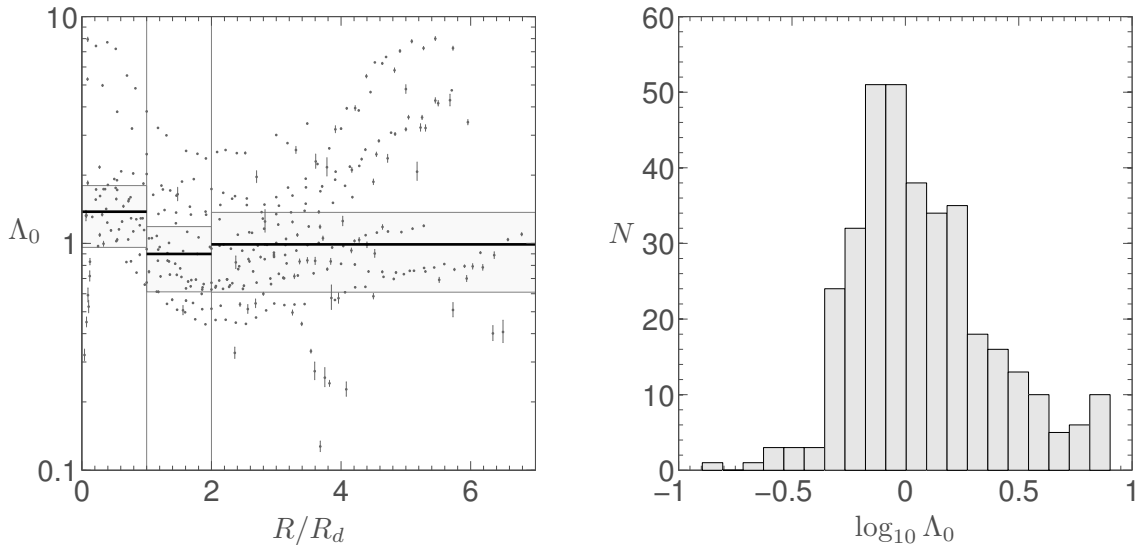


Figure 5.6.: *Left:* Plot of $\Lambda_0 = \ell_0/\ell_{T^*}$ for all data points. For each region, $R \leq R_d$, $R_d < R \leq 2R_d$, and $R > 2R_d$, the median $\text{med}\{\Lambda_0\}$ as well as the median absolute deviation is indicated. *Right:* Histogram of Λ_0 across all data points. The unimodal distribution justifies the use of the median to characterize the sample.

problematic because the median could be at a value that does not occur very often in the distribution and is thus not representative. While this is not the case for Λ_0 , the distributions of Q_{eff} and $\bar{\lambda}$ are somewhat more complicated and the issue shall be discussed again later.

Moreover, note that Λ_0 at small radii tends to be larger than at larger radii. If one focuses the investigation on $R > 2R_d$ — which is the only region where Λ_0 is actually important for computation of the turbulent MSC — the distribution would be even more symmetric since the tail at large Λ_0 would be diminished. As such, use of the median $\text{med}\{\Lambda_0\}$ to illustrate the two-phase region in this range is justified. However, note that the large spread about $\Lambda_0 = 1$ can have a significant effect on the size of the two-phase region, cf. figure 4.9.

Region	$\text{med}\{\Lambda_0\} \pm \text{mad}\{\Lambda_0\}$
$R \leq R_d$	1.38 ± 0.42
$R_d < R \leq 2R_d$	0.90 ± 0.29
$R > 2R_d$	0.99 ± 0.38

Table 5.2.: Median $\text{med}\{\Lambda_0\} = \text{med}\{\Lambda_0\}$ and median absolute deviation $\text{mad}\{\Lambda_0\}$ for the sample in each of the three regions. Note that Λ_0 is not a meaningful quantity in the absence of turbulent scaling.

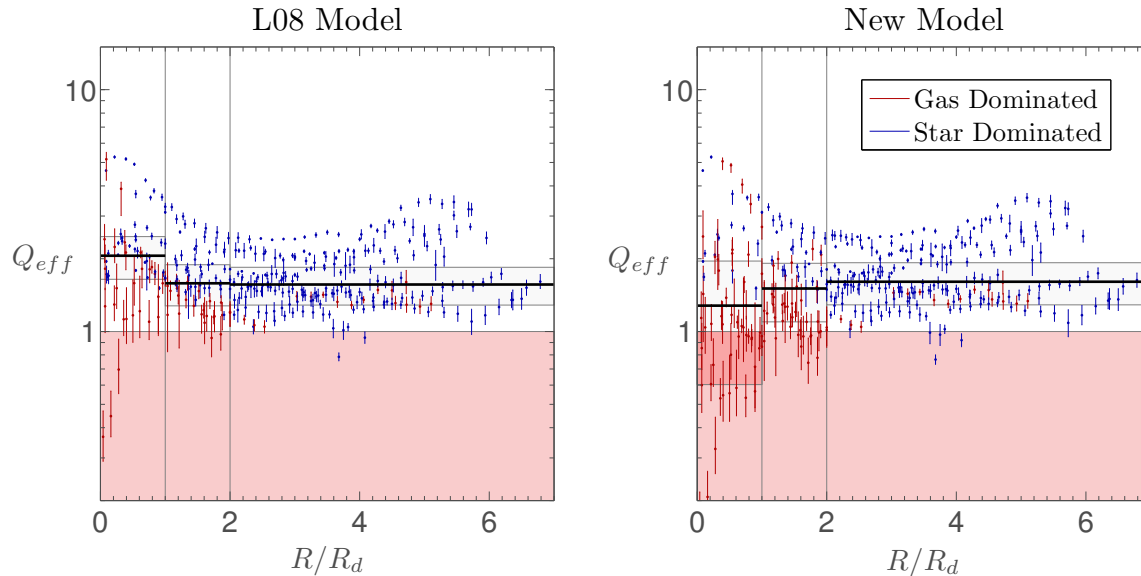


Figure 5.7.: Effective stability parameter Q_{eff} vs. scale-length normalized radius R/R_d with median values and median absolute deviation indicated for each region. Error bars on Q_{eff} mark upper and lower limits. *Left:* Q_{eff} for the original model with constant velocity dispersion $\sigma_g = 11$ km/s in all regions. *Right:* Q_{eff} for the updated model with $\sigma_g = \{5, 8, 11\}$ km/s and turbulent scaling in the outermost region.

5.3.3. Stability Threshold

Recall that the maximum of the marginal stability curve gives the value of Q above which a given system is stable against gravitational collapse on all scales. This is the stability threshold $\max\{Q\} = \bar{Q}$. If the two-component marginal stability curve is computed in terms of the stellar component, let \bar{Q} be the stability threshold, and $Q_\star = \kappa\sigma_\star/(\pi G\Sigma_\star)$ be the Toomre parameter for the stellar component, such that the condition $Q_\star \geq \bar{Q}$ guarantees stability on all scales. This can be rewritten to yield

$$Q_{\text{eff}} \equiv \frac{Q_\star}{\bar{Q}} \geq 1, \quad (5.3)$$

where Q_{eff} is an effective stability parameter similar to the one-component condition $Q \geq 1$.

The left and centre panels of figure 5.7 show Q_{eff} with upper and lower bounds¹⁰ for, respectively, (i) the unmodified (L08) model without turbulence and a constant gas velocity dispersion, and (ii) the modified (New) model gas velocity dispersion adjusted for the dominant component and turbulent scaling in the HI dominant regions. Additionally, the median $\text{med}\{Q_{\text{eff}}\}$ and the median absolute deviation $\text{mad}\{Q_{\text{eff}}\}$ are indicated for each of the three regions, also cf. table 5.3 for a tabulation.

¹⁰It is hereafter implicit that the notion of error refers to the range spanned by the upper and lower bounds derived through a simplified propagation of 1- σ uncertainties provided in L08. For more details, refer to appendix A.

Model	Region	med $\{Q_{\text{eff}}\} \pm \text{mad}\{Q_{\text{eff}}\}$	Change
L08	$R \leq R_d$	2.06 ± 0.41	
L08	$R_d < R \leq 2R_d$	1.58 ± 0.31	
L08	$R > 2R_d$	1.56 ± 0.28	
New	$R \leq R_d$	1.28 ± 0.68	-38%
New	$R_d < R \leq 2R_d$	1.51 ± 0.41	-4%
New	$R > 2R_d$	1.61 ± 0.32	+3%

Table 5.3.: Median med $\{Q_{\text{eff}}\}$ and median absolute deviation mad $\{Q_{\text{eff}}\}$ within the sample for both the original (L08) and modified (New) model. Note that for $R \leq 2R_d$, the sample interpreted with the new model tends to be less stable, while for $R > 2R_d$, the new model describes the sample as more stable.

For both models, one notices that the errors derived on Q_{eff} are larger for $R \lesssim 2R_d$ than for $R \gtrsim 2R_d$. In fact, it seems that the error on Q_{eff} is directly correlated with the location and errors of the points in the $s_0 - q_0$ plane, which means it depends strongly on \bar{Q} . In particular, for $R \leq R_d$, a significant fraction of the points is located at small values of q_0 in the gas-dominated part of the two-phase region, where the contours of \bar{Q} are very closely spaced. Similarly, in the transition region $R_d < R \leq 2R_d$, data points are clustered around the triple point, with points at $q_0 < 1$ being associated with errors that cross more tightly spaced \bar{Q} contours than points located at $q_0 > 1$. For more details, cf. figures 5.4 and 4.10.

Further note from figure 5.1 that Σ_{H_2} is generally found to be subjected to larger errors than Σ_{HI} . In addition to the previously discussed, this further enhances the error associated with H_2 dominated regions.

Similarly to the L08 case discussed in §5.2.3, one sees that only a small number of points is gravitationally unstable $Q_{\text{eff}} < 1$ in both the original and the modified model. Additionally, the median values do not deviate far from med $\{Q_{\text{eff}}\} = 1$, which supports the notion of self-regulation. Also observe that even the modified model accounting for lower gas velocity dispersion in the inner regions and turbulence in HI dominated regions is limited by the lack of a proper description of, for example, magnetic fields, and supernova feedback.

From §4.2.3 and §4.4.1, recall that the response of an infinitely thin two-component system is dominated by the less stable component, i.e. the gaseous component for $Q_g < Q_*$ and the stellar component for $Q_g > Q_*$. Colour-coding the dominating component, one notices that the stellar component dominates the response for most of the data points; particularly for the unmodified model. In fact, this explains the large spread in Q_g previously seen in the left panel of figure 5.2, which suggests that Q_g alone is not a sufficient description of the system if the stability response is dominated by the stellar component. For a more detailed discussion taking into account both infinitely thin and finite-thickness discs, see Romeo & Wiegert (2011).

The behaviour of Q_{eff} with radius differs for both models. In particular, in the original model Q_{eff} has a tendency to decrease towards the transition region and then increase at both larger and smaller radii. For the modified model, on the other hand, Q_{eff} steadily increases with radius. To quantify the difference between the two models better, they are now described for each region.

1. For $R \leq R_d$, the values of Q_{eff} of the modified model are generally smaller than the values of the original model with the median differing by 38%. Recalling that $Q_{\text{eff}} = Q_{\star}/\bar{Q}$, with $Q_{\star} = \kappa\sigma_{\star}/(\pi G\Sigma_{\star})$ being constant across different models, the change in Q_{eff} must be caused by changes in \bar{Q} .

Since a change of s_0 also causes a change in $q_0 = s_0/\alpha_0$, the data points shift along diagonal lines running from the top right towards the bottom left corner of the $s_0 - q_0$ plane, i.e. $s_0 \propto q_0$, for decreasing s_0 . In general, this means that the points are shifted to higher values of \bar{Q} , and thus to lower values of Q_{eff} , cf. figure 4.10. Note, however, that the direction of the \bar{Q} contours differs depending on the location in the $s_0 - q_0$ plane. Consequently, not all shifted data points are subjected to the same changes in \bar{Q} , respectively Q_{eff} .

This means that, while there is a clear tendency towards decreased values of Q_{eff} , not all points are affected in the same fashion. As such, the median $\text{med}\{Q_{\text{eff}}\}$ is expected to decrease while the median absolute deviation — a measure of the scatter about the median — increases.

2. For $R_d < R \leq 2R_d$, the same trend as for $R \leq R_d$ is seen, but much less strongly. This is reasonable as the change in the gas velocity dispersion is smaller than in the innermost region. As such, the data points do not shift as far as for $R \leq R_d$. Again, points are located in regions with different \bar{Q} contours which causes different changes in Q_{eff} , and thus increases the median absolute deviation.
3. For $R > 2R_d$, the overall effect of a turbulent HI component on Q_{eff} is a small increase in the stability level and an increased median absolute deviation. As discussed in the context of the two-phase region, neither s_0 nor q_0 change with the introduction of turbulence such that any change in Q_{eff} must be related to changes in \bar{Q} caused by turbulent scaling.

Since each data point is associated with a value Λ_0 which determines the contours of \bar{Q} , the distribution of Λ_0 is directly related to the distribution of Q_{eff} . From figure 4.11, recall that the \bar{Q} contours are shifted along the positive s_0 axis for $\Lambda_0 \gtrsim 1$. In this case, the turbulent system has a lower stability threshold (and is thus more stable with Q_{eff} increased) than the equivalent non-turbulent system. The reverse holds for $\Lambda_0 \lesssim 1$. Further note that the threshold between the two regimes is actually somewhat lower — approximately about $\Lambda_0 \simeq 0.8$.

Figure 5.6 indicates that Λ_0 is distributed evenly about the median $\text{med}\{\Lambda_0\} \simeq 1$ with a spread of roughly an order of magnitude in either direction. Since the majority of points is associated with $\Lambda_0 \gtrsim 0.8$, there are also more points for which Q_{eff} of the turbulent model is increased than there are points for which it is decreased.

The net effect of describing the HI component as turbulent is thus an increased median $\text{med}\{Q_{\text{eff}}\}$ together with an increased median absolute deviation. As such, it is concluded that, in general, turbulence tends to stabilize the system, but does not do so at all measurement points.

Figure 5.8 shows the histograms of Q_{eff} for the two models (separate rows) in the three regions (separate columns). The horizontal axis shows the logarithm of Q_{eff} and is centered on $Q_{\text{eff}} = 10^0 = 1$.

Comparing the different regions, it can be seen that the values of Q_{eff} are spread out more for $R \leq R_d$ than for the other two regions, where the distribution is contained in a smaller

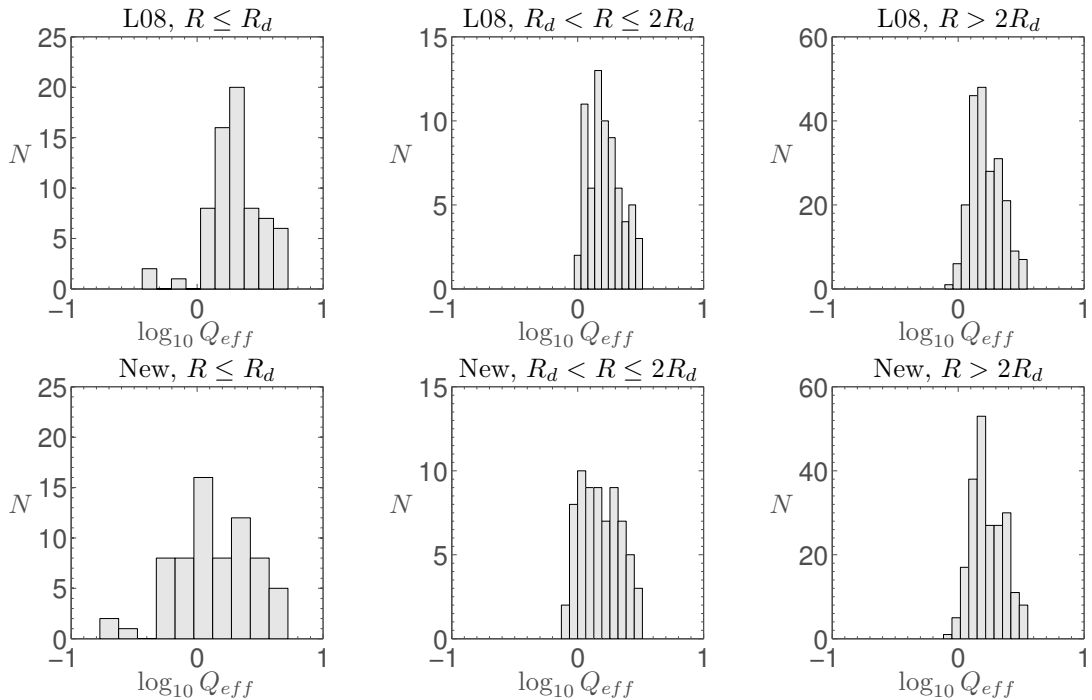


Figure 5.8.: Histogram of Q_{eff} for each of the three regions in the original (L08) and modified (New) models. The horizontal axis shows the logarithm on a linear scale and the data is divided into 10 bins.

range of Q_{eff} with a large central peak. Furthermore, note the apparent fragmentation of some of the histograms, where a secondary high peak is visible next to a low point. This is likely an artifact stemming from the choice of the number of bins.¹¹ To account for this, peaks in the histogram are only considered true peaks if the count in neighbouring bins does not differ too much from the peak count. Due to the small number counts, the choice of whether a peak deviates too much is based on visual perception because the validity of a threshold ratio can not be rigorously proven. Moreover, the potential impact on the quality of the median as a characteristic of the entire sample is evaluated on a case-by-case basis.

In the innermost region, the change of velocity dispersion causes the histogram to spread out towards lower values of Q_{eff} while approximately retaining to maximum value. This checks with the observation of a decreased median and an increased median absolute deviation. In either case, no clear bimodality, skewness or excessively long tail is visible, such that the median is deemed appropriate to describe the distribution.

For $R_d < R \leq 2R_d$, the histogram of the modified model is again wider than for the unmodified model. As before, the lower end of the distribution shifts to lower values, while the upper end remains approximately constant. The original model suggests a slight bimodality with a thin peak at smaller Q_{eff} values than the main peak. In light of the discussion above, the peak could result from unfortunate binning or be real. Either way, visual inspection of the entire histogram suggests that this peak will not affect the median adversely as it is balanced by a wider wing to the right (at higher Q_{eff} values) of the main peak.

¹¹The choice of the number of bins is a delicate point, especially for as small a number of samples as considered here. If too few bins are used, the distribution appears smeared out and features can be lost. On the other hand, if the data is placed in too many bins, the uneven distribution of points might lead to artifacts.

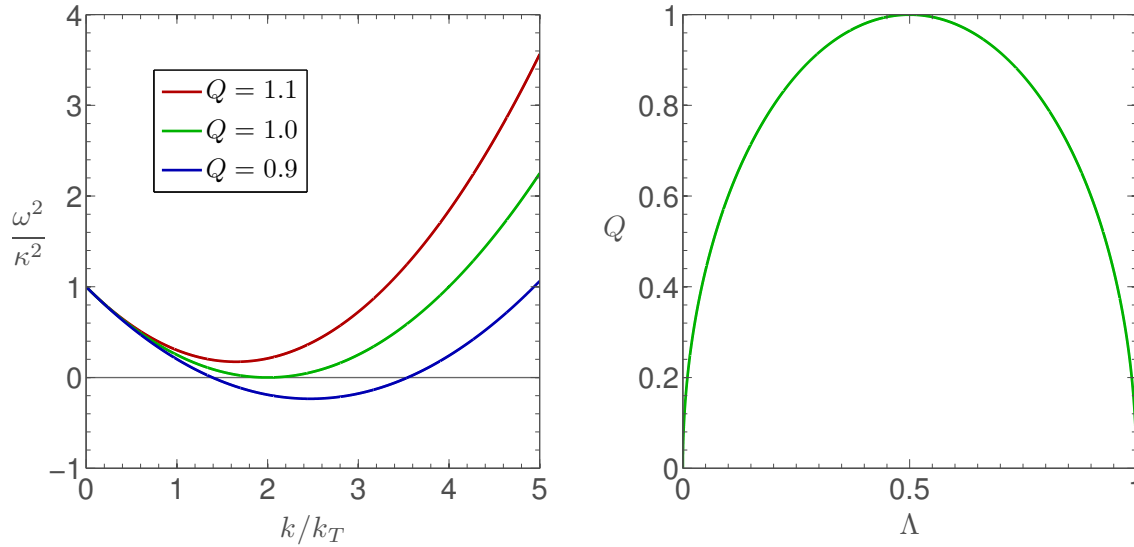


Figure 5.9.: *Left:* Dispersion relation for (i) a stable ($Q = 1.1$), (ii) a marginally stable ($Q = 1$), and (iii) an unstable system ($Q = 0.9$). Note that the minimum k_{\min} is different in each case and only coincides with the most unstable scale \bar{k} for $Q = 1$. *Right:* Marginal stability curve of the system, with the (dimensionless) most unstable scale $\bar{\Lambda} = \bar{\ell}/\ell_T = k_T/\bar{k} = 0.5$ being the scale associated with the stability threshold $\bar{Q} = \max\{Q\} = 1$.

At large radii, both the distribution of the original as well as of the modified turbulent model cover approximately the same range in Q_{eff} with high number counts concentrated towards the central peak. Apart from the central bin, the peak plateau becomes slightly wider with a bias towards larger values of Q_{eff} . Note, however, that the maximum and minimum registered values of Q_{eff} do not change. This indicates that the inclusion of a turbulent HI component tends to spread out Q_{eff} with a slight trend towards larger values. This checks with the observation of an increase in the median and the median absolute deviation, which appear valid descriptors of the distribution in the absence of pronounced skewness, bimodality, or long tails.

5.3.4. Most Unstable Scale

Most Unstable Scale at Marginal Stability

The most unstable scale $\bar{\ell}$ is the scale at which the first instabilities manifest themselves as a system becomes gravitationally unstable. While it was associated with the minimum of the dispersion relation (DR) in §3.3, this is in fact only true for marginally stable systems.

This illustrated in the left panel of figure 5.9, where the DRs for (i) a stable, (ii) a marginally stable, and (iii) an unstable one-component¹² system are shown — $Q = \{1.1, 1.0, 0.9\}$. As the stability level decreases, the wavenumber $k_{\min} = 1/\ell_{\min}$ associated with the minimum of the DR shifts to larger values.

¹²The same considerations hold for two-component systems, but the problem is illustrated much more easily for a one-component system.

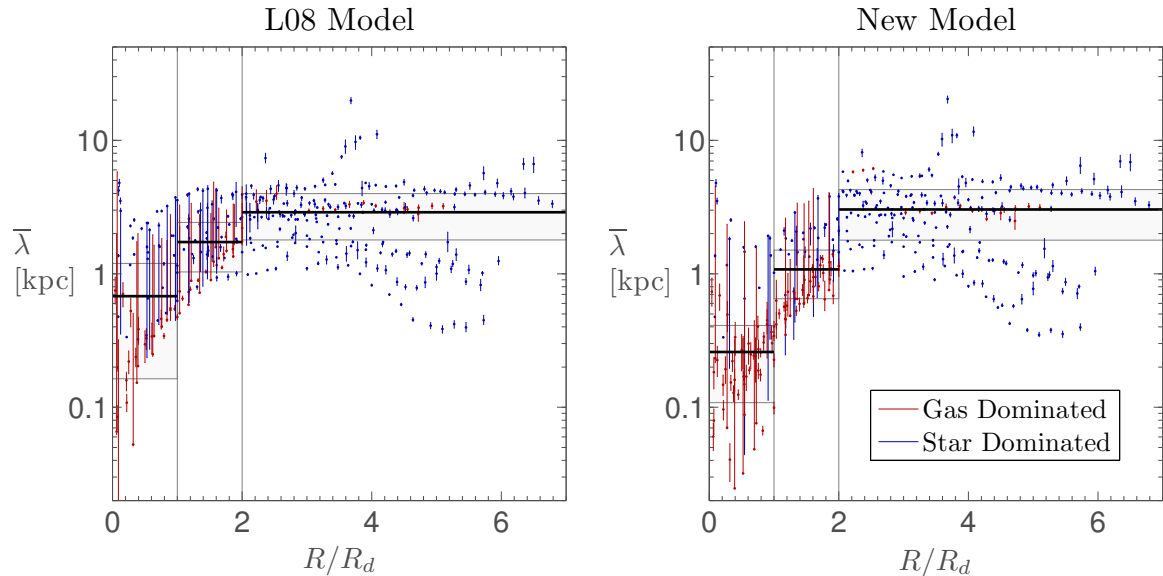


Figure 5.10.: $\bar{\lambda}$ vs. radius R/R_d with median values $\text{med}\{\bar{\lambda}\}$ and median absolute deviation $\text{mad}\{\bar{\lambda}\}$ indicated for each region. Colour-coding indicates the dominant component with respect to stability. *Left*: $\bar{\lambda}$ for the original model with constant velocity dispersion $\sigma_g = 11$ km/s. *Right*: $\bar{\lambda}$ for the updated model with $\sigma_g = \{5, 8, 11\}$ km/s and turbulent scaling in the outermost region.

Using the marginal stability curve, the most unstable scale can be obtained for any system, regardless of its stability level. This is illustrated in the right panel of figure 5.9 where the MSC for the considered one-component system is shown. Recalling that the maximum of the MSC is associated with the (dimensionless) most unstable scale $\bar{\Lambda}$, it holds that

$$\bar{\Lambda} = \frac{\bar{\ell}}{\ell_T} = \left(\frac{\bar{k}}{k_T}\right)^{-1} = \left(\frac{k_{\min}}{k_T}\right)^{-1}, \quad (\text{If Marginally Stable, } Q = 1). \quad (5.4)$$

Recalling from figure 5.7 that most points in the sample are not marginally stable, the most unstable scale is therefore obtained through considering the marginal stability curves. The results are now presented.

Most Unstable Scale in the Sample

Figure 5.10 shows the most unstable wavelengths $\bar{\lambda} = 2\pi\bar{\ell}$ for the considered subsample of 12 spirals. The left panel indicates the wavelengths for the original model used in L08, and the right panel indicates the model modified to account for lower velocity dispersion in the inner regions and turbulent HI in the outer regions. Additionally, the median values $\text{med}\{\bar{\lambda}\}$ and the median absolute deviation are indicated for each region, cf. table 5.4.

Regardless of which model is used to interpret the data, the most unstable wavelength increases with radius. Towards the galactic centres, the most unstable wavelengths are in the order of $\bar{\lambda} \sim 0.1 - 1$ kpc, whereas in the intermediate regions, they are about $\bar{\lambda} \simeq 1$ kpc, until again spanning an order of magnitude $\bar{\lambda} \sim 1 - 10$ kpc beyond $R > 2R_d$. This behaviour is also reflected in the median.

To explain this, recall from figure 5.4 that a significant number of points in the inner and transition region is located (i) at small s_0 and (ii) below the line $q_0 < 1$, where the gaseous component dominates the stability response.¹³ Since this is the part of the $s_0 - q_0$ plane where $\bar{\Lambda}$ is smallest, the corresponding values of $\bar{\lambda}$ are therefore expected to be smallest in this region. The stability of points in the outer regions, however, is for the most part dominated by the stellar component and thus associated with larger values of $\bar{\Lambda}$ — and therefore $\bar{\lambda}$.

Further note that, as for Q_{eff} , points associated with a dominant H_2 component in the inner regions tend to have larger errors than HI dominated points in the outer regions. This is caused by the majority of the points for $R \leq 2R_d$ being located in, or close to, the two-phase region. In particular, if the error in q_0 crosses the transition line, the discontinuous jump from the gaseous peak to the stellar peak (or vice versa) causes a large change in $\bar{\Lambda}$, and therefore $\bar{\lambda}$. Furthermore, Σ_{H_2} is generally associated with larger uncertainties than Σ_{HI} . This, in turn, causes larger uncertainties in points where H_2 dominates.

As before, the effects of modifications to the model are now discussed for each region.

1. For $R \leq R_d$, the most unstable scale $\bar{\lambda}$ for the modified model (where a decreased σ_{0g} causes a decrease of $s_0 = \sigma_{0g}/\sigma_*$) is generally smaller than for the unmodified model with the median of $\bar{\lambda}$ differing by 59%. On the other hand, the decreased median absolute deviation indicates a smaller scatter of the points around the median value.

From figure 4.13, recall that the behaviour of $\bar{\Lambda}$ and thus $\bar{\lambda}$ strongly depends on the location in the $s_0 - q_0$ plane. In general, the largest change in $\bar{\Lambda}$ occurs along lines running diagonally from the top left to bottom right, i.e. $s_0 \propto -q_0$. The only exception to this behaviour is the top left region $q_0 > 1$, $0.05 \leq s_0 \lesssim 0.3$, where the separatrix $\bar{\Lambda} = 0.5$ (i) curves towards $q_0 = 10$ in the non-turbulent model, and (ii) curves back onto the transition line for the turbulent mode.

As before, decreasing the gaseous velocity dispersion decreases s_0 and causes the data points to shift along lines $s_0 \propto q_0$ towards the bottom left of the $s_0 - q_0$ plane. Since most points in the inner regions are clustered in the two-phase region on either side of $q_0 = 1$, the shift causes points to either (i) move along lines almost parallel to $\bar{\Lambda}$ contours with a correspondingly small effect on the values of $\bar{\Lambda}$ associated with these points, or (ii) move across the transition line $q_0 = 1$ from the stellar-dominated region to the gas-dominated regime. In the latter case, the points cross the discontinuity in $\bar{\Lambda}$ that coincides with the transition line. This implies a significant decrease of $\bar{\lambda}$ for these points.

This means that not all points in the inner region change in $\bar{\lambda}$. However, for the points that do, the change is significant. This causes a stark decrease in the median. Since the general trend is a shift towards the bottom left part of the $s_0 - q_0$ this means that fewer points are associated with large values $\bar{\Lambda}_0 > 0.5$ and more of them with small values $\bar{\Lambda} \simeq 0.1$. As such, the median absolute deviation decreases significantly.

2. For $R_d < R \leq 2R_d$, a similar effect is observed, with a smaller decrease in the median and median absolute deviation than in the innermost regions. As before, the points experience a shift towards the lower left of the $s_0 - q_0$ region, thereby either (i) moving along lines of approximately constant $\bar{\Lambda}$, or (ii) crossing the transition line and the discontinuity to much smaller values of $\bar{\Lambda}$.

¹³For a visual impression of the fraction of points dominated in their stability by either the stellar or the gaseous component, refer to the colour-coding in figure 5.10.

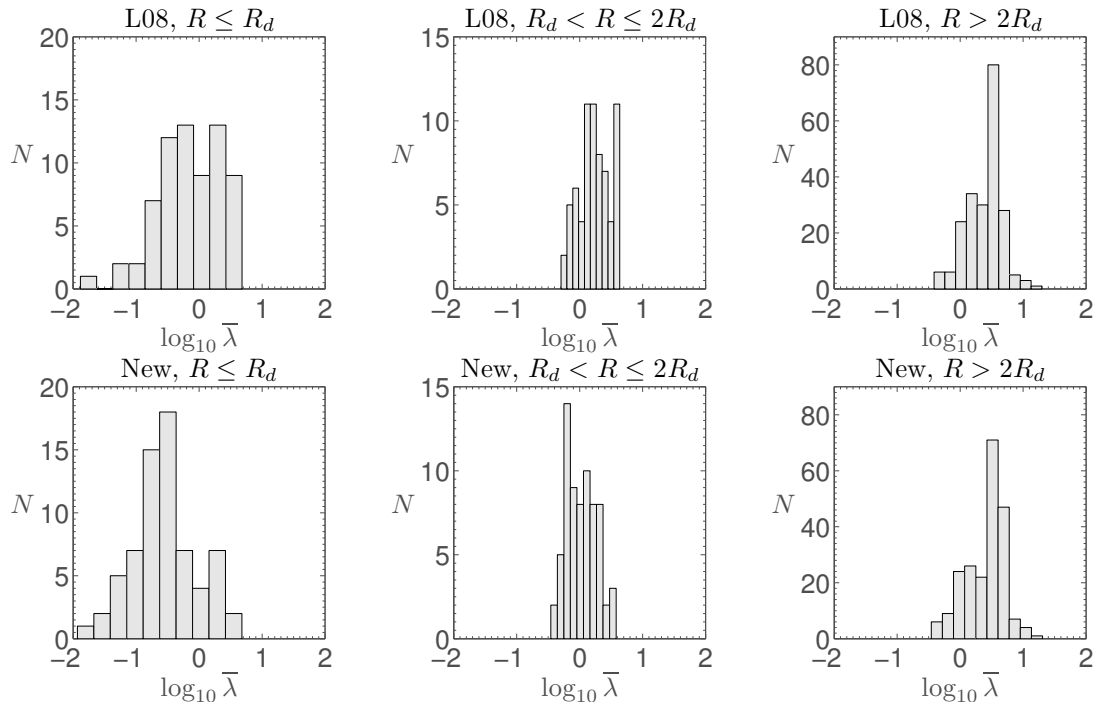


Figure 5.11.: Histograms of $\bar{\lambda}$ for each of the three regions in the original (L08) and modified (New) models. The horizontal axis shows the logarithm on a linear scale and the data is divided into 10 bins.

- For $R > 2R_d$, both the median and the median absolute deviation of $\bar{\lambda}$ increase in the model incorporating a turbulent HI component as compared to the original model. Since most of the points in this region are located in the part of the $s_0 - q_0$ plane where the separatrix $\bar{\Lambda} = 0.5$ of the non-turbulent model shifts back onto the transition line around $q_0 \simeq 1$ in the turbulent model, $\bar{\Lambda}$ for most of the points increases.

On the other hand, for $\Lambda_0 \gtrsim 0.8$, points located at values of $s_0 \gtrsim 0.5$ are in a region where the $\bar{\Lambda}$ contours of the turbulent and non-turbulent systems tend to shift along the positive s_0 axis, thereby decreasing the value of $\bar{\Lambda}$ associated with a point. For $\Lambda_0 \lesssim 0.8$, the reverse holds. Considering the distribution of Λ_0 shown in figure 5.6, note that, for the points not affected by the collapse of the separatrix $\bar{\Lambda} = 0.5$ to the transition line, an approximately equal number of points can be expected to shift to larger and smaller values of $\bar{\Lambda}$ when comparing the turbulent to the non-turbulent system.

The net effect is that tendentially more points are associated with increased values of $\bar{\Lambda}$, but that not all points are affected the same way. As such, the median as well as the median absolute deviation of $\bar{\lambda}$ increases.

Figure 5.11 shows histograms of $\bar{\lambda}$ for the original and modified models (rows) in the three regions (columns). The horizontal axis shows the logarithm and is centered on $\bar{\lambda} = 10^0 = 1$.

Compared to the transition and outer regions, $\bar{\lambda}$ is distributed over a much larger range in the inner regions. This checks with the fact that in this region, data points are located on either side of the transition line, whereby a wide range of $\bar{\Lambda}$ is covered. On the other hand, in the transition and outer regions, data points are further away from the two-phase region and thus the transition line, such that the distribution is limited to a narrower range of $\bar{\lambda}$.

Model	Region	$\text{med}\{\bar{\lambda}\} \pm \text{mad}\{\bar{\lambda}\}$ [kpc]	Change
L08	$R \leq R_d$	0.68 ± 0.52	
L08	$R_d < R \leq 2R_d$	1.73 ± 0.70	
L08	$R > 2R_d$	2.89 ± 1.10	
New	$R \leq R_d$	0.26 ± 0.15	-59%
New	$R_d < R \leq 2R_d$	1.10 ± 0.43	-36%
New	$R > 2R_d$	3.03 ± 1.24	+5%

Table 5.4.: Median $\text{med}\{\bar{\lambda}\}$ and median absolute deviation $\text{mad}\{\bar{\lambda}\}$ of the most unstable wavelength $\bar{\lambda}$ for the original (L08) and modified (New) model. For the new model, the median is decreased for $R \leq 2R_d$, and increased otherwise.

In the inner region, the decreased gas velocity dispersion causes the histogram to widen towards smaller values of $\bar{\lambda}$ while at the same time retaining the upper limit. The comparatively flat two-peaked distribution centered around $\bar{\lambda} \simeq 1$ kpc of the original model gives way to a distribution centered around a single peak at $\bar{\lambda} \simeq 10^{-0.8}$ kpc $\simeq 0.2$ kpc. Note that since neither distribution shows a pronounced skew or long tail, the median characterizes them well.

In the transition region, the widening of the histogram of the modified model as compared the original model is present, but much less pronounced than in the inner regions. The tendency of $\bar{\lambda}$ shifting to lower values is nevertheless clearly visible when considering the rightmost single bin peak in the original case, which disappears for the modified system, where instead the counts for lower values of $\bar{\lambda}$ are increased. Note that, visually, the distribution seems erratic with single bin peaks directly next to bins with much lower counts. This could either (i) indicate that too many bins are chosen, or that (ii) the distribution displays little regularity. In the latter case, the choice of the median as a representative value for the distribution might overemphasize parts of the sample.

In the outer region, there is no difference in the width of histogram when comparing the original and the modified model. This means that the width of values spanned by $\bar{\lambda}$ does not change. Instead, only the distribution within the spanned range changes. In particular, note that the heights of all bins to (and including) the left (i.e. at smaller values of $\bar{\lambda}$) of the highest bin decrease whereas the height of the bin immediately to the right of the highest bin increases.

Naively, one might conclude that this suggests that a wide range of values is mapped to approximately the same larger value. However, note that bins to the left cover a smaller range in $\bar{\lambda}$ than bins to the right because of the logarithmic scale. As such, the conclusion is of questionable validity. Proper consideration of this effect would require a histogram linear in $\bar{\lambda}$ with the size of the bins given by the smallest size of the bins. This, however, would yield a bin size too small to adequately categorize a sample as small as the present, cf. also the previous discussion in §5.3.3.

5.3.5. Tight-Winding Condition

The tight-winding condition $kR \gg 1$ discussed in §3.2 is the principal assumption that validates the stability analysis performed in this work. As such, the wavelengths associated with the most important scales of interest must fulfil this criterion. In the context of star formation,

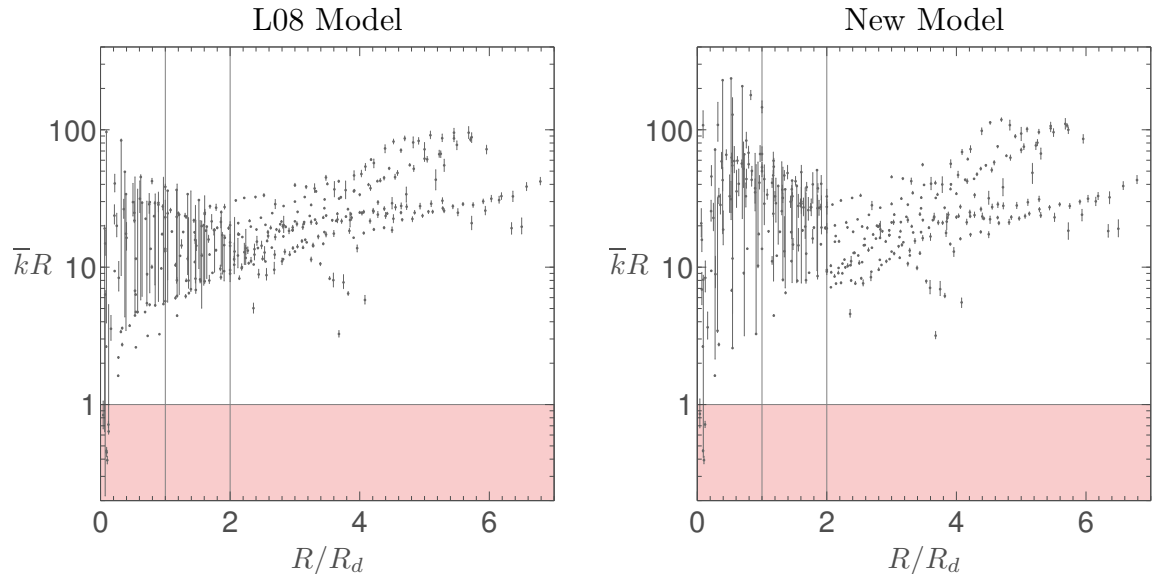


Figure 5.12.: Plot of $\bar{k}R$ vs. normalized radius to check whether the tight-winding condition $\bar{k}R \gg 1$ is fulfilled. The shading indicates the region where $\bar{k}R \leq 1$, such that the tight-winding condition is definitely not fulfilled.

the most unstable wavelength $\bar{\lambda}$ is the principal quantity of interest. The condition that must be fulfilled is thus

$$\bar{k}R \gg 1, \quad (5.5)$$

where $\bar{k} = 2\pi/\bar{\lambda}$ is the most unstable wavenumber, and R the galactocentric radius of a given data point.

Figure 5.12 shows the quantity $\bar{k}R$ as a function of radius across the subsample of 12 spiral galaxies. It can clearly be seen that the condition is fulfilled for the largest part of the sample in both the transition and outer regions. On the other hand, in the inner region, data points tend to fall to within an order of magnitude of $\bar{k}R = 1$ with a few even falling below this line.

While the analysis is technically invalid for these points, it still retains validity in a statistical sense across the entire sample. Therefore, these points are not removed from the sample.

5.4. Chapter Summary

After defining the star formation problem and briefly recapping a previous analysis of 12 nearby spiral and 11 nearby dwarf galaxies (Leroy et al., 2008), the theory introduced in §3 and further developed in §4 was applied to observations of the 12 nearby spiral galaxies also considered in Leroy et al. (2008). The most important points are now summarized.

- The conditions required for protostellar cores to form define the star formation problem on galactic scales. Any investigation therefore requires knowledge of (i) present sites of star formation as traced by the brightest stars with the shortest lifetimes and emissions from dust heated by young stars, (ii) the distribution of atomic and molecular hydrogen

on both galactic and sub-kpc scales, and (iii) the present distribution of stars. A number of recent surveys share a common subset of nearby star forming galaxies for which such data is available.

Leroy et al. (2008) aggregates this data, derives radial profiles for various quantities, and then carries out a comprehensive analysis focusing the star formation laws and thresholds. The sampled galaxies are divided a spiral and dwarf subsample, depending on total mass, luminosity and peak rotation velocity.

- To perform this analysis, several assumptions are made. Among others, (i) a fixed gaseous velocity dispersion of $\sigma_g = 11$ km/s is chosen independent of radius for all galaxies, (ii) a constant CO-to-H₂ conversion factor is adopted, (iii) the stellar velocity dispersion is derived from the stellar surface density under the assumptions of constant scale height and hydrostatic equilibrium.

While these are well-motivated and simple choices suitable as a first approximation, they can nevertheless be improved on. In particular, assumption (i) is likely an overestimate of σ_g in H₂ dominated regions where it overestimates the stability level, assumption (ii) likely overestimates H₂ mass in H₂ dominated regions, thereby underestimating the stability level, and assumption (iii) is likely a problematic estimate of the stellar velocity dispersions because the coupling between the stellar and gaseous discs is neglected.

In particular, problems associated with the CO-to-H₂ conversion factor in dwarf galaxies force a disregarding of the H₂ component in this subsample. To avoid problems, the dwarf subsample is thus not considered in this work.

- It is found that the H₂ and stellar surface densities decline exponentially with radius, while HI surface density remains approximately constant. This suggests separation of the sample into three radial regions: (i) the inner H₂ dominated region, (ii) the transition region, and (iii) the outer HI dominated region. In the H₂ and transition regions, the star formation rate per unit gas mass remains approximately constant, whereas it declines exponentially in the outer HI dominated regions.
- After separating the model into three distinct regions, the gas velocity dispersion is modified depending on the dominant gas component. In particular, in the inner H₂ dominated region, a velocity dispersion of $\sigma_g = 5$ km/s is adopted, whereas a value of $\sigma_g = 8$ km/s is chosen in the transition regime. In the outer HI dominated regions, $\sigma_g = 11$ km/s is retained, but turbulent scaling with $a_g = b_g = 1/3$ is introduced.

Turbulent scaling is not introduced in the inner and the transition region because (i) H₂ is not turbulent on the resolution scale $\ell_0 = 800$ pc, and (ii) a suitable three-component model to describe the transition region properly is unavailable.

- When placing both the dwarf and the spiral subsample in the $s_0 - q_0$ plane, it is found that the dwarf sample is significantly removed from the spiral sample. However, upon removing the H₂ contribution from the spiral galaxies, the data points are shifted into the same region. Again, this indicates that there is a significant amount of undetected H₂ in the dwarf galaxies and further justifies the choice of not considering them in this analysis.
- Considering the spiral galaxies separated into three regions, both with and without the aforementioned modifications to the model, it is found that points in the inner H₂ dominated regions tend to be found in the two-phase region, whereas points associated with larger radii are usually not found in the two-phase region. This suggests a link

between the decoupling of the stability response and the H_2 surface density, and thus the star formation rate per unit gas.

Comparing the two models, lowering the velocity dispersion causes the points in both the inner and the transition region to move further towards the two-phase region. However, especially in the innermost region, a significant portion of the data points violates the lower limit $s_0 \leq 0.05$, which suggests a problem with associating such a velocity dispersion with the gaseous component. In particular, it is possible that the overestimated stellar velocity dispersion balances the overestimate of the gaseous velocity dispersion. A proper analysis of this problem is deferred to future work.

In the outer regions, the introduction of a turbulent HI component reveals a general trend of a points in a turbulent medium to migrate towards the two-phase region. However, only one data point actually enters the two-phase region. As such, the influence of turbulence does not appear to significantly alter the stability properties with regards to decoupling.

- The effective Toomre parameter Q_{eff} is used as a stability diagnostic of two-component discs. Compared to the stability parameter based on the gaseous component alone, Q_{eff} shows a much smaller spread in values and is generally closer to marginal stability. This supports the notion of self-regulation in coupled stellar and gaseous discs.

When reducing the velocity dispersion in the inner and transition regions, Q_{eff} expectedly drops, thereby causing a number of points to enter the unstable regime. In the outer regions, introduction of a turbulence HI component increases Q_{eff} , thereby stabilising the systems. However, note that this general trend does not affect all measurement points.

Further note that Q_{eff} is affected by significant errors, especially in the inner regions of the galaxies. This is caused predominantly by (i) larger errors in the H_2 surface density as compared to the HI surface density and (ii) the behaviour of the \bar{Q} contours in the $s_0 - q_0$ plane.

- The concept of the most unstable wavelength as the wavelength at which instabilities are first manifested is clarified to apply only to marginally stable systems. As such, for systems not at marginal stability, it is obtained by considering the marginal stability curve instead of the dispersion relation.

For both the unmodified and the modified model, the most unstable wavelength is found to increase with galactocentric radius from sub-kpc ranges in the inner regions to $\bar{\lambda} \simeq 3$ kpc in the outer regions. Decreasing the gaseous velocity dispersion below $R \leq 2R_d$, it is found to further decrease $\bar{\lambda}$. On the other hand, introducing turbulence in the outer regions shifts $\bar{\lambda}$ to larger values. As with Q_{eff} , this is a general trend not followed by all points.

- The tight-winding condition is checked with respect to the most unstable wavelength and found to be fulfilled for most, but not all, data points. However, the number of data points for which the condition is violated is small enough such that the condition is still fulfilled across the entire sample in a statistical sense. As such, the violating data points are not removed from the sample.

CONCLUSIONS

In this thesis, we have used two-component models of gravitational instability to investigate the dynamical properties of two types of discs under the influence of turbulence. In particular, we have considered (i) a disc of neutral atomic hydrogen (HI) and molecular hydrogen (H_2) on scales $\ell \lesssim 100$ pc, and (ii) a disc of neutral atomic hydrogen and stars on scales $\ell \gtrsim 1$ kpc. We then applied the latter model to extend a previous analysis by Leroy et al. (2008). In §6.1, we first discuss the major conclusions drawn from this work and then point out topics for further investigation in §6.2.

Note that we have neglected effects of disc thickness in this work. For an investigation of thickness effects on the sample analysed by Leroy et al. (2008), we refer to Wiegert (2010) and Romeo & Wiegert (2011).

6.1. Conclusions

We use a phenomenological model of turbulence introduced by Romeo et al. (2010), where surface density Σ and velocity dispersion σ follow power laws $\Sigma \propto \ell^a$ and $\sigma \propto \ell^b$. These are motivated by the size-linewidth relation of giant molecular clouds (Larson, 1981; Solomon et al., 1987; Bolatto et al., 2008; Hughes et al., 2010) and power spectra of 21 cm line intensity (Begum et al., 2006; Dutta et al., 2008, 2009a,b). For the power law exponents, we adopt $(a_{\text{H}_2}, b_{\text{H}_2}) = (0, 1/2)$ for molecular hydrogen and $(a_{\text{HI}}, b_{\text{HI}}) = (1/3, 1/3)$ for neutral atomic hydrogen, which are choices consistent with results obtained from observations and simulations (Romeo et al., 2010). Further noting that the collisionless stellar component is not turbulent, our findings based on this model are now discussed.

- Clearly, the gravitational stability of a two-component disc depends on the stability of both components. However, the contribution of each component may differ.

Assuming that H_2 is bound in virialized structures, we find that the type of gravitational stability of a disc of HI and H_2 is determined by the stability of H_2 alone. Regardless of the type of stability, we further find that H_2 dominates the stability properties of the disc.

For a disc of HI and stars, we find no such disparity. Regardless of the stability of either component, the type of stability of the entire disc does not change. However, do note that (i) the stability of the disc can be dominated by either component, and that (ii) the dynamic response of the two components can become decoupled (Bertin & Romeo, 1988).

- The three most important characteristics of two-component gravitational instability are (i) the region in the parameter space where the dynamic response of the individual components decouples, (ii) the wavelength $\bar{\lambda}$ associated with the onset of instabilities, and (iii) a diagnostic $Q_{\text{eff}} \geq 1$ to determine if the disc is gravitationally stable. The latter is based upon an generalization of the Toomre criterion $Q \geq 1$ for the stability of a thin one-component disc (Toomre, 1964).
- Within the sample of galaxies first analysed by Leroy et al. (2008), turbulence in HI tends to (i) increase the region in the parameter space where stars are dynamically decoupled from HI, (ii) increase the median wavelength $\bar{\lambda}$ by 5% from 2.89 kpc to 3.03 kpc, and (iii) stabilize the disc by increasing the median of Q_{eff} by 3% from 1.56 to 1.61.
- To understand the influence of the gas velocity dispersion σ_g in regions where the density of H₂ exceeds (or is similar to) that of HI, we decrease the initial value of $\sigma_g = 11$ km/s to values of $\sigma_g = 5$ km/s (respectively $\sigma_g = 8$ km/s). We find that this tends to (i) decouple the dynamical response of the stellar and gaseous components in a larger part of the sample, (ii) decrease the median wavelength $\bar{\lambda}$ by 62% from 0.68 kpc to 0.26 kpc (36% from 1.73 kpc to 1.10 kpc), and (iii) destabilize the disc by decreasing the median of Q_{eff} by 38% from 2.06 to 1.28 (4% from 1.58 to 1.51).

Finally, we note that for the original model, 19% of all measurements have a gas dominated dynamic response. In the modified model, this percentage increases to 30%.

6.2. Topics for Further Investigation

- The analysis of nearby spiral galaxies carried out by Leroy et al. (2008) is based on state-of-the-art observations and is the among the most detailed investigations of star formation in nearby galaxies to date. However, as pointed out by the author, lacking observations of stellar velocity dispersions force it to rely on a simple model to derive them. We therefore suggest that follow-up observations of the stellar velocity dispersion could greatly benefit the accuracy of both the original analysis and our turbulent extensions.
- An in-depth investigation of gravitational instability in (turbulent) galactic discs requires a three-component model accounting for the contributions of the (i) stellar population, (ii) neutral atomic hydrogen (HI), and (iii) molecular hydrogen (H₂). Due to the complexity of such a model, a prior understanding of the subsystems is of great benefit.

While this work has focused on the stability of a disc of gas and stars, investigating a disc of HI and H₂ is more demanding. In particular, the different types of gravitational stability governing such a disc are the chief difficulty. We therefore suggest a more detailed investigation of the stability properties of a disc of HI and H₂.

COMPUTATION OF MODEL PARAMETERS AND STABILITY DIAGNOSTICS

The model of turbulence used in this thesis is described in terms of (i) the stability threshold \bar{Q} , (ii) the most unstable scale $\bar{\Lambda}$, (iii) an effective Toomre parameter Q_{eff} , and (iv) the most unstable wavelength $\bar{\lambda}$. These are computed based on the parameters s_0 , q_0 , and Λ_0 . To apply the model to the galaxies previously analysed in Leroy et al. (2008), the stability diagnostics are calculated from the physical quantities provided therein.

In this appendix, §A.1 outlines the physical quantities provided, whereafter §A.2 describes how the model parameters are computed from them. Finally, §A.3 shows how the stability diagnostics are calculated from these parameters.

Calculated values of the model properties and stability diagnostics are tabulated as radial profiles in appendix B for the sample of spiral galaxies considered in this thesis.

A.1. Physical Quantities

Leroy et al. (2008) provides a wide range of physical quantities for the sampled galaxies. For a detailed account how these are derived from observations, refer to appendices A – D in Leroy et al. (2008). All quantities are given with $1 - \sigma$ errors and the most relevant are

- H I Surface Density — Σ_{HI} ,
- H₂ Surface Density — Σ_{H_2} ,
- Stellar Surface Density — Σ_{\star} ,
- Stellar Velocity Dispersion — σ_{\star} ,
- Gaseous Velocity Dispersion (Assumed Constant) — $\sigma_g = 11$ km/s.

A.2. Model Parameters

Using the physical quantities described in §A.1, the model parameters s_0 , q_0 , and Λ_0 along with a simple error estimates are computed as follows. With the given $1 - \sigma$ error written as ε ,

and denoting upper and lower bounds for a quantity X as $X_+ = X + \varepsilon_X$ and $X_- = X - \varepsilon_X$,¹ one obtains

$$s_0 = \frac{\sigma_g}{\sigma_\star}, \quad s_{0+} = \frac{\sigma_g}{\sigma_{\star-}}, \quad s_{0-} = \frac{\sigma_g}{\sigma_{\star+}}, \quad (\text{A.1})$$

$$q_0 = \frac{\sigma_g \Sigma_\star}{\sigma_\star \Sigma_{0g}}, \quad q_{0+} = \frac{\sigma_g \Sigma_{\star+}}{\sigma_{\star-} \Sigma_{0g-}}, \quad q_{0-} = \frac{\sigma_g \Sigma_{\star-}}{\sigma_{\star+} \Sigma_{0g+}}, \quad (\text{A.2})$$

and

$$\Lambda_0 = \frac{\ell_0}{\ell_{T\star}}, \quad \Lambda_{0+} = \frac{\ell_0}{\ell_{T\star-}}, \quad \Lambda_{0-} = \frac{\ell_0}{\ell_{T\star+}}, \quad (\text{A.3})$$

where the subscript on X_0 indicates quantities measured at scale ℓ_0 , where $\ell_0 = 800$ pc for the spiral galaxies and $\ell_0 = 400$ pc for the dwarf galaxies. The stellar Toomre-scale is

$$\ell_{T\star} = \frac{2\pi G \Sigma_\star}{\kappa^2}, \quad \ell_{T\star+} = \frac{2\pi G \Sigma_{\star+}}{\kappa^2}, \quad \ell_{T\star-} = \frac{2\pi G \Sigma_{\star-}}{\kappa^2}, \quad (\text{A.4})$$

where G is the gravitational constant and κ is epicyclic frequency at radius R given as (Binney & Tremaine, 2008, Eq. 3.80)

$$\kappa^2(R) = R \frac{d\Omega^2}{dR} + 4\Omega^2, \quad (\text{A.5})$$

with the angular velocity $\Omega = v_{\text{rot}}(R)/R$ obtained from the rotation curve

$$v_{\text{rot}}(R) = v_{\text{flat}} \left[1 - \exp\left(\frac{-R}{l_{\text{flat}}}\right) \right], \quad (\text{A.6})$$

where l_{flat} and v_{flat} are given for the galaxies in Leroy et al. (2008).

A.3. Stability Diagnostics

A.3.1. Effective Stability Parameter, Most Unstable Wavelength

The effective stability parameter Q_{eff} , most unstable wavelength $\bar{\lambda}$, and their upper and lower bounds are calculated as

$$Q_{\text{eff}} = \frac{Q_\star}{Q}, \quad Q_{\text{eff}+} = \frac{Q_{\star+}}{Q_-}, \quad Q_{\text{eff}-} = \frac{Q_{\star-}}{Q_+}, \quad (\text{A.7})$$

¹In fact, $X_- = \max\{0, X - \varepsilon_X\}$ to ensure positive quantities. Where required, further checks are implemented in the code to avoid division by 0.

and

$$\bar{\lambda} = \bar{\Lambda} 2\pi\ell_{T\star}, \quad \bar{\lambda}_+ = \bar{\Lambda}_+ 2\pi\ell_{T\star+}, \quad \bar{\lambda}_- = \bar{\Lambda}_- 2\pi\ell_{T\star-}. \quad (\text{A.8})$$

,

where the stellar Toomre scale is as given in (A.4) and the stellar Toomre parameter is

$$Q_\star = \frac{\kappa\sigma_\star}{\pi G\Sigma_\star}, \quad Q_{\star+} = \frac{\kappa\sigma_{\star+}}{\pi G\Sigma_{\star-}}, \quad Q_{\star-} = \frac{\kappa\sigma_{\star-}}{\pi G\Sigma_{\star+}}, \quad (\text{A.9})$$

with epicyclic frequency κ previously given in (A.5).

A.3.2. Stability Threshold, Most Unstable Scale

The stability threshold \bar{Q} and most unstable scale $\bar{\Lambda}$ are computed numerically from the marginal stability curve. In particular, consider the curve

$$Q = Q(\Lambda, s_0, q_0, \Lambda_0, a_g, b_g), \quad (\text{A.10})$$

where $0 \leq \Lambda \leq \Lambda_{\text{Zero}}$ is the domain where $Q^2 \geq 0$ (such that $Q \in \mathbb{R}$). The stability parameters are s_0 , q_0 , and Λ_0 , and a_g and b_g are the power law exponents of the turbulent gas component (e.g. $a_g = b_g = 1/3$ for neutral atomic hydrogen). Note that the upper limit in Λ where $Q^2 \geq 0$ is a real solution $\Lambda_{\text{Zero}} \in \mathbb{R}$ of

$$0 = 1 + \frac{s_0}{q_0} \Lambda_{\text{Zero}}^{a_g} \Lambda_0^{-a_g} - \Lambda_{\text{Zero}}. \quad (\text{A.11})$$

Setting $a_g = b_g = 1/3$, evaluation of $Q^2 = Q^2(\Lambda, \Lambda_0, s_0, q_0)$ in the range $0 \leq \Lambda \leq \Lambda_{\text{Zero}}$ allows numerical location of all (at most two) maxima. The (square root of the) largest maximum gives the stability threshold \bar{Q} and is found at the most unstable scale $\bar{\Lambda}$.

Determination of \bar{Q}_+ , \bar{Q}_- , $\bar{\Lambda}_+$, and $\bar{\Lambda}_-$ requires further evaluations of the marginal stability curve. In particular, calculating $Q^2 = Q^2(\Lambda, \Lambda_0, s_0, q_0)$ with all $3^3 = 27$ possible combinations of $\{s_0, s_{0+}, s_{0-}\}$, $\{q_0, q_{0+}, q_{0-}\}$, and $\{\Lambda_0, \Lambda_{0+}, \Lambda_{0-}\}$ and subsequent location of the maxima gives the bounds for \bar{Q} and $\bar{\Lambda}$.

Note that the choice of discretization in Λ is a delicate matter. Generally, sampling Λ at $N \sim 10^3$ logarithmically spaced points is sufficient. However, if the contour $\bar{\Lambda} = 0.5$ is to be computed, mitigation of numerical instabilities requires a denser sampling of at least $N \sim 10^5$ linearly spaced points.

RADIAL PROFILES OF MODEL PARAMETERS AND STABILITY DIAGNOSTICS

In this appendix, radial profiles of the model parameters s_0 , q_0 , Λ_0 and the stability diagnostics Q_{eff} and $\bar{\lambda}$ are tabulated for the sample of 12 spiral galaxies. Refer to appendix A for details on how these values are computed. For tabulations of physical quantities Σ_* , Σ_{HI} , Σ_{H_2} , and σ_* , refer to Leroy et al. (2008).

Odd numbered tables contain model parameters and even numbered tables stability diagnostics. For a given galaxy, these are placed side-by-side across two pages beginning on the next page.

Note that quantities are unitless unless indicated.

Table B.1.: Model Parameters of NGC0628.

R [kpc]	R/R_d	Λ_0	$\sigma_g = 5$ km/s		$\sigma_g = 8$ km/s		$\sigma_g = 11$ km/s	
			s_0	q_0	s_0	q_0	s_0	q_0
0.2	0.1	$5.30^{+0.08}_{-0.08}$	$0.03^{+0.00}_{-0.00}$	$1.47^{+0.13}_{-0.12}$			$0.07^{+0.00}_{-0.00}$	$3.24^{+0.29}_{-0.26}$
0.5	0.2	$7.43^{+0.06}_{-0.06}$	$0.04^{+0.00}_{-0.00}$	$1.09^{+0.10}_{-0.09}$			$0.10^{+0.00}_{-0.00}$	$2.40^{+0.22}_{-0.19}$
0.9	0.4	$7.71^{+0.02}_{-0.02}$	$0.06^{+0.00}_{-0.00}$	$0.97^{+0.10}_{-0.08}$			$0.13^{+0.00}_{-0.00}$	$2.14^{+0.21}_{-0.18}$
1.2	0.5	$7.21^{+0.02}_{-0.02}$	$0.07^{+0.00}_{-0.00}$	$0.99^{+0.08}_{-0.07}$			$0.15^{+0.00}_{-0.00}$	$2.18^{+0.19}_{-0.16}$
1.6	0.7	$5.50^{+0.01}_{-0.01}$	$0.07^{+0.00}_{-0.00}$	$0.95^{+0.10}_{-0.08}$			$0.16^{+0.00}_{-0.00}$	$2.09^{+0.22}_{-0.18}$
1.9	0.8	$4.83^{+0.02}_{-0.02}$	$0.08^{+0.00}_{-0.00}$	$0.84^{+0.09}_{-0.08}$			$0.18^{+0.00}_{-0.00}$	$1.84^{+0.21}_{-0.17}$
2.3	1.0	$3.82^{+0.02}_{-0.02}$	$0.09^{+0.00}_{-0.00}$	$0.75^{+0.12}_{-0.09}$			$0.19^{+0.00}_{-0.00}$	$1.65^{+0.26}_{-0.20}$
2.7	1.2	$3.23^{+0.01}_{-0.01}$			$0.15^{+0.00}_{-0.00}$	$1.11^{+0.20}_{-0.15}$	$0.20^{+0.00}_{-0.00}$	$1.53^{+0.27}_{-0.20}$
3.0	1.3	$3.00^{+0.01}_{-0.01}$			$0.16^{+0.00}_{-0.00}$	$1.14^{+0.18}_{-0.14}$	$0.22^{+0.00}_{-0.00}$	$1.56^{+0.25}_{-0.19}$
3.4	1.5	$1.65^{+0.12}_{-0.11}$			$0.13^{+0.00}_{-0.00}$	$1.48^{+0.39}_{-0.29}$	$0.18^{+0.01}_{-0.01}$	$2.03^{+0.54}_{-0.40}$
3.7	1.6	$2.56^{+0.01}_{-0.01}$			$0.18^{+0.00}_{-0.00}$	$1.10^{+0.22}_{-0.16}$	$0.25^{+0.00}_{-0.00}$	$1.51^{+0.31}_{-0.22}$
4.1	1.8	$2.48^{+0.01}_{-0.01}$			$0.20^{+0.00}_{-0.00}$	$0.98^{+0.23}_{-0.16}$	$0.27^{+0.00}_{-0.00}$	$1.35^{+0.31}_{-0.22}$
4.4	1.9	$2.37^{+0.02}_{-0.02}$			$0.21^{+0.00}_{-0.00}$	$0.96^{+0.21}_{-0.15}$	$0.29^{+0.00}_{-0.00}$	$1.31^{+0.29}_{-0.20}$
4.8	2.1	$2.53^{+0.01}_{-0.01}$					$0.33^{+0.00}_{-0.00}$	$1.29^{+0.26}_{-0.19}$
5.1	2.2	$2.58^{+0.01}_{-0.01}$					$0.35^{+0.00}_{-0.00}$	$1.29^{+0.26}_{-0.19}$
5.5	2.4	$2.50^{+0.01}_{-0.01}$					$0.37^{+0.00}_{-0.00}$	$1.30^{+0.26}_{-0.19}$
5.8	2.5	$2.51^{+0.03}_{-0.03}$					$0.39^{+0.00}_{-0.00}$	$1.33^{+0.23}_{-0.18}$
6.2	2.7	$1.96^{+0.13}_{-0.11}$					$0.37^{+0.01}_{-0.01}$	$1.60^{+0.31}_{-0.25}$
6.5	2.8	$1.25^{+0.16}_{-0.13}$					$0.31^{+0.02}_{-0.02}$	$1.87^{+0.51}_{-0.40}$
6.9	3.0	$3.01^{+0.02}_{-0.02}$					$0.51^{+0.00}_{-0.00}$	$1.13^{+0.08}_{-0.07}$
7.3	3.2	$2.77^{+0.01}_{-0.01}$					$0.52^{+0.00}_{-0.00}$	$1.14^{+0.08}_{-0.07}$
7.6	3.3	$2.58^{+0.10}_{-0.09}$					$0.52^{+0.01}_{-0.01}$	$1.19^{+0.17}_{-0.14}$
8.0	3.5	$3.38^{+0.03}_{-0.03}$					$0.63^{+0.00}_{-0.00}$	$1.07^{+0.11}_{-0.09}$
8.3	3.6	$2.30^{+0.18}_{-0.16}$					$0.54^{+0.02}_{-0.02}$	$1.34^{+0.29}_{-0.24}$
8.7	3.8	$2.17^{+0.23}_{-0.19}$					$0.55^{+0.03}_{-0.02}$	$1.39^{+0.34}_{-0.27}$
9.0	3.9	$3.19^{+0.12}_{-0.11}$					$0.69^{+0.01}_{-0.01}$	$1.14^{+0.14}_{-0.12}$
9.4	4.1	$3.94^{+0.05}_{-0.05}$					$0.80^{+0.01}_{-0.00}$	$1.07^{+0.12}_{-0.10}$
9.7	4.2	$3.95^{+0.11}_{-0.10}$					$0.83^{+0.01}_{-0.01}$	$1.19^{+0.15}_{-0.13}$
10.1	4.4	$5.47^{+0.11}_{-0.11}$					$1.01^{+0.01}_{-0.01}$	$1.12^{+0.15}_{-0.12}$
10.4	4.5	$6.29^{+0.00}_{-0.00}$					$1.12^{+0.00}_{-0.00}$	$1.12^{+0.09}_{-0.08}$
10.8	4.7	$6.64^{+0.00}_{-0.00}$					$1.19^{+0.00}_{-0.00}$	$1.10^{+0.09}_{-0.08}$
11.1	4.8	$5.80^{+0.15}_{-0.15}$					$1.15^{+0.01}_{-0.01}$	$1.15^{+0.18}_{-0.15}$
11.5	5.0	$4.79^{+0.23}_{-0.21}$					$1.08^{+0.03}_{-0.02}$	$1.19^{+0.22}_{-0.18}$
11.9	5.2	$2.07^{+0.22}_{-0.18}$					$0.73^{+0.04}_{-0.03}$	$1.62^{+0.49}_{-0.36}$
12.2	5.3	$3.23^{+0.12}_{-0.11}$					$0.94^{+0.02}_{-0.02}$	$1.18^{+0.21}_{-0.17}$

Table B.2.: Stability Diagnostics of NGC0628.

R [kpc]	R/R_d	$\sigma_g = 5$ km/s		$\sigma_g = 8$ km/s		$\sigma_g = 11$ km/s		$\sigma_g = 11$ km/s, Turbulent	
		Q_{eff}	$\bar{\lambda}$ [kpc]						
0.2	0.1	4.63 ^{+0.05} _{-0.05}	0.48 ^{+0.01} _{-0.01}			4.63 ^{+0.05} _{-0.05}	0.48 ^{+0.01} _{-0.01}		
0.5	0.2	5.26 ^{+0.06} _{-0.06}	0.33 ^{+0.00} _{-0.00}			5.27 ^{+0.06} _{-0.06}	0.34 ^{+0.00} _{-0.00}		
0.9	0.4	5.05 ^{+0.17} _{-0.38}	0.02 ^{+0.30} _{-0.00}			5.17 ^{+0.06} _{-0.06}	0.32 ^{+0.00} _{-0.00}		
1.2	0.5	4.87 ^{+0.09} _{-0.32}	0.03 ^{+0.31} _{-0.00}			4.92 ^{+0.06} _{-0.06}	0.35 ^{+0.00} _{-0.01}		
1.6	0.7	4.05 ^{+0.22} _{-0.32}	0.05 ^{+0.40} _{-0.00}			4.22 ^{+0.07} _{-0.07}	0.45 ^{+0.01} _{-0.00}		
1.9	0.8	3.37 ^{+0.33} _{-0.28}	0.07 ^{+0.01} _{-0.00}			3.82 ^{+0.08} _{-0.08}	0.51 ^{+0.00} _{-0.01}		
2.3	1.0	2.70 ^{+0.37} _{-0.30}	0.10 ^{+0.01} _{-0.01}			3.28 ^{+0.11} _{-0.11}	0.63 ^{+0.02} _{-0.01}		
2.7	1.2			2.89 ^{+0.13} _{-0.16}	0.69 ^{+0.03} _{-0.45}	2.92 ^{+0.12} _{-0.12}	0.73 ^{+0.02} _{-0.03}		
3.0	1.3			2.74 ^{+0.12} _{-0.12}	0.74 ^{+0.05} _{-0.41}	2.78 ^{+0.11} _{-0.11}	0.80 ^{+0.01} _{-0.03}		
3.4	1.5			2.24 ^{+0.16} _{-0.16}	1.46 ^{+0.12} _{-0.14}	2.25 ^{+0.16} _{-0.16}	1.49 ^{+0.13} _{-0.14}		
3.7	1.6			2.41 ^{+0.15} _{-0.18}	0.80 ^{+0.10} _{-0.32}	2.46 ^{+0.14} _{-0.13}	0.94 ^{+0.03} _{-0.05}		
4.1	1.8			2.19 ^{+0.20} _{-0.22}	0.64 ^{+0.24} _{-0.11}	2.28 ^{+0.17} _{-0.16}	0.95 ^{+0.04} _{-0.05}		
4.4	1.9			2.08 ^{+0.20} _{-0.20}	0.68 ^{+0.21} _{-0.09}	2.18 ^{+0.16} _{-0.15}	1.01 ^{+0.03} _{-0.05}		
4.8	2.1					2.17 ^{+0.16} _{-0.15}	0.98 ^{+0.02} _{-0.00}	2.50 ^{+0.13} _{-0.13}	1.06 ^{+0.00} _{-0.00}
5.1	2.2					2.16 ^{+0.16} _{-0.14}	1.00 ^{+0.00} _{-0.00}	2.49 ^{+0.13} _{-0.13}	1.05 ^{+0.01} _{-0.02}
5.5	2.4					2.10 ^{+0.16} _{-0.14}	1.06 ^{+0.02} _{-0.01}	2.40 ^{+0.14} _{-0.13}	1.08 ^{+0.01} _{-0.01}
5.8	2.5					2.09 ^{+0.14} _{-0.13}	1.09 ^{+0.03} _{-0.03}	2.39 ^{+0.13} _{-0.13}	1.10 ^{+0.01} _{-0.03}
6.2	2.7					2.01 ^{+0.18} _{-0.17}	1.36 ^{+0.10} _{-0.10}	2.22 ^{+0.17} _{-0.17}	1.38 ^{+0.11} _{-0.09}
6.5	2.8					1.75 ^{+0.21} _{-0.20}	2.02 ^{+0.26} _{-0.28}	1.85 ^{+0.21} _{-0.20}	2.17 ^{+0.29} _{-0.28}
6.9	3.0					2.04 ^{+0.07} _{-0.06}	1.10 ^{+0.02} _{-0.03}	2.32 ^{+0.07} _{-0.07}	0.96 ^{+0.00} _{-0.02}
7.3	3.2					1.96 ^{+0.07} _{-0.06}	1.19 ^{+0.04} _{-0.02}	2.20 ^{+0.07} _{-0.07}	1.04 ^{+0.02} _{-0.01}
7.6	3.3					1.92 ^{+0.15} _{-0.14}	1.28 ^{+0.08} _{-0.10}	2.15 ^{+0.16} _{-0.15}	1.13 ^{+0.06} _{-0.06}
8.0	3.5					2.04 ^{+0.10} _{-0.09}	1.12 ^{+0.05} _{-0.04}	2.27 ^{+0.11} _{-0.10}	0.90 ^{+0.02} _{-0.02}
8.3	3.6					1.90 ^{+0.22} _{-0.21}	1.42 ^{+0.19} _{-0.17}	2.08 ^{+0.24} _{-0.23}	1.29 ^{+0.14} _{-0.13}
8.7	3.8					1.87 ^{+0.25} _{-0.23}	1.50 ^{+0.23} _{-0.21}	2.04 ^{+0.27} _{-0.25}	1.37 ^{+0.20} _{-0.16}
9.0	3.9					2.03 ^{+0.15} _{-0.14}	1.22 ^{+0.10} _{-0.09}	2.21 ^{+0.16} _{-0.16}	1.00 ^{+0.07} _{-0.06}
9.4	4.1					2.16 ^{+0.12} _{-0.12}	1.09 ^{+0.07} _{-0.06}	2.33 ^{+0.14} _{-0.13}	0.86 ^{+0.04} _{-0.04}
9.7	4.2					2.27 ^{+0.15} _{-0.15}	1.06 ^{+0.09} _{-0.07}	2.44 ^{+0.17} _{-0.16}	0.84 ^{+0.05} _{-0.05}
10.1	4.4					2.59 ^{+0.18} _{-0.16}	0.87 ^{+0.07} _{-0.05}	2.74 ^{+0.19} _{-0.18}	0.65 ^{+0.04} _{-0.03}
10.4	4.5					2.77 ^{+0.10} _{-0.09}	0.80 ^{+0.03} _{-0.03}	2.90 ^{+0.11} _{-0.10}	0.58 ^{+0.02} _{-0.01}
10.8	4.7					2.83 ^{+0.11} _{-0.10}	0.78 ^{+0.03} _{-0.03}	2.94 ^{+0.12} _{-0.11}	0.57 ^{+0.02} _{-0.02}
11.1	4.8					2.70 ^{+0.22} _{-0.20}	0.86 ^{+0.08} _{-0.08}	2.80 ^{+0.23} _{-0.22}	0.65 ^{+0.06} _{-0.05}
11.5	5.0					2.49 ^{+0.26} _{-0.24}	1.00 ^{+0.12} _{-0.11}	2.58 ^{+0.27} _{-0.25}	0.77 ^{+0.10} _{-0.08}
11.9	5.2					1.88 ^{+0.28} _{-0.26}	1.73 ^{+0.32} _{-0.27}	1.97 ^{+0.29} _{-0.27}	1.54 ^{+0.30} _{-0.23}
12.2	5.3					2.04 ^{+0.19} _{-0.18}	1.39 ^{+0.15} _{-0.14}	2.12 ^{+0.20} _{-0.19}	1.14 ^{+0.11} _{-0.10}

Table B.3.: Model Parameters of NGC3198.

R [kpc]	R/R_d	Λ_0	$\sigma_g = 5$ km/s		$\sigma_g = 8$ km/s		$\sigma_g = 11$ km/s	
			s_0	q_0	s_0	q_0	s_0	q_0
0.3	0.1	$0.59^{+0.05}_{-0.04}$	$0.04^{+0.00}_{-0.00}$	$0.80^{+0.68}_{-0.29}$			$0.09^{+0.00}_{-0.00}$	$1.76^{+1.49}_{-0.63}$
1.0	0.3	$1.34^{+0.02}_{-0.02}$	$0.07^{+0.00}_{-0.00}$	$1.08^{+0.57}_{-0.29}$			$0.15^{+0.00}_{-0.00}$	$2.39^{+1.25}_{-0.63}$
1.7	0.5	$1.57^{+0.02}_{-0.01}$	$0.09^{+0.00}_{-0.00}$	$1.46^{+0.38}_{-0.26}$			$0.19^{+0.00}_{-0.00}$	$3.22^{+0.85}_{-0.57}$
2.3	0.7	$1.54^{+0.01}_{-0.01}$	$0.09^{+0.00}_{-0.00}$	$1.38^{+0.24}_{-0.18}$			$0.21^{+0.00}_{-0.00}$	$3.04^{+0.53}_{-0.40}$
3.0	0.9	$1.29^{+0.01}_{-0.01}$	$0.10^{+0.00}_{-0.00}$	$1.02^{+0.20}_{-0.15}$			$0.22^{+0.00}_{-0.00}$	$2.25^{+0.45}_{-0.32}$
3.7	1.2	$1.08^{+0.01}_{-0.01}$			$0.16^{+0.00}_{-0.00}$	$1.23^{+0.20}_{-0.16}$	$0.23^{+0.00}_{-0.00}$	$1.69^{+0.28}_{-0.21}$
4.3	1.3	$1.01^{+0.01}_{-0.01}$			$0.18^{+0.00}_{-0.00}$	$1.09^{+0.17}_{-0.13}$	$0.24^{+0.00}_{-0.00}$	$1.50^{+0.24}_{-0.18}$
5.0	1.6	$0.93^{+0.01}_{-0.01}$			$0.19^{+0.00}_{-0.00}$	$1.09^{+0.13}_{-0.10}$	$0.26^{+0.00}_{-0.00}$	$1.50^{+0.17}_{-0.14}$
5.7	1.8	$0.90^{+0.00}_{-0.00}$			$0.21^{+0.00}_{-0.00}$	$1.09^{+0.10}_{-0.09}$	$0.29^{+0.00}_{-0.00}$	$1.50^{+0.14}_{-0.12}$
6.4	2.0	$0.95^{+0.01}_{-0.01}$			$0.24^{+0.00}_{-0.00}$	$1.05^{+0.11}_{-0.10}$	$0.33^{+0.00}_{-0.00}$	$1.45^{+0.16}_{-0.13}$
7.0	2.2	$0.99^{+0.01}_{-0.01}$					$0.36^{+0.00}_{-0.00}$	$1.55^{+0.12}_{-0.10}$
7.7	2.4	$1.09^{+0.01}_{-0.01}$					$0.41^{+0.00}_{-0.00}$	$1.32^{+0.12}_{-0.10}$
8.4	2.6	$1.11^{+0.01}_{-0.01}$					$0.46^{+0.00}_{-0.00}$	$1.19^{+0.11}_{-0.09}$
9.0	2.8	$1.16^{+0.01}_{-0.01}$					$0.50^{+0.00}_{-0.00}$	$1.05^{+0.09}_{-0.08}$
9.7	3.0	$1.21^{+0.01}_{-0.01}$					$0.55^{+0.00}_{-0.00}$	$0.97^{+0.09}_{-0.08}$
10.4	3.2	$1.24^{+0.01}_{-0.01}$					$0.60^{+0.00}_{-0.00}$	$0.96^{+0.08}_{-0.07}$
11.0	3.4	$1.39^{+0.00}_{-0.00}$					$0.67^{+0.00}_{-0.00}$	$0.92^{+0.05}_{-0.04}$
11.7	3.7	$1.38^{+0.02}_{-0.02}$					$0.71^{+0.00}_{-0.00}$	$0.82^{+0.07}_{-0.06}$
12.4	3.9	$1.51^{+0.00}_{-0.00}$					$0.79^{+0.00}_{-0.00}$	$0.73^{+0.05}_{-0.04}$
13.0	4.1	$1.80^{+0.00}_{-0.00}$					$0.90^{+0.00}_{-0.00}$	$0.69^{+0.04}_{-0.03}$
13.7	4.3	$2.20^{+0.00}_{-0.00}$					$1.06^{+0.00}_{-0.00}$	$0.68^{+0.04}_{-0.04}$
14.4	4.5	$1.87^{+0.05}_{-0.05}$					$1.02^{+0.01}_{-0.01}$	$0.78^{+0.11}_{-0.09}$
15.1	4.7	$2.37^{+0.10}_{-0.09}$					$1.21^{+0.03}_{-0.02}$	$0.72^{+0.13}_{-0.10}$

Table B.4.: Stability Diagnostics of NGC3198.

R [kpc]	R/R _d	$\sigma_g = 5$ km/s		$\sigma_g = 8$ km/s		$\sigma_g = 11$ km/s		$\sigma_g = 11$ km/s, Turbulent	
		Q _{eff}	$\bar{\lambda}$ [kpc]						
0.3	0.1	1.43 ^{+0.44} _{-0.52}	0.23 ^{+4.33} _{-0.02}			1.72 ^{+0.14} _{-0.14}	4.21 ^{+0.30} _{-0.35}		
1.0	0.3	2.52 ^{+0.13} _{-0.49}	1.83 ^{+0.05} _{-1.63}			2.53 ^{+0.13} _{-0.12}	1.86 ^{+0.03} _{-0.05}		
1.7	0.5	2.75 ^{+0.08} _{-0.08}	1.58 ^{+0.02} _{-0.04}			2.76 ^{+0.08} _{-0.08}	1.59 ^{+0.04} _{-0.02}		
2.3	0.7	2.67 ^{+0.07} _{-0.06}	1.59 ^{+0.04} _{-0.01}			2.68 ^{+0.06} _{-0.06}	1.62 ^{+0.04} _{-0.01}		
3.0	0.9	2.31 ^{+0.08} _{-0.25}	1.84 ^{+0.06} _{-1.52}			2.33 ^{+0.08} _{-0.08}	1.93 ^{+0.01} _{-0.04}		
3.7	1.2			1.97 ^{+0.08} _{-0.08}	2.11 ^{+0.11} _{-0.16}	1.99 ^{+0.08} _{-0.08}	2.25 ^{+0.04} _{-0.07}		
4.3	1.3			1.80 ^{+0.09} _{-0.11}	2.07 ^{+0.21} _{-0.91}	1.83 ^{+0.08} _{-0.08}	2.35 ^{+0.08} _{-0.08}		
5.0	1.6			1.69 ^{+0.07} _{-0.08}	2.18 ^{+0.21} _{-0.54}	1.73 ^{+0.06} _{-0.06}	2.58 ^{+0.05} _{-0.08}		
5.7	1.8			1.61 ^{+0.06} _{-0.06}	2.22 ^{+0.18} _{-0.31}	1.66 ^{+0.05} _{-0.05}	2.70 ^{+0.05} _{-0.05}		
6.4	2.0			1.57 ^{+0.07} _{-0.07}	2.10 ^{+0.17} _{-0.16}	1.64 ^{+0.06} _{-0.06}	2.66 ^{+0.02} _{-0.05}		
7.0	2.2					1.67 ^{+0.05} _{-0.05}	2.65 ^{+0.02} _{-0.02}	1.76 ^{+0.05} _{-0.05}	2.86 ^{+0.02} _{-0.06}
7.7	2.4					1.61 ^{+0.06} _{-0.06}	2.57 ^{+0.05} _{-0.01}	1.70 ^{+0.06} _{-0.06}	2.67 ^{+0.05} _{-0.01}
8.4	2.6					1.52 ^{+0.06} _{-0.06}	2.73 ^{+0.05} _{-0.09}	1.60 ^{+0.06} _{-0.06}	2.74 ^{+0.06} _{-0.06}
9.0	2.8					1.45 ^{+0.06} _{-0.06}	2.84 ^{+0.10} _{-0.09}	1.51 ^{+0.07} _{-0.06}	2.83 ^{+0.06} _{-0.10}
9.7	3.0					1.40 ^{+0.07} _{-0.06}	2.96 ^{+0.11} _{-0.10}	1.45 ^{+0.07} _{-0.07}	2.88 ^{+0.11} _{-0.11}
10.4	3.2					1.39 ^{+0.06} _{-0.06}	3.08 ^{+0.11} _{-0.11}	1.43 ^{+0.07} _{-0.06}	2.97 ^{+0.12} _{-0.11}
11.0	3.4					1.42 ^{+0.04} _{-0.04}	3.02 ^{+0.04} _{-0.08}	1.46 ^{+0.04} _{-0.04}	2.85 ^{+0.04} _{-0.08}
11.7	3.7					1.33 ^{+0.07} _{-0.07}	3.31 ^{+0.18} _{-0.17}	1.35 ^{+0.08} _{-0.07}	3.15 ^{+0.19} _{-0.18}
12.4	3.9					1.29 ^{+0.05} _{-0.04}	3.40 ^{+0.14} _{-0.09}	1.30 ^{+0.05} _{-0.05}	3.23 ^{+0.10} _{-0.14}
13.0	4.1					1.35 ^{+0.04} _{-0.04}	3.23 ^{+0.09} _{-0.09}	1.36 ^{+0.04} _{-0.04}	2.97 ^{+0.09} _{-0.09}
13.7	4.3					1.48 ^{+0.05} _{-0.05}	2.90 ^{+0.12} _{-0.08}	1.49 ^{+0.05} _{-0.05}	2.57 ^{+0.12} _{-0.07}
14.4	4.5					1.48 ^{+0.14} _{-0.12}	3.10 ^{+0.31} _{-0.28}	1.48 ^{+0.14} _{-0.12}	2.85 ^{+0.30} _{-0.32}
15.1	4.7					1.60 ^{+0.19} _{-0.17}	2.80 ^{+0.40} _{-0.32}	1.59 ^{+0.19} _{-0.17}	2.49 ^{+0.38} _{-0.33}

Table B.5.: Model Parameters of NGC3184.

R [kpc]	R/R_d	Λ_0	$\sigma_g = 5$ km/s		$\sigma_g = 8$ km/s		$\sigma_g = 11$ km/s	
			s_0	q_0	s_0	q_0	s_0	q_0
0.3	0.1	$0.83^{+0.03}_{-0.03}$	$0.04^{+0.00}_{-0.00}$	$0.56^{+0.18}_{-0.12}$			$0.08^{+0.00}_{-0.00}$	$1.22^{+0.40}_{-0.26}$
0.8	0.3	$1.74^{+0.01}_{-0.01}$	$0.06^{+0.00}_{-0.00}$	$0.69^{+0.13}_{-0.09}$			$0.13^{+0.00}_{-0.00}$	$1.52^{+0.28}_{-0.21}$
1.3	0.5	$1.90^{+0.01}_{-0.01}$	$0.07^{+0.00}_{-0.00}$	$0.80^{+0.12}_{-0.09}$			$0.16^{+0.00}_{-0.00}$	$1.76^{+0.27}_{-0.21}$
1.9	0.8	$2.04^{+0.01}_{-0.01}$	$0.08^{+0.00}_{-0.00}$	$0.78^{+0.12}_{-0.09}$			$0.18^{+0.00}_{-0.00}$	$1.71^{+0.25}_{-0.20}$
2.4	1.0	$2.02^{+0.01}_{-0.01}$	$0.09^{+0.00}_{-0.00}$	$0.64^{+0.11}_{-0.08}$			$0.20^{+0.00}_{-0.00}$	$1.41^{+0.25}_{-0.19}$
3.0	1.2	$1.73^{+0.01}_{-0.01}$			$0.15^{+0.00}_{-0.00}$	$0.95^{+0.16}_{-0.12}$	$0.21^{+0.00}_{-0.00}$	$1.30^{+0.22}_{-0.16}$
3.5	1.5	$1.63^{+0.01}_{-0.01}$			$0.16^{+0.00}_{-0.00}$	$0.97^{+0.18}_{-0.13}$	$0.22^{+0.00}_{-0.00}$	$1.33^{+0.24}_{-0.18}$
4.0	1.7	$1.45^{+0.01}_{-0.01}$			$0.17^{+0.00}_{-0.00}$	$1.01^{+0.19}_{-0.14}$	$0.23^{+0.00}_{-0.00}$	$1.39^{+0.27}_{-0.20}$
4.6	1.9	$1.34^{+0.00}_{-0.00}$			$0.18^{+0.00}_{-0.00}$	$1.06^{+0.12}_{-0.10}$	$0.24^{+0.00}_{-0.00}$	$1.46^{+0.17}_{-0.14}$
5.1	2.1	$1.28^{+0.01}_{-0.01}$					$0.26^{+0.00}_{-0.00}$	$1.42^{+0.11}_{-0.10}$
5.7	2.4	$0.82^{+0.06}_{-0.05}$					$0.23^{+0.01}_{-0.01}$	$1.67^{+0.39}_{-0.30}$
6.2	2.6	$1.12^{+0.01}_{-0.01}$					$0.28^{+0.00}_{-0.00}$	$1.43^{+0.20}_{-0.16}$
6.7	2.8	$1.29^{+0.01}_{-0.01}$					$0.33^{+0.00}_{-0.00}$	$1.40^{+0.17}_{-0.14}$
7.3	3.0	$1.47^{+0.00}_{-0.00}$					$0.38^{+0.00}_{-0.00}$	$1.40^{+0.14}_{-0.12}$
7.8	3.2	$1.63^{+0.01}_{-0.01}$					$0.42^{+0.00}_{-0.00}$	$1.59^{+0.08}_{-0.07}$
8.3	3.5	$1.77^{+0.01}_{-0.01}$					$0.47^{+0.00}_{-0.00}$	$1.50^{+0.08}_{-0.07}$
8.9	3.7	$1.79^{+0.02}_{-0.02}$					$0.50^{+0.00}_{-0.00}$	$1.39^{+0.08}_{-0.08}$
9.4	3.9	$2.07^{+0.01}_{-0.01}$					$0.57^{+0.00}_{-0.00}$	$1.28^{+0.07}_{-0.07}$
10.0	4.2	$2.11^{+0.05}_{-0.05}$					$0.62^{+0.01}_{-0.01}$	$1.30^{+0.09}_{-0.08}$
10.5	4.4	$2.59^{+0.03}_{-0.03}$					$0.72^{+0.00}_{-0.00}$	$1.26^{+0.07}_{-0.06}$
11.0	4.6	$2.83^{+0.04}_{-0.04}$					$0.79^{+0.01}_{-0.00}$	$1.24^{+0.10}_{-0.09}$
11.6	4.8	$3.04^{+0.05}_{-0.05}$					$0.86^{+0.01}_{-0.01}$	$1.24^{+0.12}_{-0.10}$
12.1	5.0	$3.60^{+0.07}_{-0.07}$					$0.98^{+0.01}_{-0.01}$	$1.25^{+0.10}_{-0.09}$
12.6	5.2	$3.59^{+0.08}_{-0.07}$					$1.02^{+0.01}_{-0.01}$	$1.45^{+0.14}_{-0.13}$
13.2	5.5	$4.15^{+0.12}_{-0.11}$					$1.15^{+0.02}_{-0.02}$	$1.47^{+0.17}_{-0.15}$
13.7	5.7	$4.74^{+0.00}_{-0.00}$					$1.28^{+0.00}_{-0.00}$	$1.37^{+0.11}_{-0.09}$
14.3	6.0	$3.42^{+0.09}_{-0.09}$					$1.14^{+0.02}_{-0.01}$	$1.60^{+0.20}_{-0.17}$

Table B.6.: Stability Diagnostics of NGC3184.

R [kpc]	R/R_d	$\sigma_g = 5$ km/s		$\sigma_g = 8$ km/s		$\sigma_g = 11$ km/s		$\sigma_g = 11$ km/s, Turbulent	
		Q_{eff}	$\bar{\lambda}$ [kpc]	Q_{eff}	$\bar{\lambda}$ [kpc]	Q_{eff}	$\bar{\lambda}$ [kpc]	Q_{eff}	$\bar{\lambda}$ [kpc]
0.3	0.1	$1.04^{+0.35}_{-0.23}$	$0.23^{+0.06}_{-0.06}$			$1.70^{+0.09}_{-0.12}$	$2.96^{+0.14}_{-2.61}$		
0.8	0.3	$1.79^{+0.30}_{-0.23}$	$0.15^{+0.02}_{-0.02}$			$2.36^{+0.07}_{-0.07}$	$1.40^{+0.02}_{-0.02}$		
1.3	0.5	$2.10^{+0.28}_{-0.23}$	$0.15^{+0.02}_{-0.01}$			$2.48^{+0.06}_{-0.06}$	$1.29^{+0.00}_{-0.02}$		
1.9	0.8	$2.08^{+0.27}_{-0.22}$	$0.18^{+0.02}_{-0.02}$			$2.48^{+0.08}_{-0.08}$	$1.19^{+0.02}_{-0.04}$		
2.4	1.0	$1.73^{+0.27}_{-0.21}$	$0.23^{+0.03}_{-0.03}$			$2.31^{+0.10}_{-0.10}$	$1.15^{+0.04}_{-0.06}$		
3.0	1.2			$2.00^{+0.14}_{-0.19}$	$0.48^{+0.80}_{-0.01}$	$2.06^{+0.10}_{-0.10}$	$1.31^{+0.06}_{-0.12}$		
3.5	1.5			$1.93^{+0.14}_{-0.19}$	$0.60^{+0.77}_{-0.04}$	$1.98^{+0.11}_{-0.11}$	$1.39^{+0.08}_{-0.11}$		
4.0	1.7			$1.85^{+0.12}_{-0.17}$	$1.27^{+0.28}_{-0.61}$	$1.89^{+0.10}_{-0.10}$	$1.58^{+0.07}_{-0.11}$		
4.6	1.9			$1.77^{+0.07}_{-0.09}$	$1.49^{+0.17}_{-0.61}$	$1.81^{+0.06}_{-0.06}$	$1.76^{+0.03}_{-0.08}$		
5.1	2.1					$1.73^{+0.05}_{-0.04}$	$1.85^{+0.03}_{-0.06}$	$1.87^{+0.04}_{-0.04}$	$2.09^{+0.01}_{-0.01}$
5.7	2.4					$1.50^{+0.12}_{-0.12}$	$2.90^{+0.27}_{-0.29}$	$1.56^{+0.12}_{-0.12}$	$3.24^{+0.26}_{-0.25}$
6.2	2.6					$1.59^{+0.07}_{-0.07}$	$2.17^{+0.04}_{-0.07}$	$1.69^{+0.06}_{-0.06}$	$2.42^{+0.01}_{-0.01}$
6.7	2.8					$1.63^{+0.07}_{-0.07}$	$1.96^{+0.01}_{-0.03}$	$1.76^{+0.07}_{-0.06}$	$2.14^{+0.01}_{-0.04}$
7.3	3.0					$1.69^{+0.06}_{-0.06}$	$1.82^{+0.03}_{-0.01}$	$1.83^{+0.06}_{-0.06}$	$1.90^{+0.01}_{-0.03}$
7.8	3.2					$1.82^{+0.03}_{-0.03}$	$1.73^{+0.01}_{-0.03}$	$1.97^{+0.03}_{-0.03}$	$1.72^{+0.03}_{-0.01}$
8.3	3.5					$1.82^{+0.04}_{-0.04}$	$1.68^{+0.01}_{-0.03}$	$1.98^{+0.04}_{-0.04}$	$1.63^{+0.01}_{-0.03}$
8.9	3.7					$1.76^{+0.05}_{-0.05}$	$1.73^{+0.04}_{-0.02}$	$1.90^{+0.05}_{-0.05}$	$1.66^{+0.02}_{-0.04}$
9.4	3.9					$1.79^{+0.05}_{-0.05}$	$1.64^{+0.03}_{-0.03}$	$1.93^{+0.05}_{-0.05}$	$1.47^{+0.03}_{-0.01}$
10.0	4.2					$1.81^{+0.07}_{-0.07}$	$1.67^{+0.06}_{-0.08}$	$1.94^{+0.08}_{-0.08}$	$1.49^{+0.06}_{-0.06}$
10.5	4.4					$1.95^{+0.06}_{-0.05}$	$1.48^{+0.06}_{-0.04}$	$2.08^{+0.06}_{-0.06}$	$1.27^{+0.03}_{-0.03}$
11.0	4.6					$2.01^{+0.08}_{-0.08}$	$1.43^{+0.06}_{-0.06}$	$2.13^{+0.09}_{-0.09}$	$1.19^{+0.05}_{-0.03}$
11.6	4.8					$2.06^{+0.10}_{-0.09}$	$1.40^{+0.06}_{-0.08}$	$2.17^{+0.10}_{-0.10}$	$1.16^{+0.05}_{-0.05}$
12.1	5.0					$2.25^{+0.10}_{-0.10}$	$1.25^{+0.06}_{-0.06}$	$2.34^{+0.11}_{-0.10}$	$1.01^{+0.05}_{-0.05}$
12.6	5.2					$2.40^{+0.12}_{-0.11}$	$1.19^{+0.07}_{-0.06}$	$2.48^{+0.12}_{-0.12}$	$0.98^{+0.05}_{-0.05}$
13.2	5.5					$2.60^{+0.15}_{-0.15}$	$1.07^{+0.09}_{-0.07}$	$2.65^{+0.16}_{-0.15}$	$0.86^{+0.06}_{-0.05}$
13.7	5.7					$2.71^{+0.08}_{-0.08}$	$1.02^{+0.03}_{-0.04}$	$2.73^{+0.09}_{-0.08}$	$0.80^{+0.02}_{-0.02}$
14.3	6.0					$2.44^{+0.14}_{-0.14}$	$1.24^{+0.10}_{-0.08}$	$2.48^{+0.14}_{-0.14}$	$1.05^{+0.08}_{-0.07}$

Table B.7.: Model Parameters of NGC4736.

R [kpc]	R/R_d	Λ_0	$\sigma_g = 5$ km/s		$\sigma_g = 8$ km/s		$\sigma_g = 11$ km/s	
			s_0	q_0	s_0	q_0	s_0	q_0
0.1	0.1	$1.85^{+0.04}_{-0.04}$	$0.01^{+0.00}_{-0.00}$	$2.14^{+0.30}_{-0.24}$			$0.02^{+0.00}_{-0.00}$	$4.71^{+0.65}_{-0.54}$
0.3	0.3	$2.17^{+0.03}_{-0.03}$	$0.02^{+0.00}_{-0.00}$	$1.33^{+0.23}_{-0.18}$			$0.04^{+0.00}_{-0.00}$	$2.94^{+0.51}_{-0.39}$
0.6	0.5	$1.72^{+0.01}_{-0.01}$	$0.03^{+0.00}_{-0.00}$	$1.00^{+0.15}_{-0.12}$			$0.07^{+0.00}_{-0.00}$	$2.20^{+0.33}_{-0.26}$
0.8	0.7	$1.57^{+0.00}_{-0.00}$	$0.04^{+0.00}_{-0.00}$	$0.95^{+0.12}_{-0.10}$			$0.08^{+0.00}_{-0.00}$	$2.10^{+0.26}_{-0.21}$
1.0	0.9	$1.29^{+0.00}_{-0.00}$	$0.04^{+0.00}_{-0.00}$	$1.03^{+0.19}_{-0.14}$			$0.10^{+0.00}_{-0.00}$	$2.28^{+0.42}_{-0.31}$
1.3	1.2	$1.35^{+0.00}_{-0.00}$			$0.09^{+0.00}_{-0.00}$	$1.70^{+0.58}_{-0.35}$	$0.13^{+0.00}_{-0.00}$	$2.34^{+0.79}_{-0.48}$
1.5	1.4	$1.71^{+0.00}_{-0.00}$			$0.12^{+0.00}_{-0.00}$	$2.29^{+1.99}_{-0.73}$	$0.17^{+0.00}_{-0.00}$	$3.15^{+2.74}_{-1.00}$
1.7	1.5	$1.87^{+0.00}_{-0.00}$			$0.15^{+0.00}_{-0.00}$	$4.04^{+2.34}_{-1.51}$	$0.20^{+0.00}_{-0.00}$	$5.56^{+3.21}_{-2.08}$
1.9	1.7	$1.92^{+0.00}_{-0.00}$			$0.16^{+0.00}_{-0.00}$	$6.12^{+0.62}_{-0.52}$	$0.23^{+0.00}_{-0.00}$	$8.42^{+0.85}_{-0.71}$
2.2	2.0	$1.74^{+0.00}_{-0.00}$			$0.18^{+0.00}_{-0.00}$	$6.49^{+0.77}_{-0.63}$	$0.25^{+0.00}_{-0.00}$	$8.92^{+1.06}_{-0.86}$
2.4	2.2	$1.67^{+0.01}_{-0.01}$					$0.27^{+0.00}_{-0.00}$	$9.30^{+1.28}_{-1.01}$
2.6	2.4	$1.62^{+0.00}_{-0.00}$					$0.28^{+0.00}_{-0.00}$	$9.39^{+1.38}_{-1.07}$
2.8	2.5	$1.58^{+0.00}_{-0.00}$					$0.30^{+0.00}_{-0.00}$	$9.29^{+1.78}_{-1.30}$
3.1	2.8	$1.48^{+0.00}_{-0.00}$					$0.33^{+0.00}_{-0.00}$	$9.67^{+2.56}_{-1.69}$
3.3	3.0	$1.60^{+0.00}_{-0.00}$					$0.36^{+0.00}_{-0.00}$	$9.59^{+2.84}_{-1.80}$
3.5	3.2	$1.76^{+0.01}_{-0.01}$					$0.40^{+0.00}_{-0.00}$	$10.27^{+3.14}_{-1.96}$
3.8	3.5	$1.93^{+0.01}_{-0.01}$					$0.45^{+0.00}_{-0.00}$	$10.22^{+2.92}_{-1.87}$
4.0	3.6	$2.24^{+0.01}_{-0.01}$					$0.52^{+0.00}_{-0.00}$	$10.91^{+2.96}_{-1.93}$
4.2	3.8	$2.63^{+0.02}_{-0.02}$					$0.59^{+0.00}_{-0.00}$	$11.40^{+2.77}_{-1.89}$
4.4	4.0	$3.21^{+0.03}_{-0.03}$					$0.68^{+0.00}_{-0.00}$	$12.12^{+2.39}_{-1.75}$
4.7	4.3	$3.86^{+0.02}_{-0.02}$					$0.80^{+0.00}_{-0.00}$	$11.20^{+2.36}_{-1.69}$
4.9	4.5	$4.65^{+0.04}_{-0.04}$					$0.91^{+0.00}_{-0.00}$	$10.68^{+2.53}_{-1.75}$
5.1	4.6	$6.22^{+0.07}_{-0.07}$					$1.10^{+0.01}_{-0.01}$	$8.87^{+2.16}_{-1.49}$
5.4	4.9	$7.06^{+0.10}_{-0.10}$					$1.24^{+0.01}_{-0.01}$	$7.87^{+3.18}_{-1.82}$
5.6	5.1	$7.79^{+0.13}_{-0.13}$					$1.35^{+0.01}_{-0.01}$	$6.62^{+2.43}_{-1.46}$
5.8	5.3	$7.26^{+0.13}_{-0.12}$					$1.35^{+0.01}_{-0.01}$	$6.11^{+2.04}_{-1.27}$
6.0	5.5	$8.00^{+0.16}_{-0.16}$					$1.46^{+0.01}_{-0.01}$	$4.88^{+1.97}_{-1.14}$
6.3	5.7	$7.26^{+0.15}_{-0.14}$					$1.46^{+0.01}_{-0.01}$	$4.30^{+1.49}_{-0.92}$

Table B.8.: Stability Diagnostics of NGC4736.

		$\sigma_g = 5 \text{ km/s}$		$\sigma_g = 8 \text{ km/s}$		$\sigma_g = 11 \text{ km/s}$		$\sigma_g = 11 \text{ km/s, Turbulent}$	
R [kpc]	R/R_d	Q_{eff}	$\bar{\lambda}$ [kpc]	Q_{eff}	$\bar{\lambda}$ [kpc]	Q_{eff}	$\bar{\lambda}$ [kpc]	Q_{eff}	$\bar{\lambda}$ [kpc]
0.1	0.1	$1.95^{+0.02}_{-0.02}$	$1.36^{+0.03}_{-0.03}$			$1.95^{+0.02}_{-0.02}$	$1.37^{+0.03}_{-0.03}$		
0.3	0.3	$2.07^{+0.02}_{-0.02}$	$1.16^{+0.01}_{-0.01}$			$2.07^{+0.02}_{-0.02}$	$1.16^{+0.01}_{-0.01}$		
0.6	0.5	$1.79^{+0.02}_{-0.20}$	$1.46^{+0.01}_{-1.41}$			$1.79^{+0.02}_{-0.02}$	$1.45^{+0.01}_{-0.01}$		
0.8	0.7	$1.60^{+0.08}_{-0.15}$	$0.08^{+1.51}_{-0.00}$			$1.67^{+0.02}_{-0.02}$	$1.59^{+0.00}_{-0.00}$		
1.0	0.9	$1.51^{+0.02}_{-0.15}$	$1.93^{+0.01}_{-1.81}$			$1.51^{+0.02}_{-0.02}$	$1.93^{+0.01}_{-0.01}$		
1.3	1.2			$1.50^{+0.05}_{-0.04}$	$1.84^{+0.01}_{-0.03}$	$1.51^{+0.04}_{-0.04}$	$1.85^{+0.01}_{-0.03}$		
1.5	1.4			$1.70^{+0.09}_{-0.08}$	$1.45^{+0.02}_{-0.02}$	$1.71^{+0.09}_{-0.08}$	$1.46^{+0.02}_{-0.02}$		
1.7	1.5			$1.85^{+0.05}_{-0.08}$	$1.34^{+0.00}_{-0.02}$	$1.85^{+0.05}_{-0.08}$	$1.35^{+0.00}_{-0.02}$		
1.9	1.7			$1.90^{+0.01}_{-0.01}$	$1.31^{+0.00}_{-0.00}$	$1.91^{+0.01}_{-0.01}$	$1.31^{+0.00}_{-0.00}$		
2.2	2.0			$1.81^{+0.01}_{-0.01}$	$1.45^{+0.00}_{-0.00}$	$1.81^{+0.01}_{-0.01}$	$1.45^{+0.00}_{-0.00}$		
2.4	2.2					$1.77^{+0.01}_{-0.01}$	$1.51^{+0.01}_{-0.01}$	$1.80^{+0.01}_{-0.01}$	$1.53^{+0.01}_{-0.01}$
2.6	2.4					$1.74^{+0.01}_{-0.01}$	$1.56^{+0.00}_{-0.00}$	$1.77^{+0.01}_{-0.01}$	$1.58^{+0.00}_{-0.00}$
2.8	2.5					$1.71^{+0.02}_{-0.02}$	$1.60^{+0.00}_{-0.00}$	$1.74^{+0.01}_{-0.01}$	$1.62^{+0.00}_{-0.00}$
3.1	2.8					$1.66^{+0.02}_{-0.02}$	$1.70^{+0.03}_{-0.01}$	$1.69^{+0.02}_{-0.02}$	$1.72^{+0.01}_{-0.01}$
3.3	3.0					$1.71^{+0.03}_{-0.03}$	$1.60^{+0.00}_{-0.03}$	$1.74^{+0.02}_{-0.02}$	$1.60^{+0.00}_{-0.00}$
3.5	3.2					$1.80^{+0.03}_{-0.03}$	$1.45^{+0.00}_{-0.00}$	$1.83^{+0.02}_{-0.02}$	$1.45^{+0.00}_{-0.00}$
3.8	3.5					$1.87^{+0.03}_{-0.03}$	$1.33^{+0.02}_{-0.01}$	$1.91^{+0.03}_{-0.03}$	$1.33^{+0.02}_{-0.01}$
4.0	3.6					$2.01^{+0.03}_{-0.03}$	$1.16^{+0.00}_{-0.02}$	$2.06^{+0.03}_{-0.03}$	$1.14^{+0.02}_{-0.00}$
4.2	3.8					$2.18^{+0.04}_{-0.04}$	$1.00^{+0.01}_{-0.02}$	$2.22^{+0.03}_{-0.03}$	$0.97^{+0.02}_{-0.01}$
4.4	4.0					$2.41^{+0.04}_{-0.04}$	$0.82^{+0.02}_{-0.01}$	$2.46^{+0.03}_{-0.03}$	$0.81^{+0.01}_{-0.02}$
4.7	4.3					$2.61^{+0.04}_{-0.04}$	$0.70^{+0.00}_{-0.01}$	$2.67^{+0.04}_{-0.04}$	$0.67^{+0.00}_{-0.00}$
4.9	4.5					$2.85^{+0.06}_{-0.06}$	$0.59^{+0.01}_{-0.01}$	$2.92^{+0.05}_{-0.05}$	$0.56^{+0.01}_{-0.00}$
5.1	4.6					$3.24^{+0.08}_{-0.08}$	$0.45^{+0.02}_{-0.01}$	$3.31^{+0.07}_{-0.07}$	$0.42^{+0.01}_{-0.00}$
5.4	4.9					$3.42^{+0.14}_{-0.13}$	$0.41^{+0.02}_{-0.02}$	$3.48^{+0.13}_{-0.12}$	$0.38^{+0.01}_{-0.01}$
5.6	5.1					$3.52^{+0.16}_{-0.15}$	$0.39^{+0.02}_{-0.03}$	$3.57^{+0.15}_{-0.14}$	$0.35^{+0.02}_{-0.01}$
5.8	5.3					$3.37^{+0.15}_{-0.15}$	$0.42^{+0.02}_{-0.03}$	$3.41^{+0.14}_{-0.14}$	$0.38^{+0.01}_{-0.02}$
6.0	5.5					$3.43^{+0.21}_{-0.20}$	$0.40^{+0.04}_{-0.03}$	$3.46^{+0.20}_{-0.19}$	$0.35^{+0.02}_{-0.02}$
6.3	5.7					$3.20^{+0.19}_{-0.18}$	$0.45^{+0.04}_{-0.03}$	$3.21^{+0.19}_{-0.18}$	$0.40^{+0.03}_{-0.02}$

Table B.9.: Model Parameters of NGC3351.

R [kpc]	R/R_d	Λ_0	$\sigma_g = 5$ km/s		$\sigma_g = 8$ km/s		$\sigma_g = 11$ km/s	
			s_0	q_0	s_0	q_0	s_0	q_0
0.2	0.1	$7.94^{+0.18}_{-0.17}$	$0.02^{+0.00}_{-0.00}$	$0.43^{+0.12}_{-0.08}$			$0.03^{+0.00}_{-0.00}$	$0.95^{+0.26}_{-0.18}$
0.7	0.3	$4.98^{+0.05}_{-0.05}$	$0.03^{+0.00}_{-0.00}$	$0.45^{+0.21}_{-0.11}$			$0.07^{+0.00}_{-0.00}$	$0.99^{+0.47}_{-0.25}$
1.2	0.5	$3.81^{+0.02}_{-0.02}$	$0.05^{+0.00}_{-0.00}$	$1.37^{+0.94}_{-0.44}$			$0.11^{+0.00}_{-0.00}$	$3.01^{+2.07}_{-0.98}$
1.7	0.8	$3.21^{+0.02}_{-0.02}$	$0.07^{+0.00}_{-0.00}$	$5.49^{+5.60}_{-2.53}$			$0.15^{+0.00}_{-0.00}$	$12.07^{+12.33}_{-5.56}$
2.2	1.0	$2.48^{+0.02}_{-0.02}$	$0.08^{+0.00}_{-0.00}$	$4.39^{+1.23}_{-0.80}$			$0.17^{+0.00}_{-0.00}$	$9.65^{+2.72}_{-1.76}$
2.7	1.2	$1.80^{+0.01}_{-0.01}$			$0.13^{+0.00}_{-0.00}$	$3.95^{+0.79}_{-0.57}$	$0.18^{+0.00}_{-0.00}$	$5.44^{+1.09}_{-0.79}$
3.2	1.5	$1.37^{+0.00}_{-0.00}$			$0.13^{+0.00}_{-0.00}$	$2.90^{+0.47}_{-0.36}$	$0.18^{+0.00}_{-0.00}$	$3.98^{+0.64}_{-0.49}$
3.7	1.7	$1.34^{+0.00}_{-0.00}$			$0.15^{+0.00}_{-0.00}$	$2.68^{+0.51}_{-0.37}$	$0.21^{+0.00}_{-0.00}$	$3.68^{+0.71}_{-0.51}$
4.2	1.9	$1.38^{+0.00}_{-0.00}$			$0.17^{+0.00}_{-0.00}$	$2.71^{+0.49}_{-0.36}$	$0.24^{+0.00}_{-0.00}$	$3.72^{+0.68}_{-0.50}$
4.7	2.1	$1.48^{+0.00}_{-0.00}$					$0.28^{+0.00}_{-0.00}$	$3.57^{+0.46}_{-0.37}$
5.1	2.3	$1.58^{+0.01}_{-0.01}$					$0.31^{+0.00}_{-0.00}$	$3.75^{+0.59}_{-0.45}$
5.6	2.5	$1.48^{+0.00}_{-0.00}$					$0.33^{+0.00}_{-0.00}$	$3.86^{+0.66}_{-0.49}$
6.1	2.8	$1.37^{+0.00}_{-0.00}$					$0.35^{+0.00}_{-0.00}$	$3.96^{+0.74}_{-0.54}$
6.6	3.0	$1.35^{+0.00}_{-0.00}$					$0.37^{+0.00}_{-0.00}$	$3.89^{+0.63}_{-0.48}$
7.1	3.2	$1.37^{+0.00}_{-0.00}$					$0.40^{+0.00}_{-0.00}$	$4.91^{+0.42}_{-0.36}$
7.6	3.5	$1.50^{+0.01}_{-0.01}$					$0.45^{+0.00}_{-0.00}$	$4.24^{+0.35}_{-0.30}$
8.1	3.7	$1.70^{+0.01}_{-0.01}$					$0.51^{+0.00}_{-0.00}$	$3.48^{+0.28}_{-0.24}$
8.6	3.9	$1.91^{+0.01}_{-0.01}$					$0.58^{+0.00}_{-0.00}$	$2.81^{+0.21}_{-0.19}$
9.1	4.1	$2.18^{+0.02}_{-0.02}$					$0.65^{+0.00}_{-0.00}$	$2.35^{+0.17}_{-0.15}$
9.5	4.3	$2.36^{+0.02}_{-0.02}$					$0.71^{+0.00}_{-0.00}$	$2.10^{+0.15}_{-0.14}$
10.0	4.5	$2.47^{+0.05}_{-0.05}$					$0.76^{+0.01}_{-0.01}$	$2.00^{+0.19}_{-0.17}$
10.5	4.8	$3.08^{+0.00}_{-0.00}$					$0.89^{+0.00}_{-0.00}$	$1.93^{+0.13}_{-0.12}$
11.0	5.0	$3.19^{+0.05}_{-0.05}$					$0.95^{+0.01}_{-0.01}$	$2.25^{+0.26}_{-0.22}$
11.5	5.2	$3.24^{+0.13}_{-0.12}$					$1.00^{+0.02}_{-0.02}$	$2.54^{+0.28}_{-0.25}$
12.0	5.5	$4.27^{+0.12}_{-0.11}$					$1.20^{+0.02}_{-0.02}$	$2.47^{+0.25}_{-0.22}$
12.5	5.7	$4.28^{+0.27}_{-0.24}$					$1.25^{+0.04}_{-0.04}$	$3.05^{+0.53}_{-0.45}$

Table B.10.: Stability Diagnostics of NGC3351.

R [kpc]	R/R_d	$\sigma_g = 5$ km/s		$\sigma_g = 8$ km/s		$\sigma_g = 11$ km/s		$\sigma_g = 11$ km/s, Turbulent	
		Q_{eff}	$\bar{\lambda}$ [kpc]	Q_{eff}	$\bar{\lambda}$ [kpc]	Q_{eff}	$\bar{\lambda}$ [kpc]	Q_{eff}	$\bar{\lambda}$ [kpc]
0.2	0.1	$2.47^{+0.68}_{-0.47}$	$0.01^{+0.00}_{-0.00}$			$5.16^{+0.35}_{-0.94}$	$0.01^{+0.31}_{-0.00}$		
0.7	0.3	$1.99^{+0.92}_{-0.49}$	$0.04^{+0.01}_{-0.01}$			$3.89^{+0.25}_{-0.88}$	$0.05^{+0.45}_{-0.00}$		
1.2	0.5	$3.70^{+0.13}_{-0.35}$	$0.65^{+0.01}_{-0.61}$			$3.71^{+0.13}_{-0.14}$	$0.65^{+0.01}_{-0.00}$		
1.7	0.8	$3.58^{+0.06}_{-0.09}$	$0.78^{+0.01}_{-0.01}$			$3.58^{+0.06}_{-0.08}$	$0.79^{+0.01}_{-0.01}$		
2.2	1.0	$3.11^{+0.03}_{-0.03}$	$1.02^{+0.01}_{-0.01}$			$3.11^{+0.03}_{-0.03}$	$1.02^{+0.01}_{-0.01}$		
2.7	1.2			$2.58^{+0.03}_{-0.03}$	$1.40^{+0.01}_{-0.01}$	$2.58^{+0.03}_{-0.03}$	$1.40^{+0.01}_{-0.01}$		
3.2	1.5			$2.19^{+0.03}_{-0.03}$	$1.81^{+0.03}_{-0.01}$	$2.19^{+0.03}_{-0.03}$	$1.85^{+0.01}_{-0.03}$		
3.7	1.7			$2.12^{+0.04}_{-0.04}$	$1.85^{+0.03}_{-0.01}$	$2.13^{+0.04}_{-0.04}$	$1.88^{+0.01}_{-0.03}$		
4.2	1.9			$2.12^{+0.04}_{-0.04}$	$1.80^{+0.03}_{-0.01}$	$2.13^{+0.04}_{-0.04}$	$1.83^{+0.01}_{-0.01}$		
4.7	2.1					$2.16^{+0.04}_{-0.04}$	$1.71^{+0.00}_{-0.00}$	$2.24^{+0.03}_{-0.03}$	$1.75^{+0.01}_{-0.01}$
5.1	2.3					$2.21^{+0.05}_{-0.05}$	$1.62^{+0.01}_{-0.01}$	$2.30^{+0.04}_{-0.04}$	$1.65^{+0.03}_{-0.01}$
5.6	2.5					$2.14^{+0.05}_{-0.05}$	$1.73^{+0.00}_{-0.00}$	$2.22^{+0.04}_{-0.04}$	$1.78^{+0.00}_{-0.03}$
6.1	2.8					$2.06^{+0.05}_{-0.05}$	$1.86^{+0.03}_{-0.00}$	$2.13^{+0.04}_{-0.04}$	$1.92^{+0.00}_{-0.03}$
6.6	3.0					$2.02^{+0.05}_{-0.05}$	$1.93^{+0.00}_{-0.00}$	$2.09^{+0.04}_{-0.04}$	$1.96^{+0.03}_{-0.01}$
7.1	3.2					$2.09^{+0.02}_{-0.02}$	$1.89^{+0.01}_{-0.01}$	$2.15^{+0.02}_{-0.02}$	$1.92^{+0.01}_{-0.01}$
7.6	3.5					$2.12^{+0.03}_{-0.03}$	$1.78^{+0.01}_{-0.03}$	$2.19^{+0.03}_{-0.03}$	$1.79^{+0.01}_{-0.03}$
8.1	3.7					$2.15^{+0.04}_{-0.04}$	$1.61^{+0.03}_{-0.01}$	$2.25^{+0.03}_{-0.03}$	$1.60^{+0.01}_{-0.01}$
8.6	3.9					$2.15^{+0.04}_{-0.04}$	$1.51^{+0.03}_{-0.01}$	$2.26^{+0.04}_{-0.04}$	$1.46^{+0.01}_{-0.03}$
9.1	4.1					$2.16^{+0.05}_{-0.05}$	$1.44^{+0.03}_{-0.03}$	$2.28^{+0.05}_{-0.05}$	$1.32^{+0.03}_{-0.01}$
9.5	4.3					$2.16^{+0.06}_{-0.06}$	$1.40^{+0.03}_{-0.05}$	$2.28^{+0.06}_{-0.06}$	$1.26^{+0.03}_{-0.03}$
10.0	4.5					$2.16^{+0.09}_{-0.09}$	$1.39^{+0.05}_{-0.07}$	$2.28^{+0.09}_{-0.09}$	$1.23^{+0.05}_{-0.04}$
10.5	4.8					$2.37^{+0.05}_{-0.05}$	$1.19^{+0.02}_{-0.03}$	$2.48^{+0.05}_{-0.05}$	$1.02^{+0.02}_{-0.01}$
11.0	5.0					$2.53^{+0.11}_{-0.10}$	$1.12^{+0.05}_{-0.05}$	$2.62^{+0.11}_{-0.10}$	$0.97^{+0.05}_{-0.03}$
11.5	5.2					$2.64^{+0.13}_{-0.13}$	$1.09^{+0.06}_{-0.07}$	$2.73^{+0.13}_{-0.13}$	$0.94^{+0.06}_{-0.05}$
12.0	5.5					$3.02^{+0.13}_{-0.12}$	$0.87^{+0.05}_{-0.05}$	$3.07^{+0.13}_{-0.12}$	$0.74^{+0.04}_{-0.03}$
12.5	5.7					$3.20^{+0.23}_{-0.22}$	$0.82^{+0.08}_{-0.08}$	$3.24^{+0.22}_{-0.22}$	$0.71^{+0.06}_{-0.06}$

Table B.11.: Model Parameters of NGC6946.

R [kpc]	R/R_d	Λ_0	$\sigma_g = 5$ km/s		$\sigma_g = 8$ km/s		$\sigma_g = 11$ km/s	
			s_0	q_0	s_0	q_0	s_0	q_0
0.1	0.0	$0.32^{+0.02}_{-0.02}$	$0.01^{+0.00}_{-0.00}$	$0.14^{+0.03}_{-0.03}$			$0.03^{+0.00}_{-0.00}$	$0.30^{+0.07}_{-0.06}$
0.4	0.2	$1.31^{+0.01}_{-0.01}$	$0.03^{+0.00}_{-0.00}$	$0.08^{+0.02}_{-0.02}$			$0.06^{+0.00}_{-0.00}$	$0.18^{+0.05}_{-0.03}$
0.7	0.3	$1.62^{+0.01}_{-0.01}$	$0.04^{+0.00}_{-0.00}$	$0.12^{+0.04}_{-0.02}$			$0.08^{+0.00}_{-0.00}$	$0.26^{+0.09}_{-0.05}$
1.0	0.4	$1.81^{+0.01}_{-0.01}$	$0.04^{+0.00}_{-0.00}$	$0.19^{+0.07}_{-0.04}$			$0.10^{+0.00}_{-0.00}$	$0.42^{+0.16}_{-0.09}$
1.3	0.5	$1.76^{+0.01}_{-0.01}$	$0.05^{+0.00}_{-0.00}$	$0.28^{+0.10}_{-0.06}$			$0.11^{+0.00}_{-0.00}$	$0.63^{+0.22}_{-0.13}$
1.6	0.6	$1.46^{+0.02}_{-0.02}$	$0.05^{+0.00}_{-0.00}$	$0.38^{+0.11}_{-0.07}$			$0.11^{+0.00}_{-0.00}$	$0.83^{+0.24}_{-0.16}$
1.9	0.8	$1.29^{+0.01}_{-0.01}$	$0.05^{+0.00}_{-0.00}$	$0.41^{+0.08}_{-0.06}$			$0.11^{+0.00}_{-0.00}$	$0.90^{+0.18}_{-0.13}$
2.1	0.8	$1.28^{+0.00}_{-0.00}$	$0.06^{+0.00}_{-0.00}$	$0.39^{+0.06}_{-0.05}$			$0.12^{+0.00}_{-0.00}$	$0.87^{+0.13}_{-0.10}$
2.4	1.0	$1.15^{+0.00}_{-0.00}$	$0.06^{+0.00}_{-0.00}$	$0.38^{+0.05}_{-0.04}$			$0.13^{+0.00}_{-0.00}$	$0.84^{+0.12}_{-0.09}$
2.7	1.1	$1.05^{+0.00}_{-0.00}$			$0.10^{+0.00}_{-0.00}$	$0.60^{+0.08}_{-0.06}$	$0.13^{+0.00}_{-0.00}$	$0.82^{+0.11}_{-0.09}$
3.0	1.2	$0.96^{+0.01}_{-0.01}$			$0.10^{+0.00}_{-0.00}$	$0.60^{+0.07}_{-0.06}$	$0.14^{+0.00}_{-0.00}$	$0.83^{+0.10}_{-0.08}$
3.3	1.3	$0.91^{+0.00}_{-0.00}$			$0.11^{+0.00}_{-0.00}$	$0.61^{+0.07}_{-0.06}$	$0.15^{+0.00}_{-0.00}$	$0.83^{+0.10}_{-0.08}$
3.6	1.4	$0.81^{+0.01}_{-0.01}$			$0.11^{+0.00}_{-0.00}$	$0.61^{+0.09}_{-0.07}$	$0.15^{+0.00}_{-0.00}$	$0.84^{+0.13}_{-0.10}$
3.9	1.6	$0.51^{+0.02}_{-0.02}$			$0.09^{+0.00}_{-0.00}$	$0.71^{+0.19}_{-0.14}$	$0.13^{+0.00}_{-0.00}$	$0.98^{+0.26}_{-0.19}$
4.1	1.6	$0.68^{+0.01}_{-0.01}$			$0.12^{+0.00}_{-0.00}$	$0.61^{+0.15}_{-0.10}$	$0.16^{+0.00}_{-0.00}$	$0.84^{+0.21}_{-0.14}$
4.4	1.8	$0.69^{+0.01}_{-0.01}$			$0.12^{+0.00}_{-0.00}$	$0.62^{+0.17}_{-0.11}$	$0.17^{+0.00}_{-0.00}$	$0.85^{+0.24}_{-0.15}$
4.7	1.9	$0.66^{+0.00}_{-0.00}$			$0.13^{+0.00}_{-0.00}$	$0.66^{+0.19}_{-0.12}$	$0.18^{+0.00}_{-0.00}$	$0.91^{+0.26}_{-0.17}$
5.0	2.0	$0.67^{+0.00}_{-0.00}$			$0.14^{+0.00}_{-0.00}$	$0.71^{+0.20}_{-0.13}$	$0.19^{+0.00}_{-0.00}$	$0.97^{+0.28}_{-0.18}$
5.3	2.1	$0.69^{+0.00}_{-0.00}$					$0.21^{+0.00}_{-0.00}$	$1.05^{+0.31}_{-0.20}$
5.6	2.2	$0.69^{+0.00}_{-0.00}$					$0.22^{+0.00}_{-0.00}$	$1.14^{+0.28}_{-0.19}$
5.9	2.4	$0.33^{+0.02}_{-0.02}$					$0.16^{+0.00}_{-0.00}$	$1.75^{+0.52}_{-0.37}$
6.1	2.4	$0.54^{+0.01}_{-0.01}$					$0.21^{+0.00}_{-0.00}$	$1.43^{+0.30}_{-0.22}$
6.4	2.6	$0.51^{+0.02}_{-0.02}$					$0.22^{+0.00}_{-0.00}$	$1.53^{+0.40}_{-0.29}$
6.7	2.7	$0.54^{+0.03}_{-0.02}$					$0.23^{+0.01}_{-0.01}$	$1.56^{+0.45}_{-0.31}$
7.0	2.8	$0.60^{+0.01}_{-0.01}$					$0.26^{+0.00}_{-0.00}$	$1.58^{+0.41}_{-0.28}$
7.3	2.9	$0.66^{+0.01}_{-0.01}$					$0.28^{+0.00}_{-0.00}$	$1.60^{+0.51}_{-0.32}$
7.6	3.0	$0.73^{+0.01}_{-0.01}$					$0.31^{+0.00}_{-0.00}$	$1.58^{+0.52}_{-0.32}$
7.9	3.2	$0.82^{+0.01}_{-0.01}$					$0.34^{+0.00}_{-0.00}$	$1.73^{+0.30}_{-0.23}$
8.2	3.3	$0.72^{+0.02}_{-0.02}$					$0.33^{+0.00}_{-0.00}$	$1.80^{+0.33}_{-0.26}$
8.4	3.4	$0.83^{+0.02}_{-0.02}$					$0.37^{+0.00}_{-0.00}$	$1.74^{+0.32}_{-0.25}$
8.7	3.5	$0.84^{+0.02}_{-0.02}$					$0.38^{+0.01}_{-0.01}$	$1.79^{+0.32}_{-0.25}$
9.0	3.6	$0.84^{+0.03}_{-0.03}$					$0.39^{+0.01}_{-0.01}$	$1.90^{+0.36}_{-0.28}$
9.3	3.7	$1.05^{+0.02}_{-0.02}$					$0.46^{+0.01}_{-0.00}$	$1.78^{+0.27}_{-0.22}$
9.6	3.8	$0.83^{+0.03}_{-0.02}$					$0.42^{+0.01}_{-0.01}$	$2.12^{+0.38}_{-0.30}$
9.9	4.0	$0.57^{+0.03}_{-0.03}$					$0.36^{+0.01}_{-0.01}$	$2.73^{+0.56}_{-0.45}$
10.2	4.1	$0.23^{+0.02}_{-0.02}$					$0.23^{+0.01}_{-0.01}$	$4.49^{+1.14}_{-0.87}$
10.4	4.2	$0.93^{+0.02}_{-0.02}$					$0.48^{+0.01}_{-0.01}$	$2.39^{+0.43}_{-0.34}$
10.7	4.3	$1.04^{+0.02}_{-0.02}$					$0.52^{+0.01}_{-0.01}$	$2.31^{+0.43}_{-0.33}$
11.0	4.4	$0.99^{+0.03}_{-0.03}$					$0.52^{+0.01}_{-0.01}$	$2.43^{+0.42}_{-0.33}$
11.3	4.5	$0.90^{+0.04}_{-0.03}$					$0.51^{+0.01}_{-0.01}$	$2.54^{+0.49}_{-0.39}$
11.6	4.6	$1.18^{+0.03}_{-0.03}$					$0.60^{+0.01}_{-0.01}$	$2.16^{+0.36}_{-0.28}$

Table B.12.: Stability Diagnostics of NGC6946.

R [kpc]	R/R _d	$\sigma_g = 5$ km/s		$\sigma_g = 8$ km/s		$\sigma_g = 11$ km/s		$\sigma_g = 11$ km/s, Turbulent	
		Q _{eff}	$\bar{\lambda}$ [kpc]	Q _{eff}	$\bar{\lambda}$ [kpc]	Q _{eff}	$\bar{\lambda}$ [kpc]	Q _{eff}	$\bar{\lambda}$ [kpc]
0.1	0.0	0.17 ^{+0.05} _{-0.04}	0.74 ^{+0.19} _{-0.16}			0.37 ^{+0.10} _{-0.08}	0.75 ^{+0.20} _{-0.16}		
0.4	0.2	0.21 ^{+0.06} _{-0.04}	0.69 ^{+0.15} _{-0.16}			0.45 ^{+0.12} _{-0.08}	0.71 ^{+0.15} _{-0.14}		
0.7	0.3	0.33 ^{+0.12} _{-0.07}	0.50 ^{+0.13} _{-0.13}			0.70 ^{+0.23} _{-0.14}	0.53 ^{+0.13} _{-0.13}		
1.0	0.4	0.55 ^{+0.21} _{-0.12}	0.33 ^{+0.10} _{-0.09}			1.13 ^{+0.39} _{-0.24}	0.38 ^{+0.09} _{-0.09}		
1.3	0.5	0.80 ^{+0.28} _{-0.17}	0.26 ^{+0.07} _{-0.07}			1.58 ^{+0.47} _{-0.30}	0.33 ^{+0.06} _{-0.06}		
1.6	0.6	0.95 ^{+0.27} _{-0.18}	0.25 ^{+0.06} _{-0.05}			1.82 ^{+0.34} _{-0.30}	0.34 ^{+1.30} _{-0.00}		
1.9	0.8	0.97 ^{+0.19} _{-0.14}	0.27 ^{+0.04} _{-0.04}			1.81 ^{+0.20} _{-0.22}	0.40 ^{+1.44} _{-0.00}		
2.1	0.8	0.93 ^{+0.14} _{-0.11}	0.31 ^{+0.03} _{-0.04}			1.73 ^{+0.20} _{-0.17}	0.45 ^{+1.33} _{-0.01}		
2.4	1.0	0.85 ^{+0.12} _{-0.09}	0.37 ^{+0.04} _{-0.04}			1.58 ^{+0.17} _{-0.14}	0.55 ^{+0.03} _{-0.02}		
2.7	1.1			1.19 ^{+0.14} _{-0.11}	0.50 ^{+0.04} _{-0.04}	1.47 ^{+0.14} _{-0.12}	0.65 ^{+0.03} _{-0.02}		
3.0	1.2			1.14 ^{+0.12} _{-0.10}	0.58 ^{+0.05} _{-0.04}	1.41 ^{+0.12} _{-0.11}	0.76 ^{+0.04} _{-0.01}		
3.3	1.3			1.10 ^{+0.11} _{-0.10}	0.65 ^{+0.05} _{-0.05}	1.35 ^{+0.12} _{-0.10}	0.89 ^{+0.03} _{-0.02}		
3.6	1.4			1.05 ^{+0.14} _{-0.11}	0.76 ^{+0.08} _{-0.07}	1.28 ^{+0.14} _{-0.12}	1.03 ^{+0.04} _{-0.02}		
3.9	1.6			0.97 ^{+0.24} _{-0.18}	0.88 ^{+0.19} _{-0.16}	1.18 ^{+0.11} _{-0.19}	1.23 ^{+3.64} _{-0.10}		
4.1	1.6			0.95 ^{+0.20} _{-0.15}	0.95 ^{+0.14} _{-0.14}	1.16 ^{+0.17} _{-0.16}	1.31 ^{+1.81} _{-0.01}		
4.4	1.8			0.96 ^{+0.22} _{-0.16}	1.01 ^{+0.15} _{-0.13}	1.16 ^{+0.17} _{-0.16}	1.48 ^{+1.52} _{-0.03}		
4.7	1.9			0.99 ^{+0.22} _{-0.16}	1.09 ^{+0.14} _{-0.13}	1.17 ^{+0.15} _{-0.16}	1.73 ^{+1.59} _{-0.08}		
5.0	2.0			1.04 ^{+0.23} _{-0.16}	1.14 ^{+0.15} _{-0.09}	1.20 ^{+0.13} _{-0.15}	2.20 ^{+1.15} _{-0.39}		
5.3	2.1					1.23 ^{+0.12} _{-0.13}	2.74 ^{+0.63} _{-0.68}	1.28 ^{+0.11} _{-0.10}	3.89 ^{+0.02} _{-0.13}
5.6	2.2					1.26 ^{+0.10} _{-0.10}	3.01 ^{+0.36} _{-0.56}	1.30 ^{+0.09} _{-0.09}	3.91 ^{+0.02} _{-0.07}
5.9	2.4					1.05 ^{+0.07} _{-0.07}	7.37 ^{+0.63} _{-0.60}	1.02 ^{+0.08} _{-0.08}	8.12 ^{+0.46} _{-0.57}
6.1	2.4					1.21 ^{+0.07} _{-0.07}	4.33 ^{+0.26} _{-0.36}	1.21 ^{+0.07} _{-0.07}	5.04 ^{+0.10} _{-0.17}
6.4	2.6					1.19 ^{+0.09} _{-0.09}	4.60 ^{+0.40} _{-0.49}	1.19 ^{+0.10} _{-0.09}	5.28 ^{+0.23} _{-0.31}
6.7	2.7					1.21 ^{+0.10} _{-0.10}	4.40 ^{+0.32} _{-0.52}	1.22 ^{+0.11} _{-0.10}	4.99 ^{+0.30} _{-0.29}
7.0	2.8					1.25 ^{+0.09} _{-0.09}	3.99 ^{+0.23} _{-0.22}	1.27 ^{+0.09} _{-0.08}	4.59 ^{+0.07} _{-0.14}
7.3	2.9					1.29 ^{+0.11} _{-0.10}	3.72 ^{+0.08} _{-0.18}	1.32 ^{+0.10} _{-0.10}	4.16 ^{+0.10} _{-0.10}
7.6	3.0					1.33 ^{+0.12} _{-0.11}	3.39 ^{+0.07} _{-0.12}	1.36 ^{+0.12} _{-0.11}	3.80 ^{+0.09} _{-0.09}
7.9	3.2					1.41 ^{+0.07} _{-0.07}	3.13 ^{+0.07} _{-0.02}	1.46 ^{+0.07} _{-0.07}	3.42 ^{+0.08} _{-0.07}
8.2	3.3					1.35 ^{+0.08} _{-0.08}	3.57 ^{+0.08} _{-0.13}	1.38 ^{+0.08} _{-0.08}	3.90 ^{+0.15} _{-0.15}
8.4	3.4					1.41 ^{+0.09} _{-0.09}	3.16 ^{+0.12} _{-0.08}	1.45 ^{+0.09} _{-0.09}	3.40 ^{+0.14} _{-0.14}
8.7	3.5					1.42 ^{+0.09} _{-0.09}	3.16 ^{+0.13} _{-0.13}	1.46 ^{+0.09} _{-0.09}	3.37 ^{+0.14} _{-0.14}
9.0	3.6					1.43 ^{+0.10} _{-0.09}	3.22 ^{+0.16} _{-0.16}	1.47 ^{+0.10} _{-0.10}	3.38 ^{+0.23} _{-0.17}
9.3	3.7					1.53 ^{+0.09} _{-0.08}	2.70 ^{+0.10} _{-0.10}	1.59 ^{+0.09} _{-0.09}	2.77 ^{+0.10} _{-0.10}
9.6	3.8					1.46 ^{+0.09} _{-0.08}	3.28 ^{+0.14} _{-0.14}	1.50 ^{+0.09} _{-0.08}	3.40 ^{+0.21} _{-0.15}
9.9	4.0					1.32 ^{+0.08} _{-0.08}	4.52 ^{+0.30} _{-0.23}	1.33 ^{+0.08} _{-0.08}	4.80 ^{+0.40} _{-0.32}
10.2	4.1					0.94 ^{+0.05} _{-0.05}	11.11 ^{+0.81} _{-0.81}	0.92 ^{+0.06} _{-0.06}	11.58 ^{+1.02} _{-0.84}
10.4	4.2					1.56 ^{+0.08} _{-0.08}	3.02 ^{+0.12} _{-0.11}	1.60 ^{+0.09} _{-0.08}	3.09 ^{+0.12} _{-0.16}
10.7	4.3					1.62 ^{+0.09} _{-0.09}	2.79 ^{+0.14} _{-0.14}	1.67 ^{+0.09} _{-0.09}	2.82 ^{+0.11} _{-0.14}
11.0	4.4					1.60 ^{+0.09} _{-0.09}	2.93 ^{+0.13} _{-0.16}	1.64 ^{+0.09} _{-0.09}	2.96 ^{+0.13} _{-0.17}
11.3	4.5					1.55 ^{+0.10} _{-0.09}	3.16 ^{+0.21} _{-0.20}	1.58 ^{+0.10} _{-0.10}	3.19 ^{+0.22} _{-0.17}
11.6	4.6					1.67 ^{+0.09} _{-0.09}	2.61 ^{+0.13} _{-0.13}	1.72 ^{+0.10} _{-0.09}	2.54 ^{+0.14} _{-0.10}

Table B.13.: Model Parameters of NGC3627.

R [kpc]	R/R_d	Λ_0	$\sigma_g = 5$ km/s		$\sigma_g = 8$ km/s		$\sigma_g = 11$ km/s	
			s_0	q_0	s_0	q_0	s_0	q_0
0.2	0.1	$0.45^{+0.02}_{-0.02}$	$0.01^{+0.00}_{-0.00}$	$0.39^{+0.12}_{-0.08}$			$0.03^{+0.00}_{-0.00}$	$0.86^{+0.26}_{-0.18}$
0.7	0.2	$0.97^{+0.01}_{-0.01}$	$0.02^{+0.00}_{-0.00}$	$0.32^{+0.09}_{-0.06}$			$0.05^{+0.00}_{-0.00}$	$0.71^{+0.20}_{-0.13}$
1.1	0.4	$1.24^{+0.01}_{-0.01}$	$0.03^{+0.00}_{-0.00}$	$0.43^{+0.11}_{-0.07}$			$0.07^{+0.00}_{-0.00}$	$0.94^{+0.24}_{-0.16}$
1.6	0.6	$1.15^{+0.01}_{-0.01}$	$0.04^{+0.00}_{-0.00}$	$0.54^{+0.16}_{-0.10}$			$0.08^{+0.00}_{-0.00}$	$1.18^{+0.36}_{-0.23}$
2.0	0.7	$1.04^{+0.01}_{-0.01}$	$0.04^{+0.00}_{-0.00}$	$0.46^{+0.29}_{-0.13}$			$0.09^{+0.00}_{-0.00}$	$1.01^{+0.64}_{-0.29}$
2.5	0.9	$0.89^{+0.01}_{-0.01}$	$0.05^{+0.00}_{-0.00}$	$0.34^{+0.30}_{-0.11}$			$0.10^{+0.00}_{-0.00}$	$0.74^{+0.66}_{-0.24}$
2.9	1.0	$0.75^{+0.01}_{-0.01}$			$0.08^{+0.00}_{-0.00}$	$0.49^{+0.43}_{-0.16}$	$0.11^{+0.00}_{-0.00}$	$0.68^{+0.59}_{-0.22}$
3.4	1.2	$0.72^{+0.01}_{-0.01}$			$0.09^{+0.00}_{-0.00}$	$0.53^{+0.43}_{-0.17}$	$0.12^{+0.00}_{-0.00}$	$0.72^{+0.60}_{-0.23}$
3.8	1.4	$0.73^{+0.01}_{-0.01}$			$0.10^{+0.00}_{-0.00}$	$0.75^{+0.64}_{-0.24}$	$0.14^{+0.00}_{-0.00}$	$1.03^{+0.88}_{-0.33}$
4.3	1.5	$0.71^{+0.00}_{-0.00}$			$0.11^{+0.00}_{-0.00}$	$0.99^{+0.69}_{-0.29}$	$0.16^{+0.00}_{-0.00}$	$1.35^{+0.95}_{-0.40}$
4.7	1.7	$0.65^{+0.00}_{-0.00}$			$0.12^{+0.00}_{-0.00}$	$1.14^{+0.62}_{-0.30}$	$0.16^{+0.00}_{-0.00}$	$1.56^{+0.85}_{-0.41}$
5.2	1.9	$0.63^{+0.00}_{-0.00}$			$0.13^{+0.00}_{-0.00}$	$1.25^{+0.74}_{-0.34}$	$0.18^{+0.00}_{-0.00}$	$1.72^{+1.02}_{-0.47}$
5.6	2.0	$0.63^{+0.00}_{-0.00}$			$0.14^{+0.00}_{-0.00}$	$1.36^{+0.94}_{-0.40}$	$0.19^{+0.00}_{-0.00}$	$1.87^{+1.29}_{-0.55}$
6.1	2.2	$0.63^{+0.00}_{-0.00}$					$0.21^{+0.00}_{-0.00}$	$2.04^{+1.77}_{-0.65}$
6.5	2.3	$0.67^{+0.00}_{-0.00}$					$0.23^{+0.00}_{-0.00}$	$2.11^{+2.06}_{-0.71}$
7.0	2.5	$0.65^{+0.01}_{-0.01}$					$0.25^{+0.00}_{-0.00}$	$2.47^{+2.93}_{-0.88}$
7.4	2.6	$0.75^{+0.01}_{-0.01}$					$0.28^{+0.00}_{-0.00}$	$3.48^{+3.73}_{-1.20}$
7.9	2.8	$0.85^{+0.00}_{-0.00}$					$0.32^{+0.00}_{-0.00}$	$7.75^{+2.46}_{-1.52}$
8.3	3.0	$0.91^{+0.01}_{-0.01}$					$0.35^{+0.00}_{-0.00}$	$9.33^{+2.96}_{-1.85}$
8.8	3.1	$0.99^{+0.00}_{-0.00}$					$0.38^{+0.00}_{-0.00}$	$9.98^{+2.28}_{-1.58}$

Table B.14.: Stability Diagnostics of NGC3627.

		$\sigma_g = 5 \text{ km/s}$		$\sigma_g = 8 \text{ km/s}$		$\sigma_g = 11 \text{ km/s}$		$\sigma_g = 11 \text{ km/s, Turbulent}$	
R [kpc]	R/R_d	Q_{eff}	$\bar{\lambda}$ [kpc]	Q_{eff}	$\bar{\lambda}$ [kpc]	Q_{eff}	$\bar{\lambda}$ [kpc]	Q_{eff}	$\bar{\lambda}$ [kpc]
0.2	0.1	$0.60^{+0.20}_{-0.14}$	$0.18^{+0.05}_{-0.05}$			$1.27^{+0.24}_{-0.28}$	$0.20^{+5.61}_{-0.01}$		
0.7	0.2	$0.73^{+0.21}_{-0.14}$	$0.19^{+0.05}_{-0.04}$			$1.51^{+0.39}_{-0.27}$	$0.22^{+0.04}_{-0.04}$		
1.1	0.4	$1.07^{+0.26}_{-0.18}$	$0.16^{+0.03}_{-0.03}$			$2.12^{+0.16}_{-0.32}$	$0.20^{+1.80}_{-0.00}$		
1.6	0.6	$1.28^{+0.37}_{-0.24}$	$0.17^{+0.04}_{-0.04}$			$2.15^{+0.08}_{-0.14}$	$2.13^{+0.04}_{-1.86}$		
2.0	0.7	$1.04^{+0.63}_{-0.29}$	$0.24^{+0.09}_{-0.09}$			$1.95^{+0.16}_{-0.47}$	$2.30^{+0.11}_{-1.88}$		
2.5	0.9	$0.71^{+0.60}_{-0.23}$	$0.42^{+0.19}_{-0.19}$			$1.39^{+0.50}_{-0.41}$	$0.55^{+2.24}_{-0.01}$		
2.9	1.0			$0.91^{+0.69}_{-0.29}$	$0.63^{+0.26}_{-0.24}$	$1.17^{+0.52}_{-0.35}$	$0.74^{+2.54}_{-0.02}$		
3.4	1.2			$0.94^{+0.65}_{-0.28}$	$0.73^{+0.27}_{-0.25}$	$1.19^{+0.44}_{-0.33}$	$0.89^{+2.49}_{-0.01}$		
3.8	1.4			$1.27^{+0.44}_{-0.37}$	$0.65^{+2.73}_{-0.00}$	$1.50^{+0.21}_{-0.37}$	$2.99^{+0.41}_{-1.95}$		
4.3	1.5			$1.53^{+0.17}_{-0.38}$	$0.69^{+2.82}_{-0.01}$	$1.55^{+0.16}_{-0.18}$	$3.32^{+0.20}_{-2.08}$		
4.7	1.7			$1.51^{+0.12}_{-0.24}$	$3.67^{+0.19}_{-2.82}$	$1.51^{+0.12}_{-0.12}$	$3.70^{+0.18}_{-0.31}$		
5.2	1.9			$1.49^{+0.12}_{-0.18}$	$3.80^{+0.20}_{-2.82}$	$1.50^{+0.12}_{-0.12}$	$3.87^{+0.13}_{-0.28}$		
5.6	2.0			$1.49^{+0.14}_{-0.15}$	$3.79^{+0.20}_{-2.66}$	$1.50^{+0.13}_{-0.13}$	$3.92^{+0.08}_{-0.28}$		
6.1	2.2					$1.51^{+0.15}_{-0.14}$	$3.90^{+0.13}_{-0.28}$	$1.52^{+0.14}_{-0.13}$	$4.24^{+0.03}_{-0.15}$
6.5	2.3					$1.54^{+0.17}_{-0.16}$	$3.68^{+0.12}_{-0.21}$	$1.56^{+0.16}_{-0.15}$	$4.00^{+0.09}_{-0.14}$
7.0	2.5					$1.55^{+0.17}_{-0.16}$	$3.83^{+0.09}_{-0.18}$	$1.57^{+0.16}_{-0.15}$	$4.11^{+0.10}_{-0.15}$
7.4	2.6					$1.73^{+0.14}_{-0.13}$	$3.35^{+0.03}_{-0.03}$	$1.75^{+0.13}_{-0.12}$	$3.50^{+0.08}_{-0.13}$
7.9	2.8					$1.98^{+0.04}_{-0.04}$	$2.96^{+0.05}_{-0.01}$	$2.00^{+0.04}_{-0.04}$	$3.05^{+0.01}_{-0.06}$
8.3	3.0					$2.06^{+0.04}_{-0.04}$	$2.81^{+0.02}_{-0.06}$	$2.08^{+0.04}_{-0.04}$	$2.81^{+0.07}_{-0.02}$
8.8	3.1					$2.15^{+0.03}_{-0.03}$	$2.60^{+0.01}_{-0.01}$	$2.17^{+0.03}_{-0.03}$	$2.60^{+0.05}_{-0.01}$

Table B.15.: Model Parameters of NGC5194.

R [kpc]	R/R_d	Λ_0	$\sigma_g = 5$ km/s		$\sigma_g = 8$ km/s		$\sigma_g = 11$ km/s	
			s_0	q_0	s_0	q_0	s_0	q_0
0.2	0.1	$1.33^{+0.03}_{-0.03}$	$0.01^{+0.00}_{-0.00}$	$0.32^{+0.08}_{-0.06}$			$0.03^{+0.00}_{-0.00}$	$0.71^{+0.18}_{-0.13}$
0.6	0.2	$1.56^{+0.01}_{-0.01}$	$0.02^{+0.00}_{-0.00}$	$0.21^{+0.04}_{-0.03}$			$0.04^{+0.00}_{-0.00}$	$0.47^{+0.09}_{-0.07}$
1.0	0.4	$1.74^{+0.01}_{-0.01}$	$0.03^{+0.00}_{-0.00}$	$0.18^{+0.04}_{-0.03}$			$0.06^{+0.00}_{-0.00}$	$0.39^{+0.08}_{-0.06}$
1.4	0.5	$1.92^{+0.01}_{-0.01}$	$0.04^{+0.00}_{-0.00}$	$0.18^{+0.08}_{-0.04}$			$0.08^{+0.00}_{-0.00}$	$0.39^{+0.17}_{-0.09}$
1.7	0.6	$2.08^{+0.01}_{-0.01}$	$0.04^{+0.00}_{-0.00}$	$0.18^{+0.08}_{-0.04}$			$0.09^{+0.00}_{-0.00}$	$0.39^{+0.17}_{-0.09}$
2.1	0.8	$1.60^{+0.01}_{-0.01}$	$0.05^{+0.00}_{-0.00}$	$0.19^{+0.05}_{-0.03}$			$0.10^{+0.00}_{-0.00}$	$0.41^{+0.10}_{-0.07}$
2.5	0.9	$1.20^{+0.01}_{-0.01}$	$0.05^{+0.00}_{-0.00}$	$0.23^{+0.06}_{-0.04}$			$0.10^{+0.00}_{-0.00}$	$0.50^{+0.13}_{-0.09}$
2.9	1.0	$1.05^{+0.00}_{-0.00}$			$0.08^{+0.00}_{-0.00}$	$0.56^{+0.21}_{-0.12}$	$0.11^{+0.00}_{-0.00}$	$0.77^{+0.29}_{-0.17}$
3.3	1.2	$0.94^{+0.00}_{-0.00}$			$0.09^{+0.00}_{-0.00}$	$1.00^{+0.34}_{-0.20}$	$0.12^{+0.00}_{-0.00}$	$1.37^{+0.47}_{-0.28}$
3.7	1.3	$0.84^{+0.01}_{-0.01}$			$0.09^{+0.00}_{-0.00}$	$1.15^{+0.27}_{-0.19}$	$0.13^{+0.00}_{-0.00}$	$1.58^{+0.38}_{-0.26}$
4.1	1.5	$0.73^{+0.01}_{-0.01}$			$0.10^{+0.00}_{-0.00}$	$0.77^{+0.30}_{-0.17}$	$0.13^{+0.00}_{-0.00}$	$1.06^{+0.42}_{-0.24}$
4.5	1.6	$0.63^{+0.00}_{-0.00}$			$0.10^{+0.00}_{-0.00}$	$0.52^{+0.19}_{-0.11}$	$0.14^{+0.00}_{-0.00}$	$0.72^{+0.26}_{-0.15}$
4.8	1.7	$0.55^{+0.00}_{-0.00}$			$0.10^{+0.00}_{-0.00}$	$0.48^{+0.14}_{-0.09}$	$0.14^{+0.00}_{-0.00}$	$0.66^{+0.20}_{-0.12}$
5.2	1.9	$0.51^{+0.00}_{-0.00}$			$0.10^{+0.00}_{-0.00}$	$0.52^{+0.13}_{-0.09}$	$0.14^{+0.00}_{-0.00}$	$0.72^{+0.18}_{-0.12}$
5.6	2.0	$0.52^{+0.00}_{-0.00}$			$0.11^{+0.00}_{-0.00}$	$0.72^{+0.19}_{-0.12}$	$0.15^{+0.00}_{-0.00}$	$0.99^{+0.26}_{-0.17}$
6.0	2.1	$0.53^{+0.00}_{-0.00}$					$0.17^{+0.00}_{-0.00}$	$1.62^{+0.51}_{-0.32}$
6.4	2.3	$0.65^{+0.00}_{-0.00}$					$0.20^{+0.00}_{-0.00}$	$2.03^{+0.47}_{-0.34}$
6.8	2.4	$0.79^{+0.00}_{-0.00}$					$0.23^{+0.00}_{-0.00}$	$2.15^{+0.27}_{-0.22}$
7.2	2.6	$0.85^{+0.01}_{-0.01}$					$0.26^{+0.00}_{-0.00}$	$2.11^{+0.31}_{-0.24}$
7.6	2.7	$0.98^{+0.01}_{-0.01}$					$0.29^{+0.00}_{-0.00}$	$1.86^{+0.29}_{-0.23}$
8.0	2.9	$0.99^{+0.01}_{-0.01}$					$0.31^{+0.00}_{-0.00}$	$1.76^{+0.31}_{-0.23}$
8.3	3.0	$0.89^{+0.01}_{-0.01}$					$0.30^{+0.00}_{-0.00}$	$1.79^{+0.35}_{-0.25}$
8.7	3.1	$0.71^{+0.01}_{-0.01}$					$0.28^{+0.00}_{-0.00}$	$1.92^{+0.39}_{-0.28}$
9.1	3.2	$0.50^{+0.01}_{-0.01}$					$0.25^{+0.00}_{-0.00}$	$2.34^{+0.52}_{-0.38}$
9.5	3.4	$0.44^{+0.01}_{-0.01}$					$0.24^{+0.00}_{-0.00}$	$2.70^{+0.59}_{-0.43}$
9.9	3.5	$0.33^{+0.01}_{-0.01}$					$0.22^{+0.00}_{-0.00}$	$3.29^{+0.80}_{-0.57}$
10.3	3.7	$0.13^{+0.01}_{-0.01}$					$0.14^{+0.00}_{-0.00}$	$5.83^{+1.84}_{-1.26}$
10.7	3.8	$0.24^{+0.01}_{-0.01}$					$0.20^{+0.00}_{-0.00}$	$4.62^{+1.42}_{-0.94}$

Table B.16.: Stability Diagnostics of NGC5194.

		$\sigma_g = 5 \text{ km/s}$		$\sigma_g = 8 \text{ km/s}$		$\sigma_g = 11 \text{ km/s}$		$\sigma_g = 11 \text{ km/s, Turbulent}$	
R [kpc]	R/R_d	Q_{eff}	$\bar{\lambda}$ [kpc]	Q_{eff}	$\bar{\lambda}$ [kpc]	Q_{eff}	$\bar{\lambda}$ [kpc]	Q_{eff}	$\bar{\lambda}$ [kpc]
0.2	0.1	$0.85^{+0.23}_{-0.16}$	$0.08^{+0.02}_{-0.02}$			$1.82^{+0.46}_{-0.33}$	$0.08^{+0.02}_{-0.02}$		
0.6	0.2	$0.61^{+0.12}_{-0.09}$	$0.15^{+0.03}_{-0.02}$			$1.29^{+0.25}_{-0.19}$	$0.16^{+0.02}_{-0.03}$		
1.0	0.4	$0.53^{+0.11}_{-0.08}$	$0.22^{+0.04}_{-0.04}$			$1.12^{+0.22}_{-0.16}$	$0.24^{+0.04}_{-0.04}$		
1.4	0.5	$0.56^{+0.24}_{-0.13}$	$0.27^{+0.08}_{-0.08}$			$1.17^{+0.47}_{-0.26}$	$0.30^{+0.08}_{-0.08}$		
1.7	0.6	$0.58^{+0.25}_{-0.14}$	$0.30^{+0.09}_{-0.09}$			$1.21^{+0.48}_{-0.27}$	$0.34^{+0.09}_{-0.09}$		
2.1	0.8	$0.53^{+0.13}_{-0.09}$	$0.40^{+0.08}_{-0.08}$			$1.10^{+0.25}_{-0.17}$	$0.46^{+0.08}_{-0.08}$		
2.5	0.9	$0.57^{+0.15}_{-0.10}$	$0.45^{+0.09}_{-0.09}$			$1.15^{+0.27}_{-0.19}$	$0.53^{+0.09}_{-0.09}$		
2.9	1.0			$1.22^{+0.41}_{-0.25}$	$0.42^{+0.10}_{-0.09}$	$1.54^{+0.38}_{-0.29}$	$0.51^{+1.75}_{-0.00}$		
3.3	1.2			$1.87^{+0.09}_{-0.33}$	$0.35^{+2.27}_{-0.00}$	$1.88^{+0.09}_{-0.09}$	$2.58^{+0.05}_{-0.11}$		
3.7	1.3			$1.80^{+0.06}_{-0.11}$	$2.87^{+0.07}_{-2.44}$	$1.80^{+0.06}_{-0.06}$	$2.93^{+0.02}_{-0.10}$		
4.1	1.5			$1.31^{+0.34}_{-0.26}$	$0.60^{+2.74}_{-0.00}$	$1.53^{+0.12}_{-0.23}$	$3.12^{+0.24}_{-2.21}$		
4.5	1.6			$0.87^{+0.28}_{-0.17}$	$0.94^{+0.20}_{-0.20}$	$1.09^{+0.29}_{-0.20}$	$1.16^{+0.17}_{-0.08}$		
4.8	1.7			$0.74^{+0.20}_{-0.13}$	$1.16^{+0.21}_{-0.22}$	$0.94^{+0.22}_{-0.15}$	$1.40^{+0.19}_{-0.15}$		
5.2	1.9			$0.78^{+0.17}_{-0.12}$	$1.22^{+0.20}_{-0.19}$	$0.97^{+0.18}_{-0.14}$	$1.53^{+0.16}_{-0.11}$		
5.6	2.0			$1.01^{+0.21}_{-0.15}$	$1.08^{+0.16}_{-0.12}$	$1.20^{+0.10}_{-0.15}$	$1.74^{+2.74}_{-0.10}$		
6.0	2.1					$1.38^{+0.07}_{-0.07}$	$4.57^{+0.09}_{-0.20}$	$1.38^{+0.07}_{-0.07}$	$4.96^{+0.10}_{-0.03}$
6.4	2.3					$1.55^{+0.06}_{-0.06}$	$3.76^{+0.07}_{-0.06}$	$1.57^{+0.05}_{-0.06}$	$4.03^{+0.08}_{-0.02}$
6.8	2.4					$1.68^{+0.04}_{-0.04}$	$3.10^{+0.05}_{-0.01}$	$1.72^{+0.04}_{-0.04}$	$3.37^{+0.01}_{-0.06}$
7.2	2.6					$1.70^{+0.06}_{-0.06}$	$2.92^{+0.03}_{-0.07}$	$1.76^{+0.05}_{-0.05}$	$3.13^{+0.03}_{-0.03}$
7.6	2.7					$1.73^{+0.07}_{-0.07}$	$2.54^{+0.05}_{-0.05}$	$1.81^{+0.06}_{-0.06}$	$2.77^{+0.02}_{-0.06}$
8.0	2.9					$1.69^{+0.08}_{-0.08}$	$2.56^{+0.02}_{-0.05}$	$1.77^{+0.08}_{-0.07}$	$2.75^{+0.06}_{-0.02}$
8.3	3.0					$1.62^{+0.08}_{-0.08}$	$2.80^{+0.06}_{-0.06}$	$1.68^{+0.08}_{-0.07}$	$3.05^{+0.07}_{-0.02}$
8.7	3.1					$1.49^{+0.07}_{-0.07}$	$3.53^{+0.09}_{-0.09}$	$1.52^{+0.07}_{-0.07}$	$3.85^{+0.10}_{-0.04}$
9.1	3.2					$1.34^{+0.06}_{-0.06}$	$5.03^{+0.20}_{-0.20}$	$1.33^{+0.07}_{-0.07}$	$5.39^{+0.22}_{-0.14}$
9.5	3.4					$1.30^{+0.05}_{-0.05}$	$5.64^{+0.18}_{-0.10}$	$1.29^{+0.05}_{-0.05}$	$6.05^{+0.20}_{-0.20}$
9.9	3.5					$1.18^{+0.04}_{-0.04}$	$7.54^{+0.15}_{-0.25}$	$1.16^{+0.04}_{-0.04}$	$7.86^{+0.27}_{-0.15}$
10.3	3.7					$0.79^{+0.03}_{-0.03}$	$19.84^{+1.07}_{-1.07}$	$0.77^{+0.03}_{-0.03}$	$20.39^{+1.10}_{-1.38}$
10.7	3.8					$1.04^{+0.04}_{-0.04}$	$10.46^{+0.32}_{-0.32}$	$1.02^{+0.04}_{-0.04}$	$10.91^{+0.33}_{-0.48}$

Table B.17.: Model Parameters of NGC3521.

R [kpc]	R/R_d	Λ_0	$\sigma_g = 5$ km/s		$\sigma_g = 8$ km/s		$\sigma_g = 11$ km/s	
			s_0	q_0	s_0	q_0	s_0	q_0
0.3	0.1	$0.53^{+0.04}_{-0.03}$	$0.01^{+0.00}_{-0.00}$	$2.04^{+0.64}_{-0.45}$			$0.03^{+0.00}_{-0.00}$	$4.50^{+1.40}_{-0.98}$
0.8	0.3	$1.09^{+0.02}_{-0.02}$	$0.02^{+0.00}_{-0.00}$	$0.86^{+0.17}_{-0.13}$			$0.05^{+0.00}_{-0.00}$	$1.90^{+0.37}_{-0.28}$
1.3	0.4	$1.14^{+0.01}_{-0.01}$	$0.03^{+0.00}_{-0.00}$	$0.57^{+0.05}_{-0.05}$			$0.07^{+0.00}_{-0.00}$	$1.25^{+0.12}_{-0.10}$
1.8	0.6	$1.25^{+0.01}_{-0.01}$	$0.04^{+0.00}_{-0.00}$	$0.43^{+0.03}_{-0.02}$			$0.08^{+0.00}_{-0.00}$	$0.95^{+0.06}_{-0.05}$
2.3	0.8	$1.13^{+0.01}_{-0.01}$	$0.04^{+0.00}_{-0.00}$	$0.40^{+0.03}_{-0.03}$			$0.09^{+0.00}_{-0.00}$	$0.87^{+0.06}_{-0.06}$
2.9	1.0	$0.94^{+0.00}_{-0.00}$	$0.05^{+0.00}_{-0.00}$	$0.39^{+0.04}_{-0.03}$			$0.10^{+0.00}_{-0.00}$	$0.86^{+0.08}_{-0.07}$
3.4	1.2	$0.84^{+0.00}_{-0.00}$			$0.08^{+0.00}_{-0.00}$	$0.67^{+0.07}_{-0.06}$	$0.11^{+0.00}_{-0.00}$	$0.92^{+0.09}_{-0.08}$
3.9	1.3	$0.83^{+0.01}_{-0.01}$			$0.09^{+0.00}_{-0.00}$	$0.69^{+0.08}_{-0.07}$	$0.13^{+0.00}_{-0.00}$	$0.95^{+0.11}_{-0.09}$
4.4	1.5	$0.78^{+0.01}_{-0.01}$			$0.10^{+0.00}_{-0.00}$	$0.66^{+0.07}_{-0.06}$	$0.14^{+0.00}_{-0.00}$	$0.91^{+0.10}_{-0.08}$
4.9	1.7	$0.69^{+0.00}_{-0.00}$			$0.11^{+0.00}_{-0.00}$	$0.64^{+0.07}_{-0.06}$	$0.15^{+0.00}_{-0.00}$	$0.88^{+0.09}_{-0.08}$
5.4	1.9	$0.64^{+0.00}_{-0.00}$			$0.11^{+0.00}_{-0.00}$	$0.68^{+0.09}_{-0.07}$	$0.15^{+0.00}_{-0.00}$	$0.94^{+0.12}_{-0.10}$
6.0	2.1	$0.65^{+0.00}_{-0.00}$					$0.17^{+0.00}_{-0.00}$	$1.03^{+0.16}_{-0.13}$
6.5	2.2	$0.69^{+0.01}_{-0.01}$					$0.20^{+0.00}_{-0.00}$	$1.12^{+0.19}_{-0.14}$
7.0	2.4	$0.77^{+0.01}_{-0.01}$					$0.22^{+0.00}_{-0.00}$	$1.25^{+0.18}_{-0.14}$
7.5	2.6	$0.83^{+0.01}_{-0.01}$					$0.25^{+0.00}_{-0.00}$	$1.39^{+0.19}_{-0.15}$
8.0	2.8	$0.87^{+0.01}_{-0.01}$					$0.27^{+0.00}_{-0.00}$	$1.43^{+0.19}_{-0.15}$
8.6	3.0	$0.87^{+0.01}_{-0.01}$					$0.29^{+0.00}_{-0.00}$	$1.36^{+0.17}_{-0.14}$
9.1	3.1	$0.89^{+0.01}_{-0.01}$					$0.31^{+0.00}_{-0.00}$	$1.28^{+0.15}_{-0.13}$
9.6	3.3	$0.93^{+0.01}_{-0.01}$					$0.34^{+0.00}_{-0.00}$	$1.24^{+0.16}_{-0.13}$
10.1	3.5	$0.98^{+0.01}_{-0.01}$					$0.36^{+0.00}_{-0.00}$	$1.36^{+0.12}_{-0.10}$
10.6	3.7	$1.00^{+0.01}_{-0.01}$					$0.39^{+0.00}_{-0.00}$	$1.29^{+0.14}_{-0.12}$
11.2	3.9	$0.96^{+0.01}_{-0.01}$					$0.40^{+0.00}_{-0.00}$	$1.25^{+0.15}_{-0.13}$
11.7	4.0	$0.97^{+0.01}_{-0.01}$					$0.42^{+0.00}_{-0.00}$	$1.18^{+0.16}_{-0.13}$
12.2	4.2	$1.03^{+0.01}_{-0.01}$					$0.45^{+0.00}_{-0.00}$	$1.09^{+0.15}_{-0.12}$
12.7	4.4	$1.09^{+0.01}_{-0.01}$					$0.48^{+0.00}_{-0.00}$	$1.02^{+0.14}_{-0.11}$
13.2	4.6	$1.12^{+0.01}_{-0.01}$					$0.51^{+0.00}_{-0.00}$	$1.00^{+0.14}_{-0.11}$
13.7	4.7	$1.13^{+0.01}_{-0.01}$					$0.53^{+0.00}_{-0.00}$	$0.97^{+0.15}_{-0.12}$
14.3	4.9	$1.12^{+0.01}_{-0.01}$					$0.55^{+0.00}_{-0.00}$	$0.95^{+0.14}_{-0.11}$
14.8	5.1	$1.16^{+0.01}_{-0.01}$					$0.58^{+0.00}_{-0.00}$	$0.98^{+0.14}_{-0.11}$
15.3	5.3	$1.20^{+0.01}_{-0.01}$					$0.61^{+0.00}_{-0.00}$	$1.02^{+0.12}_{-0.10}$

Table B.18.: Stability Diagnostics of NGC3521.

		$\sigma_g = 5 \text{ km/s}$		$\sigma_g = 8 \text{ km/s}$		$\sigma_g = 11 \text{ km/s}$		$\sigma_g = 11 \text{ km/s, Turbulent}$	
R [kpc]	R/R_d	Q_{eff}	$\bar{\lambda}$ [kpc]	Q_{eff}	$\bar{\lambda}$ [kpc]	Q_{eff}	$\bar{\lambda}$ [kpc]	Q_{eff}	$\bar{\lambda}$ [kpc]
0.3	0.1	$1.68^{+0.06}_{-0.06}$	$4.79^{+0.30}_{-0.30}$			$1.68^{+0.06}_{-0.06}$	$4.80^{+0.30}_{-0.30}$		
0.8	0.3	$2.03^{+0.32}_{-0.30}$	$0.07^{+2.28}_{-0.00}$			$2.32^{+0.04}_{-0.04}$	$2.29^{+0.04}_{-0.04}$		
1.3	0.4	$1.38^{+0.13}_{-0.11}$	$0.12^{+0.01}_{-0.01}$			$2.26^{+0.03}_{-0.03}$	$2.18^{+0.02}_{-0.05}$		
1.8	0.6	$1.09^{+0.07}_{-0.06}$	$0.19^{+0.01}_{-0.01}$			$2.12^{+0.11}_{-0.10}$	$0.25^{+1.71}_{-0.01}$		
2.3	0.8	$0.95^{+0.07}_{-0.06}$	$0.26^{+0.02}_{-0.02}$			$1.85^{+0.11}_{-0.10}$	$0.34^{+0.02}_{-0.02}$		
2.9	1.0	$0.86^{+0.08}_{-0.07}$	$0.34^{+0.03}_{-0.03}$			$1.65^{+0.13}_{-0.11}$	$0.47^{+0.02}_{-0.02}$		
3.4	1.2			$1.29^{+0.12}_{-0.10}$	$0.46^{+0.04}_{-0.03}$	$1.61^{+0.11}_{-0.11}$	$0.59^{+2.21}_{-0.00}$		
3.9	1.3			$1.31^{+0.13}_{-0.11}$	$0.53^{+0.04}_{-0.04}$	$1.60^{+0.09}_{-0.12}$	$0.72^{+2.06}_{-0.01}$		
4.4	1.5			$1.20^{+0.12}_{-0.10}$	$0.66^{+0.04}_{-0.05}$	$1.47^{+0.11}_{-0.11}$	$0.90^{+1.93}_{-0.01}$		
4.9	1.7			$1.10^{+0.10}_{-0.09}$	$0.81^{+0.05}_{-0.06}$	$1.33^{+0.10}_{-0.09}$	$1.11^{+0.04}_{-0.02}$		
5.4	1.9			$1.10^{+0.12}_{-0.10}$	$0.91^{+0.06}_{-0.07}$	$1.32^{+0.09}_{-0.10}$	$1.35^{+1.99}_{-0.03}$		
6.0	2.1					$1.35^{+0.08}_{-0.10}$	$2.90^{+0.53}_{-1.26}$	$1.39^{+0.07}_{-0.06}$	$4.12^{+0.03}_{-0.09}$
6.5	2.2					$1.39^{+0.08}_{-0.09}$	$2.98^{+0.32}_{-0.81}$	$1.44^{+0.07}_{-0.07}$	$3.85^{+0.03}_{-0.03}$
7.0	2.4					$1.47^{+0.07}_{-0.07}$	$2.87^{+0.18}_{-0.24}$	$1.53^{+0.07}_{-0.06}$	$3.47^{+0.03}_{-0.03}$
7.5	2.6					$1.54^{+0.07}_{-0.07}$	$2.80^{+0.10}_{-0.13}$	$1.61^{+0.06}_{-0.06}$	$3.25^{+0.03}_{-0.03}$
8.0	2.8					$1.55^{+0.07}_{-0.07}$	$2.75^{+0.06}_{-0.10}$	$1.63^{+0.06}_{-0.06}$	$3.11^{+0.03}_{-0.03}$
8.6	3.0					$1.50^{+0.07}_{-0.07}$	$2.78^{+0.06}_{-0.10}$	$1.57^{+0.06}_{-0.06}$	$3.15^{+0.03}_{-0.03}$
9.1	3.1					$1.45^{+0.07}_{-0.07}$	$2.76^{+0.06}_{-0.06}$	$1.53^{+0.07}_{-0.07}$	$3.14^{+0.02}_{-0.07}$
9.6	3.3					$1.44^{+0.08}_{-0.07}$	$2.72^{+0.06}_{-0.02}$	$1.52^{+0.08}_{-0.07}$	$3.05^{+0.03}_{-0.07}$
10.1	3.5					$1.51^{+0.05}_{-0.05}$	$2.67^{+0.05}_{-0.02}$	$1.59^{+0.05}_{-0.05}$	$2.88^{+0.06}_{-0.02}$
10.6	3.7					$1.48^{+0.07}_{-0.06}$	$2.72^{+0.06}_{-0.06}$	$1.55^{+0.07}_{-0.06}$	$2.91^{+0.02}_{-0.06}$
11.2	3.9					$1.41^{+0.07}_{-0.07}$	$2.89^{+0.06}_{-0.06}$	$1.48^{+0.08}_{-0.07}$	$3.09^{+0.07}_{-0.07}$
11.7	4.0					$1.37^{+0.08}_{-0.08}$	$2.96^{+0.11}_{-0.07}$	$1.43^{+0.09}_{-0.08}$	$3.13^{+0.07}_{-0.12}$
12.2	4.2					$1.34^{+0.09}_{-0.08}$	$2.97^{+0.15}_{-0.11}$	$1.39^{+0.09}_{-0.09}$	$3.06^{+0.12}_{-0.12}$
12.7	4.4					$1.32^{+0.08}_{-0.08}$	$3.00^{+0.10}_{-0.10}$	$1.37^{+0.09}_{-0.08}$	$3.02^{+0.11}_{-0.10}$
13.2	4.6					$1.31^{+0.09}_{-0.08}$	$3.04^{+0.14}_{-0.14}$	$1.36^{+0.09}_{-0.09}$	$3.03^{+0.11}_{-0.15}$
13.7	4.7					$1.29^{+0.10}_{-0.09}$	$3.13^{+0.15}_{-0.14}$	$1.33^{+0.11}_{-0.10}$	$3.08^{+0.16}_{-0.15}$
14.3	4.9					$1.27^{+0.09}_{-0.08}$	$3.23^{+0.16}_{-0.15}$	$1.30^{+0.10}_{-0.09}$	$3.20^{+0.17}_{-0.16}$
14.8	5.1					$1.30^{+0.09}_{-0.08}$	$3.21^{+0.16}_{-0.15}$	$1.34^{+0.10}_{-0.09}$	$3.13^{+0.17}_{-0.16}$
15.3	5.3					$1.34^{+0.08}_{-0.07}$	$3.16^{+0.16}_{-0.15}$	$1.37^{+0.08}_{-0.08}$	$3.09^{+0.12}_{-0.16}$

Table B.19.: Model Parameters of NGC2841.

R [kpc]	R/R_d	Λ_0	$\sigma_g = 5$ km/s		$\sigma_g = 8$ km/s		$\sigma_g = 11$ km/s	
			s_0	q_0	s_0	q_0	s_0	q_0
3.8	0.9	$1.84^{+0.01}_{-0.01}$	$0.05^{+0.00}_{-0.00}$	$2.72^{+5.35}_{-1.10}$			$0.12^{+0.00}_{-0.00}$	$5.99^{+11.77}_{-2.42}$
4.4	1.1	$1.64^{+0.01}_{-0.01}$			$0.10^{+0.00}_{-0.00}$	$2.43^{+1.48}_{-0.68}$	$0.13^{+0.00}_{-0.00}$	$3.35^{+2.04}_{-0.93}$
5.1	1.3	$1.40^{+0.01}_{-0.01}$			$0.10^{+0.00}_{-0.00}$	$2.27^{+1.21}_{-0.59}$	$0.14^{+0.00}_{-0.00}$	$3.12^{+1.66}_{-0.81}$
5.8	1.4	$1.23^{+0.01}_{-0.01}$			$0.11^{+0.00}_{-0.00}$	$2.46^{+1.89}_{-0.75}$	$0.15^{+0.00}_{-0.00}$	$3.38^{+2.60}_{-1.04}$
6.5	1.6	$1.13^{+0.00}_{-0.00}$			$0.12^{+0.00}_{-0.00}$	$2.51^{+2.44}_{-0.83}$	$0.16^{+0.00}_{-0.00}$	$3.45^{+3.36}_{-1.15}$
7.2	1.8	$1.06^{+0.00}_{-0.00}$			$0.13^{+0.00}_{-0.00}$	$2.37^{+2.59}_{-0.82}$	$0.17^{+0.00}_{-0.00}$	$3.26^{+3.56}_{-1.13}$
7.9	2.0	$0.96^{+0.01}_{-0.01}$			$0.13^{+0.00}_{-0.00}$	$2.36^{+2.07}_{-0.77}$	$0.18^{+0.00}_{-0.00}$	$3.25^{+2.85}_{-1.05}$
8.5	2.1	$0.98^{+0.00}_{-0.00}$					$0.20^{+0.00}_{-0.00}$	$3.41^{+2.39}_{-1.00}$
9.2	2.3	$0.95^{+0.01}_{-0.01}$					$0.21^{+0.00}_{-0.00}$	$3.61^{+1.46}_{-0.82}$
9.9	2.5	$0.93^{+0.00}_{-0.00}$					$0.22^{+0.00}_{-0.00}$	$4.55^{+0.20}_{-0.19}$
10.6	2.6	$0.94^{+0.01}_{-0.01}$					$0.24^{+0.00}_{-0.00}$	$4.09^{+0.18}_{-0.17}$
11.3	2.8	$0.99^{+0.00}_{-0.00}$					$0.26^{+0.00}_{-0.00}$	$3.74^{+0.16}_{-0.15}$
12.0	3.0	$1.01^{+0.01}_{-0.01}$					$0.28^{+0.00}_{-0.00}$	$3.74^{+0.17}_{-0.16}$
12.6	3.1	$1.05^{+0.01}_{-0.01}$					$0.30^{+0.00}_{-0.00}$	$3.91^{+0.22}_{-0.20}$
13.3	3.3	$1.09^{+0.02}_{-0.02}$					$0.32^{+0.00}_{-0.00}$	$4.13^{+0.51}_{-0.42}$
14.0	3.5	$1.19^{+0.01}_{-0.01}$					$0.36^{+0.00}_{-0.00}$	$3.93^{+0.47}_{-0.39}$
14.7	3.7	$1.18^{+0.02}_{-0.02}$					$0.37^{+0.00}_{-0.00}$	$3.58^{+0.28}_{-0.25}$
15.4	3.9	$0.57^{+0.08}_{-0.06}$					$0.27^{+0.02}_{-0.02}$	$4.91^{+1.26}_{-1.03}$
16.1	4.0	$1.25^{+0.06}_{-0.06}$					$0.42^{+0.01}_{-0.01}$	$3.33^{+0.43}_{-0.37}$
16.7	4.2	$1.60^{+0.01}_{-0.01}$					$0.49^{+0.00}_{-0.00}$	$2.98^{+0.20}_{-0.18}$

Table B.20.: Stability Diagnostics of NGC2841.

		$\sigma_g = 5 \text{ km/s}$		$\sigma_g = 8 \text{ km/s}$		$\sigma_g = 11 \text{ km/s}$		$\sigma_g = 11 \text{ km/s, Turbulent}$	
R [kpc]	R/R_d	Q_{eff}	$\bar{\lambda}$ [kpc]	Q_{eff}	$\bar{\lambda}$ [kpc]	Q_{eff}	$\bar{\lambda}$ [kpc]	Q_{eff}	$\bar{\lambda}$ [kpc]
3.8	0.9	$3.59^{+0.11}_{-0.11}$	$1.37^{+0.01}_{-0.03}$			$3.59^{+0.11}_{-0.11}$	$1.38^{+0.01}_{-0.03}$		
4.4	1.1			$3.27^{+0.11}_{-0.11}$	$1.52^{+0.03}_{-0.01}$	$3.27^{+0.11}_{-0.10}$	$1.52^{+0.03}_{-0.01}$		
5.1	1.3			$2.99^{+0.10}_{-0.10}$	$1.77^{+0.03}_{-0.01}$	$2.99^{+0.10}_{-0.10}$	$1.78^{+0.03}_{-0.01}$		
5.8	1.4			$2.80^{+0.12}_{-0.11}$	$2.02^{+0.04}_{-0.01}$	$2.80^{+0.11}_{-0.11}$	$2.03^{+0.04}_{-0.01}$		
6.5	1.6			$2.67^{+0.13}_{-0.12}$	$2.21^{+0.04}_{-0.04}$	$2.67^{+0.13}_{-0.12}$	$2.21^{+0.04}_{-0.01}$		
7.2	1.8			$2.56^{+0.15}_{-0.14}$	$2.33^{+0.04}_{-0.04}$	$2.57^{+0.15}_{-0.14}$	$2.34^{+0.04}_{-0.04}$		
7.9	2.0			$2.43^{+0.14}_{-0.13}$	$2.57^{+0.06}_{-0.06}$	$2.43^{+0.14}_{-0.13}$	$2.58^{+0.06}_{-0.06}$		
8.5	2.1					$2.44^{+0.12}_{-0.11}$	$2.55^{+0.04}_{-0.01}$	$2.49^{+0.10}_{-0.10}$	$2.66^{+0.01}_{-0.05}$
9.2	2.3					$2.41^{+0.08}_{-0.08}$	$2.66^{+0.02}_{-0.05}$	$2.45^{+0.07}_{-0.07}$	$2.74^{+0.02}_{-0.06}$
9.9	2.5					$2.42^{+0.02}_{-0.02}$	$2.72^{+0.01}_{-0.01}$	$2.46^{+0.01}_{-0.01}$	$2.79^{+0.01}_{-0.01}$
10.6	2.6					$2.39^{+0.02}_{-0.02}$	$2.70^{+0.02}_{-0.02}$	$2.44^{+0.02}_{-0.02}$	$2.77^{+0.02}_{-0.02}$
11.3	2.8					$2.41^{+0.02}_{-0.02}$	$2.55^{+0.01}_{-0.01}$	$2.47^{+0.02}_{-0.02}$	$2.62^{+0.01}_{-0.01}$
12.0	3.0					$2.41^{+0.02}_{-0.02}$	$2.51^{+0.01}_{-0.01}$	$2.47^{+0.02}_{-0.02}$	$2.62^{+0.01}_{-0.05}$
12.6	3.1					$2.46^{+0.03}_{-0.03}$	$2.45^{+0.02}_{-0.02}$	$2.52^{+0.03}_{-0.03}$	$2.52^{+0.02}_{-0.06}$
13.3	3.3					$2.51^{+0.05}_{-0.05}$	$2.35^{+0.03}_{-0.03}$	$2.57^{+0.05}_{-0.05}$	$2.42^{+0.03}_{-0.07}$
14.0	3.5					$2.57^{+0.05}_{-0.05}$	$2.18^{+0.02}_{-0.05}$	$2.65^{+0.05}_{-0.05}$	$2.22^{+0.02}_{-0.02}$
14.7	3.7					$2.52^{+0.05}_{-0.05}$	$2.19^{+0.04}_{-0.04}$	$2.60^{+0.05}_{-0.05}$	$2.26^{+0.04}_{-0.08}$
15.4	3.9					$1.89^{+0.16}_{-0.14}$	$4.39^{+0.54}_{-0.54}$	$1.89^{+0.17}_{-0.15}$	$4.51^{+0.63}_{-0.56}$
16.1	4.0					$2.52^{+0.11}_{-0.11}$	$2.12^{+0.10}_{-0.13}$	$2.61^{+0.11}_{-0.11}$	$2.16^{+0.10}_{-0.13}$
16.7	4.2					$2.73^{+0.05}_{-0.05}$	$1.73^{+0.01}_{-0.04}$	$2.86^{+0.05}_{-0.05}$	$1.72^{+0.01}_{-0.04}$

Table B.21.: Model Parameters of NGC5055.

R [kpc]	R/R_d	Λ_0	$\sigma_g = 5$ km/s		$\sigma_g = 8$ km/s		$\sigma_g = 11$ km/s	
			s_0	q_0	s_0	q_0	s_0	q_0
0.2	0.1	$1.32^{+0.07}_{-0.07}$	$0.01^{+0.00}_{-0.00}$	$0.40^{+0.10}_{-0.08}$			$0.03^{+0.00}_{-0.00}$	$0.89^{+0.22}_{-0.17}$
0.7	0.2	$1.73^{+0.01}_{-0.01}$	$0.02^{+0.00}_{-0.00}$	$0.34^{+0.07}_{-0.05}$			$0.05^{+0.00}_{-0.00}$	$0.74^{+0.15}_{-0.11}$
1.2	0.4	$1.42^{+0.01}_{-0.01}$	$0.03^{+0.00}_{-0.00}$	$0.40^{+0.06}_{-0.05}$			$0.06^{+0.00}_{-0.00}$	$0.88^{+0.14}_{-0.11}$
1.7	0.5	$1.02^{+0.00}_{-0.00}$	$0.03^{+0.00}_{-0.00}$	$0.48^{+0.05}_{-0.04}$			$0.07^{+0.00}_{-0.00}$	$1.06^{+0.10}_{-0.09}$
2.2	0.7	$0.83^{+0.00}_{-0.00}$	$0.04^{+0.00}_{-0.00}$	$0.49^{+0.03}_{-0.03}$			$0.08^{+0.00}_{-0.00}$	$1.07^{+0.07}_{-0.07}$
2.7	0.8	$0.74^{+0.00}_{-0.00}$	$0.04^{+0.00}_{-0.00}$	$0.46^{+0.04}_{-0.03}$			$0.09^{+0.00}_{-0.00}$	$1.01^{+0.09}_{-0.07}$
3.2	1.0	$0.67^{+0.00}_{-0.00}$	$0.05^{+0.00}_{-0.00}$	$0.50^{+0.06}_{-0.05}$			$0.11^{+0.00}_{-0.00}$	$1.09^{+0.12}_{-0.10}$
3.7	1.2	$0.61^{+0.00}_{-0.00}$			$0.09^{+0.00}_{-0.00}$	$0.86^{+0.11}_{-0.09}$	$0.12^{+0.00}_{-0.00}$	$1.18^{+0.14}_{-0.12}$
4.2	1.3	$0.54^{+0.00}_{-0.00}$			$0.09^{+0.00}_{-0.00}$	$0.83^{+0.10}_{-0.08}$	$0.13^{+0.00}_{-0.00}$	$1.14^{+0.13}_{-0.11}$
4.7	1.5	$0.51^{+0.00}_{-0.00}$			$0.10^{+0.00}_{-0.00}$	$0.75^{+0.09}_{-0.07}$	$0.14^{+0.00}_{-0.00}$	$1.04^{+0.13}_{-0.10}$
5.1	1.6	$0.50^{+0.00}_{-0.00}$			$0.11^{+0.00}_{-0.00}$	$0.67^{+0.08}_{-0.07}$	$0.15^{+0.00}_{-0.00}$	$0.92^{+0.11}_{-0.09}$
5.6	1.7	$0.46^{+0.00}_{-0.00}$			$0.11^{+0.00}_{-0.00}$	$0.66^{+0.07}_{-0.06}$	$0.16^{+0.00}_{-0.00}$	$0.91^{+0.09}_{-0.08}$
6.1	1.9	$0.44^{+0.00}_{-0.00}$			$0.12^{+0.00}_{-0.00}$	$0.73^{+0.06}_{-0.05}$	$0.17^{+0.00}_{-0.00}$	$1.00^{+0.08}_{-0.07}$
6.6	2.1	$0.46^{+0.00}_{-0.00}$					$0.18^{+0.00}_{-0.00}$	$1.03^{+0.10}_{-0.08}$
7.1	2.2	$0.46^{+0.00}_{-0.00}$					$0.20^{+0.00}_{-0.00}$	$0.99^{+0.09}_{-0.08}$
7.6	2.4	$0.45^{+0.00}_{-0.00}$					$0.21^{+0.00}_{-0.00}$	$0.95^{+0.10}_{-0.08}$
8.1	2.5	$0.44^{+0.00}_{-0.00}$					$0.22^{+0.00}_{-0.00}$	$0.97^{+0.12}_{-0.10}$
8.6	2.7	$0.47^{+0.00}_{-0.00}$					$0.24^{+0.00}_{-0.00}$	$1.08^{+0.12}_{-0.10}$
9.1	2.8	$0.51^{+0.00}_{-0.00}$					$0.27^{+0.00}_{-0.00}$	$1.17^{+0.14}_{-0.11}$
9.5	3.0	$0.54^{+0.00}_{-0.00}$					$0.29^{+0.00}_{-0.00}$	$1.22^{+0.15}_{-0.12}$
10.0	3.1	$0.53^{+0.00}_{-0.00}$					$0.30^{+0.00}_{-0.00}$	$1.32^{+0.20}_{-0.15}$
10.5	3.3	$0.54^{+0.00}_{-0.00}$					$0.32^{+0.00}_{-0.00}$	$1.32^{+0.21}_{-0.16}$
11.0	3.4	$0.54^{+0.00}_{-0.00}$					$0.33^{+0.00}_{-0.00}$	$1.29^{+0.24}_{-0.17}$
11.5	3.6	$0.27^{+0.03}_{-0.02}$					$0.25^{+0.01}_{-0.01}$	$2.04^{+0.54}_{-0.42}$
12.0	3.8	$0.26^{+0.03}_{-0.02}$					$0.25^{+0.01}_{-0.01}$	$2.20^{+0.54}_{-0.43}$
12.5	3.9	$0.56^{+0.00}_{-0.00}$					$0.39^{+0.00}_{-0.00}$	$1.49^{+0.14}_{-0.12}$
13.0	4.1	$0.61^{+0.00}_{-0.00}$					$0.42^{+0.00}_{-0.00}$	$1.42^{+0.14}_{-0.12}$
13.5	4.2	$0.64^{+0.00}_{-0.00}$					$0.44^{+0.00}_{-0.00}$	$1.45^{+0.15}_{-0.13}$
14.0	4.4	$0.64^{+0.00}_{-0.00}$					$0.46^{+0.00}_{-0.00}$	$1.56^{+0.15}_{-0.13}$
14.4	4.5	$0.58^{+0.02}_{-0.02}$					$0.45^{+0.01}_{-0.01}$	$1.81^{+0.26}_{-0.22}$
14.9	4.7	$0.71^{+0.00}_{-0.00}$					$0.52^{+0.00}_{-0.00}$	$1.70^{+0.23}_{-0.18}$
15.4	4.8	$0.70^{+0.01}_{-0.01}$					$0.53^{+0.00}_{-0.00}$	$1.79^{+0.35}_{-0.26}$
15.9	5.0	$0.73^{+0.00}_{-0.00}$					$0.56^{+0.00}_{-0.00}$	$1.78^{+0.28}_{-0.21}$
16.4	5.1	$0.76^{+0.00}_{-0.00}$					$0.59^{+0.00}_{-0.00}$	$1.96^{+0.28}_{-0.22}$
16.9	5.3	$0.78^{+0.00}_{-0.00}$					$0.61^{+0.00}_{-0.00}$	$2.14^{+0.36}_{-0.27}$
17.4	5.4	$0.78^{+0.00}_{-0.00}$					$0.63^{+0.00}_{-0.00}$	$2.24^{+0.41}_{-0.30}$
17.9	5.6	$0.81^{+0.00}_{-0.00}$					$0.66^{+0.00}_{-0.00}$	$2.22^{+0.30}_{-0.24}$
18.4	5.7	$0.77^{+0.01}_{-0.01}$					$0.66^{+0.00}_{-0.00}$	$2.32^{+0.38}_{-0.29}$
18.9	5.9	$0.79^{+0.01}_{-0.01}$					$0.69^{+0.00}_{-0.00}$	$2.53^{+0.32}_{-0.27}$
19.3	6.0	$0.79^{+0.02}_{-0.02}$					$0.70^{+0.01}_{-0.01}$	$3.07^{+0.55}_{-0.43}$
19.8	6.2	$0.78^{+0.02}_{-0.02}$					$0.72^{+0.01}_{-0.01}$	$3.65^{+0.79}_{-0.59}$
20.3	6.3	$0.40^{+0.03}_{-0.03}$					$0.53^{+0.02}_{-0.02}$	$5.36^{+1.73}_{-1.22}$
20.8	6.5	$0.41^{+0.05}_{-0.04}$					$0.54^{+0.03}_{-0.03}$	$5.63^{+2.35}_{-1.57}$

Table B.22.: Stability Diagnostics of NGC5055.

		$\sigma_g = 5 \text{ km/s}$		$\sigma_g = 8 \text{ km/s}$		$\sigma_g = 11 \text{ km/s}$		$\sigma_g = 11 \text{ km/s, Turbulent}$	
R [kpc]	R/R_d	Q_{eff}	$\bar{\lambda}$ [kpc]	Q_{eff}	$\bar{\lambda}$ [kpc]	Q_{eff}	$\bar{\lambda}$ [kpc]	Q_{eff}	$\bar{\lambda}$ [kpc]
0.2	0.1	$1.14^{+0.32}_{-0.23}$	$0.06^{+0.02}_{-0.01}$			$2.41^{+0.37}_{-0.48}$	$0.07^{+1.92}_{-0.00}$		
0.7	0.2	$1.08^{+0.22}_{-0.16}$	$0.10^{+0.02}_{-0.02}$			$2.24^{+0.42}_{-0.31}$	$0.11^{+0.02}_{-0.02}$		
1.2	0.4	$1.16^{+0.18}_{-0.14}$	$0.13^{+0.02}_{-0.02}$			$2.34^{+0.28}_{-0.26}$	$0.15^{+1.59}_{-0.00}$		
1.7	0.5	$1.17^{+0.11}_{-0.09}$	$0.17^{+0.02}_{-0.01}$			$2.19^{+0.03}_{-0.06}$	$2.40^{+0.01}_{-2.17}$		
2.2	0.7	$1.05^{+0.07}_{-0.06}$	$0.24^{+0.02}_{-0.01}$			$1.93^{+0.02}_{-0.02}$	$2.93^{+0.05}_{-0.01}$		
2.7	0.8	$0.94^{+0.08}_{-0.07}$	$0.34^{+0.03}_{-0.02}$			$1.77^{+0.03}_{-0.09}$	$3.22^{+0.05}_{-2.72}$		
3.2	1.0	$0.96^{+0.10}_{-0.09}$	$0.40^{+0.04}_{-0.04}$			$1.66^{+0.04}_{-0.05}$	$3.56^{+0.06}_{-2.91}$		
3.7	1.2			$1.43^{+0.15}_{-0.12}$	$0.57^{+0.04}_{-0.04}$	$1.58^{+0.04}_{-0.04}$	$3.90^{+0.06}_{-0.11}$		
4.2	1.3			$1.29^{+0.13}_{-0.11}$	$0.72^{+0.05}_{-0.05}$	$1.46^{+0.04}_{-0.04}$	$4.30^{+0.13}_{-0.13}$		
4.7	1.5			$1.14^{+0.12}_{-0.10}$	$0.90^{+0.07}_{-0.05}$	$1.35^{+0.04}_{-0.08}$	$4.33^{+0.25}_{-2.99}$		
5.1	1.6			$1.01^{+0.10}_{-0.09}$	$1.10^{+0.07}_{-0.08}$	$1.23^{+0.08}_{-0.09}$	$1.58^{+2.76}_{-0.00}$		
5.6	1.7			$0.95^{+0.08}_{-0.07}$	$1.29^{+0.08}_{-0.08}$	$1.15^{+0.08}_{-0.07}$	$1.89^{+0.16}_{-0.03}$		
6.1	1.9			$1.00^{+0.07}_{-0.06}$	$1.40^{+0.07}_{-0.06}$	$1.17^{+0.04}_{-0.05}$	$4.10^{+0.73}_{-1.84}$		
6.6	2.1					$1.17^{+0.04}_{-0.05}$	$3.98^{+0.65}_{-1.22}$	$1.17^{+0.04}_{-0.04}$	$5.82^{+0.02}_{-0.02}$
7.1	2.2					$1.12^{+0.05}_{-0.05}$	$3.47^{+0.78}_{-0.48}$	$1.13^{+0.04}_{-0.04}$	$5.80^{+0.10}_{-0.10}$
7.6	2.4					$1.06^{+0.06}_{-0.06}$	$3.53^{+0.69}_{-0.28}$	$1.07^{+0.05}_{-0.05}$	$5.98^{+0.11}_{-0.11}$
8.1	2.5					$1.05^{+0.06}_{-0.06}$	$3.98^{+0.59}_{-0.37}$	$1.05^{+0.06}_{-0.05}$	$6.14^{+0.12}_{-0.11}$
8.6	2.7					$1.11^{+0.05}_{-0.05}$	$4.38^{+0.31}_{-0.29}$	$1.10^{+0.05}_{-0.05}$	$5.84^{+0.01}_{-0.01}$
9.1	2.8					$1.16^{+0.05}_{-0.05}$	$4.42^{+0.19}_{-0.18}$	$1.16^{+0.05}_{-0.05}$	$5.51^{+0.01}_{-0.01}$
9.5	3.0					$1.19^{+0.06}_{-0.05}$	$4.35^{+0.07}_{-0.12}$	$1.20^{+0.05}_{-0.05}$	$5.22^{+0.01}_{-0.01}$
10.0	3.1					$1.21^{+0.07}_{-0.06}$	$4.53^{+0.07}_{-0.13}$	$1.21^{+0.07}_{-0.06}$	$5.38^{+0.01}_{-0.09}$
10.5	3.3					$1.20^{+0.07}_{-0.07}$	$4.63^{+0.08}_{-0.07}$	$1.20^{+0.07}_{-0.07}$	$5.43^{+0.01}_{-0.09}$
11.0	3.4					$1.18^{+0.08}_{-0.07}$	$4.68^{+0.08}_{-0.08}$	$1.17^{+0.08}_{-0.07}$	$5.49^{+0.10}_{-0.17}$
11.5	3.6					$1.03^{+0.09}_{-0.09}$	$9.00^{+1.07}_{-1.02}$	$0.99^{+0.10}_{-0.10}$	$10.22^{+1.08}_{-1.18}$
12.0	3.8					$1.01^{+0.09}_{-0.08}$	$9.73^{+1.08}_{-1.17}$	$0.97^{+0.10}_{-0.09}$	$10.91^{+1.23}_{-1.34}$
12.5	3.9					$1.23^{+0.04}_{-0.04}$	$4.79^{+0.02}_{-0.02}$	$1.23^{+0.04}_{-0.04}$	$5.34^{+0.10}_{-0.10}$
13.0	4.1					$1.24^{+0.05}_{-0.04}$	$4.62^{+0.08}_{-0.08}$	$1.24^{+0.05}_{-0.05}$	$5.08^{+0.10}_{-0.10}$
13.5	4.2					$1.26^{+0.05}_{-0.05}$	$4.51^{+0.09}_{-0.08}$	$1.27^{+0.05}_{-0.05}$	$4.91^{+0.17}_{-0.10}$
14.0	4.4					$1.29^{+0.05}_{-0.04}$	$4.55^{+0.09}_{-0.09}$	$1.30^{+0.05}_{-0.05}$	$4.88^{+0.10}_{-0.10}$
14.4	4.5					$1.30^{+0.07}_{-0.07}$	$4.87^{+0.20}_{-0.26}$	$1.30^{+0.08}_{-0.07}$	$5.22^{+0.30}_{-0.22}$
14.9	4.7					$1.38^{+0.06}_{-0.06}$	$4.22^{+0.11}_{-0.06}$	$1.39^{+0.06}_{-0.06}$	$4.48^{+0.13}_{-0.13}$
15.4	4.8					$1.38^{+0.09}_{-0.08}$	$4.31^{+0.21}_{-0.15}$	$1.39^{+0.09}_{-0.08}$	$4.57^{+0.17}_{-0.23}$
15.9	5.0					$1.40^{+0.07}_{-0.06}$	$4.22^{+0.11}_{-0.11}$	$1.41^{+0.07}_{-0.07}$	$4.42^{+0.13}_{-0.13}$
16.4	5.1					$1.47^{+0.06}_{-0.06}$	$4.07^{+0.11}_{-0.11}$	$1.48^{+0.06}_{-0.06}$	$4.20^{+0.13}_{-0.12}$
16.9	5.3					$1.52^{+0.07}_{-0.06}$	$3.96^{+0.11}_{-0.10}$	$1.54^{+0.07}_{-0.07}$	$4.03^{+0.18}_{-0.12}$
17.4	5.4					$1.54^{+0.07}_{-0.07}$	$3.94^{+0.16}_{-0.10}$	$1.56^{+0.08}_{-0.07}$	$4.01^{+0.18}_{-0.12}$
17.9	5.6					$1.56^{+0.06}_{-0.05}$	$3.91^{+0.11}_{-0.10}$	$1.57^{+0.06}_{-0.06}$	$3.93^{+0.12}_{-0.11}$
18.4	5.7					$1.54^{+0.07}_{-0.07}$	$4.08^{+0.16}_{-0.16}$	$1.55^{+0.08}_{-0.07}$	$4.15^{+0.17}_{-0.17}$
18.9	5.9					$1.60^{+0.06}_{-0.06}$	$3.94^{+0.16}_{-0.15}$	$1.61^{+0.06}_{-0.06}$	$3.96^{+0.17}_{-0.11}$
19.3	6.0					$1.67^{+0.09}_{-0.08}$	$3.85^{+0.21}_{-0.20}$	$1.69^{+0.09}_{-0.09}$	$3.85^{+0.22}_{-0.21}$
19.8	6.2					$1.73^{+0.09}_{-0.09}$	$3.78^{+0.21}_{-0.20}$	$1.74^{+0.09}_{-0.09}$	$3.78^{+0.22}_{-0.21}$
20.3	6.3					$1.35^{+0.10}_{-0.10}$	$6.64^{+0.70}_{-0.58}$	$1.34^{+0.10}_{-0.10}$	$6.96^{+0.75}_{-0.71}$
20.8	6.5					$1.37^{+0.14}_{-0.13}$	$6.64^{+0.85}_{-0.91}$	$1.36^{+0.14}_{-0.14}$	$6.87^{+1.00}_{-0.95}$

Table B.23.: Model Parameters of NGC7331.

R [kpc]	R/R_d	Λ_0	$\sigma_g = 5$ km/s		$\sigma_g = 8$ km/s		$\sigma_g = 11$ km/s	
			s_0	q_0	s_0	q_0	s_0	q_0
0.4	0.1	$0.72^{+0.04}_{-0.04}$	$0.01^{+0.00}_{-0.00}$	$2.82^{+1.36}_{-0.77}$			$0.03^{+0.00}_{-0.00}$	$6.21^{+2.99}_{-1.69}$
1.1	0.3	$1.00^{+0.03}_{-0.02}$	$0.02^{+0.00}_{-0.00}$	$1.63^{+0.75}_{-0.41}$			$0.05^{+0.00}_{-0.00}$	$3.58^{+1.64}_{-0.90}$
1.8	0.5	$1.04^{+0.01}_{-0.01}$	$0.03^{+0.00}_{-0.00}$	$0.90^{+0.27}_{-0.17}$			$0.06^{+0.00}_{-0.00}$	$1.98^{+0.59}_{-0.38}$
2.5	0.8	$0.83^{+0.01}_{-0.01}$	$0.03^{+0.00}_{-0.00}$	$0.58^{+0.09}_{-0.07}$			$0.07^{+0.00}_{-0.00}$	$1.28^{+0.20}_{-0.15}$
3.2	1.0	$0.66^{+0.00}_{-0.00}$	$0.04^{+0.00}_{-0.00}$	$0.51^{+0.08}_{-0.06}$			$0.08^{+0.00}_{-0.00}$	$1.11^{+0.18}_{-0.14}$
3.9	1.2	$0.61^{+0.01}_{-0.01}$			$0.07^{+0.00}_{-0.00}$	$0.79^{+0.14}_{-0.11}$	$0.09^{+0.00}_{-0.00}$	$1.09^{+0.20}_{-0.15}$
4.6	1.4	$0.56^{+0.01}_{-0.01}$			$0.08^{+0.00}_{-0.00}$	$0.76^{+0.13}_{-0.10}$	$0.11^{+0.00}_{-0.00}$	$1.04^{+0.18}_{-0.14}$
5.3	1.6	$0.56^{+0.01}_{-0.01}$			$0.09^{+0.00}_{-0.00}$	$0.83^{+0.17}_{-0.12}$	$0.12^{+0.00}_{-0.00}$	$1.15^{+0.23}_{-0.17}$
6.1	1.8	$0.60^{+0.01}_{-0.01}$			$0.11^{+0.00}_{-0.00}$	$0.97^{+0.23}_{-0.16}$	$0.15^{+0.00}_{-0.00}$	$1.33^{+0.31}_{-0.22}$
6.8	2.1	$0.64^{+0.01}_{-0.01}$					$0.17^{+0.00}_{-0.00}$	$1.47^{+0.25}_{-0.19}$
7.5	2.3	$0.64^{+0.01}_{-0.01}$					$0.19^{+0.00}_{-0.00}$	$1.35^{+0.21}_{-0.16}$
8.2	2.5	$0.63^{+0.01}_{-0.01}$					$0.21^{+0.00}_{-0.00}$	$1.30^{+0.17}_{-0.14}$
8.9	2.7	$0.67^{+0.01}_{-0.01}$					$0.23^{+0.00}_{-0.00}$	$1.32^{+0.15}_{-0.13}$
9.6	2.9	$0.70^{+0.01}_{-0.01}$					$0.26^{+0.00}_{-0.00}$	$1.31^{+0.18}_{-0.14}$
10.3	3.1	$0.70^{+0.01}_{-0.01}$					$0.27^{+0.00}_{-0.00}$	$1.25^{+0.18}_{-0.14}$
11.0	3.3	$0.72^{+0.01}_{-0.01}$					$0.30^{+0.00}_{-0.00}$	$1.24^{+0.16}_{-0.13}$
11.8	3.6	$0.74^{+0.01}_{-0.01}$					$0.32^{+0.00}_{-0.00}$	$1.37^{+0.13}_{-0.11}$
12.5	3.8	$0.77^{+0.01}_{-0.01}$					$0.35^{+0.00}_{-0.00}$	$1.38^{+0.15}_{-0.13}$
13.2	4.0	$0.81^{+0.01}_{-0.01}$					$0.38^{+0.00}_{-0.00}$	$1.37^{+0.12}_{-0.11}$
13.9	4.2	$0.81^{+0.01}_{-0.01}$					$0.40^{+0.00}_{-0.00}$	$1.25^{+0.11}_{-0.10}$
14.6	4.4	$0.75^{+0.01}_{-0.01}$					$0.40^{+0.00}_{-0.00}$	$1.25^{+0.09}_{-0.08}$
15.3	4.6	$0.75^{+0.01}_{-0.01}$					$0.42^{+0.00}_{-0.00}$	$1.19^{+0.09}_{-0.08}$
16.0	4.8	$0.74^{+0.01}_{-0.01}$					$0.44^{+0.00}_{-0.00}$	$1.13^{+0.10}_{-0.09}$
16.7	5.1	$0.76^{+0.00}_{-0.00}$					$0.46^{+0.00}_{-0.00}$	$1.06^{+0.11}_{-0.09}$
17.5	5.3	$0.75^{+0.00}_{-0.00}$					$0.48^{+0.00}_{-0.00}$	$1.07^{+0.11}_{-0.10}$
18.2	5.5	$0.69^{+0.02}_{-0.02}$					$0.48^{+0.01}_{-0.01}$	$1.14^{+0.17}_{-0.14}$
18.9	5.7	$0.51^{+0.04}_{-0.03}$					$0.43^{+0.02}_{-0.01}$	$1.30^{+0.32}_{-0.25}$
19.6	5.9	$0.70^{+0.02}_{-0.02}$					$0.52^{+0.01}_{-0.01}$	$1.12^{+0.20}_{-0.16}$
20.3	6.2	$0.91^{+0.01}_{-0.01}$					$0.62^{+0.00}_{-0.00}$	$1.05^{+0.17}_{-0.13}$
21.0	6.4	$0.89^{+0.03}_{-0.03}$					$0.63^{+0.01}_{-0.01}$	$1.26^{+0.27}_{-0.20}$
21.7	6.6	$1.04^{+0.01}_{-0.01}$					$0.70^{+0.00}_{-0.00}$	$1.41^{+0.26}_{-0.20}$
22.4	6.8	$1.10^{+0.02}_{-0.02}$					$0.75^{+0.01}_{-0.01}$	$1.54^{+0.27}_{-0.21}$
23.2	7.0	$1.06^{+0.02}_{-0.02}$					$0.76^{+0.01}_{-0.01}$	$1.74^{+0.27}_{-0.21}$

Table B.24.: Stability Diagnostics of NGC7331.

R [kpc]	R/R _d	$\sigma_g = 5$ km/s		$\sigma_g = 8$ km/s		$\sigma_g = 11$ km/s		$\sigma_g = 11$ km/s, Turbulent	
		Q _{eff}	$\bar{\lambda}$ [kpc]						
0.4	0.1	2.10 ^{+0.06} _{-0.06}	3.51 ^{+0.18} _{-0.18}			2.10 ^{+0.06} _{-0.06}	3.52 ^{+0.18} _{-0.18}		
1.1	0.3	2.44 ^{+0.05} _{-0.05}	2.53 ^{+0.06} _{-0.06}			2.44 ^{+0.05} _{-0.05}	2.53 ^{+0.06} _{-0.06}		
1.8	0.5	2.18 ^{+0.26} _{-0.41}	0.09 ^{+2.37} _{-0.00}			2.39 ^{+0.05} _{-0.05}	2.40 ^{+0.03} _{-0.03}		
2.5	0.8	1.28 ^{+0.20} _{-0.15}	0.19 ^{+0.03} _{-0.02}			2.04 ^{+0.04} _{-0.04}	2.95 ^{+0.06} _{-0.02}		
3.2	1.0	0.99 ^{+0.15} _{-0.12}	0.30 ^{+0.04} _{-0.04}			1.76 ^{+0.04} _{-0.07}	3.74 ^{+0.03} _{-3.29}		
3.9	1.2			1.39 ^{+0.23} _{-0.18}	0.46 ^{+0.05} _{-0.06}	1.65 ^{+0.05} _{-0.11}	3.97 ^{+0.09} _{-3.36}		
4.6	1.4			1.27 ^{+0.19} _{-0.15}	0.60 ^{+0.06} _{-0.07}	1.53 ^{+0.05} _{-0.13}	4.18 ^{+0.16} _{-3.38}		
5.3	1.6			1.34 ^{+0.23} _{-0.18}	0.68 ^{+3.67} _{-0.07}	1.51 ^{+0.06} _{-0.08}	4.22 ^{+0.16} _{-3.21}		
6.1	1.8			1.53 ^{+0.10} _{-0.21}	0.75 ^{+3.31} _{-0.01}	1.56 ^{+0.07} _{-0.07}	3.94 ^{+0.14} _{-0.24}		
6.8	2.1					1.60 ^{+0.06} _{-0.06}	3.74 ^{+0.08} _{-0.18}	1.62 ^{+0.06} _{-0.06}	4.18 ^{+0.03} _{-0.09}
7.5	2.3					1.53 ^{+0.06} _{-0.06}	3.57 ^{+0.18} _{-0.21}	1.56 ^{+0.06} _{-0.06}	4.15 ^{+0.03} _{-0.03}
8.2	2.5					1.47 ^{+0.06} _{-0.06}	3.60 ^{+0.18} _{-0.27}	1.50 ^{+0.06} _{-0.06}	4.24 ^{+0.04} _{-0.04}
8.9	2.7					1.47 ^{+0.06} _{-0.06}	3.38 ^{+0.17} _{-0.16}	1.51 ^{+0.05} _{-0.05}	4.04 ^{+0.03} _{-0.03}
9.6	2.9					1.46 ^{+0.07} _{-0.07}	3.28 ^{+0.16} _{-0.15}	1.51 ^{+0.07} _{-0.07}	3.93 ^{+0.03} _{-0.09}
10.3	3.1					1.41 ^{+0.08} _{-0.08}	3.32 ^{+0.12} _{-0.16}	1.46 ^{+0.07} _{-0.07}	3.92 ^{+0.03} _{-0.03}
11.0	3.3					1.40 ^{+0.07} _{-0.07}	3.31 ^{+0.07} _{-0.11}	1.44 ^{+0.07} _{-0.07}	3.87 ^{+0.03} _{-0.03}
11.8	3.6					1.44 ^{+0.05} _{-0.05}	3.37 ^{+0.08} _{-0.03}	1.48 ^{+0.05} _{-0.05}	3.84 ^{+0.03} _{-0.09}
12.5	3.8					1.45 ^{+0.07} _{-0.06}	3.37 ^{+0.05} _{-0.05}	1.49 ^{+0.07} _{-0.07}	3.73 ^{+0.11} _{-0.10}
13.2	4.0					1.46 ^{+0.05} _{-0.05}	3.32 ^{+0.03} _{-0.07}	1.50 ^{+0.06} _{-0.05}	3.59 ^{+0.08} _{-0.08}
13.9	4.2					1.38 ^{+0.05} _{-0.05}	3.44 ^{+0.08} _{-0.08}	1.42 ^{+0.06} _{-0.06}	3.72 ^{+0.09} _{-0.09}
14.6	4.4					1.33 ^{+0.05} _{-0.04}	3.74 ^{+0.03} _{-0.08}	1.36 ^{+0.05} _{-0.05}	4.06 ^{+0.10} _{-0.10}
15.3	4.6					1.29 ^{+0.05} _{-0.05}	3.85 ^{+0.09} _{-0.09}	1.31 ^{+0.05} _{-0.05}	4.19 ^{+0.10} _{-0.10}
16.0	4.8					1.24 ^{+0.06} _{-0.05}	4.04 ^{+0.10} _{-0.15}	1.26 ^{+0.06} _{-0.06}	4.35 ^{+0.18} _{-0.11}
16.7	5.1					1.20 ^{+0.06} _{-0.05}	4.14 ^{+0.14} _{-0.08}	1.22 ^{+0.06} _{-0.06}	4.47 ^{+0.16} _{-0.16}
17.5	5.3					1.20 ^{+0.06} _{-0.06}	4.27 ^{+0.14} _{-0.14}	1.21 ^{+0.06} _{-0.06}	4.63 ^{+0.17} _{-0.23}
18.2	5.5					1.18 ^{+0.09} _{-0.08}	4.59 ^{+0.25} _{-0.30}	1.19 ^{+0.09} _{-0.09}	4.96 ^{+0.36} _{-0.34}
18.9	5.7					1.10 ^{+0.14} _{-0.13}	5.68 ^{+0.66} _{-0.62}	1.09 ^{+0.14} _{-0.13}	6.45 ^{+0.99} _{-0.81}
19.6	5.9					1.17 ^{+0.11} _{-0.10}	4.78 ^{+0.35} _{-0.33}	1.17 ^{+0.11} _{-0.10}	5.12 ^{+0.56} _{-0.44}
20.3	6.2					1.26 ^{+0.10} _{-0.09}	4.15 ^{+0.22} _{-0.26}	1.27 ^{+0.10} _{-0.09}	4.24 ^{+0.30} _{-0.28}
21.0	6.4					1.35 ^{+0.13} _{-0.12}	4.03 ^{+0.36} _{-0.34}	1.36 ^{+0.14} _{-0.13}	4.10 ^{+0.46} _{-0.36}
21.7	6.6					1.52 ^{+0.12} _{-0.10}	3.54 ^{+0.25} _{-0.23}	1.54 ^{+0.12} _{-0.11}	3.50 ^{+0.21} _{-0.25}
22.4	6.8					1.61 ^{+0.11} _{-0.10}	3.35 ^{+0.19} _{-0.22}	1.63 ^{+0.12} _{-0.11}	3.27 ^{+0.20} _{-0.23}
23.2	7.0					1.65 ^{+0.10} _{-0.09}	3.34 ^{+0.19} _{-0.18}	1.67 ^{+0.10} _{-0.09}	3.30 ^{+0.20} _{-0.19}

BIBLIOGRAPHY

- Agertz, O., Lake, G., Teyssier, R., Moore, B., Mayer, L., & Romeo, A. B. 2009a, MNRAS, 392, 294
- Agertz, O., Teyssier, R., & Moore, B. 2009b, MNRAS, 397, L64
- Barroso, J. F. 2003, PhD thesis, University of Nottingham
- Begum, A., Chengalur, J. N., & Bhardwaj, S. 2006, MNRAS, 372, L33
- Bertin, G., & Romeo, A. B. 1988, A&A, 195, 105
- Binney, J., & Merrifield, M. 1998, Galactic Astronomy (Princeton University Press, Princeton, NJ, US)
- Binney, J., & Tremaine, S. 2008, Galactic Dynamics: Second Edition (Princeton University Press, Princeton, NJ, US)
- Blitz, L. 1993, in Protostars and Planets III, ed. E. H. Levy & J. I. Lunine, 125–161
- Bolatto, A. D., Leroy, A. K., Rosolowsky, E., Walter, F., & Blitz, L. 2008, ApJ, 686, 948
- Bonazzola, S., Heyvaerts, J., Falgarone, E., Perault, M., & Puget, J. L. 1987, A&A, 172, 293
- Bournaud, F., & Elmegreen, B. G. 2009, ApJL, 694, L158
- Bournaud, F., et al. 2008, A&A, 486, 741
- Burkert, A. 2006, Comptes Rendus Physique, 7, 433
- Burkert, A., et al. 2010, ApJ, 725, 2324
- Ceverino, D., & Klypin, A. 2009, ApJ, 695, 292
- Cowie, L. L., Hu, E. M., & Songaila, A. 1995, AJ, 110, 1576
- Cresci, G., et al. 2009, ApJ, 697, 115
- Daddi, E., Cimatti, A., Renzini, A., Fontana, A., Mignoli, M., Pozzetti, L., Tozzi, P., & Zamorani, G. 2004, ApJ, 617, 746
- de Blok, W. J. G., Walter, F., Brinks, E., Trachternach, C., Oh, S., & Kennicutt, R. C. 2008, AJ, 136, 2648
- Dehnen, W., & Binney, J. J. 1998, MNRAS, 298, 387
- Dekel, A., Sari, R., & Ceverino, D. 2009a, ApJ, 703, 785
- Dekel, A., et al. 2009b, Nature, 457, 451

- Dutta, P., Begum, A., Bharadwaj, S., & Chengalur, J. N. 2008, *MNRAS*, 384, L34
- . 2009a, *MNRAS*, 398, 887
- . 2009b, *MNRAS*, 397, L60
- Elmegreen, B. G. 1999, in *Star Formation 1999*, ed. T. Nakamoto, 3–5
- Elmegreen, B. G., & Elmegreen, D. M. 2005, *ApJ*, 627, 632
- Elmegreen, B. G., Elmegreen, D. M., Fernandez, M. X., & Lemonias, J. J. 2009, *ApJ*, 692, 12
- Elmegreen, B. G., Kim, S., & Staveley-Smith, L. 2001, *ApJ*, 548, 749
- Elmegreen, B. G., & Scalo, J. 2004, *ARAA*, 42, 211
- Elmegreen, D. M., Elmegreen, B. G., & Hirst, A. C. 2004, *ApJL*, 604, L21
- Elmegreen, D. M., Elmegreen, B. G., Rubin, D. S., & Schaffer, M. A. 2005, *ApJ*, 631, 85
- Engargiola, G., Plambeck, R. L., Rosolowsky, E., & Blitz, L. 2003, *ApJS*, 149, 343
- Field, G. B., Goldsmith, D. W., & Habing, H. J. 1969, *ApJL*, 155, L149+
- Förster Schreiber, N. M., et al. 2009, *ApJ*, 706, 1364
- Fridman, A. M., Polyachenko, V. L., Aries, A. B., & Poliakov, I. N. 1984, *Physics of gravitating systems. I. Equilibrium and stability.* (Springer Verlag, Berlin, Germany)
- Frisch, U. 1995, *Turbulence. The legacy of A. N. Kolmogorov.* (Cambridge University Press, Cambridge, UK)
- Fukui, Y., et al. 1999, *PASJ*, 51, 745
- Genzel, R., et al. 2006, *Nature*, 442, 786
- . 2008, *ApJ*, 687, 59
- Gil de Paz, A., et al. 2007, *ApJS*, 173, 185
- Helfer, T. T., Thornley, M. D., Regan, M. W., Wong, T., Sheth, K., Vogel, S. N., Blitz, L., & Bock, D. 2003, *ApJS*, 145, 259
- Hubble, E. P. 1936, *Realm of the Nebulae* (Yale University Press, New Haven, CT, US)
- Hughes, A., et al. 2010, *MNRAS*, 406, 2065
- Jog, C. J., & Solomon, P. M. 1984, *ApJ*, 276, 114
- Karttunen, H., Krüger, P., Oja, H., Poutanen, M., & Donner, K. J., eds. 2007, *Fundamental Astronomy* (Springer Verlag, Berlin, Germany)
- Kennicutt, Jr., R. C. 1998, *ARAA*, 36, 189
- Kennicutt, Jr., R. C., et al. 2003, *PASP*, 115, 928
- Kim, S., Dopita, M. A., Staveley-Smith, L., & Bessell, M. S. 1999, *AJ*, 118, 2797
- Kim, S., et al. 2007, *ApJS*, 171, 419
- Kim, W.-T., & Ostriker, E. C. 2007, *ApJ*, 660, 1232
- Kolmogorov, A. 1941, *Akademiia Nauk SSSR Doklady*, 30, 301
- Krumholz, M., & Burkert, A. 2010, *ApJ*, 724, 895
- Larson, R. B. 1981, *MNRAS*, 194, 809

- Lazarian, A., & Pogosyan, D. 2000, *ApJ*, 537, 720
- Leroy, A. K., Walter, F., Brinks, E., Bigiel, F., de Blok, W. J. G., Madore, B., & Thornley, M. D. 2008, *AJ*, 136, 2782
- Leroy, A. K., et al. 2009, *AJ*, 137, 4670
- Lin, C. C., & Shu, F. H. 1966, *Proceedings of the National Academy of Science*, 55, 229
- Lin, C. C., Yuan, C., & Shu, F. H. 1969, *ApJ*, 155, 721
- Madore, B. F. 1977, *MNRAS*, 178, 1
- McKee, C. F., & Ostriker, E. C. 2007, *ARAA*, 45, 565
- Pahre, M. A., Ashby, M. L. N., Fazio, G. G., & Willner, S. P. 2004, *ApJS*, 154, 235
- Petric, A. O., & Rupen, M. P. 2007, *AJ*, 134, 1952
- Puech, M. 2010, *MNRAS*, 406, 535
- Rafikov, R. R. 2001, *MNRAS*, 323, 445
- Robertson, B. E., & Bullock, J. S. 2008, *ApJL*, 685, L27
- Romeo, A. B. 1990, PhD thesis, SISSA, Trieste, Italy
- . 1992, *MNRAS*, 256, 307
- . 1994, *A&A*, 286, 799
- Romeo, A. B., Burkert, A., & Agertz, O. 2010, *MNRAS*, 407, 1223
- Romeo, A. B., & Wiegert, J. 2011, Preprint (arXiv:1101.4519)
- Safronov, V. S. 1960, *Annales d'Astrophysique*, 23, 979
- Shapiro, K. L., et al. 2008, *ApJ*, 682, 231
- Shu, F. H. 1968, *Astronomical Journal*, Vol. 73, p. 201, 73, 201
- . 1992, *The physics of astrophysics. Volume II: Gas dynamics.* (University Science Books, Mill Valley, CA, US)
- Solomon, P. M., Rivolo, A. R., Barrett, J., & Yahil, A. 1987, *ApJ*, 319, 730
- Tacconi, L. J., et al. 2010, *Nature*, 463, 781
- Tamburro, D., Rix, H., Leroy, A. K., Mac Low, M., Walter, F., Kennicutt, R. C., Brinks, E., & de Blok, W. J. G. 2009, *AJ*, 137, 4424
- Toomre, A. 1964, *ApJ*, 139, 1217
- van Dyke, M. 1982, *An album of fluid motion* (Parabolic Press, Stanford, CA, US)
- Vazquez-Semadeni, E., & Gazol, A. 1995, *A&A*, 303, 204
- Wada, K., Meurer, G., & Norman, C. A. 2002, *ApJ*, 577, 197
- Wadadekar, Y., Casertano, S., & de Mello, D. 2006, *AJ*, 132, 1023
- Walter, F., Brinks, E., de Blok, W. J. G., Bigiel, F., Kennicutt, R. C., Thornley, M. D., & Leroy, A. 2008, *AJ*, 136, 2563
- Wang, B., & Silk, J. 1994, *ApJ*, 427, 759
- Wiegert, J. 2010, Master's thesis, University of Gothenburg, Sweden

Wilson, T. L., Rohlfs, K., & Hüttemeister, S. 2009, Tools of Radio Astronomy (Springer-Verlag, Berlin, Germany)